SEISMIC AND ROCK-PHYSICS CHARACTERIZATION OF FRACTURED RESERVOIRS

A DISSERTATION
SUBMITTED TO THE DEPARTMENT OF GEOPHYSICS
AND THE COMMITTEE ON GRADUATE STUDIES
OF STANFORD UNIVERSITY
IN PARTIAL FULFILLMENT OF THE REQUIREMENTS
FOR THE DEGREE OF
DOCTOR OF PHILOSOPHY

By
Li Teng
June, 1998

I certify that I have read this dissertation and that in my opinion it is fully adequate, in scope and quality, as a dissertation for the degree of Doctor of Philosophy.

Gerald M. Mavko
(Principal Adviser)

I certify that I have read this dissertation and that in my opinion it is fully adequate, in scope and quality, as a dissertation for the degree of Doctor of Philosophy.

Jerry M. Harris

I certify that I have read this dissertation and that in my opinion it is fully adequate, in scope and quality, as a dissertation for the degree of Doctor of Philosophy.

Mark D. Zoback

Approved for the University Committee on Graduate Studies:

ABSTRACT

Aligned fractures induce anisotropy into rock mechanical properties. Seismic shear-wave splitting techniques have been used successfully to recover the symmetry-plane orientation and the magnitude of the shear-wave anisotropy. This orientation and magnitude correlate with the subsurface fractures' orientation and intensity. Shear-wave data are not affected by the fluid properties. P-wave data are cheaper to acquire, have a higher signal-to-noise ratio, contain pore-fluid information, and are more available in 3D. However, the use of P-wave data in fracture detection and characterization is not fully exploited.

I develop a methodology for using single-component 3D P-wave data in characterizing naturally-occurring subsurface fractures, with the help of prior knowledge acquired from geological observations, logs, and shear wave surveys. This characterization includes determining the fracture orientation, density distribution, aperture, and fracture-filling material under the in-situ temperature and pressure conditions.

I combine the elastic properties of fractured rocks and the reflectivity formulas in anisotropic media to derive the relationship between P-wave amplitude anisotropy and fracture physical properties. Using Hudson's penny-shaped crack model, I show that:

1) reflectivity anisotropy increases with crack density and fracture-filling fluid bulk modulus, and decreases with crack aspect ratio;

2) under high-frequency conditions, it decreases with the background rock's Poisson's ratio;

3) the same fracture set induces more reflectivity anisotropy under high-frequency conditions than under low-frequency conditions.

I demonstrate the first-order mathematical equivalence among three commonly used fracture models, including Hudson's first-order penny-shaped-crack model, Schoenberg-Muir's thin-layer model, and Pyrak-Nolte's frequency-dependent slip-interface model. This equivalence shows that we can explain the observed seismic anisotropy in terms of different fracture network configuration models. The suitability of each fracture interpretation should be judged by the in situ fracture observations.

The above results serve as a guide for fracture interpretation in field studies. I use the seismic datasets from the Fort Fetterman site to explore and test the feasibility and reliability of the using P-wave anisotropy in conjunction with S-wave data and other available information to characterize the subsurface fracture network. The Fort-Fetterman site is located at the southwestern margin of the Powder River Basin, in Converse County, east-central Wyoming. The target reservoirs at the Niobrara and the Frontier formations belong to the lower Cretaceous strata. The data available for this study include well log data, multi-component VSP data, 2D shear wave data (Line GRI-1 along north-south direction, and Line GRI-4 along east-west direction), and 3D P-wave data. Geological observations of outcrops and FMS logs show that a set N110^{o}E+/-15^{o} fractures appear in the Tertiary formations, and locally in the Cretaceous formations; a set of N70^{o}E+/-10^{o} only occurs in the Cretaceous formations, including the Niobrara and the Frontier formations. Dipole-sonic-log analysis shows that the fracture orientation is along the N80^{o}E+/-10^{o} direction at the reservoir level, and that the fractures tend to concentrate in low-porosity, high-clay-content, thin layers rather than distributed evenly over large intervals. These results are consistent with the outcrop observations. Shear-wave rotation analysis was applied to both VSP and 2D-surface-shear-wave data. Whole-trace rotation shows a direction of N96^{o}E+/-10^{o} for the VSP data, N105^{o}E+/-10^{o} for the 2D data along Line GRI-4, N105^{o}E+/-15^{o} for the south part of Line GRI-1, and N75^{o}E+/-15^{o} for the north

part of Line GRI-1. To recover the fracture information at the reservoir level, layer-stripping analysis to remove the overburden effects is required. Layer-stripping analysis is only successful in the CDP ranges along Line GRI-4 where the signal-to-noise ratio is high. At those CDP locations, the shear-wave data give a fracture orientations of N75°E+/-10° at the reservoir level. I derive the crack density from the shear-wave data. The P-wave traveltime anisotropy predicts an apparent fracture direction of N39°E+/-8°. This direction, however, is likely to be caused by the effect of dip. In order to get meaniful fracture information from the P-wave traveltime data, we need a fracture effect larger than the dip effect, or a higher signal-to-noise ratio. P-wave amplitude analysis also gives a fracture orientation of N87°E+/-18°. The magnitude of P-wave amplitude azimuthal variation is also higher than that predicted by modeling. This is because the average crack density inferred from the P- and S-wave traveltime data can be much less than the crack density in the thin fractured layers inferred from the P-wave amplitude azimuthal variation at the boundary of the thin fractured layers.

I investigate the type of subsurface fracture information that can be extracted from seismic shear wave analysis, and show how rock physics and geostatistics can be combined to give realistic interpretations. The synthetic results show that seismic analysis can help to constrain predictions of the spatial distribution of fracture densities, which, in turn, have a very important impact on fluid flow responses. However, the inference of fracture densities from shear wave splitting analysis can be unreliable due to uncertainties about some key parameters, including fracture specific stiffness, fracture orientation, and background lithology variations. The uncertainty in fracture orientation distribution does not affect significantly the final fracture density estimates. The common assumption that anisotropy is induced by a single set of parallel fractures can lead to misinterpretation of the fracture density field. In addition, the length and orientation distributions of the fractures are crucial factors determining connectivity of the fracture system and, therefore, have an important impact on fluid recovery. The uncertainties can be reduced by considering additional

information about the subsurface fracture system such as that coming from analog outcrop data, geomechanical studies and production data. A reliable knowledge of the lithology of the matrix rock is also important.

ACKNOWLEDGMENTS

I feel very privileged to have studied at Stanford University for five and one-half years. Now that my Ph.D. program has almost come to a close, I want to thank all the faculty members, staff members, and students in the Geophysics Department who have made my stay a rewarding and pleasant experience.

I sincerely thank my advisor, Professor Gary Mavko, for his inspiring advice, countless hours of scientific discussions, teaching of invaluable presentation skills, and continuous support. I am grateful to him and Professor Amos Nur, whose continuous effort makes many research projects possible and fruitful at the Stanford Rock Physics Group. I would like to express my gratitude to Professors Jim Berryman, Kefeng Liu, Jerry Harris, and Mark Zoback for serving on my committee and providing constructive suggestions.

I would like to thank Professor Francis Muir, Atilla Aydin, Jack Dvorkin, Biondo Biondi, Tapan Mukerji , Dan Moos, Colleen Barton, and Wei Chen for many insightful talks; Emmanual Gringarten for his help and contribution to the work presented in this thesis; Ralf Schulz for letting me modify and use his reflectivity program. I thank Margaret Muir and Linda Farwell for their great deal of help during my study here. I thank Fannie Toldi for her help with editing my thesis. I thank Madhumita Sengupta, Tapan Mukerji, Mario Gutierrez, Mickaele Ravelec, and Christina Chan for once being my officemates, and always being my friends. I am grateful to Dr. Barbara Mavko for her encouragement and friendship. My stay at Stanford was made enjoyable by many other people: Manika Prasad, Ran Bachrach, Rubina Sen, Yuguang Liu, Hui Wang, Per Avseth, Doron Galmudi, James Packwood and many, many others. I thank them.

My research was partly funded by the Gas Research Institute Contract 5094-210-3235 and the Department of Energy. I am grateful for their financial support. The scientists with Arco Exploration and Production, especially Keith Katahara, Robert Withers, Dennis Corrigan, Gayle Laurin, and Tracey Skopinski, offered me a tremendous amount of help in getting me the data and discussing the research. I benefited from many discussions and a wonderful summer time working with Leon Thomsen and Mike Mueller at Amoco World Wide Exploration and Production Company. I also thank William Soroka, Wenjie Dong, and Paul Cunningham for the fruitful summer with Mobil Technology Company. I thank Bertram Nolte, with M.I.T., and Ilya Tsvankin, with Colorado School of Mines for sending me their papers for references.

Last but not least, I thank my parents for their support and encouragement during all the easy and tough time of my life.

CONTENTS

LIST OF TABLES

LIST OF FIGURES

CHAPTER 1

INTRODUCTION

1.1 Research Motivation and Objectives

Because fractures largely control in-situ permeability and rock strength, fracture detection is very important in hydrocarbon recovery, mine stability, waste isolation, and earthquake studies.

In the oil and gas industry, the emphasis is shifting from basic exploration to improved recovery rates of existing fields. When there are fracture-controlled reservoirs, understanding the subsurface fracture networks is important to optimize well planning and production. A large portion of oil and natural gas in the world is trapped in tight reservoirs (Nelson, 1985). In such formations, often the only practical means of extracting the gas/oil is to use the increased drainage surface provided by natural fractures, which controls fluid storage and mobility. The reverse effect is that fractures can provide the paths for the injected steam or water to bypass the matrix pores, and cause the slow-down or termination of hydrocarbon production (Massonnat, 1994). In both situations, locating the subsurface fractured zones and obtaining the fractures' physical properties, such as fracture orientation and aperture, will help to optimize the field development plan.

Although many logging tools and log-analysis methods, such as the borehole televiewer and formation MicroScanner (Schlumberger, 1989), have been designed to view the subsurface fractures cutting through a borehole, their usage is limited by the high cost and small sampling area. The information obtained is very valuable direct information about the subsurface fractures' geometry, fluid content, spacing, and connectivity. However, the interpolation of fracture-network properties over a field is inevitably inaccurate when there are only a few wells with fracture information.

A seismic survey has the advantages of low cost, wide coverage, and deep penetration. Theoretical and laboratory studies (Nur, 1971; Crampin and Bamford, 1977; Hudson, 1980, 1981, 1990, 1994; Yin, 1992) have shown that fractures can induce anisotropy into seismic properties of the rocks. The seismic survey has the potential to be a powerful tool to detect and characterize subsurface fractures. The mainstream in seismic fracture detection uses the shear-wave splitting techniques first suggested by Alford (1986). These techniques have been used successfully in locating the fractured zones in many field studies (Queen and Rizer, 1990; Liu, Crampin, and Queen, 1991; Mueller, 1991, 1992, 1994; Lewis et al., 1991; Winterstein and Meadows, 1991a, b).

P-wave data are cheaper to acquire, have a higher signal-to-noise ratio, and are more commonly available in 3D than shear-wave data. However, the use of P-wave data in fracture detection and characterization is not fully exploited. There have been both theoretical work and field observations showing the correlation between the fractured zones and the azimuthal variation in P-wave amplitude and velocity (Crampin and Bamford., 1977; Lefeuvre, 1993; Lynn et al., 1996; Ramos and Davis, 1997; Rueger 1996). The outputs of these studies were often the anisotropy mapped over the survey areas. Some authors converted the amount of anisotropy to crack density, according to the penny-shaped crack model (Hudson, 1980, 1981, 1990, 1994). However, they did not take into account realistic in-situ physical conditions, including subsurface temperature, pressure, nature of fracture-filling material, seismic frequency, and the hydraulic interaction between fractures. Critical problems remain in estimating the subsurface fracture properties under in-situ reservoir conditions. Gaps also exist in integrating all the information measured at core, log, and seismic (including P- and S-wave surveys) scales for fracture characterization.

The objective of this thesis is to develop methodologies for characterizing naturally-occurring subsurface fractures, with emphasis on using single-component 3D P-wave data with the help of prior knowledge acquired from logs and shear wave surveys. This characterization includes determining the fracture orientation, density distribution, aperture, fracture-filling material, and fracture hydraulic connectivity under the in-situ temperature and pressure conditions. The significance of the fracture-distribution mapping over the 3D-survey area is the potential for constraining the underlying permeability distribution, which is critical for field planning and development.

1.2 Description of Chapters

The chapters in this thesis present the theories and applications by which subsurface fractures can be characterized by the use of P-wave data, with the help of the rock and fracture information acquired from well logs and shear-wave seismic surveys.

Chapter 2 describes the methodology of fracture-network characterization using seismic anisotropy. I first discuss various elasticity theories of fractured media; these theories link the physical properties of fractures to seismic anisotropy. These theories include the first-order penny-shaped crack model (Hudson, 1981, 1990; Thomsen, 1995), the thin-layer model (Schoenberg and Muir, 1989), and the frequency-dependent slip-interface model (Pyrak-Nolte et al., 1990a, b). I found that these models are mathematically equivalent descriptions of fractured media. The same amount of anisotropy in a fractured rock can be caused by either penny-shaped cracks or large fractures cutting through the rock. To use the acquired seismic data to characterize the in-situ fractures, we need prior knowledge of the fracture shape, so we can choose the appropriate model.

I then review the fracture-induced traveltime/velocity anisotropy in both P- and S-wave data, and derive the equations for P-wave reflectivity at the boundaries of fractured rocks. When parallel vertical fractures are the sources for anisotropy, the traveltime and the P-wave reflectivity vary with azimuth. I explore the effects of fracture intensity, aperture, fracture-filling fluids, subsurface temperature, pressure, fracture hydraulic connectivity, and seismic frequency, on the velocity and amplitude azimuthal variations.

The seismic response over fractured formations is frequency-dependent (Biot, 1956; Mavko and Nur, 1979). I analyzed the characteristic frequency of local fluid flow between fractures and the surrounding matrix through the fractures' permeable walls.

In the last section of Chapter 2, I provide an example of using a probability method to quantify the uncertainty in the fracture density estimation based on shear wave splitting data. This is an anisotropic extension of the probability method proposed by Mavko and Mukerji (1995) to quantify the uncertainty in hydrocarbon indicators.

With this theoretical framework, I proceed to apply and test the methodology on field data. I have access to data from well logs, a 4-component shear-wave VSP survey, two 2D lines of a 9-component surface seismic survey, and a 3D P-wave survey collected over a tight gas reservoir at the Fort Fetterman site, in the Powder River Basin, east-central Wyoming. The data were made available by the funding from the Gas Research Institute, Department of Energy, ARCO, and AMOCO.

Chapter 3 analyzes the well-log data at the Fort Fetterman site, and gathers the typical rock property data at the reservoir level. These properties include the P- and S-wave velocities, densities, clay content, pore fluids, evidence of overpressure, and fracture indicators. The main goal is to assist fracture interpretation by the use of the seismic anisotropy described in Chapter 4. Understanding the basic rock properties is also an integral part of understanding the fractured reservoirs.

Chapter 4 analyzes the velocity anisotropy in the VSP and 2D surface shear-wave data, and the azimuthal variation in the 3-D P-wave velocity and amplitude. I give an integrated interpretation of the subsurface fracture system at the reservoir level.

This interpretation is based on the seismic anisotropy as well as the results of the well-log analysis.

Chapter 5 presents the collaborative work with Emmanuel Gringarten, Gary Mavko, and André Journel. We investigate the types of subsurface fracture information that can be extracted from seismic shear-wave analysis; show how rock physics and geostatistics can be combined to give realistic interpretations; illustrate the variability (non-uniqueness) in the interpretations by showing equally probable fracture predictions; and evaluate the uncertainty in rock physics interpretations by looking at the results of some simple fluid-flow simulation.

In the appendix, I give readers an overview of the structural features, regional stratigraphy, and fracture observations at the study site. It contains a summary of the report, "Regional Geological Framework and Site Description" (Walters, Chen, and Mavko, 1994). I also review observations of fracture existence and attributes in the southern Powder River Basin (May et al., 1996), and at Moxa Arch and the adjacent Green River Basin in southwestern Wyoming (Laubach, 1991, 1992a, 1992b; Dutton et al., 1992).

1.3 References

Alford, R. M., 1986, Shear data in the presence of azimuthal anisotropy: Dilley, Texas, SEG 56th Annual Meeting Expanded Abstracts.

Biot, M.A., 1956, Theory of propagation of elastic waves in a fluid saturated porous solid. I. Low frequency range and II. Higher-frequency range, J. Acoust. Soc. Amer., **28**, 168-191.

Crampin, S., and Bamford, D., 1977, Inversion of P-wave velocity anisotropy, Geophys. J R. astr. Soc., **49**, 123.

Dutton, S.P., Hamlin, H. S., and Laubach, S. E., 1992, Geologic controls on reservoir properties of low-permeability sandstone, Frontier Formation, Moxa Arch, southwest Wyoming: The University of Texas at Austin, Bureau of Economic

Geology, topical report no. GRI-92/0127, prepared for the Gas Research Institute, 199 p.

Hudson, J. A., 1980, Overall properties of a cracked solid, Math. Proc. Camb. Phil. Soc., **88**, 371-384.

Hudson, J. A., 1981, Wave speeds and attenuation of elastic waves in material containing cracks: Geophys. J. Roy. Astr. Soc., **64**, 133-150.

Hudson, J. A., 1990, Overall elastic properties of isotropic materials with arbitrary distribution of circular cracks, Geophys. J. Int., **102**, 465-469.

Hudson, J. A., 1994, Overall properties of anisotropic materials containing cracks, Geophys. J. Int., **116**, 279-282.

Laubach, S.E., 1991, Fracture patterns in low-permeability-sandstone gas reservoir rocks in the Rocky Mountain region, SPE Paper 231853, Proceedings, Joint SPE Rocky Mountain regional meeting/low-permeability reservoir symposium, 501-510.

Laubach, S.E., 1992a, Identifying key reservoir elements in low-permeability sandstones: natural fractures in the Frontier Formation, southwestern Wyoming, In Focus-Tight Gas Sands, GRI, Chicago, IL, **8**, No. 2, 3-11.

Laubach, S.E., 1992b, Fracture networks in selected Cretaceous sandstones of the Green River and San Juan basins, Wyoming, New Mexico, and Colorado, in Geological Studies Relevant to Horizontal Drilling in Western North America, ed. Schmoker, J.W., Coalson, E.B., Brown, C.A., 115-127.

Lefeuvre, Frederic, 1993, Fracture related anisotropy detection and analysis; and if the P-waves were enough?, SEG Expanded Abstracts, **64**, 942-945.

Lewis, C., Davis, T.L., and Vuillermoz, C., 1991, Three-dimensional multicomponent imaging of reservoir heterogeneity, Silo Field, Wyoming, Geophysics, **56**, 2048-2056.

Liu, E., Crampin, S., and Queen, J., 1991, Fracture detection using crosshole surveys and reverse vertical seismic profiles at the Conoco Borehole Test Facility, Oklahoma, Geophys. J. Int., **107**, 449-463.

Lynn, H., Simon, K. M., Bates, R., and Van Dok, R., Azimuthal anisotropy in P-wave 3-D (multiazimuth) data, 1996, Leading Edge, **15**, No. 8, 923-928.

Massonnat, G. J., Umbhauer, F., and Odonne, F., 1994, The use of 3-D seismic in the understanding and monitoring of waterflooding in a naturally fractured gas reservoir, AAPG Bulletin, **78,** no. 7, 1155.

Mavko, G., and Mukerji, T., 1995, A rock physics strategy for quantifying uncertainty in common hydrocarbon indicators, American Geophysical Union 1995 fall meeting Eos Transactions, **76**, No. 46, 600.

Mavko, G., and Nur, A., 1979, Wave attenuation in partially saturated rocks, Geophysics, **44**, No. 2, 161-178.

May, J., Mount, V., Krantz, B., Parks, S., and Gale, M., 1996, Structural framework of southern Powder River Basin: a geologic context for deep, northeast-trending basement fractures, ARCO-GRI fractured reservoir project report.

Mueller, M. C., 1991, Prediction of lateral variability in fracture intensity using multicomponent shear-wave surface seismic as a precursor to horizontal drilling in the Austin Chalk, Geophys. J. Int., **107**, 409-415.

Mueller, M. C., 1992, Using shear waves to predict lateral variability in vertical fracture intensity, Geophysics: The Leading Edge of Exploration, **11**, No. 2, 29.

Mueller, M.C., 1994, case studies of the dipole shear anisotropy log, SEG Expanded Abstract, **64**, 1143-1146.

Nelson, R. A., 1985, Geologic Analysis of Naturally Fractured Reservoirs, Houston : Gulf Pub. Co., Book Division, c1985.

Nur, A., 1971, Effects of stress on velocity anisotropy in rocks with cracks, J. Geophys. Res., **76**, 2022-2034.

Pyrak-Nolte, L. J., Myer, L. R., Cook, N. G. W., 1990a, Transmission of seismic waves across single natural fractures, J. Geophys. Res., **95**, No. B6, 8617-8638.

Pyrak-Nolte, L. J., Myer, L. R., Cook, N. G. W., 1990b, Anisotropy in seismic velocities and amplitudes from multiple parallel fractures, J. Geophys. Res., **95** No. B7, 11345-11358.

Queen, J.H., Rizer, W.D., 1990, An integrated study of seismic anisotropy and the natural fracture system at the Conoco borehole test facility, Kay county, Oklahoma, J. Geophys. Res., **95**, 11255-11273

Ramos, A.C.B., Davis, T., 1997, 3-D AVO analysis and modeling applied to fracture detection in coalbed methane reservoirs, Geophysics, **62**, 1683-1695

Rueger, A., 1996, Variation of P-wave reflectivity with offset and azimuth in anisotropic media, SEG Annual Meeting Abstracts, **66**, 1810-1813.

Schlumberger, 1989, Log interpretation principles/applications, Schlumberger Educational Services.

Schoenberg, M and Muir, F, 1989, A calculus for finely layered anisotropic media, Geophysics, **54**, 581-589.

Thomsen, L., 1995, Elastic anisotropy due to aligned cracks in porous rock, Geophysical Prospecting, **43**, No. 6, 805-829.

Walters, R., Chen, W., Mavko, G., 1994, Regional geological framework and site description, DOE report.

Winterstein, D.F., Meadows, M.A., 1991a, Shear-wave polarizations and subsurface stress directions at Lost Hills field, Geophysics, **56**, 1331-1348.

Winterstein, D.F., Meadows, M.A., 1991b, Changes in shear-wave polarization azimuth with depth in Cymric and Railroad Gap oil fields, Geophysics, **56**, 1349-1364.

Yin, H., 1992, Acoustic velocity and attenuation of rocks: isotropy, intrinsic anisotropy, and stress-induced anisotropy, Ph.D. dissertation, Stanford University, Stanford, California.

CHAPTER 2

METHODOLOGY OF FRACTURE-NETWORK CHARACTERIZATION USING SEISMIC ANISOTROPY

2.1 Introduction

Aligned fractures induce anisotropy into the mechanical properties of rocks. The anisotropy will be observed in the velocity and amplitude of seismic waves passing through the fractured rocks. Therefore, to detect fractures, we can use the measurements of seismic anisotropic phenomena.

To date, the most common approach for seismic fracture-detection has been the use of shear-wave anisotropy. Nur and Simmons (1969) were among the first to observe fracture-induced shear anisotropy in the lab. Most modern field applications of shear-wave splitting techniques are based on a tensor rotation of wavefield as published by Alford (1986). There have been many successful applications in which shear-wave splitting was used to locate the fractured zones and predict the fracture orientation in the field. However, compared to P-wave data, shear-wave data are more expensive to collect, have lower signal-to-noise ratio, and are often not available in 3D. Furthermore, the previous studies often take the seismic-velocity anisotropy as the final results. They have rarely been used to determine the fractures' physical properties. These properties include the fracture density distribution, aperture, fracture-filling material, and fracture hydraulic connectivity under in-situ temperature and pressure conditions.

I present in this chapter the theoretical framework for clarifying the links between seismic velocity and amplitude anisotropy and the fractures' physical properties. Section 2.2 reviews, for fractured rocks, the elasticity theories that link the seismic properties of the rocks with the physical properties of the rocks, the fractures, and the pore fluids. I will show the first-order mathematical equivalence among three commonly used fracture models, including the first-order penny-shaped crack model (Hudson, 1981, 1990; Thomsen, 1995), the thin-layer model (Schoenberg and Muir, 1989), and the frequency-dependent slip-interface model (Pyrak-Nolte et al., 1990a, 1990b). This equivalence shows that we can explain the observed seismic anisotropy in terms of different models of fracture network configuration. The suitability of each fracture interpretation should be judged by the in situ fracture observations.

I review in Section 2.3 the published studies of the relationship between the P- and S-wave velocity anisotropy and the fracture-network physical parameters. I will show the numerical modeling results of the velocity anisotropy patterns of rocks containing parallel fractures, cone distribution of fractures, and two perpendicular sets of fractures for the different fracture-filling fluids under various temperature and pressure conditions.

When vertical, parallel fractures are present in the rocks, the reflectivity will vary with azimuth as well as offset. I call this the **a**mplitude **v**ersus **o**ffset and a**z**imuth variation (AVOZ). I deduce in Section 2.4 the analytical formulation for the P-wave AVOZ at the boundaries of fractured rocks that contain parallel fractures. I apply the formulation to predict the AVOZ at a variety of realistic shale/sandstone interfaces when the sandstone is fractured. The results will serve as a guide for field fracture-interpretation in later chapters.

I derive in Section 2.5 the characteristic frequency for local fluid-flow between fractures and the surrounding matrix porosity across the fractures' permeable walls. The characteristic frequency helps us to determine the frequency-dependent seismic attributes, including velocity and amplitude.

In Section 2.6, I present the application of probability method in quantifying the uncertainty in shear wave splitting analysis. This is the anisotropic extension of Mavko and Mukerji's (1995) probability application to quantify the uncertainty in hydrocarbon indicators.

2.2 Three Elasticity Theories of Fractured Rocks and Their Relationships

To detect and characterize fractures from seismic or sonic log data, we need to use elasticity theories that link the mechanical properties of fractured rocks to the fractures' physical properties. Each of the three well-known models, Hudson's penny-shaped-crack model, Schoenberg and Muir's slip-interface model, and Pyrak-Nolte's frequency-dependent slip-interface model, gives a different elasticity formulation. I demonstrate that the first two models and the low-frequency limit of Pyrak-Nolte's model are mathematically equivalent to first order. The significance of this equivalence is that different types of fracture configuration can give the same seismic anisotropy pattern. Using seismic data cannot distinguish anisotropy induced by penny-shaped cracks from that induced by long parallel-wall fractures. The suitability of each model's use in seismic fracture interpretation can be judged only by in-situ fracture observations.

2.2.1 Introduction

Fracture detection and characterization is of great importance to hydrocarbon recovery and waste isolation because fractures greatly impact the rocks' overall permeability and fluid flow (Nelson 1985). In order to characterize the physical properties of fractures from the measurements of rock mechanical properties, including seismic velocity, we need to use the elasticity theories of fractured rocks (I call them fracture models for simplicity) that link the fractures' physical descriptions to rock elasticity.

There are three widely used fracture models: Hudson's (1980, 1981, 1990, 1994) penny-shaped-crack model, Schoenberg and Muir's (1983, 1988, 1989) thin-layer model, and Pyrak-Nolte's (1990a, b) slip-interface model. They have different assumptions, and are suitable for different fracture configurations. Hudson's and Schoenberg and Muir's models are the long-wavelength-limit effective medium theories. In contrast, Pyrak-Nolte's model is not derived for long wavelength limit. It takes fracture inertial effect into account and gives frequency-dependent seismic wave velocities. I show how these models are mathematically equivalent to each other to the first order. Their equivalence reveals that penny-shaped cracks and an equivalent amount of parallel-wall long fractures can generate the same seismic anisotropic response. The only way to distinguish between them is to rely on in-situ fracture observations in cores and outcrops.

2.2.2 Relationship Between Hudson's and Schoenberg and Muir's Models

I first review the two effective medium theories given by Hudson (1980, 1981, 1990, 1994), and Schoenberg and Muir (1983, 1988, 1989), and then show their equivalence.

Hudson's model is an intuitive, effective-medium theory that assumes an elastic solid with an internal distribution of thin penny-shaped ellipsoidal cracks. Hudson used crack density (e) and aspect ratio (α) to describe the structure of fracture systems. The crack density e is defined as:

$$e = \frac{N}{V} a^3 = \frac{3\phi}{4\pi\alpha} \quad , \tag{2.1}$$

where a is crack radius, N/V is the number of cracks per unit volume, ϕ is crack-induced porosity, and α is aspect ratio. The effective moduli are given as

$$C_{ij}^{eff} = C_{ij}^{0} + C_{ij}^{1} + C_{ij}^{2} \ , \tag{2.2}$$

where C_{ij}^{0}'s are the isotropic background moduli and C_{ij}^{1}'s, C_{ij}^{2}'s are the first- and second-order corrections, respectively, that depend on the crack orientation, density, and aspect ratio. We can calculate crack-induced porosity based on Equation 2.1 and apply fluid substitution relationships in this model. Moreover, this theory is well developed for diverse crack distributions, including one or more sets of parallel fractures, conical distribution, and random distribution. The major limitation is that it works only for small crack density (e < 0.1) and small aspect ratio. For a single crack set with crack normals aligned along the 3-axis, the cracked medium shows transversely isotropic symmetry, and the first order corrections are

$$C_{11}^{1} = -\frac{\lambda^2}{\mu} e U_3 \tag{2.3a}$$

$$C_{13}^{1} = -\frac{\lambda(\lambda + 2\mu)}{\mu} e U_3 \tag{2.3b}$$

$$C_{33}^{1} = -\frac{(\lambda + 2\mu)^2}{\mu} e U_3 \tag{2.3c}$$

$$C_{44}^{1} = -\mu e U_1 \tag{2.3d}$$

$$C_{66}^{1} = 0 \tag{2.3e}$$

where λ and μ are the Lamé constants of the unfractured rock, U_1, U_3 depend on crack conditions. For dry cracks, U_1, U_3 are

$$U_1 = \frac{16(\lambda + 2\mu)}{3(3\lambda + 4\mu)} \tag{2.4a}$$

$$U_3 = \frac{4(\lambda + 2\mu)}{3(\lambda + \mu)} \tag{2.4b}$$

For "weak" inclusions, when $\mu\alpha / [K' + (4/3)\mu']$ is of the order of 1 and is not small enough to be neglected (Mavko, Mukerji, and Dvorkin, 1998), Equations 2.4a and b become

$$U_1 = \frac{16(\lambda + 2\mu)}{3(3\lambda + 4\mu)} \frac{1}{1 + M} \tag{2.5a}$$

$$U_3 = \frac{4(\lambda + 2\mu)}{3(\lambda + \mu)} \frac{1}{1 + \kappa} \tag{2.5b}$$

where

$$M = \frac{4\mu'(\lambda + 2\mu)}{\pi\alpha\mu(3\lambda + 4\mu)} \tag{2.5c}$$

$$\kappa = \frac{[K' + (4/3)\mu'](\lambda + 2\mu)}{\pi\alpha\mu(\lambda + \mu)} \tag{2.5d}$$

with K' and μ' the bulk and shear modulus of the inclusion material.

Schoenberg and Muir's slip-interface model is based on the Backus average (1962) and represents fractures by infinitely thin layers. This model works for one or more sets of parallel fractures, and it does not have the low-density limitation. However, because it uses an infinitely-thin-compliant-layer description that does not contain porosity information, we cannot apply fluid substitution here. For one set of parallel fractures with normals aligned along the 3-axis, the effective compliance matrix is

$$S_{ij}^{eff} = S_{ij}^{0} + \Delta S_{ij} \tag{2.6}$$

where S_{ij}^{0} is the isotropic background compliance, and

$$\Delta S_{ij} = h_f * \begin{bmatrix} 0 & 0 & 0 & 0 & 0 & 0 \\ 0 & 0 & 0 & 0 & 0 & 0 \\ 0 & 0 & S_N & 0 & 0 & 0 \\ 0 & 0 & 0 & S_T & 0 & 0 \\ 0 & 0 & 0 & 0 & S_T & 0 \\ 0 & 0 & 0 & 0 & 0 & 0 \end{bmatrix} \tag{2.7}$$

with S_N and S_T the normal and shear compliance of dimension length/stress. They are defined as the fracture displacement per unit stress applied. "h_f" is the volume fraction of the fractures, i.e., the ratio of fracture thickness to fracture spacing. Schoenberg (1983) also gave the effective stiffness expressions:

$$C_{11} = [1 - 4(1-\gamma)E_N]C_{33} \tag{2.8a}$$

$$C_{13} = (1 - 2\gamma)C_{33} \tag{2.8b}$$

$$C_{33} = \frac{\mu}{\gamma + E_N} \tag{2.8c}$$

$$C_{44} = \frac{\mu}{1 + E_T} \tag{2.8d}$$

$$C_{66} = \mu \tag{2.8e}$$

where

$$E_N = \frac{\mu}{H\kappa_N} = \frac{N}{L}\frac{\mu}{\kappa_N} \tag{2.9a}$$

$$E_T = \frac{\mu}{H\kappa_T} = \frac{N}{L}\frac{\mu}{\kappa_T} \tag{2.9b}$$

$$\gamma = \frac{V_S^{\ 2}}{V_P^{\ 2}} = \frac{\mu}{\lambda + 2\mu} \tag{2.9c}$$

Here, μ is the shear modulus of the unfractured rock, κ_N and κ_T are the normal and shear specific stiffness of the fractures, H is the fracture spacing, L is the length of a rock sample, and N is the number of fractures inside the rock sample.

Using the relationship between stiffness matrix and compliance matrix,

$$\tilde{C} = \left(\tilde{S}\right)^{-1} \tag{2.10}$$

we transform Equation 2.7 to stiffness domain, by

$$\begin{aligned}\Delta\tilde{C} &= \tilde{C}^{eff} - \tilde{C}^{0} \\ &= \left(\tilde{S}^{eff}\right)^{-1} - \tilde{C}^{0} \\ &= \left(\tilde{S}^{0} + \Delta\tilde{S}\right)^{-1} - \tilde{C}^{0} \\ &= \left(\left(\tilde{C}^{0}\right)^{-1} + \Delta\tilde{S}\right)^{-1} - \tilde{C}^{0}\end{aligned} \tag{2.11}$$

The analytical results of Equation 2.11 are

$$\Delta C_{11} = -\frac{\lambda^2 h_f S_N}{1 + (\lambda + 2\mu)h_f S_N} \tag{2.12a}$$

$$\Delta C_{13} = -\frac{\lambda(\lambda + 2\mu)h_f S_N}{1 + (\lambda + 2\mu)h_f S_N} \tag{2.12b}$$

$$\Delta C_{33} = -\frac{(\lambda + 2\mu)^2 h_f S_N}{1 + (\lambda + 2\mu)h_f S_N} \tag{2.12c}$$

$$\Delta C_{44} = -\frac{\mu^2 h_f S_T}{1 + \mu h_f S_T} \tag{2.12d}$$

$$\Delta C_{66} = 0 \tag{2.12e}$$

Comparing Equation 2.12 with Equations 2.3 and 2.8, we get

$$\frac{1}{H\kappa_N} = h_f S_N = \frac{U_3 e}{\mu - (\lambda + 2\mu)U_3 e} \tag{2.13a}$$

$$\frac{1}{H\kappa_T} = h_f S_T = \frac{U_1 e}{\mu - \mu U_1 e} \tag{2.13b}$$

The above formulae demonstrate that the elastic anisotropy describe by the first-order Hudson’s model is equivalent to that of Schoenberg and Muir’s slip-interface model even though the fracture description is very different. Nichols (1990) used group theory approaches and derived similar results. With these relationships, we can derive the porosity information from Schoenberg and Muir’s parameters: we transform the spacing and specific stiffness of fractures to crack density and aspect ratio, and then use fluid substitution. Equations 2.13a and 2.13b also explain Hudson’s small-crack-density limitation: large crack density can give negative denominators in Equations 2.13a and 2.13b, and yield unrealistic negative fracture stiffness.

2.2.3 Relationship between Pyrak-Nolte's Model and Two Effective-Medium Theories

Pyrak-Nolte characterized fractures by fracture spacing and specific stiffness, as in Schoenberg and Muir's model. But she took the fracture inertial effect into account. She considered each fracture as a scattering boundary. This model gives a frequency-dependent group velocity. The P-wave group velocity propagating perpendicular to the fracture plane is

$$U_{eff} = \frac{U\left\{1+\left[\omega/\left(2\kappa_N/Z\right)\right]^2\right\}}{1+\left[\omega/\left(2\kappa_N/Z\right)\right]^2+\left(NUZ/2L\kappa_N\right)} \tag{2.14}$$

with κ_N the normal specific stiffness of fractures, ω the wave frequency, and Z the seismic impedance of the isotropic background rock:

$$Z = \rho U \tag{2.15}$$

In order to find the connection between Pyrak-Nolte's and Schoenberg and Muir's models, we compare the group velocity derived from the two theories. For Pyrak-Nolte's low-frequency long-wavelength limit ($\omega \to 0$), Equation 2.14 reduces to

$$U_{eff} = \frac{U}{1+\left(NUZ/2L\kappa_N\right)} \tag{2.16}$$

The first-order approximation is

$$U_{eff} \approx U\left[1-\left(NUZ/2L\kappa_N\right)\right] = U\left[1-\frac{\lambda+2\mu}{2H\kappa_N}\right] \tag{2.17}$$

On the other hand, because the phase velocity and the group velocity are the same for waves propagating along the symmetry axis of a transversely isotropic medium, we can derive the group velocity from Schoenberg and Muir's Equation 2.8, as follows:

$$C_{33} = \frac{\mu}{\gamma+E_N} \approx \left(\lambda+2\mu\right)\left[1-\frac{\lambda+2\mu}{H\kappa_N}\right] \tag{2.18}$$

$$U_{eff} = V_{eff} = \sqrt{\frac{C_{33}}{\rho}} = \sqrt{\frac{(\lambda + 2\mu)\left[1 - \frac{\lambda + 2\mu}{H\kappa_N}\right]}{\rho}} \approx U\left[1 - \frac{\lambda + 2\mu}{2H\kappa_N}\right] \qquad (2.19)$$

Equation 2.19 gives the same group-velocity expression as Equation 2.17. This shows that Schoenberg and Muir's effective-medium theory is equivalent to Pyrak-Nolte's low-frequency limit. Moreover, because Hudson's first-order theory is equivalent to Schoenberg and Muir's model, it should also be consistent with Pyrak-Nolte's low frequency limit. This suggests that the inertial effect is indeed a geometrical dispersion effect, and that we should be aware of it when the wavelength is not long compared to the fracture geometry. For fracture size ranges from 1mm to 10m, the comparable wavelength 1mm to 10m corresponds to frequency range from 100 Hz to 10^{6} Hz. Below 100 Hz, i.e., in the seismic frequency range, the inertial effect can be ignored.

2.2.4 Discussion

The construction of fracture models is important for fracture characterization from rock mechanical properties such as elastic-wave velocity. We proved that the first-order Hudson's model, Schoenberg and Muir's model, and the low-frequency limit of Pyrak-Nolte's model are mathematically equivalent in the first order. This tells us that penny-shaped cracks and long parallel-wall fractures are seismically indistinguishable. We need to rely on the geological observations to determine which model is more suitable for seismic fracture characterization in the field.

The relationships among the three models enable us to take advantage of each of them. We can transform Schoenberg and Muir's description of fractures to Hudson's description, and conduct fluid substitution. We can also use Pyrak-Nolte's description of fractures to estimate the magnitude of the frequency dispersion effects when seismic waves pass through fractured rocks.

2.3 Review of Fracture-induced Anisotropy in P- and S-wave Velocities

In this section, I review the formulas for P- and S-wave velocity/traveltime anisotropy when the fractured rocks are described by Hudson's model. These relationships will be used in Chapter 4 for interpreting the observed seismic anisotropy in terms of fracture density and the physical parameters of cracks.

2.3.1 Thomsen's Anisotropic Parameters

Hudson's penny-shape-crack model (1980, 1981, 1990, 1994) gives expressions for the effective moduli in the form of

$$C_{ij}^{eff} = C_{ij}^{0} + C_{ij}^{1} + C_{ij}^{2} \tag{2.20}$$

where C_{ij}^0's are the isotropic background moduli and C_{ij}^1's, and C_{ij}^2's are the first-and second-order corrections that depend on the crack orientation, crack density, aspect ratio, and the properties of crack-filling materials. The crack density e is defined as:

$$e = \frac{N}{V} a^3 = \frac{3\phi}{4\pi\alpha} \tag{2.21}$$

where a is crack radius, N/V is the number of cracks per unit volume, ϕ is crack-induced porosity, and α is aspect ratio. Rocks containing one set of parallel cracks with their normals along the 3-axis show transverse isotropic symmetry. The first-order corrections C_{ij}^1's are defined in Equations (2.3) to (2.5) where λ and μ are the Lamé constants of the unfractured rock. If the anisotropy is weak (Thomsen, 1986), the fracture-induced anisotropy can also be expressed in terms of Thomsen's anisotropic parameters ε , γ , and δ , as follows:

$$\varepsilon = \frac{C_{11} - C_{33}}{2C_{33}} \approx \frac{2(\lambda + \mu)U_3}{\lambda + 2\mu} e$$

$$\gamma = \frac{C_{66} - C_{44}}{2C_{44}} \approx \frac{U_1}{2} e$$

$$\delta = \frac{(C_{13} + C_{44})^2 - (C_{33} - C_{44})^2}{2C_{33}(C_{33} - C_{44})} \approx 2\left(U_3 - \frac{2\mu}{\lambda + 2\mu} U_1 \right) e \qquad (2.22)$$

Combining Equation 2.22 and the P- and S-wave velocity/traveltime anisotropy formulas in terms of ε , γ , and δ , I show the fracture-induced velocity/traveltime anisotropy formulas in Sections 2.3.2 and 2.3.3.

2.3.2 P-wave Velocity/Traveltime Anisotropy

In transversely isotropic media with a horizontal symmetry axis (TIH), the P-wave velocity depends on both incidence angle θ and azimuth ϕ . The P-wave group velocity was given by Sena (1991) in terms of ε , γ , and δ , as follows:

$$V_p \approx V_{p0}\left(a_0 + a_1 \sin^2\theta + a_2 \sin^4\theta\right)^{-1/2} \qquad (2.23)$$

$$a_0 = 1 - 2\varepsilon$$

$$a_1 = (4\varepsilon - 2\delta)\cos^2\phi$$

$$a_2 = (-2\varepsilon + 2\delta)\cos^4\phi$$

where V_{p0} is the P-wave velocity along the elastic symmetry axis. When there are parallel vertical fractures in the rock, the elastic property of the rock is transversely isotropic with a horizontal symmetry axis (TIH). P-wave velocity for P-waves propagating parallel to the fracture plane is the fastest, and that perpendicular to the fracture plane is the slowest. Based on Equation 2.23, Chen (1995) derived the P-wave velocity/traveltime anisotropy

$$\frac{\Delta T_P}{T_P} \approx \frac{\Delta V_P}{V_P} \approx (2\varepsilon - \delta)\cos^2(\phi)\sin^2(\theta) \tag{2.24}$$

where V_P is the average P-wave velocity, ΔV_P is the fracture-induced velocity variation, T_P is the total two-way traveltime in the interval between two events, and ΔT_P is the traveltime lag generated in this interval. Equation 2.24 applies to small-to-moderate incidence angle as large as 30 degree (Chen, 1995). Combining Equations 2.22 and 2.24, we get the fracture-induced P-wave velocity/traveltime anisotropy in terms of the physical parameters of cracks:

$$\frac{\Delta V_P}{V_P} \approx \frac{\Delta T_P}{T_P} \approx \left(\frac{2\lambda U_3 + 4\mu U_1}{\lambda + 2\mu} e\right)\cos^2(\phi)\sin^2(\theta) \tag{2.25}$$

where U_1 and U_3 are given in Equations 2.4 and 2.5.

Equation 2.25 shows that, at a fixed incident angle, the P-wave traveltime between two horizontal reflectors is a cosine curve of the azimuth. Because U_1 and U_3 depend on the crack physical parameters, traveltime azimuthal variation is a function of crack density, aspect ratio, and crack-filling material.

2.3.3 S-wave Velocity/Traveltime Anisotropy

In rocks containing vertical parallel fractures, vertically propagating shear-waves split into a fast shear-wave polarized parallel to the fracture plane, and a slow shear-wave polarized perpendicular to the fracture plane. Because shear-waves are not sensitive to pore fluids, the traveltime lag between the fast and slow events is only related to the fracture density.

In weak anisotropic environments (Thomsen, 1986), the traveltime anisotropy induced by vertical parallel fractures can be expressed as:

$$\frac{\Delta T_S}{T_S} = \frac{\Delta Vs}{Vs} \approx \gamma = \frac{C_{66} - C_{44}}{2C_{44}} \tag{2.26}$$

Combining Equations 2.22 and 2.26, we get

$$\gamma = \frac{C_{66} - C_{44}}{2C_{44}} \approx \frac{\mu e U_1}{2\mu} = \left[\frac{16(\lambda + 2\mu)}{3(3\lambda + 4\mu)}\right]\frac{e}{2} = \left(\frac{16M}{9M - 6\mu}\right)\frac{e}{2} \tag{2.27}$$

where M is the P-wave modulus, and $M = \lambda + 2\mu$. Combining Equations 2.26 and 2.27, we get the expression for the crack density e as a function of the shear-wave velocity/traveltime anisotropy,

$$e = \frac{9M - 6\mu}{8M}\frac{\Delta T_S}{T_S} = \left(\frac{15}{24} + \frac{2}{16 - 24\sigma}\right)\frac{\Delta T_S}{T_S} \tag{2.28}$$

where σ is the Poisson's ratio of the unfractured rock. We can make a few observations of equation (2.28):

1) fracture-induced shear-wave velocity/traveltime anisotropy is proportional to the crack density;

2) fracture-induced shear-wave velocity/traveltime aniostropy is not affected by crack-filling fluids;

3) for the same amount of shear-wave anisotropy, the larger the Poisson's ratio of the unfractured rock, the larger the crack density estimation.

Equations 2.25 and 2.28 give the P- and S-wave velocity/traveltime anisotropy as functions of crack density and cracks' physical properties. They will be used in Chapter 4 to interpret the measured velocity/traveltime anisotropy in seismic P- and S-wave data in terms of fractures.

2.4 Fracture-Induced Anisotropy in P-wave Reflectivity

2.4.1 Abstract

This section analyzes the relationship between fracture-induced P-wave reflectivity anisotropy and the physical parameters of the fracture network. These parameters include crack density, aspect ratio, and filling fluids, as well as the embedding rock moduli and the seismic-wave frequency. By combining the analytical reflectivity formula for weakly anisotropic media given by Rueger with the penny-shaped crack model developed by Hudson and Thomsen, I show the equations for P-wave reflectivity induced by vertical parallel fractures under both high-frequency (relative to the squirt-flow relaxation time) and low-frequency conditions. My synthetic modeling shows three main conclusions:

1) reflectivity anisotropy increases with crack density and fracture-filling fluid bulk modulus, and decreases with crack aspect ratio;

2) under high-frequency conditions, it decreases with the background rock's Poisson's ratio;

3) the same fracture set induces more reflectivity anisotropy under high-frequency conditions than under low-frequency conditions.

To apply these results, I predict the reflectivity anisotropy at a variety of realistic shale/sandstone interfaces caused by penny-shaped cracks in the sandstone.

2.4.2 Introduction

Aligned fractures induce anisotropy into rock mechanical properties. To relate the anisotropy to the fracture network configuration, various effective media models can be used; for example, the penny-shaped crack models (Hudson, 1981, 1990; Thomsen, 1995) and the slip-interface models (Schoenberg and Muir, 1989). Once we have the effective moduli of fractured rocks, we can calculate the seismic reflectivity at the boundary of the fractured rocks. For this calculation, I solve the Zoeppritz equations in anisotropic media using the numerical method given by Keith and Crampin (1977) or Rueger's (1995, 1996) weakly anisotropic approximation.

This section analyzes the relationship between reflectivity anisotropy and fracture physical parameters, as well as pore fluid and rock properties. The penny-shaped crack models are used for both high-frequency and low-frequency conditions (Mavko and Jizba, 1991; Mukerji and Mavko, 1994; Thomsen 1995).

For realistic applications, I use the velocity and density data of adjacent shale and sandstone sets collected by Castagna and Smith (1994) as the embedding rock properties. I categorize the sandstones into four classes, according to their isotropic AVO behavior (Shuey, 1985; Rutherford and Williams, 1989; Castagna and Swan, 1997), and analyze the fracture-induced anisotropy superimposed on the isotropic AVO for the four classes of gas sands and the corresponding brine sands.

2.4.3 Analytical Solutions

To show the analytical expressions of P-wave reflectivity at the boundaries of fractured rocks, I combine the elasticity theories of fractured rocks and the analytical expressions of P-wave reflectivity in weakly anisotropic media.

Review of Elasticity Theories of Fractured Rocks

Subsurface fracture networks can have various configurations, and each fracture can have a unique geometry. The elastic properties of a full fracture network are by far too complicated to be described with present-day techniques. To show the relationship between the statistical average of fracture properties the fractured rock's elastic behavior, various elastic models have been suggested (Hudson, 1981, 1990; Schoenberg and Muir, 1989; Thomsen, 1995). While these models are conceptually different, many of the resulting elastic behaviors can be shown to be equivalent (Teng and Mavko, 1995), as we discussed in Section 2.2. I chose to use the penny-shaped crack models, which work well when the wavelength is long compared to the crack size, and which allow us to explore the influence of pore fluids and crack geometry on P-wave reflectivity.

In a later part of this section, I will specifically address the frequency dependence associated with pore fluids. Seismic waves passing through the rock induce spatial variation of pore-fluid pressure. When the wave frequency is too high for the fluids in the thin fractures and the equant pores to reach pressure equilibrium, or if the fractures are sealed for fluid flow, we call this a high-frequency condition. Hudson's (1981, 1990) penny-shaped crack model describes the high-frequency conditions, because each crack is treated as isolated with respect to flow. When the wave frequency is low and the pore fluids reach pressure equilibrium, we call this a low-frequency condition. The elastic behavior of fractured rocks under low-frequency conditions can be modeled by Thomsen's (1995) low-frequency penny-shaped crack model, or by the anisotropic fluid-substitution theories for low-frequency conditions (Brown and Korringa, 1975; Mukerji and Mavko, 1994).

An advantage of penny-shaped crack models is that, in describing the fracture-network configuration, they use physically intuitive parameters, including crack density, aspect ratio, and filling fluid. The crack density e is defined as

$$e = \frac{N}{V} a^3 = \frac{3\phi_c}{4\pi\alpha} \tag{2.29}$$

where N/V is the number of cracks in a unit volume, a is the crack radius, α is the crack aspect ratio, and ϕ_c is the crack porosity. When the fractures are parallel with their normals along the 3-axis (vertical direction), the rock is transversely isotropic with a vertical symmetry axis (TIV). Under high-frequency conditions, the rock elastic moduli can be calculated by Hudson's first-order weak inclusion theory:

$$C_{IJ} = C_{IJ}{}^0 + C_{IJ}{}^1 \tag{2.30a}$$

where

$$\begin{aligned}
C_{11}{}^1 &= -\frac{\lambda^2}{\mu} e U_3 \\
C_{13}{}^1 &= -\frac{\lambda(\lambda + 2\mu)}{\mu} e U_3 \\
C_{33}{}^1 &= -\frac{(\lambda + 2\mu)^2}{\mu} e U_3 \\
C_{44}^1 &= -\mu e U_1 \\
C_{66}^1 &= 0 \\
U_1 &= \frac{16(\lambda + 2\mu)}{3(3\lambda + 4\mu)} \frac{1}{(1 + M)} \\
U &= \frac{4(\lambda + 2\mu)}{3(\lambda + \mu)} \frac{1}{(1 + \kappa)} \\
M &= \frac{4\mu'(\lambda + 2\mu)}{\pi a \mu (3\lambda + 4\mu)} \\
\kappa &= \frac{[K' + (4/3)\mu']\,(\lambda + 2\mu)}{\pi a \mu (\lambda + \mu)}
\end{aligned} \tag{2.30b}$$

with λ and μ being the Lamé constants of the unfractured background rock, and *K'* and μ' the bulk and shear modulus of the inclusion material. The inclusion is a fluid with bulk modulus K_f, $K' = K_f$, and $\mu' = 0$.

For low-frequency conditions, I use Thomsen's equations in terms of the anisotropic parameters ε, γ, and δ (Thomsen 1986):

$$\varepsilon = \frac{C_{11} - C_{33}}{2C_{33}} = \frac{8}{3}\left(1 - \frac{K_f}{K}\right) D_{ci} \left[\frac{\left(1 - \nu^{*2}\right)E}{\left(1 - \nu^2\right)E^*}\right] e$$

$$\gamma = \frac{C_{66} - C_{44}}{2C_{44}} = \frac{8}{3}\frac{\left(1 - \nu^*\right)}{\left(2 - \nu^*\right)} e$$

$$\delta = \frac{\left(C_{13} + C_{44}\right)^2 - \left(C_{33} - C_{44}\right)^2}{2C_{33}\left(C_{33} - C_{44}\right)} = 2\left(1 - \nu\right)\varepsilon - 2\left(\frac{1 - 2\nu}{1 - \nu}\right)\gamma \tag{2.31a}$$

where

$$D_{ci}\left(lo\right) = \left\{1 - \frac{K_f}{K_s} + \frac{K_f}{K^* \phi_t}\left[\left(1 - \frac{K^*}{K_s}\right) + A_c \nu^* e\right]\right\}^{-1}$$

$$A_c\left(\nu^*\right) = \frac{16}{9}\left(\frac{1 - \nu^{*2}}{1 - 2\nu^*}\right) \tag{2.31b}$$

In Equations (2.31a) and (2.31b), "lo" stands for low-frequency condition; K, E, and ν are the bulk modulus, Young's modulus, and Poisson's ratio of the unfractured background rock; ϕ_t denotes the total porosity; and the subscript/superscript *, *s*, and *f* denote the properties of the corresponding dry rock, solid grain, and pore fluids, respectively. Thomsen (1995) also gives the expression of D_{ci} under high-frequency conditions:

$$D_{ci}(mh) = \left\{1 - \frac{K_f}{K_s} + \frac{K_f}{K^*}\left[A_c \nu^* \frac{e}{\phi_c}\frac{\left(1 - K_f / K_s\right)}{\left(1 - K_f / K\right)}\right]\right\}^{-1} \qquad (2.31c)$$

and shows that this agrees with Hudson's model. "mh" stands for moderate high frequency, i.e., high-frequency conditions, but ones that is not yet high enough to generate significant Raleigh scattering effect (Thomsen , 1995).

Review of P-wave Reflectivity in Isotropic and Weakly Anisotropic Media

Recall the isotropic AVO formula given by Shuey (1985):

$$R_{P=ISO}(\theta) = R_{P0} + \left[A_0 R_{P0} + \frac{\Delta\sigma}{(1-\sigma)^2}\right]\sin^2(\theta) + \frac{1}{2}\frac{\Delta\alpha}{\overline{\alpha}}\left[\tan^2(\theta) - \sin^2(\theta)\right]$$

$$A_0 = B - 2(1+B)\frac{1-2\sigma}{1-\sigma}$$

$$B = \frac{\left(\Delta\alpha / \overline{\alpha}\right)}{\left(\Delta\alpha / \overline{\alpha}\right) + \left(\Delta\rho / \overline{\rho}\right)} \qquad (2.32a)$$

where

$$\begin{aligned} \overline{\alpha} &= (\alpha_1 + \alpha_2)/2 & \Delta\alpha &= \alpha_2 - \alpha_1 \\ \overline{\beta} &= (\beta_1 + \beta_2)/2 & \Delta\beta &= \beta_2 - \beta_1 \\ \overline{\rho} &= (\rho_1 + \rho_2)/2 & \Delta\rho &= \rho_2 - \rho_1 \end{aligned} \qquad (2.32b)$$

and α, β, ρ and σ are the P- and S-wave velocities, density, and Poisson's ratio, respectively. The isotropic reflectivity has two terms: the first term is the normal incidence reflectivity, i.e., AVO intercept; the second and third terms are the AVO gradient terms. At near offset, the third term can be ignored, and the AVO curve increases with $\sin^2\theta$.

In anisotropic environments, the reflectivity can be solved by the Zoeppritz equations, or by use of the weakly anisotropic approximation given by Rueger (1995, 1996). When the fractures are vertical and parallel, and have normals along the 1-axis as shown in Figure 2.1, the fractured rock is transversely isotropic with a horizontal symmetry axis (TIH). Using a perturbation method, Chen (1995) and Rueger (1996) developed the formula for reflectivity in TIH media:

$$
\begin{aligned}
&R_P(\theta,\phi) = R_{P-ISO}(\theta) + R_{P-ANISO}(\theta,\phi) \\
&R_{P-ANISO}(\theta,\phi) = \frac{1}{2}\left[\Delta\delta^{(V)} + 2\left(\frac{2\bar{\beta}}{\bar{\alpha}}\right)\Delta\gamma\right]\cos^2(\phi)\sin^2(\theta) + \\
&\qquad \frac{1}{2}\left[\Delta\varepsilon^{(V)}\cos^4(\phi) + \Delta\delta^{(V)}\sin^2(\phi)\cos^2(\phi)\right]\sin^2(\theta)\tan^2(\theta)
\end{aligned}
\tag{2.33a}
$$

The parameters $\varepsilon^{(V)}$ and $\delta^{(V)}$ are the anisotropic parameters in the TIH media. They can be related to Thomsen's parameters in TIH media by

$$
\begin{aligned}
\varepsilon^{(V)} &= -\frac{\varepsilon}{1+2\varepsilon} \\
\delta^{(V)} &= \frac{\delta - 2\varepsilon(1+\varepsilon/\xi)}{(1+2\varepsilon)(1+2\varepsilon/\xi)} \\
\xi &= 1 - \frac{\beta_0{}^2}{\alpha_0{}^2}
\end{aligned}
\tag{2.33b}
$$

The vertical P-wave velocity α and the vertical velocity of the S-wave polarized parallel to the fracture plan β in Equation (2.33a) are defined as

$$
\begin{aligned}
\alpha &= \alpha_0\sqrt{1+2\varepsilon} \\
\beta &= \beta_0\sqrt{1+2\gamma}
\end{aligned}
\tag{2.33c}
$$

where α_0 and β_0 are the unfractured rock P- and S-wave velocities.

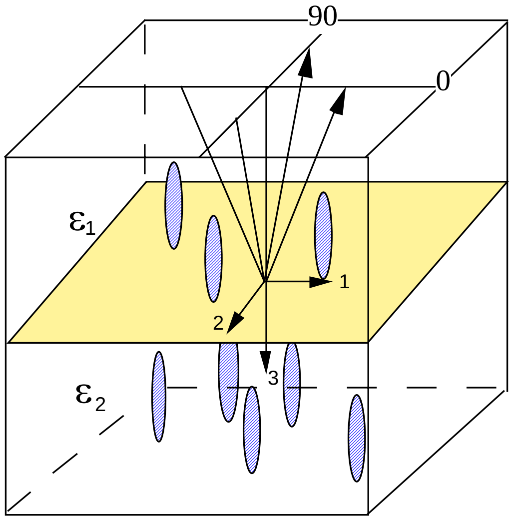

Figure 2.1: Reflection at the boundary between two fractured layers. The fractures are in the 90° azimuth plane with their normals pointing in the 0° azimuth direction.

P-wave Reflectivity at a Boundary of Fractured Rock

When the source of anisotropy in both the upper and lower media is vertical parallel fractures with their normals along the 1-axis direction, the reflectivity under high-frequency conditions can be related to the fracture's physical parameters. I combine and simplify Equation (2.30) from Hudson's model and Equation (2.33) from Reuger's weakly anisotropic reflectivity approximation:

$$R_{P-ANISO} = P_2 - P_1 \tag{2.34a}$$

$$P_i = -\frac{4}{3}e_i\left\{\begin{array}{l}\left(2\sigma_i F_i - \dfrac{2-4\sigma_i}{2-\sigma_i}\right)\cos^2(\phi)\sin^2(\theta)\\ +\left[F_i\cos^4(\phi)+\left(2\sigma_i F_i+\dfrac{2-4\sigma_i}{2-\sigma_i}\right)\sin^2(\phi)\cos^2(\phi)\right]\sin^2(\theta)\tan^2(\theta)\end{array}\right\}$$

where F_i describes the fracture-filling fluid effect in the *i*th medium:

$$F_i = \frac{1}{1 + \frac{4}{3\pi\alpha_i}\frac{K_{fi}}{K_i}\frac{1-\sigma_i{}^2}{1-2\sigma_i}} \qquad (2.34b)$$

To evaluate the reflectivity of low-frequency conditions, I use Equation (2.33a) where Thomsen's anisotropic parameters are given by Equation (2.33b). The combined form cannot be simplified as in Equation (2.34).

To check the accuracy, I consider a simple case in which the only source of anisotropy is one set of vertical parallel fractures in the lower medium. I assume that these fractures can be modeled by penny-shaped cracks. The upper medium is isotropic with zero crack density. Hence, we don't need to consider the anisotropic radiation pattern and anisotropic attenuation, and can attribute the P-wave amplitude anisotropy solely to the reflectivity anisotropy.

As an accuracy check, the weakly anisotropic solution is compared with the Zoeppritz solution. The two solutions are compared in polar plots for all azimuths (Figure 2.2a) and cross-section plots for 0° and 90° azimuths (Figure 2.2b). I choose the crack density to be 0.08, aspect ratio to be 0.01, and fracture-filling fluid to be brine (bulk modulus 2.8GPa, density 1.0g/cm^3) under high-frequency conditions. Figure 2.2 shows that at a small (<35°) incident angle, the Zoeppritz equation solution is well approximated by the analytical approximation. At a large incident angle, the approximation no longer works well. Because the first term of Equation (2.34a) dominates at near offset, the reflectivity anisotropy roughly increases with $\sin^2\theta$, and reaches its peak and trough at 0° and 90° azimuths, as shown in Figure 2.2a. The peak-trough difference at the 30° incident angle $Rp(\theta=30,\phi=0)-Rp(\theta=30,\phi=90)$ will be used to represent the magnitude of reflectivity anisotropy.

Using Equations (2.29) to (2.34), I calculate the reflectivity anisotropy for various parameters as follows:

crack density range:	0-0.1
crack aspect ratio range:	0.00001-0.1
crack-filling fluids:	brine (bulk modulus 2.8 GPa, density 1.0 g/cm^3)
	oil (bulk modulus 1.6 GPa, density 0.88 g/cm^3)
	gas under 0.1MPa and $20^{\circ}\mathrm{C}$ (near the surface)
	gas under 15MPa and $47^{\circ}\mathrm{C}$ (≅1.5 km depth)
	gas under 30MPa and $75^{\circ}\mathrm{C}$ (≅3 km depth)
matrix rock Poisson's ratio:	0.1-0.4
wave frequency:	both low and high

For natural gas (the specific gravity of methane is 0.56), the bulk modulus and density under various pressures and temperatures can be estimated with Batzle and Wang's (1992) empirical formula.

Figure 2.3 shows the reflectivity anisotropy as a function of crack density for various fluids under both high-frequency and low-frequency conditions. I notice these results: 1) the reflectivity anisotropy increases with crack density except at very low crack density under low-frequency conditions; 2) the reflectivity anisotropy under high-frequency conditions is larger than that under low-frequency conditions; 3) stiffer fracture-filling fluids give a larger reflectivity anisotropy than softer fluids; 4) reflectivity anisotropy increases with temperature and pressure when the crack-filling fluid is gas; and, 5) the reflectivity anisotropy under high-frequency conditions is more sensitive to the gas pressure change and less sensitive to stiffer fluids' bulk modulus change (brine vs. oil) than that under low-frequency conditions.

Figure 2.4 shows the reflectivity anisotropy as a function of crack aspect ratio. The thinner the cracks, the larger the reflectivity anisotropy. This effect is obvious under high-frequency conditions, especially for gas-filled cracks. It is negligible under low-frequency conditions.

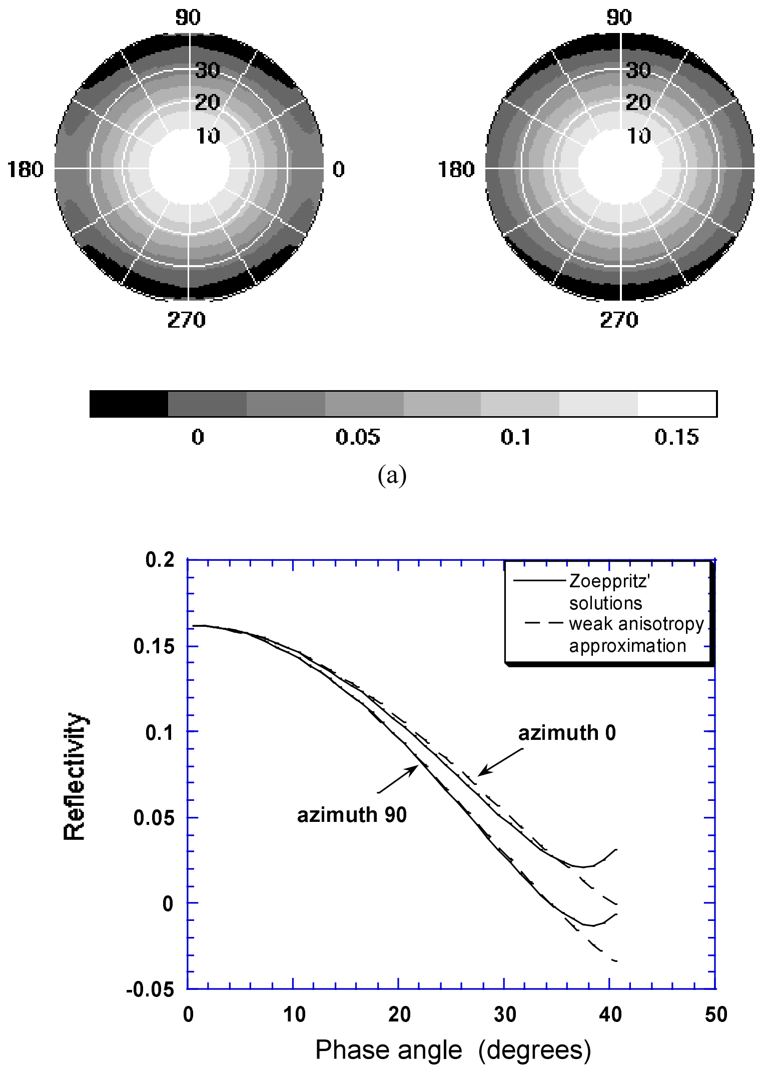

(a)

(b)

Figure 2.2: a) Gray scale contours of the reflectivity at the top of a fractured rock calculated by the Zoeppritz equations (left) and the weak anisotropy approximation (right); b) Reflectivity as a function of incident phase angle at 0° and 90° azimuth cross-sections. The Zoeppritz solution (solid lines) is well approximated by the weak anisotropy analytical solution (dashed lines) for incident angle less than 35°. For this example, the overburden rock is isotropic with Vp=3.60km/s Vs=1.85km/s and density=2.63g/cm3. The fractured layer has background properties Vp=5.03km/s Vs=3.32km/s and density=2.61km/s. These values are from the 25 sets of shale sandstone data collected by Castagna and Smith (1994). The fractures in the lower medium are in the 90° azimuth plane with crack density 0.08, aspect ratio 0.01, and filling fluid brine under high-frequency conditions.

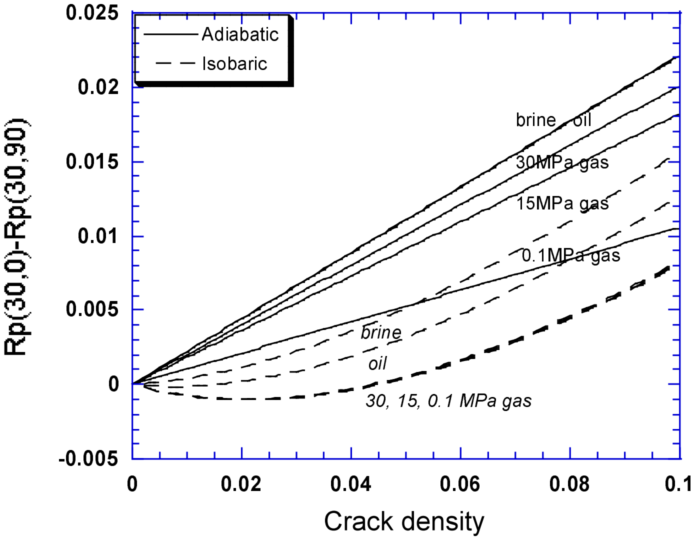

Figure 2.3: Reflectivity anisotropy versus crack density in a fractured rock at the interface between an isotropic rock with Poisson's ratio 0.3 and the fractured rock with Poisson's ratio 0.2. The reflectivity anisotropy is represented by Rp(30,0)-Rp(30,90), i.e. the reflectivity difference between 0° and 90° azimuths at 30° incident angle. The fractured rock contains a set of vertical parallel fractures with crack density 0.08, aspect ratio 0.01, and various filling fluids under high-frequency conditions (solid lines) and low-frequency conditions (dashed lines).

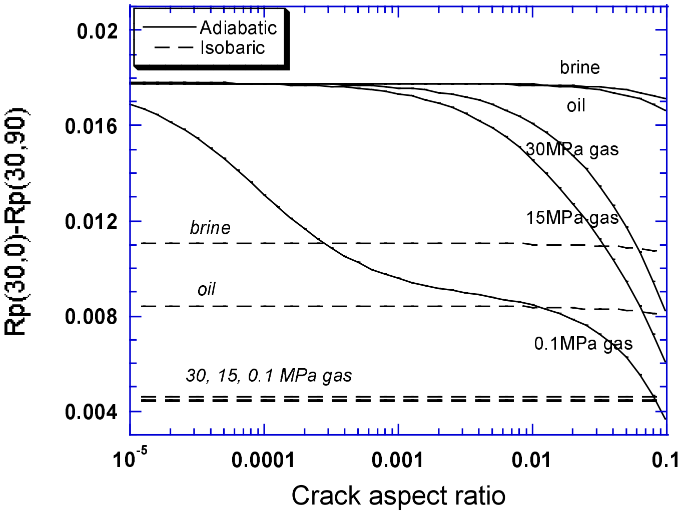

Figure 2.4: Reflectivity anisotropy versus crack aspect ratio at the interface between an isotropic rock with Poisson's ratio 0.3 and a fractured rock with Poisson's ratio 0.2. The fractured rock contains a set of vertical parallel fractures with crack density 0.08, and various filling fluids under high-frequency conditions (solid lines) and low-frequency conditions (dashed lines).

Figure 2.5 shows that, under high-frequency conditions, the reflectivity anisotropy decreases with the Poisson's ratio. Under low-frequency conditions, the reflectivity anisotropy depends not only on the Poisson's ratio of the embedding rock, but also on the moduli of the solid grains, dry rocks, and porosity, as shown in Equation (2.31).

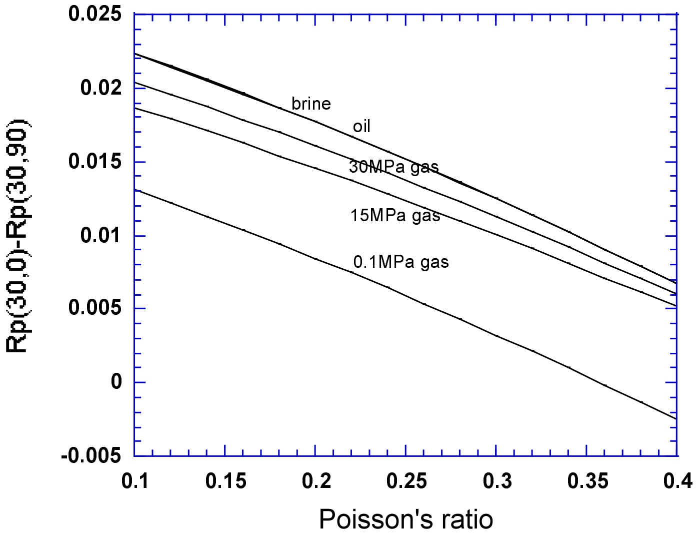

Figure 2.5: Reflectivity anisotropy versus Poisson's ratio of a fractured rock at the interface between an isotropic rock with Poisson's ratio 0.3 and the fractured rock with specified Poisson's ratio. The fractured rock contains a set of vertical parallel fractures with crack density 0.08, aspect ratio 0.01, and various filling fluids under high-frequency conditions.

2.4.4 Reflectivity at Shale-Sandstone Interfaces

For realistic examples, I use the 25 sets of P-, S-wave velocity and density data collected by Castagna and Smith (1994) as the rock matrix properties. The fracture-induced reflectivity anisotropy superimposed on the isotropic AVO curves were predicted for reflections at the shale/sandstone interfaces.

Isotropic AVO Classification

Figure 2.6 shows the P-wave velocity versus S-wave velocity for the sands. When the fluid in the sandstone changes from gas to brine, that change may increase or decrease the S-wave velocity, but it uniformly increases the P-wave velocity because the fluid increases the bulk modulus of a rock more than it does the density. This condition may lead to the reduction of impedance contrast between shale and sandstone, and hence also reduce the absolute values of normal incidence reflectivity, especially for rocks with large porosity.

According to their AVO behavior, the 25 sets of gas sands are categorized into four classes (Rutherford and Williams, 1989; Castagna and Swan, 1997), as shown in Figure 2.7. To show the fluid-substitution effects on AVO, I plot the corresponding brine sands with the same shapes of symbols. For Class I tight gas sandstones, fluid substitution with brine mainly moves the normal incidence reflectivity to the positive direction; for Class III and IV loosely consolidated sands, it reduces the absolute values of the normal incidence reflectivity as well as changes the AVO gradient. The AVO behavior of shale-brine sandstone follows a linear trend passing through the origin. These effects agree with what Castagna and Swan (1997) proposed.

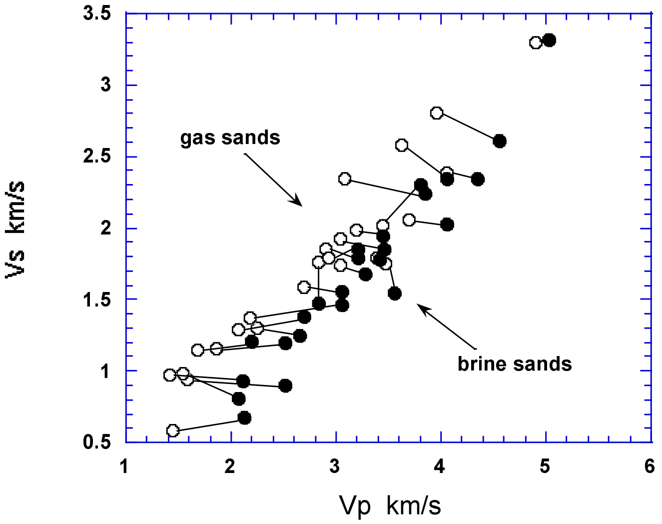

Figure 2.6: P- versus S-wave velocity for the gas sands and brine sands collected by Castagna and Smith (1994). Notice the increase in P-wave velocity from the gas sands to the adjacent brine sands.

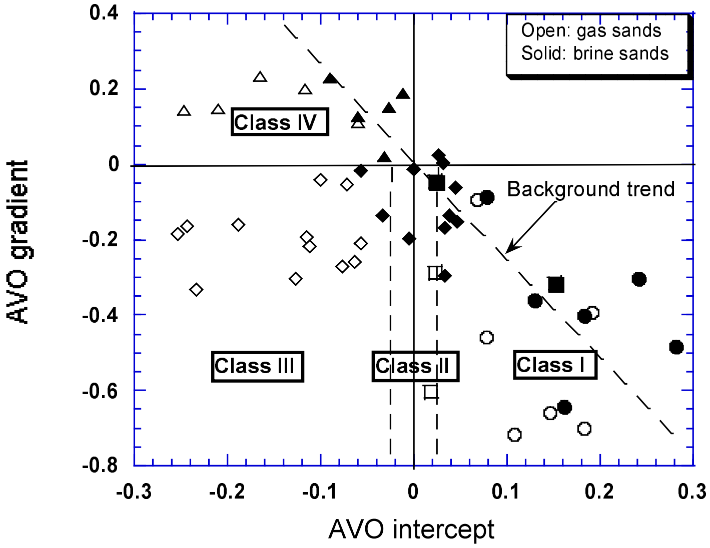

Figure 2.7: Classification of the gas sands (open symbols) based on the AVO behavior. The corresponding brine sands (solid symbols) and its AVO background trend (dashed line) proposed by Castagna and Swan (1997) are also shown in the graph. Notice that the fluid substitution from gas to brine moves the AVO normal incident reflectivity and gradient towards the background trend.

Fracture-Induced Anisotropy in Reflectivity

I assume that the only source of the azimuthal anisotropy is a set of vertical parallel fractures in the sandstones. The possible anisotropy in the overburden shale is transversely isotropic, and will not affect the reflectivity azimuthal variation.

When I calculate the reflectivity anisotropy at the 25 shale-sand interfaces, I assume that the fractures are vertical and parallel, with a crack density of 0.08 and aspect ratios of 0.001 and 0.1, respectively. The fluids in the fractures are the same as those in the rock matrix. The calculated reflectivity anisotropy under both high-frequency conditions and low-frequency conditions are shown in Figure 2.8. The relationships between the reflectivity anisotropy and the various fracture and embedding-rock parameters are summarized as follows:

1. Under high-frequency conditions, the reflectivity anisotropy decreases as the embedding rock Poisson's ratio increases. But there is no distinct range of Poisson's ratio that separates different sandstone classes. Hence, there is no distinct range of reflectivity anisotropy for different sandstone classes. Under low-frequency conditions, the reflectivity anisotropy as a function of Poisson's ratio does not have a linear pattern, because of the influence of other parameters, including total porosity, grain bulk modulus, and dry rock moduli.
2. The clusters of different fluid types (gas vs. brine) are distinguishable under both high-frequency and low-frequency conditions. However, gas-saturated cracks in gas sands may give higher or lower reflectivity anisotropy than brine-saturated cracks in adjacent brine sands. This depends on the tradeoff between the fracture-filling fluid effect on reflectivity anisotropy and the matrix-fluid effect on Poisson's ratio, which affects the reflectivity as discussed earlier.

   Because the change in pore pressure affects the bulk modulus of the fracture-filling gas, it also influences the reflectivity. However, as we see in Figure 2.8, the pore pressure effect is significant only for very thin cracks (aspect ratio 0.001) under high-frequency conditions.
3. By comparing Figure 2.8a to 2.8c, we see that thinner cracks can give larger reflectivity anisotropy under high-frequency conditions; and by comparing Figure 2.8b to 2.8d, we see that the aspect-ratio impact is negligible under low-frequency conditions.

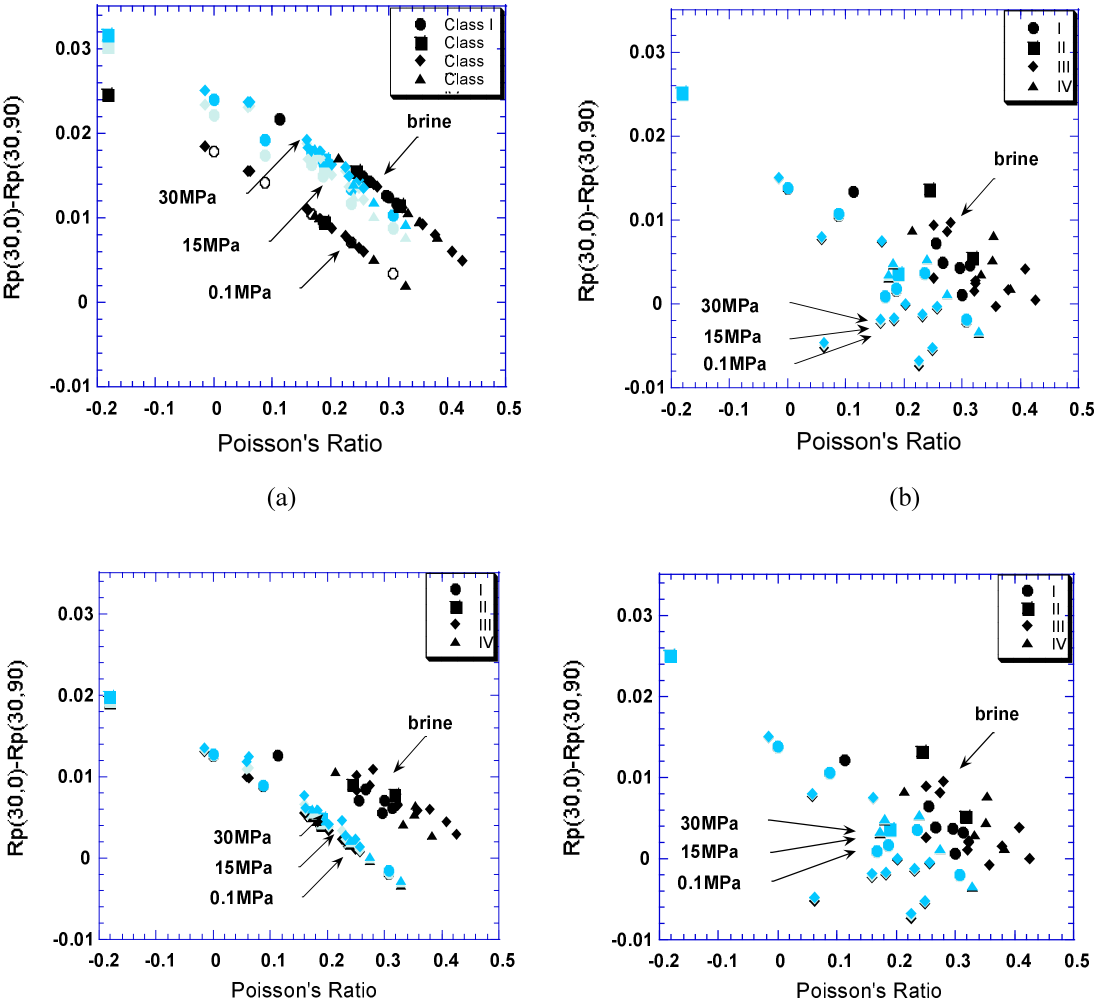

(a) (b)

(c) (d)

Figure 2.8: Reflectivity anisotropy versus Poisson's ratio at the shale/sandstone interfaces. The reflectivity anisotropy is expressed as the reflectivity difference between 0° and 90° azimuths at 30° incident angle. The background rocks include the four types of gas sands (open symbols for atmospheric pressure and gray symbols for high pressure) and corresponding brine sands (solid black symbols). The overburden shale is assumed to be unfractured, and the sandstones contain a set of vertical parallel fractures with crack density 0.08. The reflectivity anisotropy is induced a) by the cracks with aspect ratio 0.001 under high-frequency conditions; b) by the cracks with aspect ratio 0.001 under low-frequency conditions; c) by the cracks with aspect ratio 0.1 under high-frequency conditions; d) by the cracks with aspect ratio 0.1 under low-frequency conditions.

2.4.5 Discussion

The results of reflectivity modeling show that the P-wave reflectivity anisotropy is a function of crack density, aspect ratio, filling-fluid bulk moduli, embedding-rock Poisson's ratio, and wave frequency. In some situations, we should consider the correlation of various physical parameters. For example, the fluid in the fractures is often the same as the fluid in the rock matrix. Therefore, there is a tradeoff between the fracture-filling fluid's impact on reflectivity anisotropy and the matrix-fluid impact on Poisson's ratio and reflectivity anisotropy.

There are more issues that should be taken into account in the field analysis of reflection amplitudes. On one hand, anisotropic attenuation and anisotropic radiation pattern ought to be compensated before reflectivity anisotropy is analyzed; on the other hand, other factors, depending on the in-situ environments, should be considered. These include the fluid saturation, fluid mixture, high-pressure compartments, and depth-related lithology change. Other models (Schoenberg and Muir, 1989) are also used in the analysis of fracture-induced anisotropy (Sayers and Rickett, 1997). The suitability of one model over the other depends on which one better describes the in-situ fractures.

2.5 The Characteristic Frequency of Local Fluid-Flow in Fractured Rocks

I study the characteristic frequency of local fluid-flow between fractures and the surrounding matrix through the fracture's permeable walls. The results show that the characteristic frequency of this type of fluid flow is proportional to matrix permeability, porosity, pore fluid bulk modulus, the inverse of the fracture aperture squared, and the inverse of fluid viscosity. The characteristic frequency can range from 0.1Hz to 10^8 Hz depending on the properties of fracture, pore fluid, and rock matrix. This range includes low seismic frequency and high ultrasonic frequency.

2.5.1 Introduction

In fluid flow, two well-known mechanisms that can induce velocity dispersion include global flow (Biot, 1956a, 1962), and local flow (Biot, 1956b; Mavko and Nur, 1975). The latter often plays a more important role in rocks with medium to low permeability. The characteristic frequency that separates high-frequency conditions and low-frequency conditions for local flow is estimated by O'Connell and Budiansky (1977) as

$$f_I = \frac{K_0}{\eta}\left(\frac{c}{a}\right)^3 \tag{2.35}$$

where c and a are shown in Figure 2.9; c/a is the aspect ratio of the cracks; K_0 is the solid matrix bulk modulus; and η is the fluid viscosity. This estimate of characteristic frequency applies to fluid flow between closely spaced micro cracks with impermeable walls. Thomsen (1995) gives a comprehensive analysis of the elastic behaviors of rocks with penny-shaped cracks under both high-frequency conditions and low-frequency conditions.

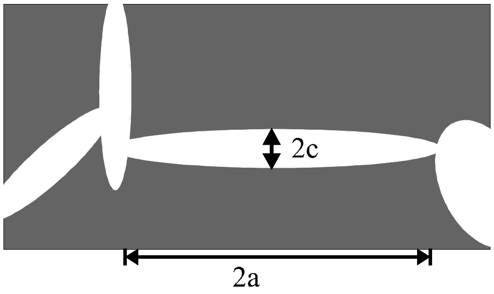

Figure 2.9: Diagram of local fluid flow in closely spaced cracks.

For fractured rocks, the fractures are much longer than the grain size and can be bounded by two permeable walls that consist of many grains, as shown in Figure

2.10. In this case, when a passing wave squeezes a fracture, the fluid in the fracture flows into the surrounding rock matrix through the permeable walls. This mechanism differs from the previous one. I study the corresponding characteristic frequency.

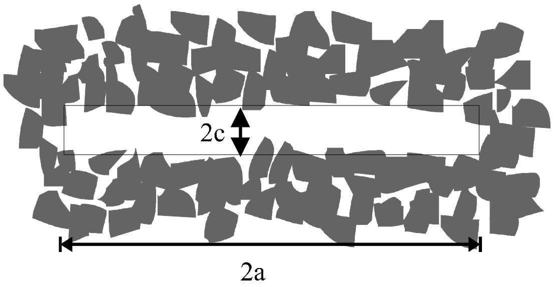

Figure 2.10: Diagram of local fluid flow in fractures with permeable walls.

2.5.2 Theory

Consider a fracture with uniform aperture 2c and permeable walls. When a wave passes, the thickness of the pore 2c is a function of time t:

$$c(t) = c_0\left[1 + \varepsilon \exp(i\omega t)\right] \quad (2.36)$$

where ε is a small constant: $\varepsilon << 1$.

Dvorkin et al. (1990) give the resulting fluid pressure within the fracture as a function of wave angular frequency ω. The modulus of the pore pressure can be expressed as

$$Abs(P) = \frac{c\varepsilon\sqrt{\omega}}{\sqrt{\kappa^2/\chi\eta^2 + \omega c^2/K_{fl}^2 + \frac{c\kappa}{\eta K_{fl}}\sqrt{2\omega/\chi}}} \quad (2.37a)$$

where

$$\chi = \kappa \mathrm{K}_{\mathrm{fl}} / (\phi \eta) \tag{2.37b}$$

with κ the matrix permeability, ϕ the porosity, η the fluid viscosity, and K_{fl} the fluid bulk modulus. We can re-write equation (2.37) as:

$$\mathrm{Abs}(\mathrm{P}) = \frac{\mathrm{A}\sqrt{\mathrm{y}}}{\sqrt{1 + \mathrm{y} + \sqrt{2\mathrm{y}}}} \tag{2.38a}$$

where

$$\mathrm{y} = \mathrm{c}^2 \chi \eta^2 / (\kappa \mathrm{K}_{\mathrm{fl}})^2 \omega \tag{2.38b}$$

A is a constant independent of ω. At the characteristic frequency, the slope of the pore pressure (i.e., the first derivative) as the function of the frequency reaches its maximum, and the second derivative goes to zero:

$$\frac{\partial^2 \mathrm{Abs}(\mathrm{P})}{\partial y^2} = 0 \tag{2.39}$$

This equation yields:

$$f_{II} = 2\pi\omega = 2\pi \frac{\kappa \phi K_{fl}}{c^2 \eta} \tag{2.40}$$

This is the characteristic frequency corresponding to the second type of local fluid flow between fractures and permeable matrix. It shows that the larger the matrix permeability and porosity, the easier the fluid flow, hence the larger the characteristic frequency. On the other hand, the more viscous the fluid, the more difficult the flow, and the lower the characteristic frequency.

2.5.3 Examples

To explore this relation, I use three sets of sandstone porosity and permeability data, measured in cores and logs (Dvorkin, personal communication), as the rock matrix properties surrounding the fractures. These sandstones vary from tight gas sands to high-porosity, loosely consolidated sandstones. Figure 2.11 shows the porosity versus permeability trend for the 74 samples. While the porosity increases within an order of magnitude, the permeability increases several orders of magnitude. Hence, we can tell from equation (2.40) that a small change in porosity may correspond to a big change in the critical frequency of flow through permeable walls.

Figure 2.12 shows that the predicted pore pressure changes with the wave frequency. The characteristic frequency evaluated by equation (2.40) is indicated by the dots on the pressure curves.

Using equation (2.40), I estimate the characteristic frequency versus porosity for the sandstones, when the fluid is water (viscosity 1cP), normal oil (viscosity 10cP), and heavy oil (viscosity 500cP), respectively. Figure 2.13 shows the results. We can see that the characteristic frequency ranges from smaller than 0.1Hz to larger than 10^5Hz, depending on both the fluid viscosity and the rock matrix permeability and porosity.

2.5.4 Conclusions

I showed the characteristic frequency for local fluid flow between a fracture and its surrounding matrix through permeable walls, as a function of fracture aperture, fluid bulk modulus and viscosity, and rock matrix porosity and permeability. I predicted, as an example, the characteristic frequency for various fractured sandstones. Through this study we learn that for fractured, permeable rocks, we cannot simply treat laboratory ultrasonic measurements as high-frequency conditions, and seismic surveys as low-frequency conditions. The characteristic frequency depends on the properties of fractures, pore fluid, and rock matrix.

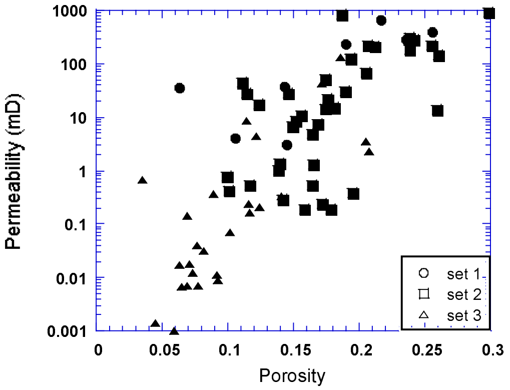

Figure 2.11: Permeability versus porosity for the three sets of rock samples (Dvorkin, personal communication).

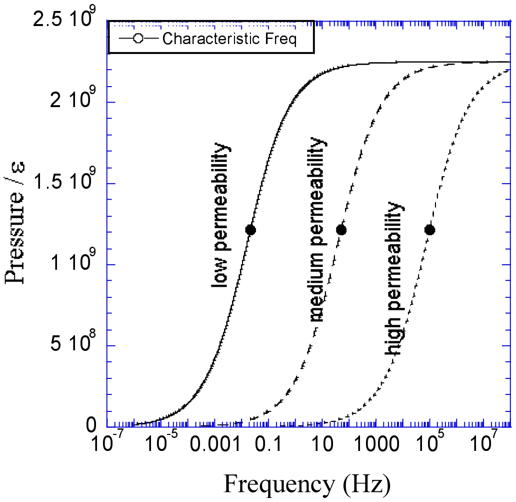

Figure 2.12: Pressure magnitude (Pa) normalized by ε (as in equation 2.36) in a fracture with permeable walls versus wave frequency. The three curves correspond to three rock samples with highest, lowest, and medium permeability among the 74 sandstone samples.

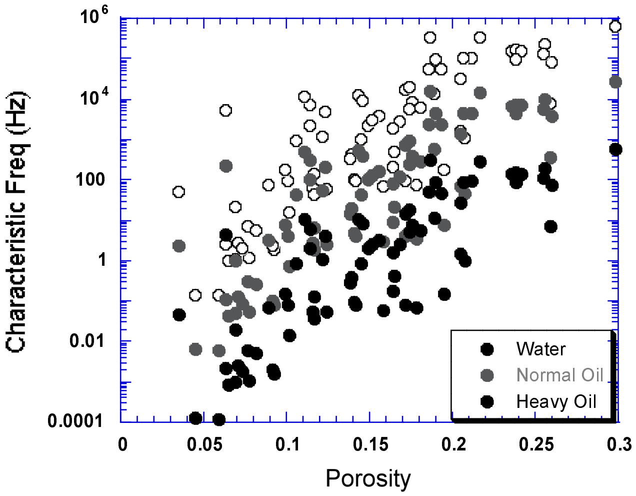

Figure 2.13: Characteristic frequency of local fluid flow in fractures with permeable walls versus embedding-rock porosity, based on the 74 sandstone porosity and permeability data.

2.6 Using Probability Functions to Quantify the Uncertainty in Fracture Characterization

In fracture characterization, there are always many assumptions and unknowns. I present a strategy in which the uncertainty in fracture system properties can be quantified by a combination of statistical techniques with a deterministic rock-physics model of fractured formation. This method was first proposed by Mavko and Mukerji (1995) for hydrocarbon detection in isotropic environments.

I demonstrate how to use the combined rock-physics and statistics approach to evaluate the uncertainty in fracture density detection; this use is based on the observed shear wave splitting in seismic data in the presence of realistic uncertainties in log and seismic data. In this case, the deterministic part of the formulation is Hudson's penny-shaped-crack model and the shear-wave splitting theory. The formulation identifies the most likely fracture-system properties. The variances of seismic or sonic-log velocity and anisotropy determine the uncertainty of the fracture interpretation.

With the uncertainty estimation technique, we can also evaluate the advantages and disadvantages of one measurement against others. I show, as an example, that the estimation of fracture density can be more accurate when it is based on the traveltime lag in shear-wave data, than when it uses the results of shear-wave moveout velocity analysis.

The new technique can also be extended to include other sources of input uncertainty and measurement errors that are not considered here.

2.6.1 Introduction

During the last two decades, rock physics has played a role in a number of successful strategies for identifying lithologies and detecting hydrocarbons from seismic data. The best examples are bright spots and conventional AVO analysis. These deterministic methods are easily understood.

However, the practical problem is that rock-physics interpretations are virtually never unique because of the complexity of the real world. For fracture characterization, there are even more uncertainties involved than in generally isotropic environments, because of the anisotropic properties of fractured rocks. When the reference information varies, the deterministic approach is to create several alternative mappings. For example, instead of having a constant unfractured-rock moduli over the survey area, we often need to consider a distribution of possible values. For fracture-density estimation based on shear-wave splitting, we apply the mapping for each different frame moduli assumption. Each of these mappings can incorporate rock-physics knowledge derived from well logs, cores, seismic data, and theories, but we are still left with the problem of choosing among the interpretations.

Mavko and Mukerji (1995) have presented a strategy for hydrocarbon detection, in which statistical techniques are combined with deterministic rock-physics relations derived from the laboratory and theory. In this paper, I extend the same approach to fracture characterization.

2.6.2 Methodology

Consider the case of a fractured reservoir in which the fracture system consists of parallel vertical fractures filled by gas. In order to locate the best drilling positions, we can use shear-wave-splitting techniques to locate the fractured zones.

The deterministic Equation (2.28) relates the shear-wave traveltime anisotropy $\Delta T_S / T_S$ to crack density *e* and unfractured rock moduli. This approach takes fixed values of the unfractured rocks' P-wave modulus M and S-wave modulus μ, and estimate the fracture density *e*.

Consider the case of shaly sandstones. Han (1986) studied a set of 80 sandstones with porosities ranging from 5% to 30% and clay volume fractions varying from 0% to 55%, as shown is Figure 2.14. We can choose the background moduli in Equation (2.28) to be the average value of the moduli measured by Han (1986). Figure 2.15 shows the resulting fracture density corresponding to various possible traveltime anisotropy $\Delta T_S / T_S$. The crack density increases with the observed traveltime anisotropy, because more fractures will induce more anisotropy into the mechanical properties of the rocks.

Even though the deterministic approach gives us a reasonable answer, we do not know how reliable the result is, because the method ignores the variation of the background moduli. In this case, the range of the moduli throughout Han's dataset is quite large. One way to compensate for this pitfall is to try various background moduli and compare the results. Another way is to ask, what is the probability distribution of the crack density at the observed $\Delta T_S / T_S$, when all possible background moduli are taken into account.

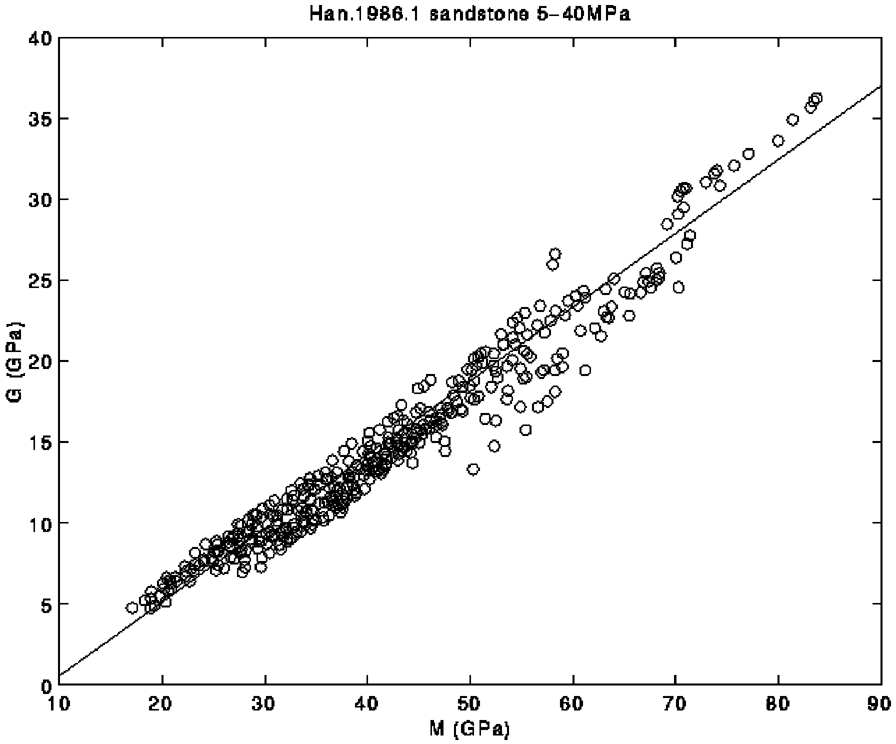

Figure 2.14: Laboratory measurement of bulk and shear moduli of 80 sandstone samples measured by Han under various confining pressures.

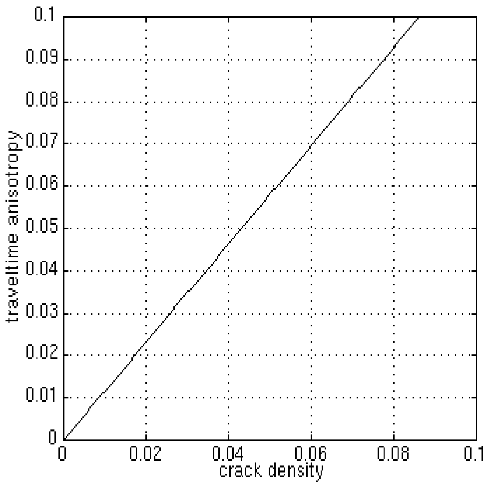

Figure 2.15: Crack density as a function of traveltime anisotropy, calculated with the deterministic approach. The background moduli are taken to be the average of Han's data.

To solve this problem, I begin by assuming that there are sufficient data from logs and core measurements to calibrate or characterize the natural spread of background rock properties within the reservoir interval of interest. From these data I infer the probability density functions (pdfs) of background P-wave moduli and S-wave moduli.

The deterministic Equation (2.28) allows us to relate the probability distribution of crack density, given the observed traveltime anisotropy, to the distribution of the background moduli:

$$P_\varepsilon(e \mid \gamma = \gamma_{obs}, M)d\varepsilon = P_\mu(\mu(e, \gamma_{obs}) \mid M)d\mu \tag{2.41}$$

where $P_\varepsilon(e \mid \gamma = \gamma_{obs}, M)$ is the conditional pdf of crack density e given M, and $P_\mu(\mu(e, \gamma_{obs}) \mid M)$ is the conditional pdf of μ given M. The left side of Equation (2.41) gives the probability of occurrence of fracture density in the interval $[e, e + de]$, given the observed traveltime anisotropy $\Delta T \ / T$, which is equal to γ, as shown by Equation (2.26); and the right side is the probability of the corresponding reference background shear modulus in the interval $[\mu, \mu + d\mu]$. Unless there is some additional constraint, we need to integrate the probability density function over the range of possible background P-wave modulus M:

$$P_\varepsilon(e \mid \gamma = \gamma_{obs}) = \int_M P_\mu(\mu(e, \gamma_{obs}) \mid M) \left|\frac{d\mu}{de}\right|_{\gamma_{obs}, M} P_M(M)dM \tag{2.42}$$

Equation (2.42) is the main result of this section. It allows us to evaluate the pdf of the crack density, given the observed traveltime anisotropy represented by γ_{obs}. The maximum-likelihood crack density is the one whose e maximizes $P_\varepsilon(e \mid \gamma = \gamma_{obs})$. On the right-hand side, $P_\mu(\mu(e, \gamma_{obs}) \mid M)$ and $P_M(M)$ are evaluated from the reference data, for example logs and cores. The Jacobian $|d\mu / de|$ follows from Equation (2.27). Most importantly, Equation (2.42) offers a strategy for implementing Hudson's equation and the shear-wave splitting formula in the realistic case when the reference background moduli span a range of values.

To determine the Jacobian, I transform Equation (2.27) to

$$\mu = \frac{9M\gamma - 8Me}{6\gamma} \tag{2.43}$$

Hence,

$$\left|\frac{d\mu}{de}\right| = \frac{4M}{3\gamma} \tag{2.44}$$

Substituting into Equation (2.42), we get the analytical formulation for calculating crack density pdf:

$$P_\varepsilon(e \mid \gamma = \gamma_{obs}) = \int_M P_\mu(\mu(e, \gamma_{obs}) \mid M) \frac{4M}{3\gamma_{obs}} P_M(M) dM \tag{2.45}$$

The pdf in Equation (2.45) is plotted in Figure 2.16. Each horizontal row of pixels can be interpreted as the pdf of crack density given a measured traveltime anisotropy (darker color indicates higher probability). The maximum-likelihood crack density at each observed traveltime anisotropy γ_{obs} is that with the highest probability density. It corresponds to the diagonal black ridge in Figure 2.16. Notice that the most likely crack density is close to the deterministic result based on the average background moduli, represented by the white solid line plotted along the peak. Hence, the maximum-likelihood crack density can be roughly estimated from the deterministic equations, when the average unfractured rock moduli are used as the input. However, the statistical approach highlights the problem often overlooked by the deterministic approaches. The natural variation of rock moduli leads to a range of possible crack densities consistent with an observed velocity. For example, an 8% observed traveltime anisotropy $\left|\Delta T_S / T_S\right|_{obs}$ can correspond to a most likely crack density of 0.07, but crack densities ranging from 0.06 to 0.08 are also possible with smaller probability.

The resulting range of crack density corresponding to an observed traveltime anisotropy is fairly narrow in this case even though the background moduli span a wide range. This narrow distribution can be explained by Equation (2.28), which shows that the crack density depends on the ratio of P- to S-wave moduli. Because the unfractured rock P- and S-wave moduli we used here have a strong linear relationship, the standard deviation of the ratio of the moduli is rather small, which gives a small standard deviation in crack density for each observed traveltime anisotropy.

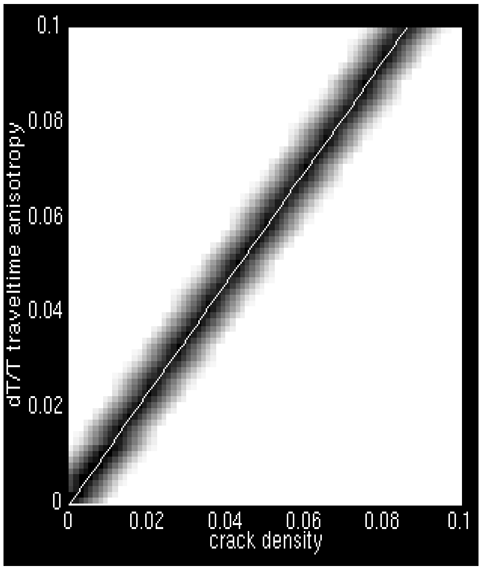

Figure 2.16: Crack density probability as a function of observed traveltime anisotropy. Darker color represents higher probability. The superimposed white line is the deterministic relationship between crack density and traveltime anisotropy. Notice the deterministic result is close to the most likely crack density at each observed dT/T.

2.6.3 Evaluating One Method Against Another

We can use the uncertainty evaluation technique to choose the best method that gives the least uncertainty in fracture characterization.

The previous section shows an example of predicting fracture density by shear-wave splitting. When the background P- and S-wave moduli have a good linear correlation, this method gives a small uncertainty in fracture-density detection. Other methods can give a wider probability function for the same reference moduli. For example, instead of measuring the shear-wave splitting, we could use well log or 2-D far-offset S-wave data to obtain the slow shear-wave velocity. Then the shear wave moduli can be determined by

$$\mu_{obs} = \rho V_{obs}^2 \tag{2.46}$$

Based on the deterministic relation between the crack density and the slow shear wave modulus,

$$\mu_{obs} = \mu - \mu e U_1 \tag{2.47}$$

I derived the corresponding probability function of crack density for an observed shear modulus:

$$P_\varepsilon(e \mid \mu = \mu_{obs}) = \int_M P_\mu(\mu(e, \mu_{obs}) \mid M) \left| \frac{d\mu}{de} \right|_{\mu_{obs}, M} P_M(M) dM \tag{2.48}$$

The resulting crack density, shown in Figure 2.17, has a much larger uncertainty than that in Figure 2.16. Hence, to evaluate the crack density for this set of reference data, where the P- and S-wave moduli have a strong linear relationship, the traveltime anisotropy is a better approach than the shear wave velocity.

2.6.4 Discussion

The interpretation of the observed seismic anisotropy in terms of fractures' physical properties is probably not unique. I have presented a strategy for quantifying the uncertainty in fracture characterization. In this strategy, statistical techniques are combined with deterministic rock physics relations. I showed that this technique can help one to evaluate the effectiveness of one method against another, and choose the method that gives less uncertainty.

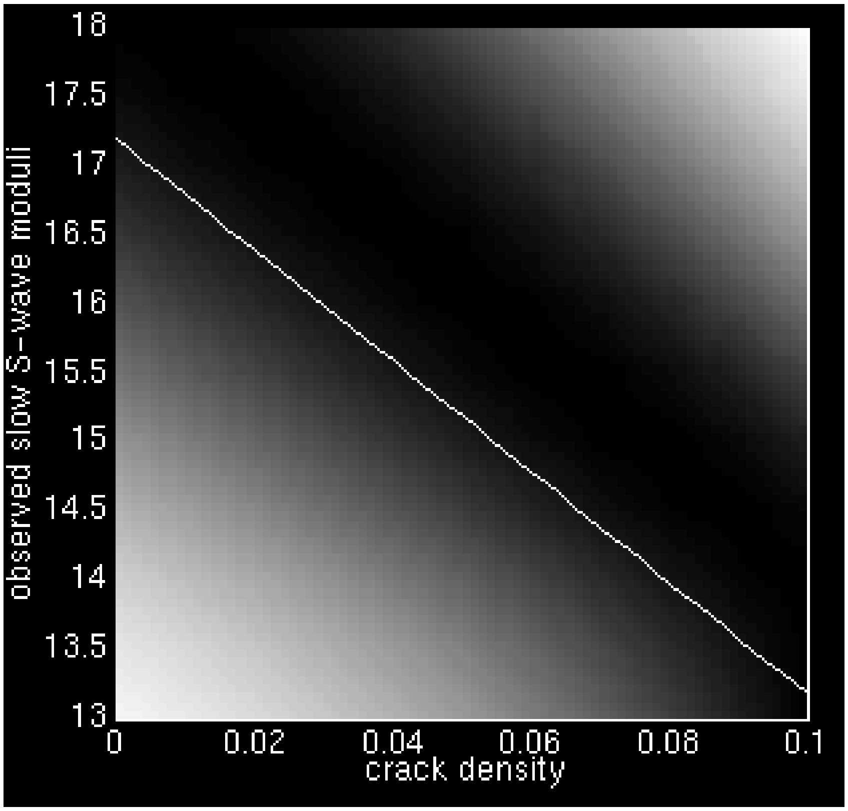

Figure 2.17: Crack-density probability as a function of observed shear modulus. Darker color represents higher probability. The superimposed solid white line is the deterministic relationship between crack density and shear moduli. Notice that this method gives larger uncertainty in crack density at each observed shear modulus than the previous figure.

2.7 References

Alford, R. M., 1986, Shear data in the presence of azimuthal anisotropy: Dilley, Texas, SEG Abstract.

Backus, G. E., 1962, Lone-wave elastic anisotropy produced by horizontal layering, J. Geophys. Res., **67**, p. 4427-4440.

Batzle, M., and Wang, Z., 1992, Seismic properties of pore fluids: Geophys., **57**, No. 11, 1396-1408.

Biot, M.A., 1956a, Theory of propagation of elastic waves in a fluid saturated porous solid. I. Low-frequency range: J. Acoust. Soc. Amer., **28**, 168-178.

Biot, M.A., 1956b, Theory of propagation of elastic waves in a fluid saturated porous solid. II. Higher-frequency range: J. Acoust. Soc. Amer., **28**, 179-191.

Biot, M.A., 1962, Mechanics of deformation and acoustic propagation in porous media: J. Appl, Phys., **33**, 1482-1498.

Brown, R., and Korringa, J., 1975, On the dependence of the elastic properties of a porous rock on the compressibility of the pore fluid, Geophys., **40**, 608-616.

Castagna, J., and Smith, S., 1994, Comparison of AVO indicators: A modeling study, Geophys., **12**, 1849-1855.

Castagna, J., and Swan, H., 1997, Principles of AVO crossplotting, Geophysics Leading Edge, **16**, 337-342.

Chen, W., 1995, AVO in azimuthally anisotropic media , fracture detection using P-wave data, and a seismic study of naturally fractured tight gas reservoirs, Ph.D. thesis, Stanford University.

Dvorkin, J., Mavko, G., and Nur, A., 1990, The oscillations of a viscous compressible fluid in an arbitrary-shaped pore: Mechanics of Materials, **9**, 165-179.

Han, D. H., 1986, Effects of porosity and clay content on acoustic properties of sandstones and unconsolidated sediments, PH.D. thesis, Stanford University.

Hudson, J. A., 1980, Overall properties of a cracked solid, Math. Proc. Camb. Phil. Soc., **88**, p. 371-384.

Hudson, J. A., 1981, Wave speeds and attenuation of elastic waves in material containing cracks: Geophys. J. Roy. Astr. Soc., **64**, p. 133-150.

Hudson, J. A., 1990, Overall elastic properties of isotropic materials with arbitrary distribution of circular cracks, Geophys. J. Int., **102**, p. 465-469.

Hudson, J. A., 1994, Overall properties of anisotropic materials containing cracks, Geophys. J. Int., **116**, p. 279-282.

Keith, C., and Crampin,, S., 1977, Seismic body waves in anisotropic media: reflection and refraction at a plane interface, Geophys. J. R. Astr. Soc., **49**, 181.

Mavko, G., and Jizba, D., 1991, Estimating grain-scale fluid effects on velocity dispersion in rocks: Geophysics, **56**, 1940-1949.

Mavko, G., and Mukerji, T., 1995, A rock physics strategy for quantifying uncertainty in common hydrocarbon indicators, American Geophysical Union 1995 fall meeting Eos Transactions, **76**, No. 46, Suppl., 600.

Mavko, G., Mukerji, T., Dvorkin, J., 1998, The rock physics handbook, Tools for seismic analysis in porous media, Cambridge University Press, 329 p.

Mavko, G., and Nur, A., 1975, Melt squirt in the asthenosphere: J. Geophys. Res., **80**, 1444-1448.

Mukerji, T., and Mavko, G., 1994, Pore fluid effects on seismic velocity in anisotropic rocks: Geophysics, **59**, 233-244.

Nelson, R. A., 1985, Geologic Analysis of Naturally Fractured Reservoirs, IN: Contributions in petroleum geology and engineering, Gulf Publ. Co., 320p.

Nichols, D., 1990, A comparison of two models for the elastic properties of fractured rock, Stanford Exploration Project Report, **60,** 261-270.

Nur, A., Simmons, G., 1969, Stress-induced velocity anisotropy in rock - an experimental study, Jour. Geophys. Research, **74**, no. 27, 6667-6674.

O'Connell, R., and Budiansky, B., 1977, Viscoelastic Properties of Fluid-Saturated Cracked Solids: Journal of Geophysical Research, **82**, 5719-5735.

Pyrak-Nolte, L. J., Myer, L. R., and Cook, N. G. W., 1990a, Transmission of seismic waves across single natural fractures, J. Geophys. Res., **95**, p. 8617-8638 .

Pyrak-Nolte, L. J., Myer, L. R., and Cook, N. G. W., 1990b, Anisotropy in seismic velocities and amplitudes from multiple parallel fractures, J. Geophys. Res., **95**, p. 11345-11358.

Rueger, A., 1995, P-wave reflection coefficients for transversely isotropic media with vertical and horizontal axis of symmetry, SEG Annual Meeting Abstracts, **65**, 278-281.

Rueger, A., 1996, Variation of P-wave reflectivity with offset and azimuth in anisotropic media, SEG Annual Meeting Abstracts, **66**, 1810-1813.

Rutherford, S., and Williams, R., 1989, Amplitude-versus-offset variations in gas sands, Geophysics, **54**, 680-688.

Sayers, C., and Rickett, J., 1997, Azimuthal variation in AVO response for fractured gas sands, Geophysical Prospecting, **45**, 165-182.

Sena, A. G., 1991, Seismic traveltime equations for azimuthally anisotropic and isotropic media: Estimation of interval elastic properties, Geophys., **56**, 2090-2101.

Schoenberg, M., 1983, Reflection of elastic waves from periodically stratified media with interfacial slip, Geophys. Prosp. **31**, p. 265-292.

Schoenberg, M and Douma, J., 1988, Elastic wave propagation in media with parallel fractures and aligned cracks, Geophys. Prosp., **36**, p. 571-590.

Schoenberg, M and Muir, F, 1989, A calculus for finely layered anisotropic media, Geophysics, **54**, 581-589.

Shuey, R.T., 1985, A simplification of the Zoeppritz equations, Geophysics, **50**, 609-614.

Teng, L., and Mavko, G., 1995, Comparison of fracture models, SRB Annual Report, **58**, G3.

Thomsen, L., 1986, Weak elastic anisotropy: Geophysics, **51**, No. 10, 1954-1966.

Thomsen, L., 1995, Elastic anisotropy due to aligned cracks in porous rock, Geophysical Prospecting: **43**, 805-829.

CHAPTER 3

RESERVOIR ROCK PROPERTIES OF FORT FETTERMAN SITE

3.1 Introduction

In this chapter, I analyze the well-log data, and gather the typical rock properties at the reservoir level; these properties include the P- and S-wave velocities, density, clay content, pore fluids, evidence of overpressure, and fractures. The main goal is for this information to assist the next chapter's fracture interpretation, which uses seismic anisotropy. Understanding the basic rock properties is also an integral part of understanding the fractured environments.

The data to which I apply and test the fracture-induced anisotropy theories are from the Fort Fetterman site. It is located at the southwestern margin of the Powder River Basin, north of the town of Douglas, in Converse County, east central Wyoming. A review of the regional geological framework can be found in the appendix. Oil and gas have been produced from the Upper Cretaceous Niobrara and Frontier Formations. Because of the low permeability of the reservoir rocks, fracturing is an important reservoir component related to economical production.

To understand the subsurface fracture network, log data and multi-component seismic data were collected. Because the seismic anisotropy is a combined effect of the characteristics of the matrix rock, pore fluids, fractures, and seismic wave frequency, we need to analyze and understand the physics of the formation rocks and pore fluids before we can make any sense of the seismic fracture interpretation.

3.2 Overview of Well Logs at the Survey Area

Fort Fetterman field has decades of producing history. As shown in the basemap in Figure 3.1, a 3D cube of P-wave data (GRI-3D) and two 2D lines of multi-component data (GRI-1 and GRI-4) were collected at this field for the fracture study sponsored by the Gas Research Institute. Most of well logs in the survey area were available only in paper form. Digital well-log data were available from five wells as listed in Table 4.1. Among them, the Red Mountain, the State #1-36, and the Wallis wells have sonic log data that are crucial for the seismic study. Only the Red Mountain well has, available for us, density logs along the whole depth range, while the others have only segments of the density logs at the Niobrara and Frontier levels. I analyzed, in this chapter, the logs mainly from the Red Mountain well.

Figure 3.2 shows the formation tops at these well locations. The target reservoirs at the Niobrara and Frontier formations are marked on all three wells. The Niobrara Formation consists of a series of fractured, marine chalks and limestones interbedded with calcareous shales and bentonites. The Frontier Formation includes sand bodies interbedded with marine shale. This formation ranges up to 1000 feet thick in central and northeast Wyoming (Barlow and Haun, 1966). The uppermost sand body, the first Frontier Sand, is a finely grained, "tight" sandstone with high acoustic velocities, as observed in the sonic logs. A more detailed geological description can be found in the appendix.

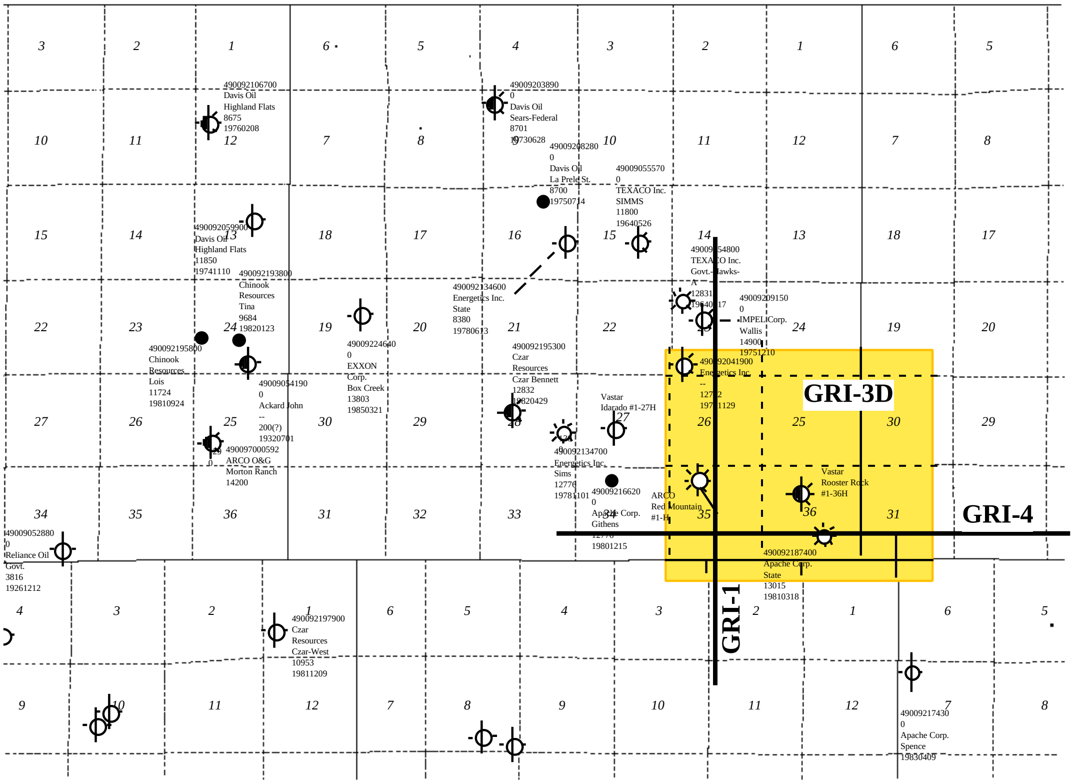

Figure 3.1: Base map of the Fort Fetterman site showing the locations of the 2D multi-component seismic lines GRI-1 and GRI-4, the 3D survey area GRI-3D in gray, and the well location.

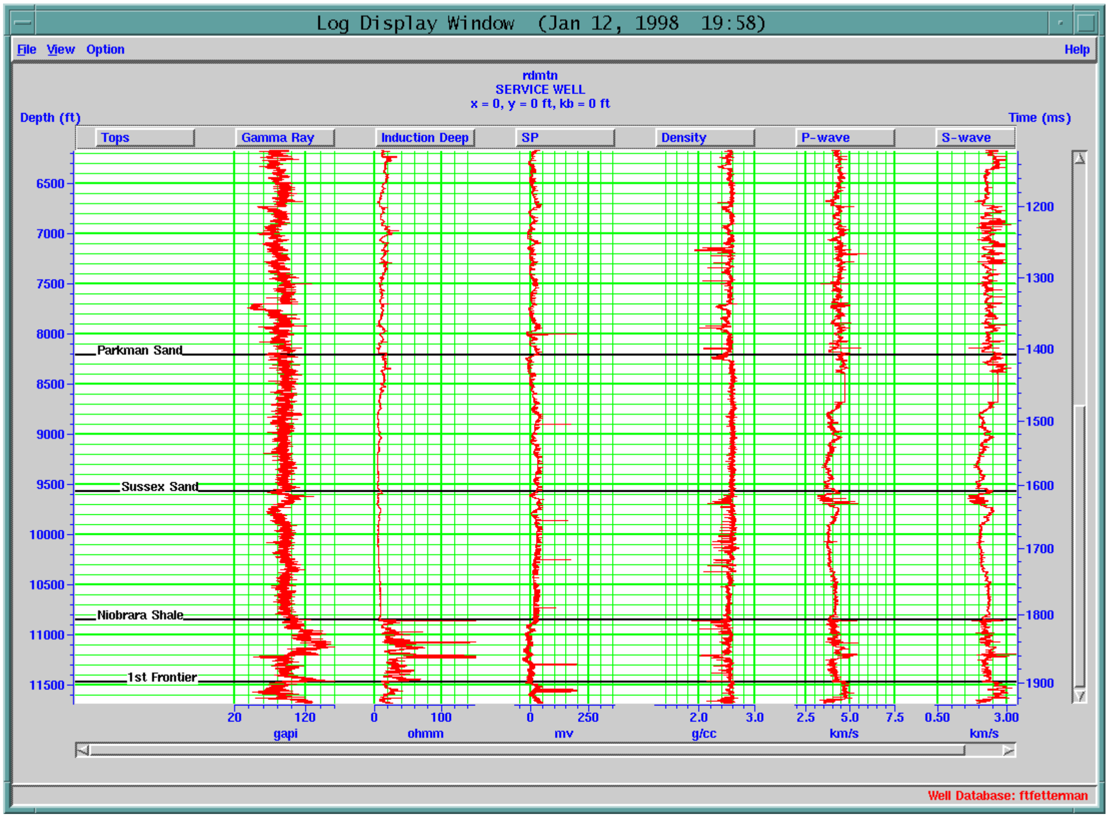

Figure 3.2: (a) Formation tops superimposed on the well logs from the Red Mountain well.

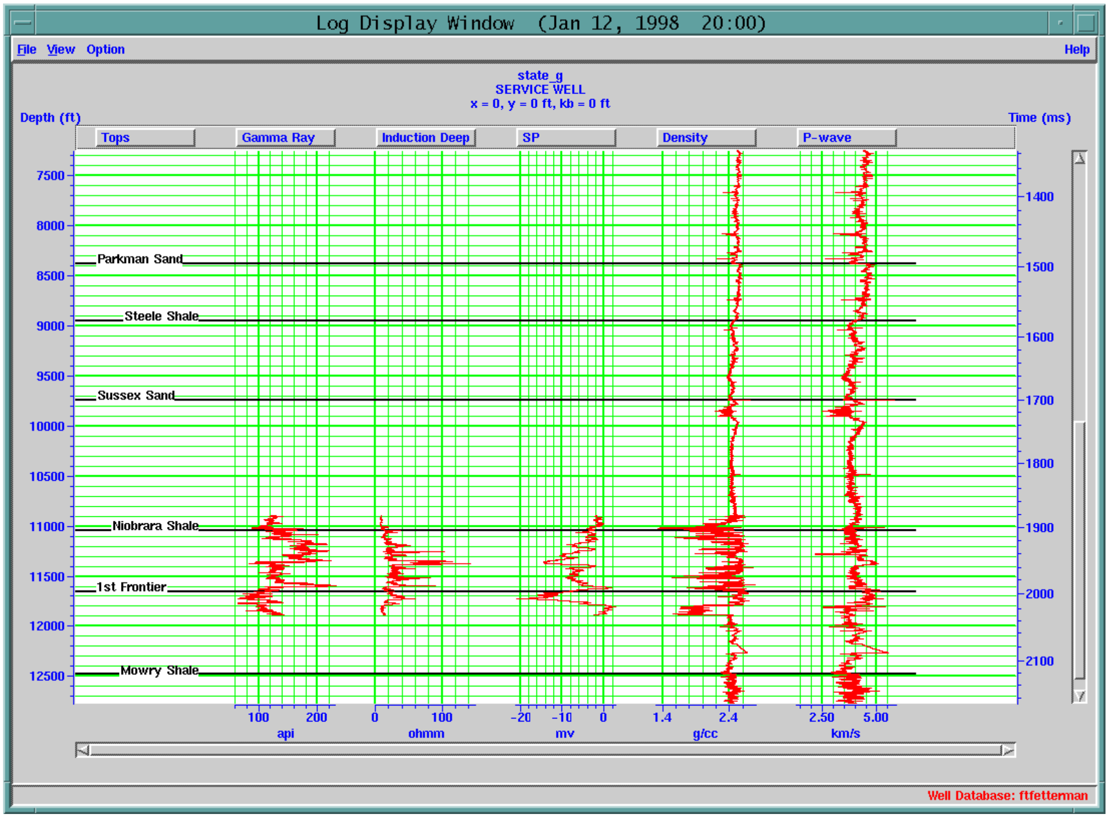

Figure 3.2: (b) Formation tops superimposed on the well logs the State #1-36 well. At this well, the density data were estimated using Gardner's equation outside the region of the Niobrara Shale and the 1st Frontier Sand.

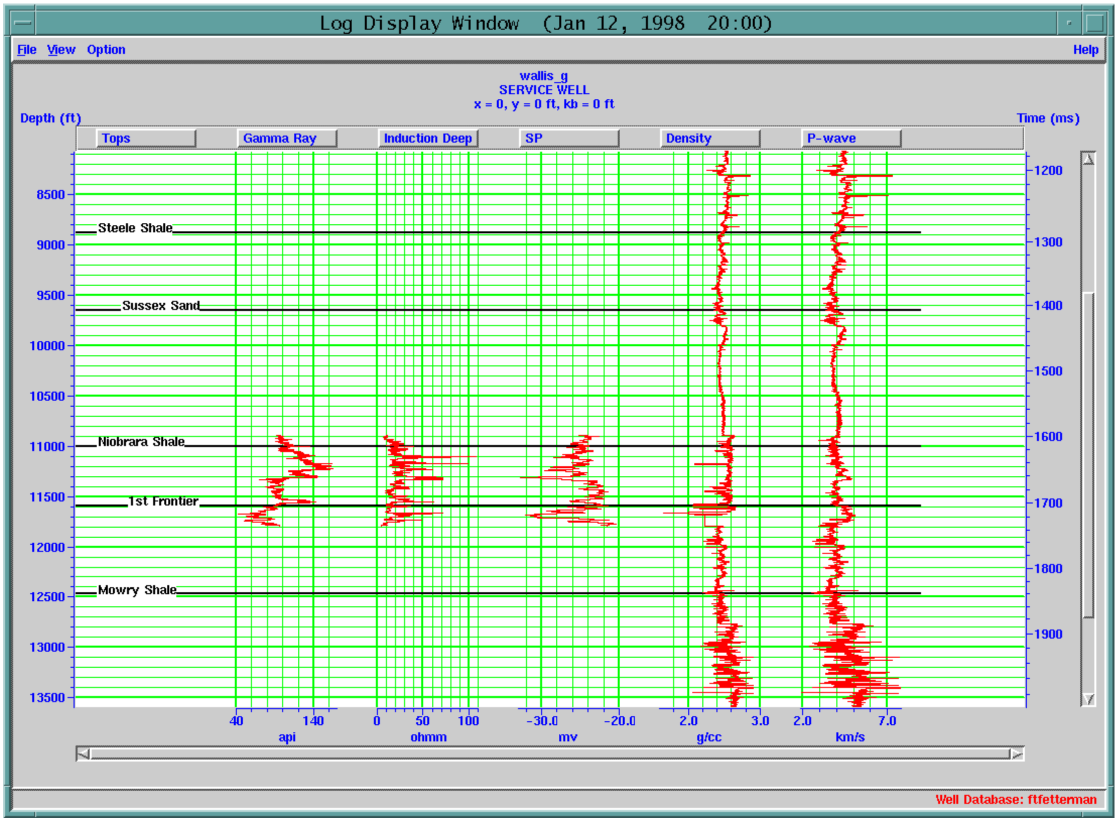

Figure 3.2: (c) Formation tops superimposed on the well logs the Wallis well. At this well, the density data were estimated using Gardner's equation outside the region of the Niobrara Shale and the 1st Frontier Sand.

It is particularly worth mentioning that the Arco Red Mountain #1-H well, which targeted fractured Niobrara and Frontier reservoirs, gives a wide range of log types. A pilot hole (straight hole) was drilled first. The P- and S-wave sonic logs, dipole shear logs, density logs, spectral gamma ray logs, and resistivity logs were recorded along the pilot hole. Multi-component VSP data were conducted with the receivers in the borehole, and the sources at four different surface locations. Details about the VSP survey are explained in the next chapter. To intersect the fractures, a highly deviated hole (horizontal well) was drilled after the pilot hole. Figure 3.3 shows its trajectory. To obtain fracture images and bedding information, formation MicroScanner Logs ran through the horizontal well. The direct observation of the subsurface fractures gives us the fracture-number count as well as the fracture-aperture information. Our main effort is focused on analyzing the data from this well.

Table 3.1. Five wells supplying digital well-log data.

Operator	Well Name	Location	Digital Logs
Apache	State #1-36	T33N R71W s36	SP, GR, Density, Neutron, Resistivity, Sonic (P only)
Vastar	Idarado #1-27H	T33N R71W s27	SP, GR, Density, Neutron, Resistivity
Arco	Red Mountain #1-H	T33N R71W s35	SP, SpectralGR, Density, Neutron, Resistivity, Sonic (P and S), Dipole Shear Sonic, FMS
Vastar	Rooster Rock #1-36H	T33N R71W s36	SP, GR, Density, Neutron, Resistivity
Impel	Wallis #1	T33N R71W s23	SP, GR, Density, Neutron, Resistivity, Sonic (P only)

3.3 Spectral Gamma-Ray Logs and Clay Content

I used the spectral gamma-ray logs along the Red Mountain well in my analysis of the clay content of the rocks at the reservoir level: the Niobrara Formation and the first Frontier Sand.

The usual gamma-ray log records the sum of radiation emanating from naturally occurring uranium, thorium, and potassium. It is a good shale indicator because shale, among the sedimentary rocks, has a high concentration of thorium and potassium. However, it can be misleading in carbonate formations that have a high

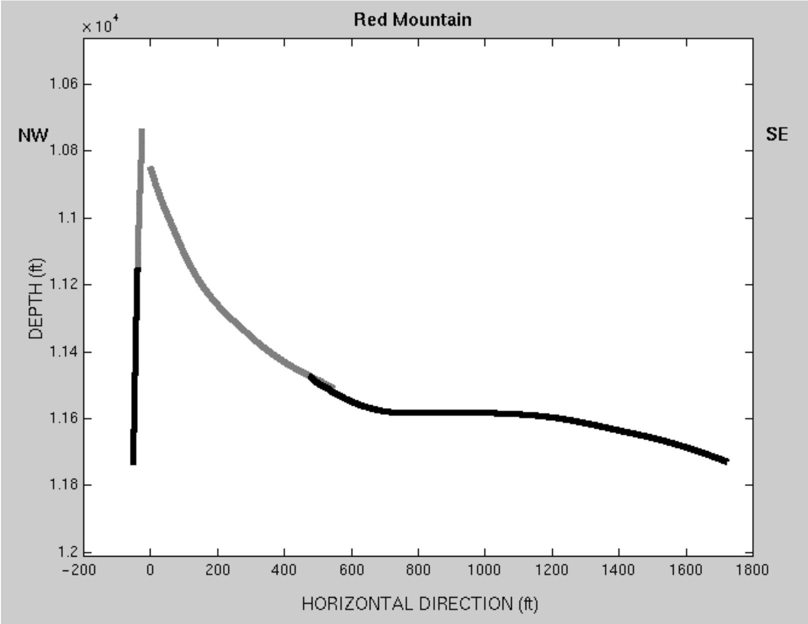

(3.3a)

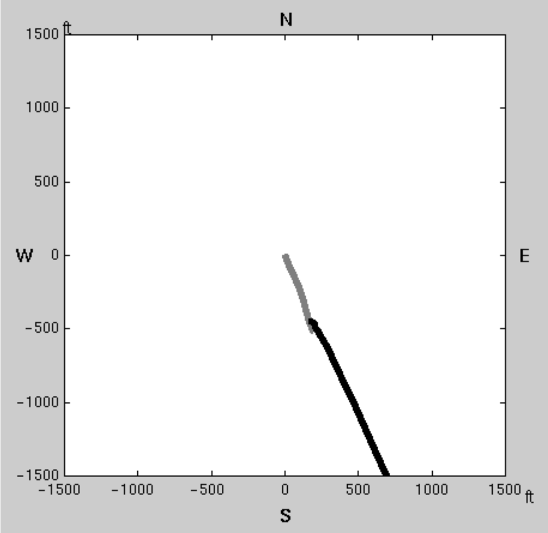

(3.3b)

Figure 3.3: (a) Well trajectories of the Red Mountain well showing both the vertical hole (pilot hole) and the highly deviated hole (horizontal hole); (b) Map view of the highly deviated hole showing that its azimuth is about N155°E.

uranium content (Rider, 1991). Figure 3.4 shows the spectral gamma-ray logs recorded along the Red Mountain well. We can clearly see that the high gamma-ray values at the Niobrara Formation are mainly attributed to the uranium. This is consistent with the geology of the Niobrara Formation, which has a high percentage of chalk and calcareous shale that can be the source of the uranium radiation. Therefore, the spectral gamma-ray log of thorium and potassium is more appropriate for the clay-content analysis.

To derive the shale content, I adapt the shale Index given by Bassiouni (1994):

$$(I_{sh})_{KTh} = \left[(C_K C_{Th})_{\log} - (C_K C_{Th})_c\right] / \left[(C_K C_{Th})_{sh} - (C_K C_{Th})_c\right] \qquad (3.1)$$

where $(C)_{\log}$'s are the curve readings in the zone of interest, and $(C)_c$'s are the curve readings in the cleanest formation, and $(C)_{sh}$'s are those in pure shales. This shale index is more representative than those using potassium only or thorium only, because it is virtually independent of clay type (Bassiouni, 1994). The clay content V_{sh} for pre-tertiary rocks is given below, as a function of the shale index:

$$V_{sh} = 0.33(2^{2I_{sh}} - 1) \qquad (3.2)$$

The Niobrara Formation and the first Frontier Sand belong to the upper Cretaceous (pre-tertiary) stratigraphy. Their clay contents are derived according to equations 3.1 and 3.2. Figure 3.5 shows the statistical distribution of the clay contents. The Niobrara Formation has a mean value of clay content 34.3%, and a standard deviation of 17.3%; the first Frontier Sand has a mean of 30.3%, and a standard deviation of 20.8%. The high clay-content values require us, in our velocity and density analyses, to treat the reservoir rocks as shaly formations rather than as pure carbonate rocks or sandstones.

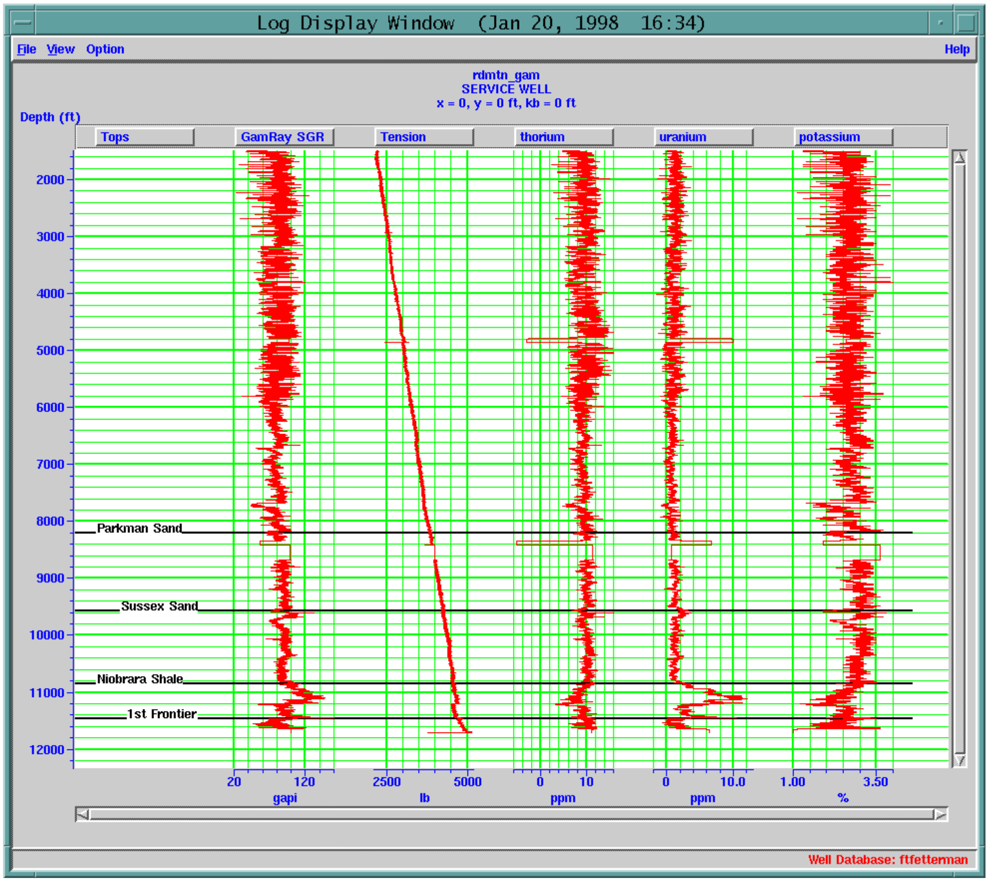

Figure 3.4: The spectral gamma ray logs recorded along the Red Mountain well showing from left to right the sum of all gamma ray radiation, the cable tension, the thorium, urianium, and potassium logs.

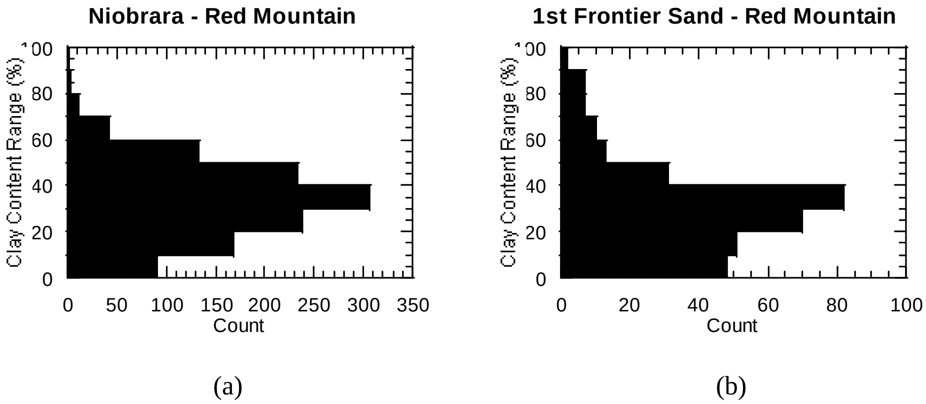

(a) (b)

Figure 3.5: Statistical distribution of clay content of (a) the Niobrara Formation and (b) the first Frontier Sand.

It is worth mentioning that there are two other independent indicators of the clay content: the spontaneous potential log and the separation between density-log porosity and neutron-log porosity (Rider, 1991). The former is due to the different self-potentials of shale and sandstone; and the latter is due to the fact that shale has higher density as well as higher neutron-porosity values relative to sand. A detailed explanation can be found in Rider (1991). Figure 3.6 shows the curves of the SP logs and the product of bulk density and neutron porosity, next to the K-Th shale-index curve. We can see that they resemble each other at most depth levels with local dissimilarities near depth 10350 ft and 10850 ft. The resemblance demonstrates that Equation 3.1 gives a good shale indicator. Since the SP logs record the combined effect of shaliness, formation-water salinity, drilling fluid/mud resistivity, formation permeability, and other factors, the local dissimilarities in the SP curve could be due to formation or drilling fluid resistivity change, or permeability change.

3.4 Pore Fluids

Hydrocarbons have a higher electrical resistivity than those of brine and water. The induction logs use this effect to detect hydrocarbons. Figure 3.7 shows the deep induction logs expressed in resistivity. The Niobrara and Frontier formations have a higher average resistivity than the formations above, and could contain hydrocarbons. They were the drilling targets.

After the horizontal well was drilled, the producing interval at the Red Mountain well was the Frontier Formation. The initial 24-hour testing production yielded 1068 Mcf. gas, 32 bbl. oil, and 3 bbl. water. The oil gravity in the API unit is 53. The gas-oil ratio (GOR) based on the initial production record is 33,375 scf/bbl. I assumed that the volume fraction of each fluid in the pore is the same as that in the production record. In reality, the GOR at the surface could be different from the GOR at the reservoir depth. More gas could be in solution in the reservoir. On production, gas

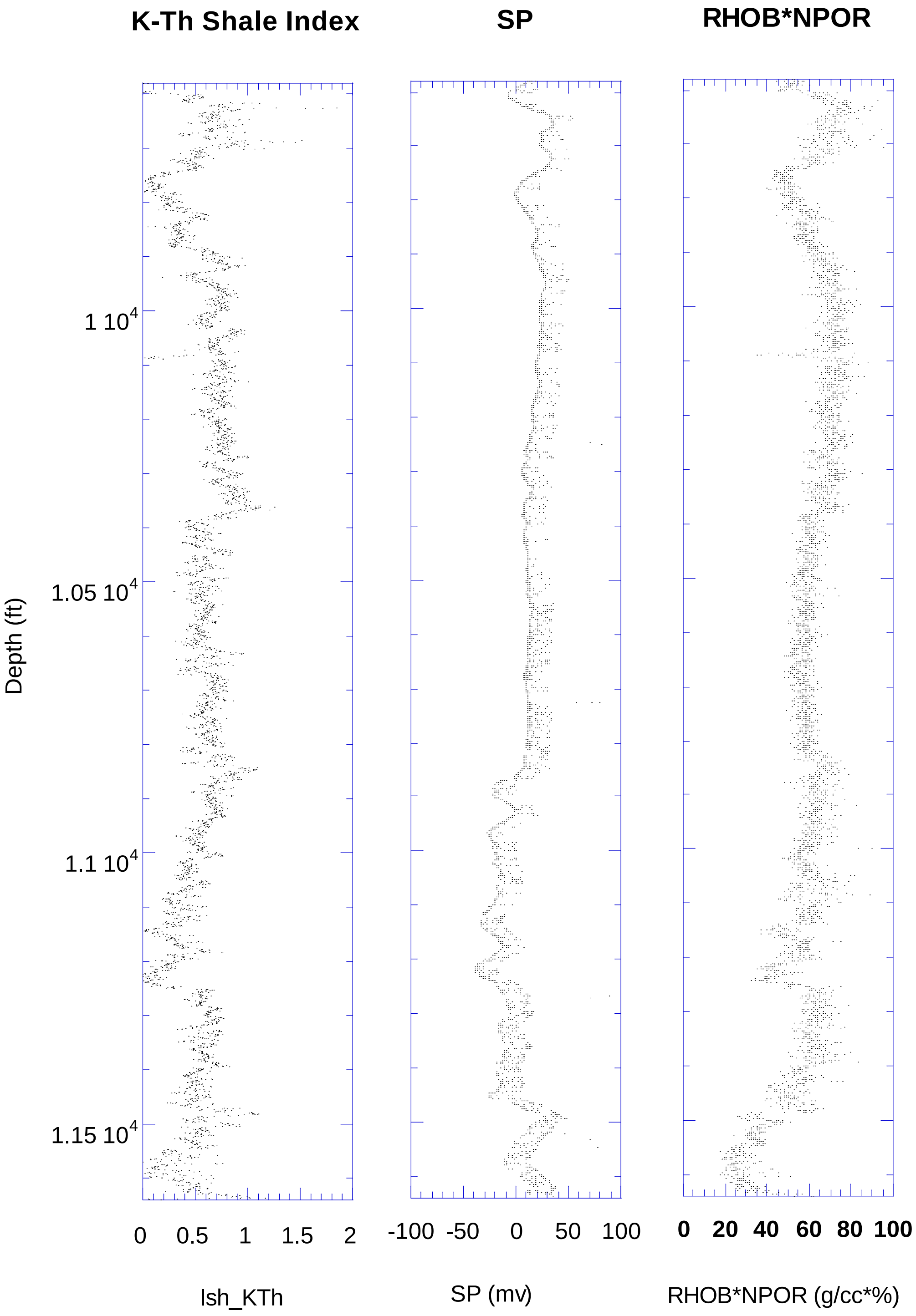

Figure 3.6: a)K-Th shale index; b) SP; c) the product of density and neutron porosity. Each curve is an independent shale indicator, therefore, they resemble each other.

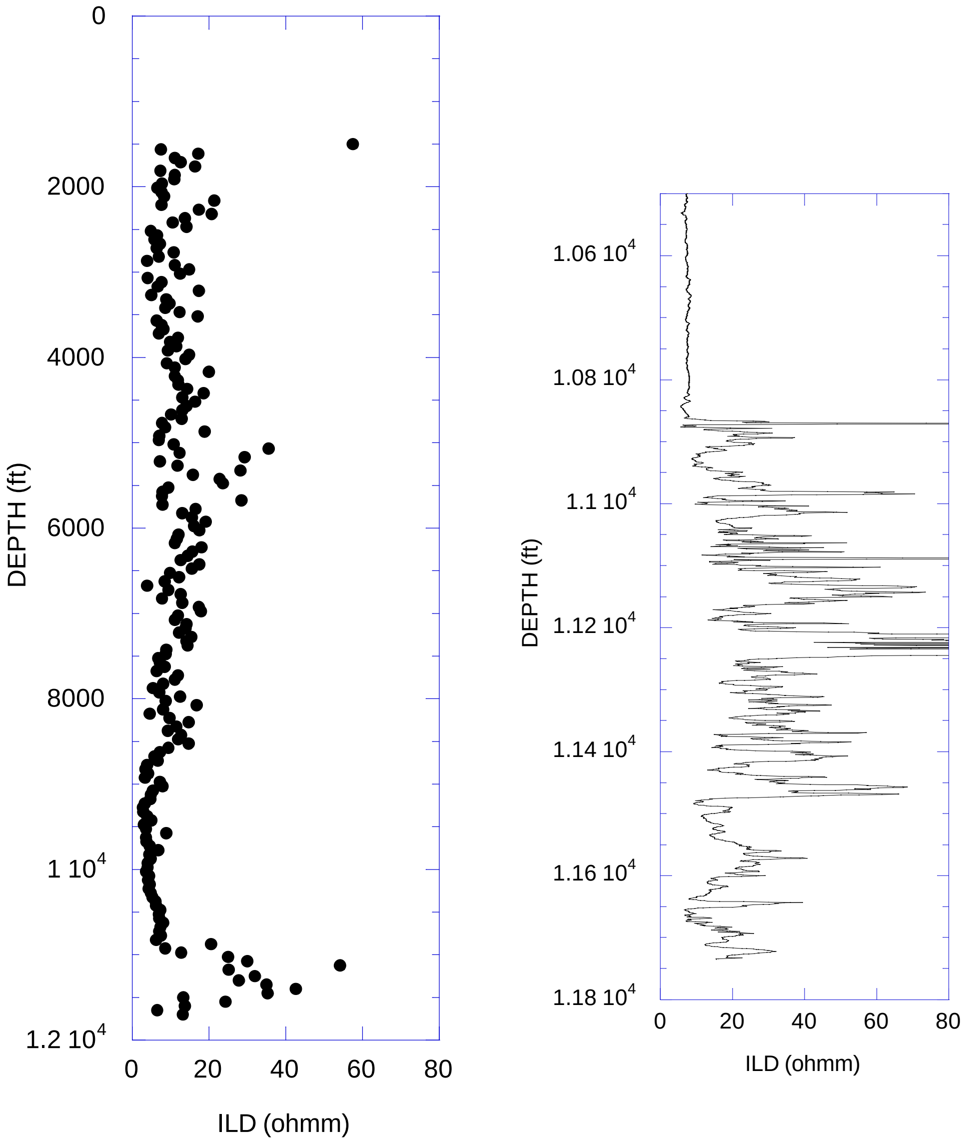

(a) (b)

Figure 3.7: ILD deep induction logs expressed as resistivity along the Red Mountain well. (a) shows the entire depth range; (b) shows the zoomed in section at the reservoir depth.

comes out of solution. Therefore, there is an uncertainty in the reservoir fluid properties. I assumed that this uncertainty is not significant since the GOR is very high already. An even higher GOR will not make much difference on acoustic properties.

To calculate the density and acoustic velocity of the fluid mixture, we also need to know the temperature and pressure. At the depth of the first Frontier Sand, the rock temperature and pore pressure estimated using the universal empirical formulae from the Petrotool Software package are 183^{o}F, and 5169 psi. Under this condition, the fluid mixture has a density of 0.3 g/cc, and a velocity of 2000 ft/sec (0.6 km/sec). However, a gas-producing formation often has a higher temperature and pore pressure than the surrounding rocks. At the Powell-Ross Field in Converse County, same county as the study area is located in, the temperature and pore pressure of the Frontier reservoir is about 262^{o}F and 8000 psi as listed by Hando (1976). Under this condition, the gas-oil mixture will instead have a density of 0.33 g/cc and a velocity of 2400 ft/sec (0.72 km/sec). The fluid density and velocity are required in porosity calculation and fluid substitution calculation.

No fluid type record is available for the Niobrara Formation. Several attempts to provide an accurate fluid content were not conclusive because of the high clay content and low porosity. Therefore, for the velocity and density analyses in the next section, I keep an open range of pore fluid type in the Niobrara Formation: from 100% brine to 100% gas.

3.5 Velocity and Density Analyses

The velocity and density logs recorded along the pilot hole of the Red Mountain well give the isotropic elastic properties of the rocks at known depth levels. Getting these properties is a necessary step toward the seismic anisotropy analysis. This section analyzes the velocity and density logs along the Red Mountain well.

Figure 3.8 shows the statistics, based on the well logs from the Red Mountain well, of the P- and S-wave velocities, density, and porosity of the Niobrara Formation. The porosity calculation is based on the density log and uses the following equation for shaly formations (Bassiouni, 1994):

$$r_b = f r_{fl} + V_{sh} r_{sh} + \left(1 - f - V_{sh}\right) r_{matrix} \tag{3.3}$$

where f is the intergranular porosity, V_{sh} is the clay volume fraction, and r_b, r_{fl}, r_{sh}, and r_{matrix} are the bulk, fluid, shale, and matrix densities. Note that the intergranular porosity in this context does not include the porosity in the clay material, and should be lower than the apparent/total porosity. I assumed a matrix density r_{matrix} of 2.71 g/cc, corresponding to that of a limestone, and a shale density r_{sh} of 2.60 g/cc, corresponding to the bulk density at a 100% clay content point within the Niobrara Formation. The pore fluid in the Niobrara Formation, as we discussed previously, can range from pure water to pure gas. The mean value and standard deviation of each entry are given below:

	Mean	Standard Deviation
Vp	4.158 km/sec	0.265 km/sec
Vs	2.287 km/sec	0.148 km/sec
Density	2.50 g/cc	0.10 g/cc
Porosity (water)	9.95%	6.02%
Porosity (gas)	6.92%	4.19%

Velocities, density, and clay content are correlated properties. The cross plots of P-wave velocity versus density, clay content, S-wave velocity, and Vp-Vs ratio are shown in Figure 3.9. Within the Niobrara Formation, the density change, from 2.4 g/cc to 2.6 g/cc, is small compared to the clay-content change, from 0 to above 60%. The P-wave velocity increases as the clay content drops, but shows no obvious change with the density, simply because of the small density range. The S-wave velocity increases with the P-velocity, and their relationship matches the Greenberg-Castagna empirical relation (Greenberg and Castagna, 1992) for a 60%-limestone and 40%-shale mixture. The Vp-Vs ratio is about 1.8 for the Niobrara Formation.

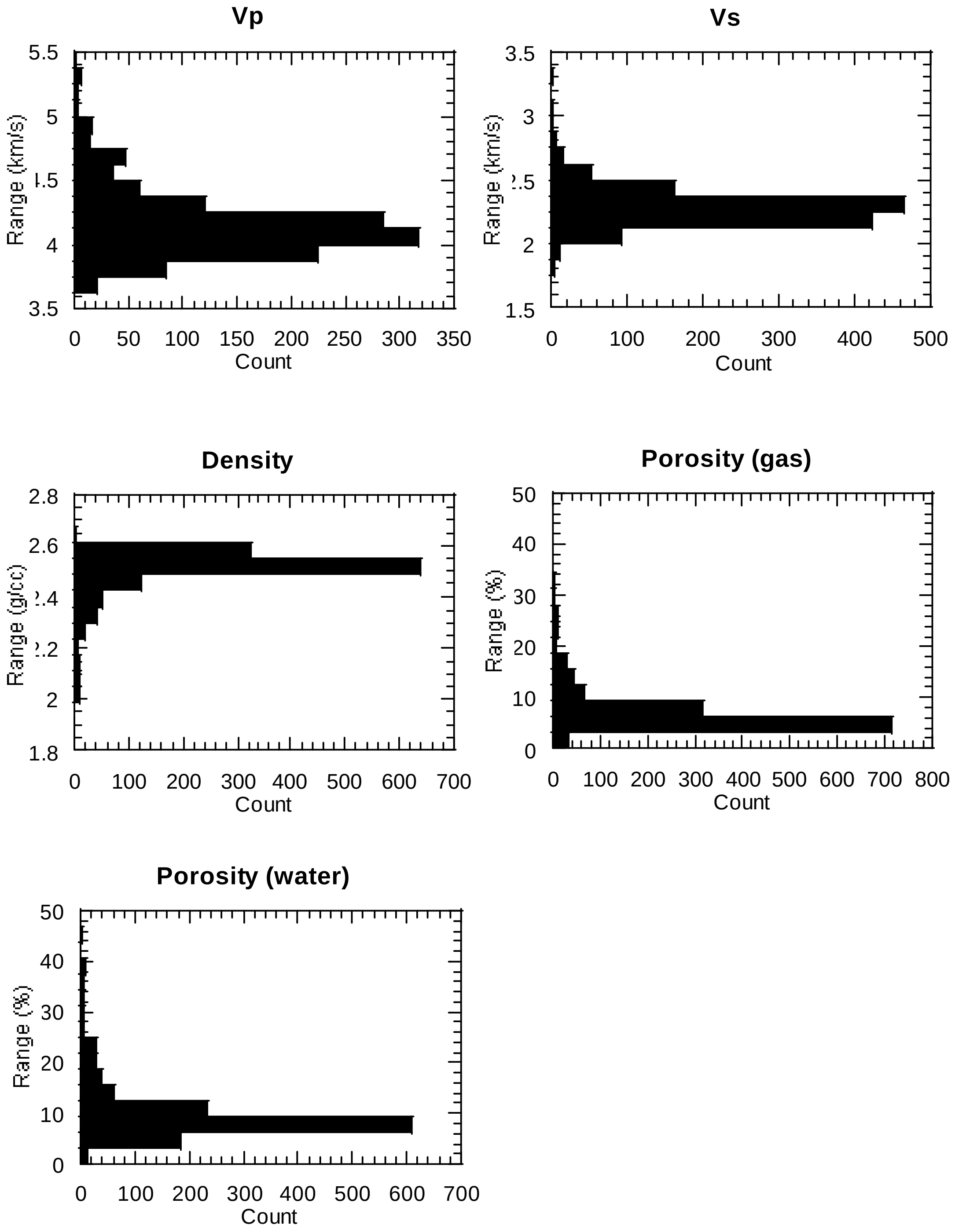

Figure 3.8: Range of the P-, S-wave velocities, density, and porosity assuming the pore fluid is gas or water based on the log measurement of the Niobrara Formation along the Red Mountain well.

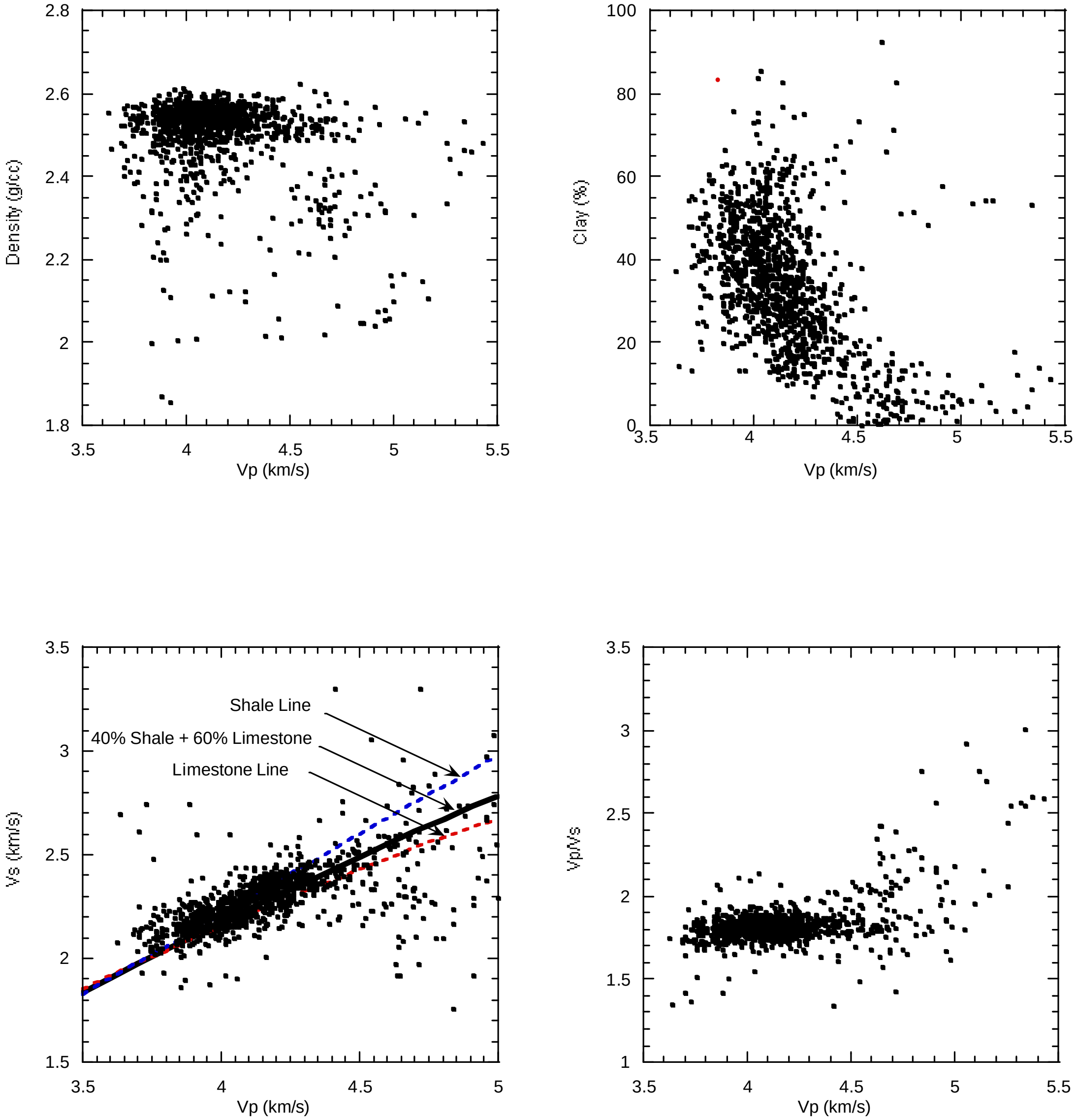

Figure 3.9: Crossplots of the P-wave velocity versus density, clay content, S-wave velocity, and Vp-Vs ratio for the Niobrara Formation. The data are based on the log measurements at the Red Mountain well.

Figure 3.10 shows the velocity, density, and porosity statistics for the first Frontier Sand. For the porosity calculation, I assumed a matrix density r_{matrix} of 2.65 g/cc as that of the quartz, and a shale density r_{sh} of 2.60 g/cc corresponding to the bulk density at a 100% clay content point within the first Frontier Sand. The pore fluid is taken to be the fluid mixture with a gas/oil ratio of 33,375 scf/bbl as described in the previous section. The porosity is calculated using Equation 3.3. The means and standard deviations are summarized as follows:

	Mean	Standard Deviation
Vp	4.683 km/sec	0.146 km/sec
Vs	2.714 km/sec	0.166 km/sec
Density	2.56 g/cc	0.04 g/cc
Porosity (gas+oil)	3.05%	1.89%

The first Frontier Sand appears to have an extremely low porosity. If the matrix is not pure quartz, but mixed with heavy minerals, the mean porosity can be somewhat higher than the calculated 3.05%. Yet it is still a very tight formation, and fracturing is a necessary factor for economical production.

The cross-plots of P-wave velocity versus density, clay content, S-wave velocity, and Vp-Vs ratio of the first Frontier Sand are shown in Figure 3.11. The P-wave velocity increases as the clay content drops, but shows no apparent relationship with the density. The Vp Vs cross-plot shows a discrepancy between the log-based Vp-Vs relationship and the Greensberg-Castagna prediction. This could be due to the fracturing because the S-wave is more sensitive to fractures than the P-wave, and has a lower velocity than the empirical prediction. The Vp-Vs ratio is about 1.7 for the first Frontier Sand.

This analysis provides a baseline for the seismic fracture analysis. The log data will be used to generate a synthetic seismogram that ties with the field seismic data, and to model the AVO behaviors at the formation boundaries.

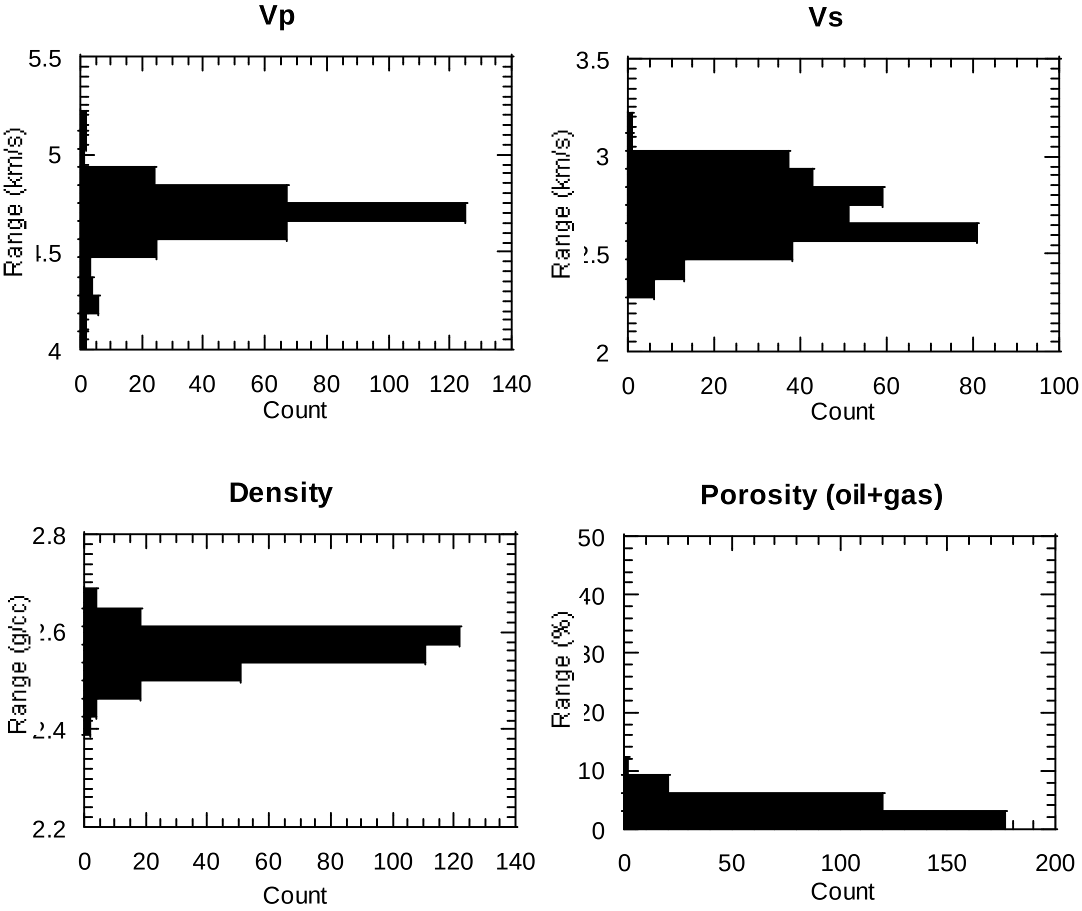

Figure 3.10: Range of the P-, S-wave velocities, density, and porosity assuming the pore fluid is a gas-oil mixture with gas-oil ratio 33,375 scf/bbl based on the log measurement of the first Frontier Sand along the Red Mountain well.

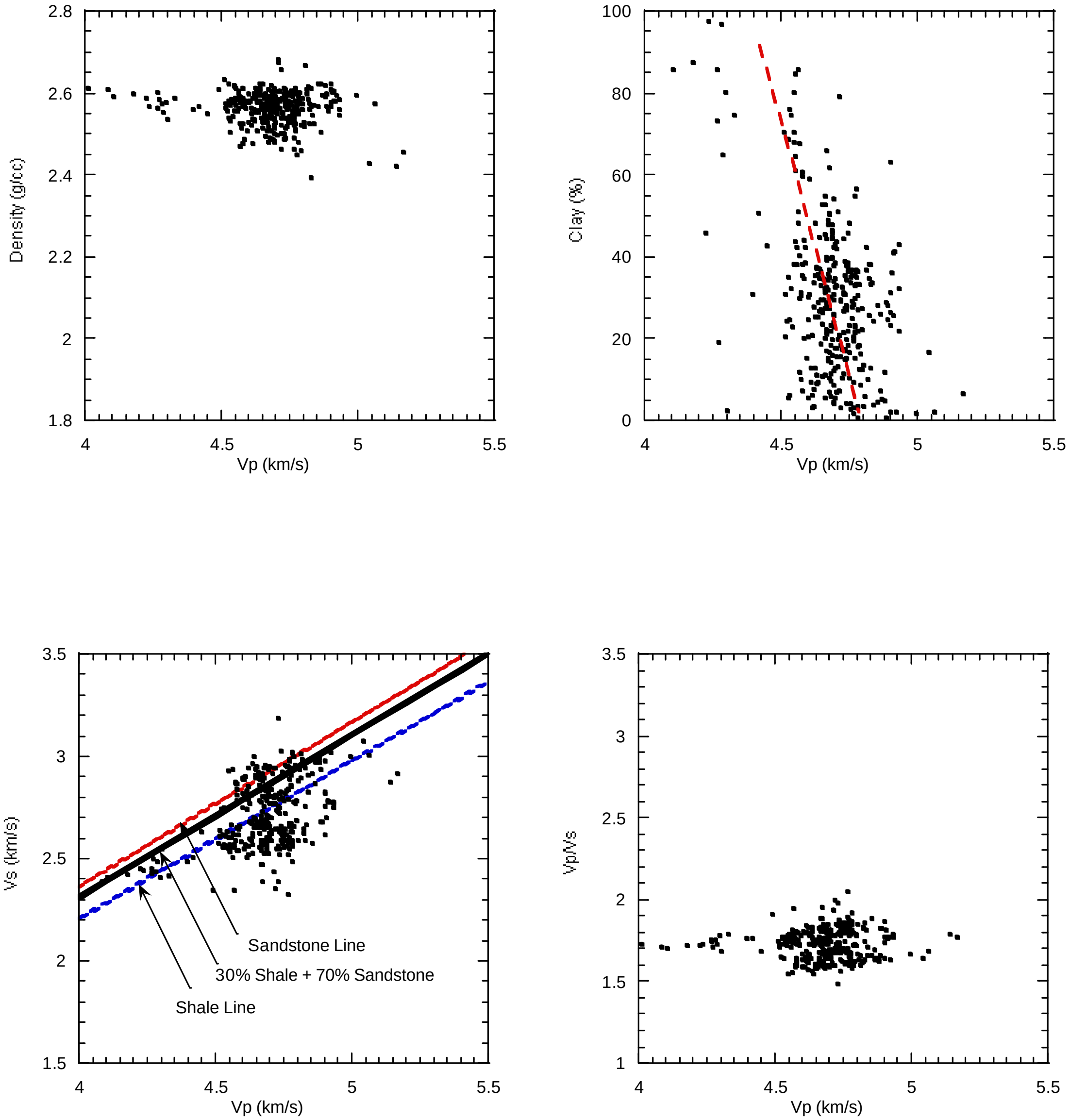

Figure 3.11: Crossplots of the P-wave velocity versus density, clay content, S-wave velocity, and Vp-Vs ratio for the first Frontier Sand. The data are based on the log measurements at the Red Mountain well.

3.6 Evidence of Overpressure

The generation, partial expulsion, and subsequent cracking of liquid hydrocarbons in the Cretaceous sandstones and shales caused regional overpressure compartments in the Powder River Basin (Surdam, et al., 1994). The elevated fluid pressure can make the rocks more brittle and susceptible to fracturing. Therefore, finding the evidence of overpressure helps to locate the fracture-prone regions.

During a normal compaction process, fluids in shale will be gradually squeezed out as the burial gets deeper and deeper. This will correspond to a gradual increase in the shale density, and a gradual decrease in shale conductivity. However, if the fluids were trapped and could not get out during compaction, overpressure will occur (Rider, 1991). The elevated fluid pressure will preserve more porosity, and break the normal compaction trend of both the density logs and the conductivity logs. A lower density and a higher conductivity than normal could mean an overpressure zone. Figure 3.12 shows the conductivity log and the density log at the Red Mountain well. Both curves break away from the normal compaction trend below 10500 feet depth. This could indicate that the pore-fluid pressure of the Niobrara and Frontier formations is higher than normal, and hence the rocks are more susceptible to fracturing. This again substantiates the direct observations of fractures at the Niobrara and Frontier levels.

3.7 Indirect Evidences of Fractures

Schafer (1980) proposed to use the comparison of density-log porosity with the sonic-log porosity to identify fractured zones. When the sonic P-wave passes the fractured rock, Fermat's principle implies that it chooses the fastest way from the emitter to the receiver, and is not sensitive to the presence of fractures. In other words, the P-wave mainly samples the matrix. The density log measures the bulk density that contains both the intergranualar porosity and the fracture-induced

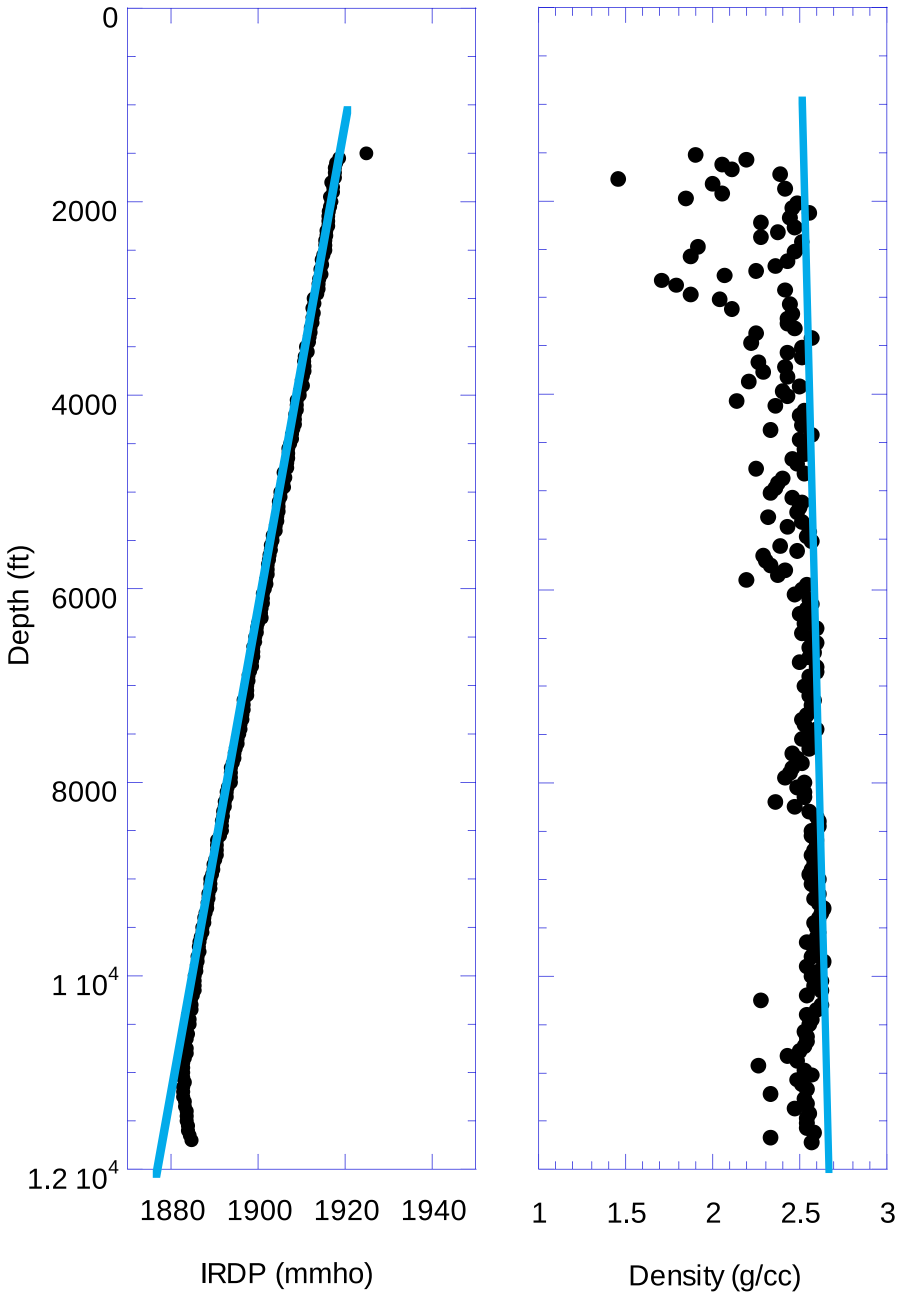

Figure 3.12: The conductivity log and the density log along the Red Mountain well. The normal compaction trends are shown by the gray lines. Below the depth of 10500 ft, the conductivity is higher than the trend, and the density is lower than the trend. It could indicate an overpressure zone.

porosity, and should predict a lower porosity than the sonic-log porosity. On the cross-plot of sonic wave traveltime and density, the same P-wave traveltime corresponds to a lower density in a fractured zone than that in an unfractured zone.

Figure 3.13 shows the cross-plot of the sonic wave traveltime and the bulk density of the Niobrara Formation based on the log data from the Red Mountain, the State #1-36, and the Wallis wells. When the P-wave traveltime is below 70 μs/ft, most density values are above 2.5 g/cc, indicating a dense rock. However, there are points that have much lower density but high P-wave velocity. Most of these points are from logs along the Red Mountain and the State #1-36 wells. It could be due to fractures. Based on this graph, there are probably more fractures at the Red Mountain and State #1-36 well locations than at the Wallis well location.

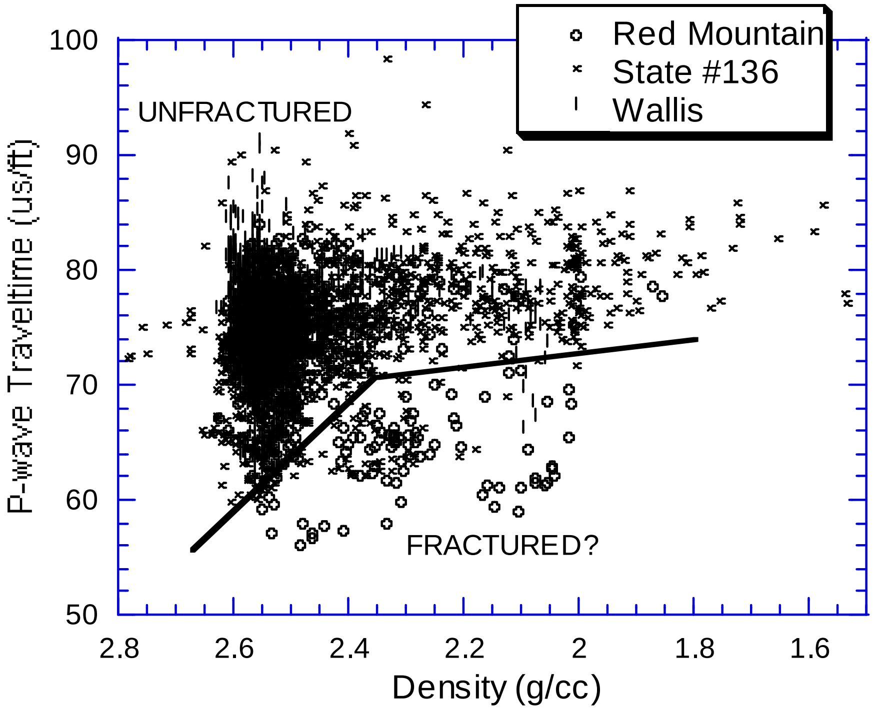

Figure 3.13: Cross-plot of P-wave traveltime versus density of the Niobrara Formations based on logs from the Red Mountain, the State #1-36, and the Wallis wells. The points with high velocity but low density could correspond to fractured intervals.

This indirect fracture indicator should not be used alone without other confirmation of fracture occurrence because the cross-plot may be showing lithological differences rather than the presence of fractures. One example showing how incorrect inferences can be made can be found in Rider's book (1991).

3.8 FMS Logs and Fracture Number Count

The Formation MicroScanner (FMS) tools obtain oriented, high-resolution imagery of electrical conductivity around the borehole wall with four arrays of button electrodes (Schlumberger, 1989). The FMS tool has 1cm vertical resolutions and can detect fractures 1cm apart. Two runs of FMS logs were conducted along the horizontal borehole of the Red Mountain well: from 10850 feet to 11750 feet, and from 11660 feet to 12970 feet. Figure 3.14 shows a segment of the FMS display. The conductivity images measured by the four pads are displayed side by side. Two vertical fractures with large apertures cutting through the borehole can be identified easily at depth of approximately 12637 ft, and 12639 ft.

Arco scientists processed the two runs of FMS logs with a similar analysis method using Schlumberger's FLIP/FRACVIEW software (Sovich, 1996, May et. al, 1996). I counted the fracture number within various aperture ranges and fracture strike ranges based on their results, and show fracture number distributions in Figure 3.15. Several observations are summarized below:

(1) 93% of the fractures in the shallower depth range (10865 feet to 11750 feet) and 75% of the fractures in the deeper depth range (11750 feet to 12970 feet) are trending along the N70^{o}E $\pm$ 10^o direction. This is the only one prevailing strike.

(2) The average horizontal spacing of large-aperture fractures (aperture > 0.2mm) is about 3.2 feet in the shallower section, and 12.1 feet in the deeper section.

(3) Arco's FMS analysis shows more small-aperture fractures in the deeper depth range than in the shallower depth range. I believe that this is a result of the different processing accuracy for the two runs of FMS data. By comparing the

aperture distribution near the overlapping region of the shallower and deeper depth ranges, I observed a sudden increase in the number of the small-aperture fractures from the shallower to the deeper depth. Generally, the number of fractures at a given aperture range will not change drastically unless it is across the formation boundary. Since the overlapping region is not a formation boundary, I believe that this change is mainly due to the different processing accuracy for the two runs rather than the actual change.

(4) Except at very small apertures where the fractures are under-sampled, the frequency of fractures with a given aperture decreases as the aperture increases. This is consistent with Barton and Zoback's observation (1992) in the Cajon Pass well. Whether the aperture distribution obeys the power law, as suggested by Barton and Zoback (1992), is worth further analysis.

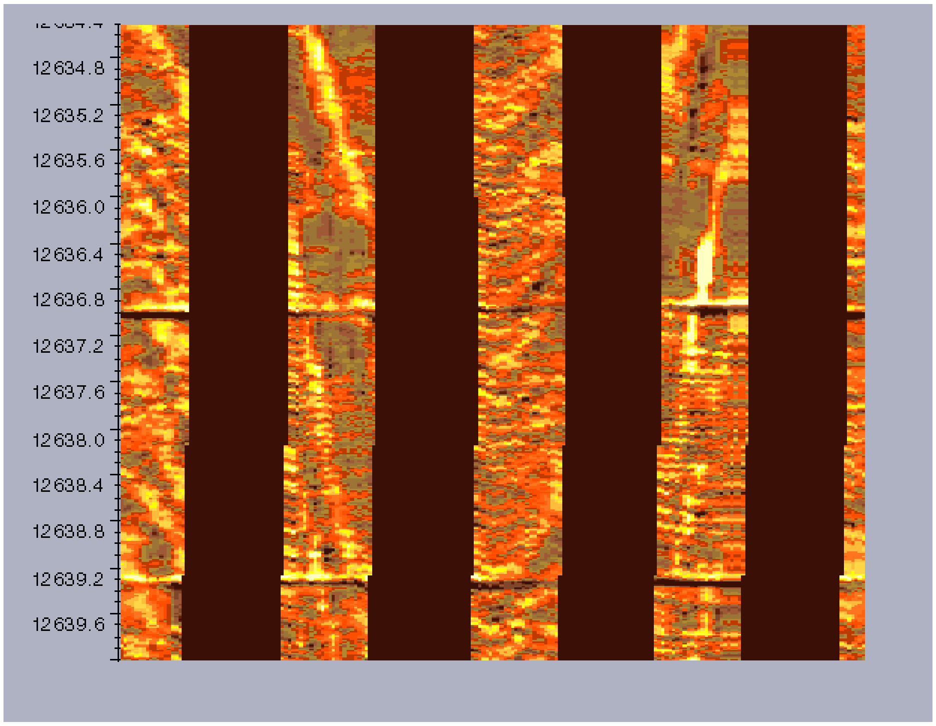

Figure 3.14: FMS display showing open fractures at the Frontier Formation level. Note that the FMS logs ran along the highly deviated hole. The near-vertical fractures appear at low dip angle. The bedding appears at high dip angles. The depth is the measured depth in feet along the borehole rather than the true vertical depth.

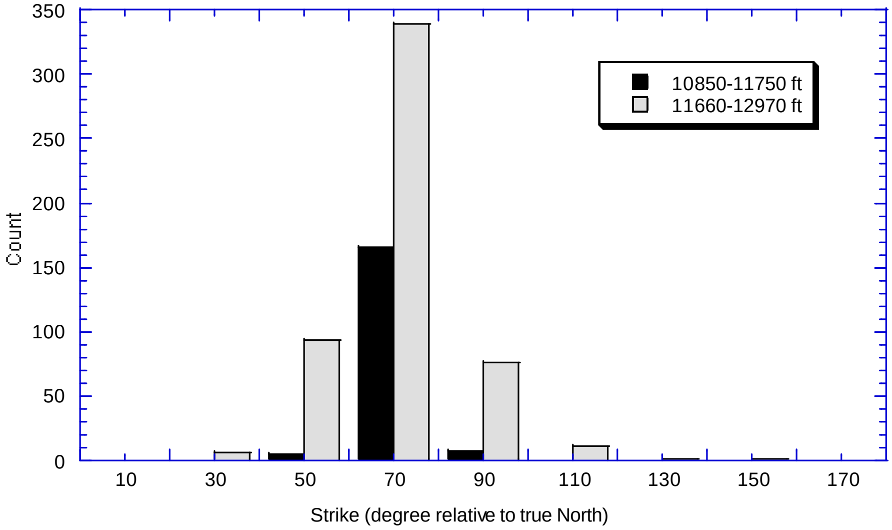

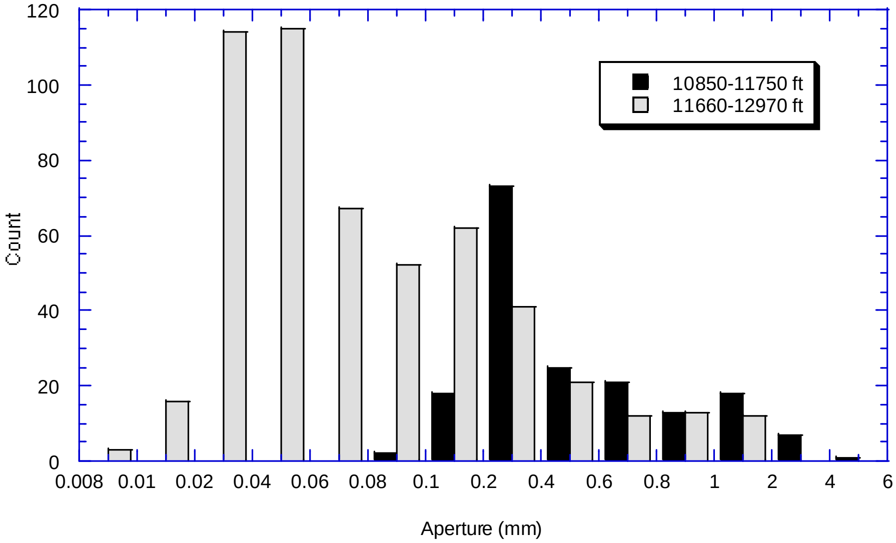

Figure 3.15: The distributions of fracture strike and aperture based on the FMS logs. The original FMS data of the two runs (10850-11750ft & 11660-12970ft) were subjected to a similar analysis by Arco's scientists. These number counts are based on Arco's plots. Note that only fractures between 11750 to 12970 feet were counted for the second run from 11660 to 12970 feet due to the data availability on Arco's plots.

3.9 Anisotropy in Dipole Sonic Logs

Dipole shear sonic logs record the waveforms of the shear waves emitted from two perpendicular sources, and received by two perpendicular receivers. After Alford (1986) rotation to the principle directions, i.e. parallel and perpendicular to the fracture orientation, we get a fast and a slow shear waves polarized in the principle directions. The traveltime lag between the fast and slow shear wave can be caused by the fracture-induced anisotropy. The shear wave birefringence parameter is calculated using:

$$g = \frac{\Delta m}{m} \cong \frac{\Delta V_S}{V_S} \cong \frac{\Delta T}{T} \qquad (3.4)$$

where g is the shear wave birefringence parameter or the Thomsen shear-wave parameter for weak anisotropy (1986), Δ represents the difference between the fast and slow shear waves, V_S is the sonic shear velocity, T is the transit time, m is the shear modulus of the rock. Derivation of this equation can be found in Chapter 2.

The shear wave data were given to us after the Alford rotation done by ARCO, Schlumberger, and Nolte and Cheng (1996) at M.I.T. Figure 3.16 shows the 10-feet average values of the fast shear wave (S1) polarization azimuth, transit time, birefringence parameter, K-Th shale index, and P-wave sonic velocity. Unlike the tightly clustered fracture orientation observed the FMS data, the S1 polarization wanders around between N40^{o}E and N170^{o}E, with a mean of N91^{o}E and a standard deviation of 24^{o}. The shear wave birefringence parameter has a mean of 5.6%, and a standard deviation of 6.9%.

Three main zones of shear wave splitting A, B, and C are marked on Figure 3.16. Zones A and B are within the Niobrara Formation. Zone C corresponds to the first Frontier Sand. A closer look at these three zones shows that the S1 azimuth stays close to N80^{o}E within these zones. This indicates that outside these zones where the

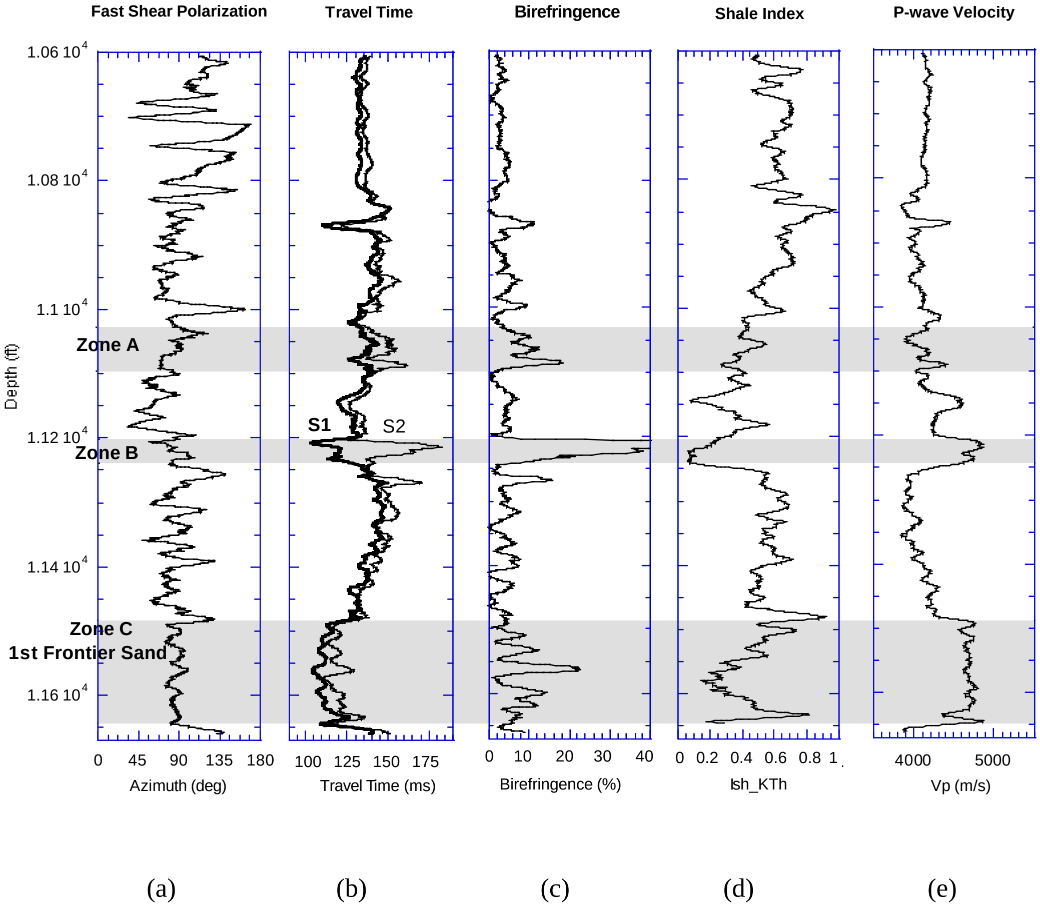

Figure 3.16: Dipole sonic log (a) fast shear wave azimuth; (b) traveltime of the fast and slow shear waves; and (c) shear wave birefringence. Those plotted next to the dipole logs are (d) K-Th shale index and (e) P-wave sonic velocity. Three main zones of shear wave splitting are marked by Zone A, B, and C. Zone C corresponds to the first Frontier Sand.

birefringence is small, the uncertainty in the Alford rotation angle is probably large, and causes the wandering of the S1 polarization direction. Within the first Frontier Sand, the shear wave birefringence has a mean value of 7.6% and a standard deviation of 4.8%.

Notice that both Zone B and Zone C have low clay content and high P-wave velocity. Outcrop and core observations at the study site (May et al., 1996) show that "all fractures, regardless of orientation, are better developed in thinner-bedded, well-cemented lithologies and commonly terminate at thin shale or bentonite beds." The dipole sonic log results are consistent with the outcrop observations. Furthermore, it demonstrates that the dipole sonic logs and seismic surveys can be good fracture detection tools.

3.10 Conclusions

In this chapter, I analyzed the log data and gathered information about clay content, pore-fluid properties, formation velocities and density, and evidence of overpressure and fractures at the Niobrara and Frontier levels. The clay content analysis confirmed the prior geological information of the formations. The elastic properties of rocks and pore fluids are essential for the seismic analysis in the next chapter.

Natural fractures have been directly observed and measured on the FMS logs. The prevailing strike of the fractures is N70^{o}E at the Niobrara and Frontier levels. The apparent aperture of fractures ranges from 0.008 mm to above 4mm. The fracture frequency at a given aperture decreases as the aperture increases. The dipole sonic logs show a fast shear wave polarization around N80^{o}E in the zones where shear wave splitting is comparatively large. This roughly agrees with the FMS observations. The correlation between the main shear wave splitting zones and high P-wave velocity, low clay content agrees with the outcrop and core observations (May et al., 1996) that the fractures at the study site are better developed in tight layers and tend to terminate at shale or bentonite beds.

Log measurements of fractures have the advantage of high depth resolution, and the disadvantage of low area coverage. In order to get the subsurface fracture information in the Fort Fetterman field, 2D multi-component and 3D P-wave seismic surveys were conducted. In the next chapter, I will analyze the anisotropy in the seismic data, and map the fracture distribution and properties over the survey area.

The log data will be used in conjunction with the seismic data to give a realistic fracture property mapping.

3.11 References

Alford, R.M., 1986, Shear data in the presence of azimuthal anisotropy, SEG 56th Annual Meeting Technical Program

Barlow, J. A., and Haun, J. D., 1966, Regional stratigraphy of Frontier Formation and relation to Salt Creek field, Wyoming: AAPG Bulleting, **50**, 2185-2196

Barton, C.A., and Zoback, M.D., 1992, Self-similar distribution and properties of macroscopic fractures at depth in crystalline rock in the Cajon Pass scientific drill hole, Journal of Geophys. Res., **97**, No B4, 5181-5200

Bassiouni, Z., 1994, Theory, measurement, and interpretation of well logs, First Printing, Society of Petroleum Society

Greenberg, M.L. and Castagna, J.P., 1992, Shear-wave velocity estimation in porous rocks: theoretical formulation, preliminary verification and applications, Geophysical Prospecting, **40**, 195-209.

Hando, R. E., 1976, Powell-Ross Field Converse County, Wyoming, Twenty-eighth American Field Conference, Wyoming Geological assoc Guidebook

May, J., Mount, V., Krantz, B., parks, S., Gale, M., 1996, Structural framework of southern Powder River Basin: A geological context for deep northeast trending basement fractures, Gas Research Institute research report

Nolte, B., and Cheng, C.H., 1996, Estimation of non-orthogonal shear-wave polarizations and shear-wave velocities from four-component dipole logs, MIT: borehole Acoustics & Logging; Reservoir Delineation Consortia Annal Report, p2-1-2-20

Rider, M. H., 1991, The Geological Interpretation of Well Logs, Revised Edition

Schafer, J.N., 1980, A practical method of well evaluation and acreage development for the natural fractured Austin chalk formation, Log Analyst,**XXI**(1), 10-23

Schlumberger, 1989, Log interpretation principles/applications

Sovich, J., 1996, ARCO Exploration and Production Technology Internal Correspondence

Surdam, R.C., Jiao, Z.S., and Martinsen, R.S., 1994, The regional pressure regime in Cretaceous sandstones and shales in the Powder River Basin, P. Ortoleva and Z Al-Shaieb, eds., Pressure Compartments and Seals, Am. Assoc. Petro. Geol. Memoir, **61**, 213-233

Thomsen, L., 1986, Weak elastic anisotropy, Geophysics, **51**, 1954-1966

CHAPTER 4

INTEGRATED SEISMIC INTERPRETATION OF FRACTURE NETWORKS

4.1 Introduction

In this chapter, using the seismic datasets from the Fort Fetterman site, I explore and test the feasibility and reliability of using P-wave anisotropy, in conjunction with S-wave data and other available information, to characterize subsurface fracture networks.

Shear-wave splitting techniques have been used successfully in detecting fractures in many field examples. However, shear waves are not sensitive to the fluids in pores and fractures. Seismic shear-wave data are rarely available in 3D. P-wave data are cheaper to acquire, have higher signal-to-noise ratio, and are more readily available in 3D than are shear-wave data. However, the use of P-wave data in fracture detection and characterization is not fully exploited.

At the Fort Fetterman site, various seismic surveys were conducted for the fracture study. The available seismic data include the multi-component shear-wave VSP data at the Red Mountain well location, two 2D lines of multi-component seismic data, and a 3D cube of P-wave data. The 2D and 3D seismic survey map is shown in Figure 3.1 in Chapter 3. The advantages of having different types of surveys are that each survey samples different areas of the earth, and has different resolutions. Moreover, the P- and S-waves sample different physical properties. P-waves are sensitive to a change in fracture-filling fluids, but S-waves are not. VSP data have direct time-to-depth correspondence because the depths of the downhole receiver are known. 2D four-component shear-wave surveys allow us to map the fracture distribution along the 2D lines. The anisotropy in 3D P-wave velocity and amplitude makes it possible for us to identify the fracture-filling fluids, as well as to map the fracture distribution over the larger 3D survey area. I analyze and interpret the anisotropy in the VSP and the 2D S-wave velocities, and the 3D P-wave velocity and amplitude, in Sections 4.2 to 4.5. Section 4.6 summarizes the integrated fracture interpretation of this field, lessons learned, and the general applicability of these methods.

4.2 VSP shear-wave birefringence and 1D fracture-density distribution

Vertical seismic profiling (VSP) data consist of records from surface sources to downhole geophones. They provide direct seismic ties of time to depth on a relatively fine scale (Hardage, 1984). Multi-component shear-wave VSP data can capture the fracture-induced anisotropy in the Earth at fine depth resolution. It has been used successfully in fracture detection and orientation prediction (Queen and Rizer, 1990; Winterstein and Meadows, 1991a, b).

At the Red Mountain well location, VSP data were collected with P- and S-wave sources at four different offsets (Figure 4.1). For my fracture analysis, I used the four-component shear-wave data with sources at 277-ft offset. This offset is much smaller than the depth range from 1499.9 feet to 11500.5 feet, so the data can be treated as approximately zero-offset VSP data. At the source location, there are two perpendicular shear sources, S2 and S3. The S3 baseplate first motion is N36^{o}E relative to true north. This angle is the sum of the measured angle by magnetic compass and the magnetic declination. The magnetic declination is +11^{o} in Converse

County, Wyoming. The S2 baseplate motion is perpendicular to that of S3. As shown in Figure 4.2, the sonde interval is approximately 500 ft between depths of 1499.9 ft and 7720 ft. Below 7720-ft depth, the average sonde interval is 67.5 ft.

The raw VSP data were recorded by a tri-axial geophone whose polarization changes at each depth. Before conducting the Alford rotation, we must first rotate the data such that the polarizations of the sources and receivers are in the same directions. In the deep borehole, the orientation of the geophone can be determined by the far-offset P-wave data. How to determine the downhole tri-axial geophone from the P-wave data, and how to rotate the data to a desired coordinate system are beyond the scope of this thesis. Details can be found in Greenhalgh and Mason (1995), and Knowlton and Spensor (1996). This work was performed by ARCO. They rotated the shear-wave data into the XY coordinates, where the X-direction is along N126^{o}E, and the Y-direction along N36^{o}E, parallel to the S2 and S3 sources directions, respectively.

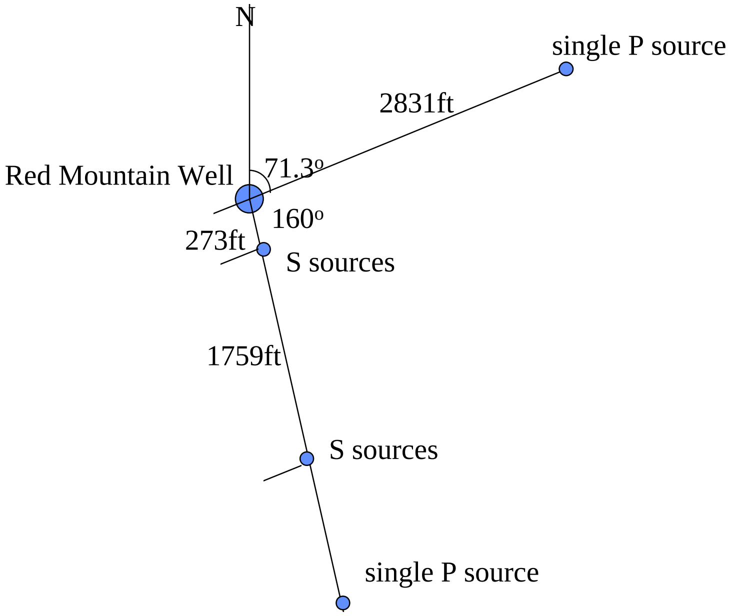

Figure 4.1: VSP survey map. The 273-ft near-offset VSP shear-wave data are used in the shear-wave splitting analysis.

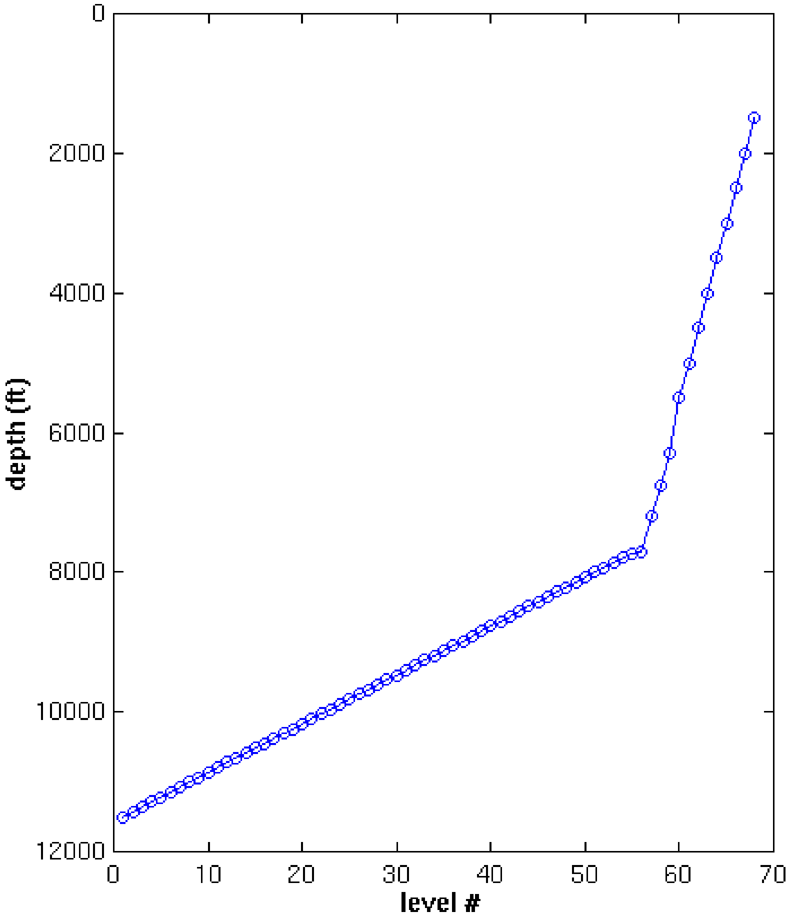

Figure 4.2: The 64 depth levels of the downhold geophone for the VSP survey. The sonde interval is approximately 500 ft between 1499.9-ft and 7720-ft depth. Below this depth, the sonde interval is much closer with an average of 67.5 ft.

Figure 4.3 shows the four S-wave components named XX, XY, YX, YY. The first letter of each component name indicates the source direction, and the second letter indicates the receiver direction after geophone orientation has been applied. If the medium is isotropic, the shear-wave generated by the X source should be received only by the X receiver, and the Y source by the Y receiver. Figure 4.3 shows strong energy in the cross traces XY and YX. This energy indicates the existence of subsurface anisotropy that causes shear-wave splitting during propagation.

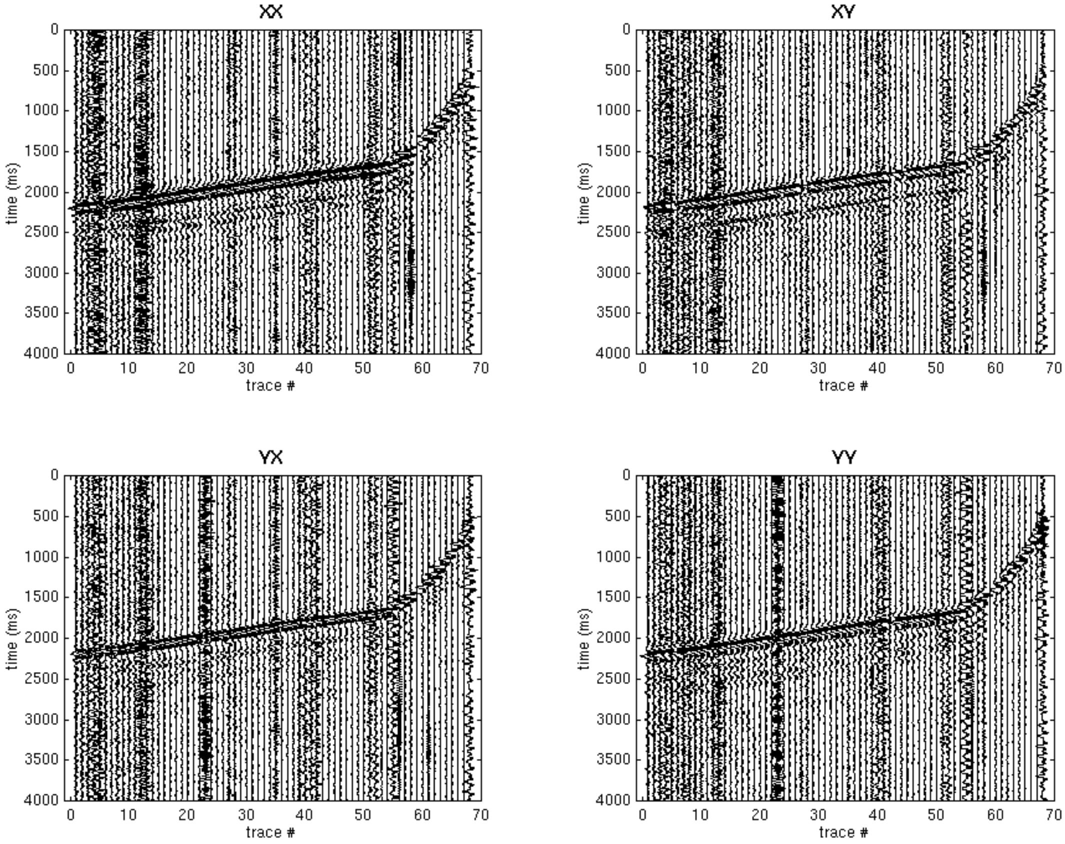

Figure 4.3: The four VSP S-wave components XX, XY, YX, and YY before the Alford rotation. X is in the N126°E direction, and Y is in N36°E direction. The strong energy in the mismatched traces XY and YX indicates subsurface anisotropy.

To determine the natural-anisotropy symmetry directions of the subsurface rocks, which often indicate the fracture orientation, I applied the Alford rotation (1986) to the VSP shear-wave data. The procedure will rotate the source-receiver acquisition direction from the XY directions to a new set of directions X'Y'. A single rotation angle is applied to all VSP traces. The rotation angles that I tried range from 10^{o} to 90^{o}, with a step of 10^{o}. Figures 4.4 (a) to (d) shows the S-wave components after Alford rotations of 20^{o}, 30^{o}, 40^{o}, and 60^{o}, respectively. When the target X'Y' coordinates are parallel to the symmetry planes of the fractured medium, the cross-talk energy in X'Y' and Y'X' sections will be minimized. We can see that the rotation of 30° gives the smallest cross-talk energy in X'Y' and Y'X' sections. The fast direction X' (N96°E) is, therefore, the predicted fracture orientation. Figure 4.5 compares the S-wave traces received at depth level #61 after rotations of angles ranging from 20° to 40°, with a step of 1°. There is no significant change over any range of 10° or less. Therefore, I consider the uncertainty of the estimated fracture direction to be about +/- 10°. May et al. (1996) point out that a set of N110°E+/-15° fractures was observed in the Tertiary strata, and locally in the Cretaceous strata; a set of N70°E+/-10° fractures was observed in the Cretaceous, but not in the Tertiary strata. The trend of N96°E fast-VSP-shear-wave direction is based on the rotation of the data at all depth levels, and hence is the average fracture direction over both the Tertiary and Cretaceous intervals. If we assume that the N70°E and the N110°E fractures generate equal amounts of anisotropy, the average anisotropy symmetry-plane direction is along N90°E. The finding of the average fracture direction of N96°E+/- 10° at the Red Mountain well location is consistent with the geological observations.

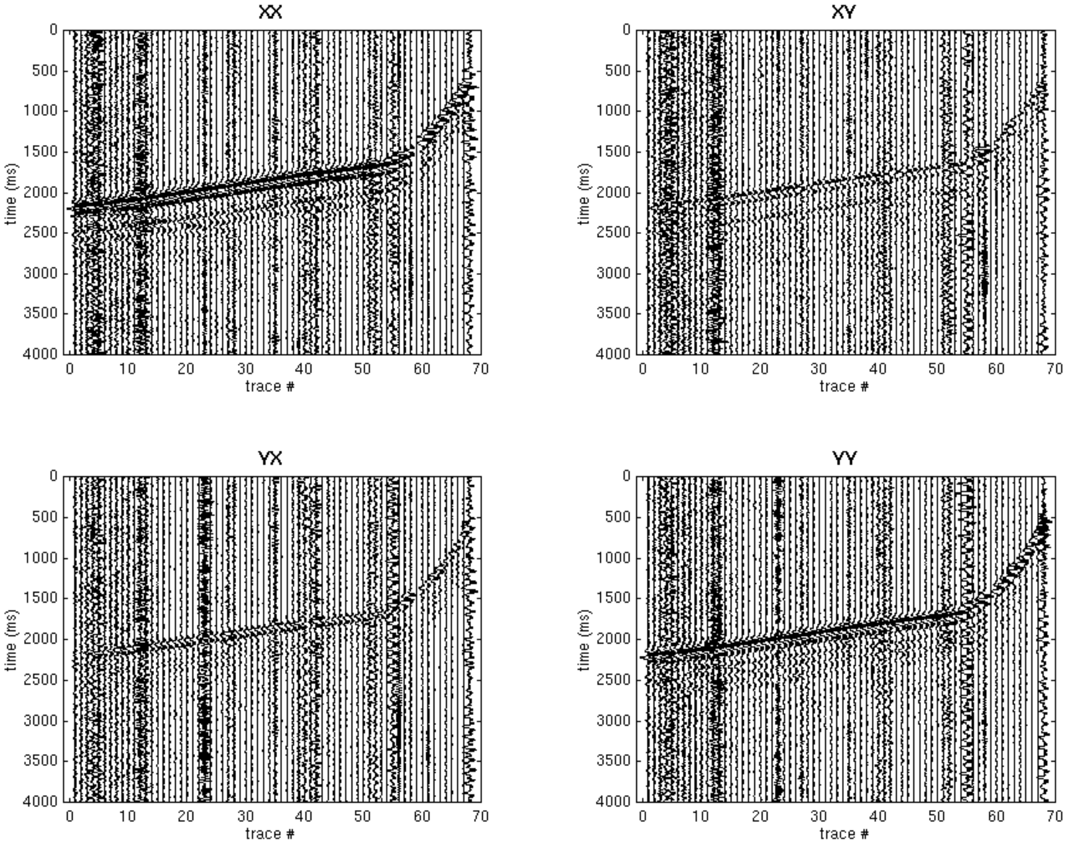

Figure 4.4: (a) The four VSP S-wave components X'X', X'Y', Y'X', Y'Y' after the Alford rotation of 20^o.

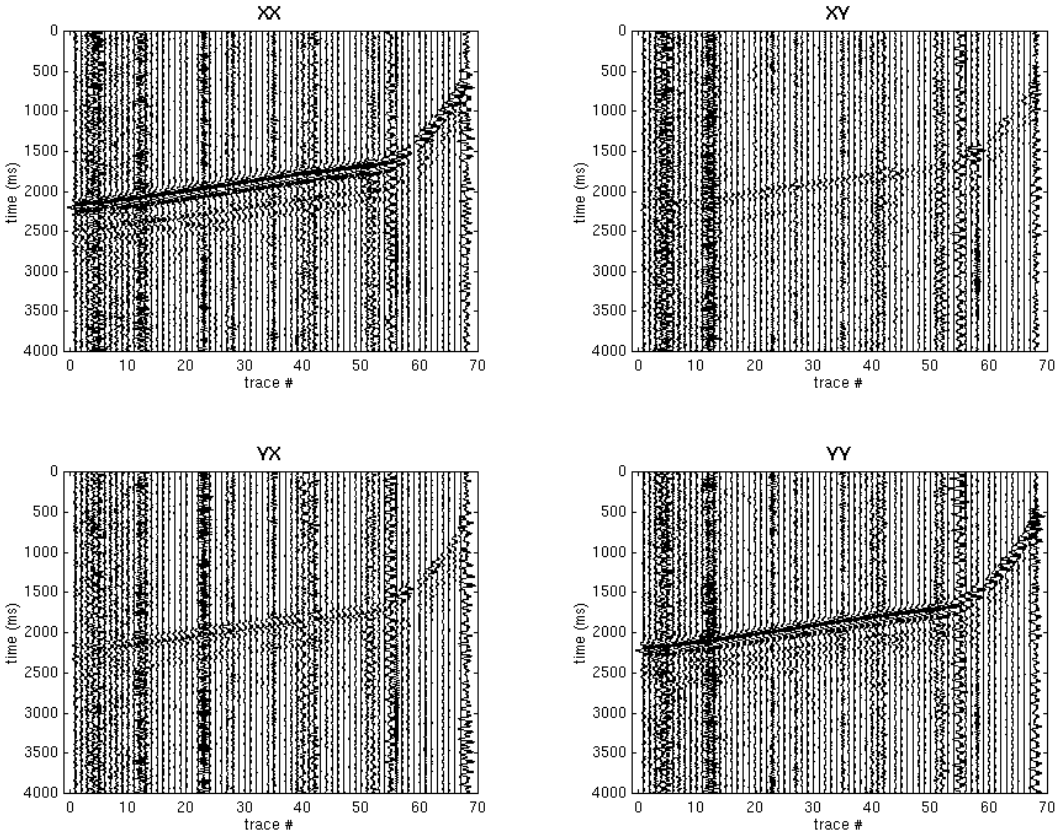

Figure 4.4: (b) The four VSP S-wave components X'X', X'Y', Y'X', Y'Y' after the Alford rotation of 30^o. The optimum rotation angle 30^o corresponds to the minimum energy in X'Y' and Y'X' components.

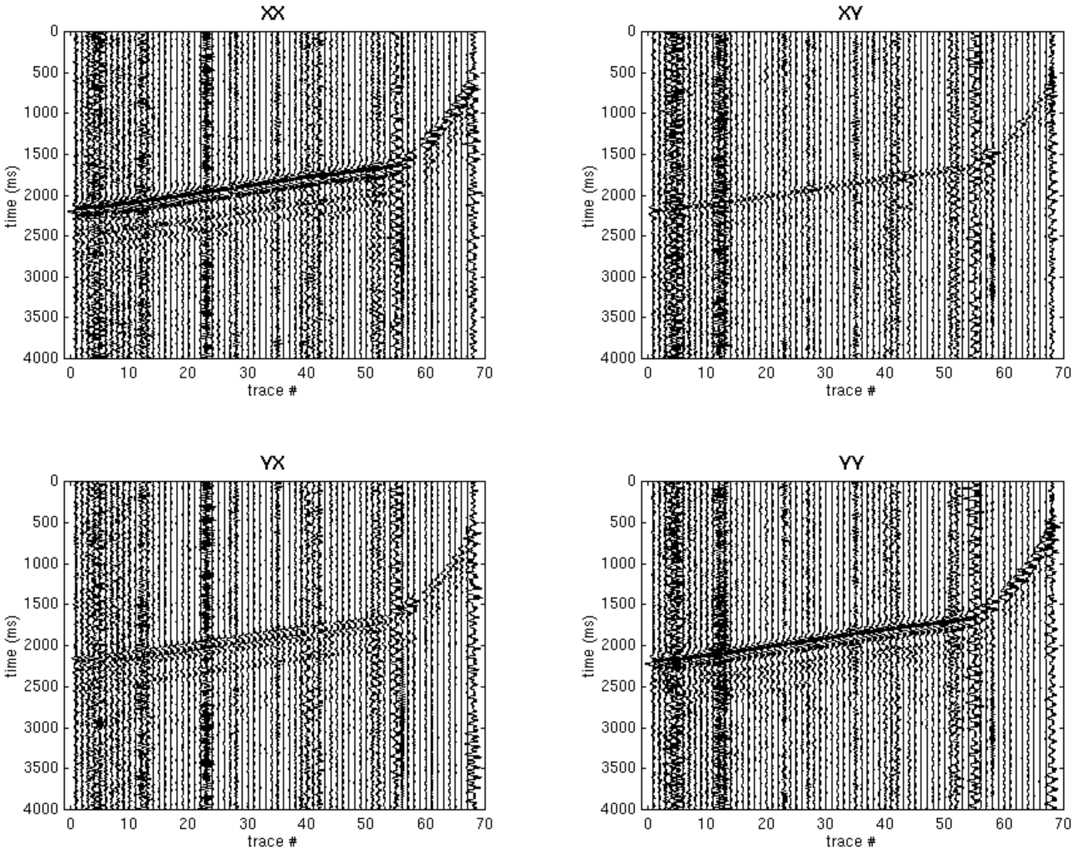

Figure 4.4: (c) The four VSP S-wave components X'X', X'Y', Y'X,' Y'Y' after the Alford rotation of 40^o.

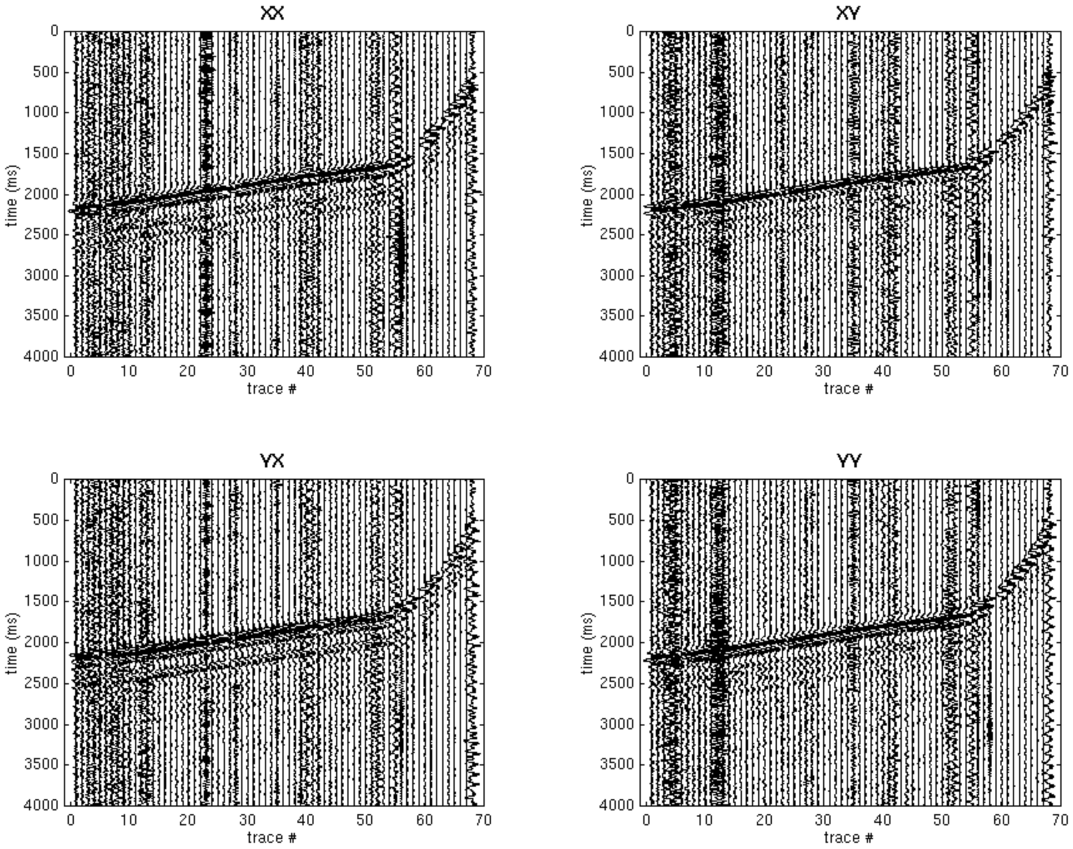

Figure 4.4: (d) The four VSP S-wave components X'X', X'Y', Y'X', Y'Y' after the Alford rotation of 60^o.

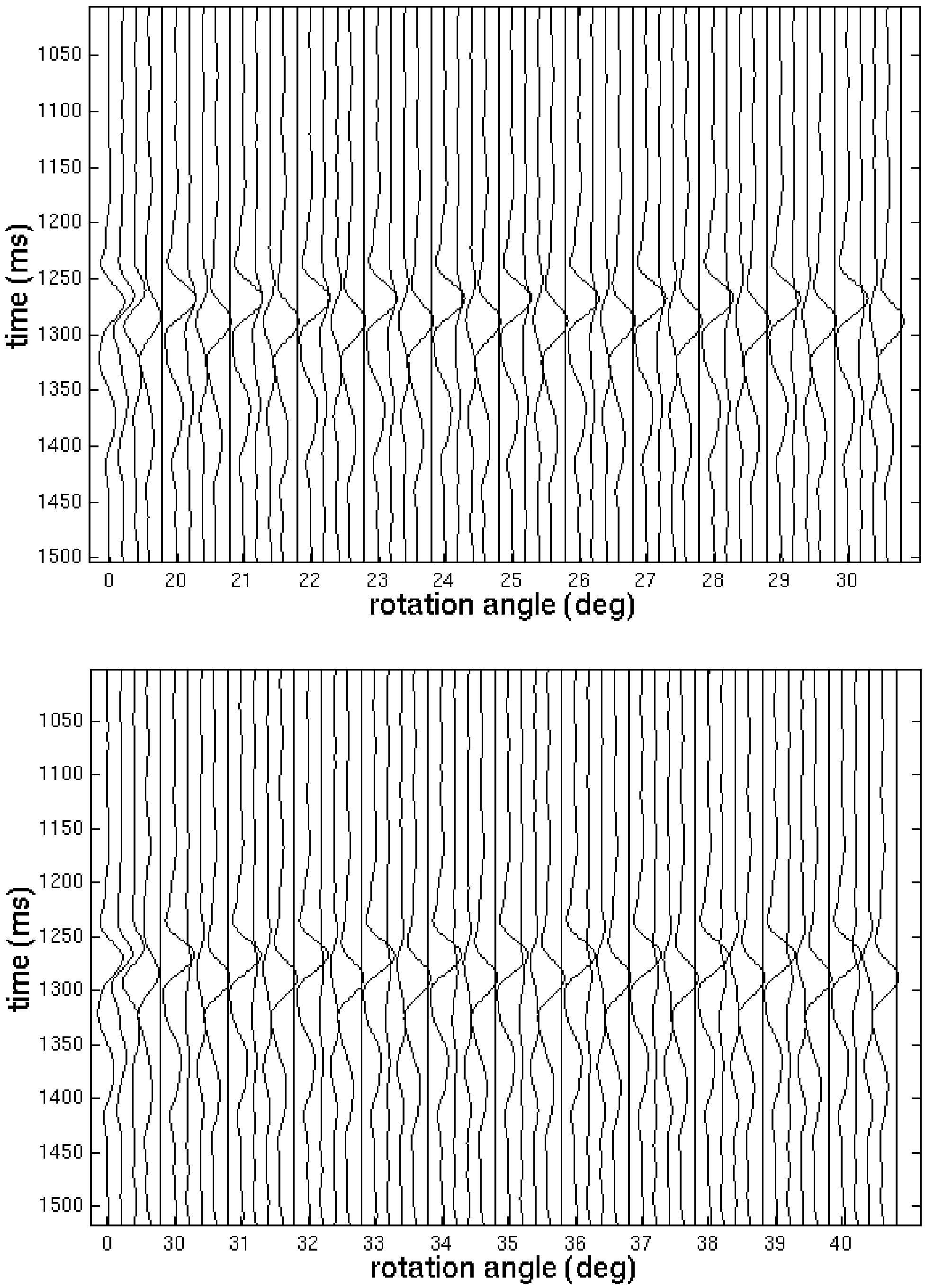

Figure 4.5: The four VSP S-wave components X'X', X'Y', Y'X', Y'Y' received at level #61 (depth 5000.3 ft) after a rotation of 20^o to 40^o angle, with a step of 1^o. The similarity in the rotation results shows that we cannot have a resolution higher than 10^o. The four leftmost traces are the shear-wave data before the Alford rotation. They are displayed as a reference.

After the optimum rotation of 30°, the traveltime lag ΔT_S between the fast and slow shear-wave components, X'X' and Y'Y', can be estimated at each depth. If we assume an even distribution of crack density along the whole depth range, the traveltime lag should increase linearly with depth. The picks of the traveltime lag and a least-squares fitting line through them are shown in Figure 4.6. The traveltime lag ΔT_S increases by 9 ms from 2000 ft to 11500 ft. The total traveltime T_S through this depth interval is about 1500 ms. The corresponding percentage of shear-wave traveltime anisotropy $\Delta T_S / T_S$ is 0.6%. According to Hudson's theory, $\Delta T_S / T_S$ can be directly related to the crack density e by this equation:

$$e = \frac{9M - 6m}{8M}\frac{\Delta T_S}{T_S} = \left(\frac{15}{24} + \frac{2}{16 - 24s}\right)\frac{\Delta T_S}{T_S} \tag{4.1}$$

where M, m, and s are the P- and S-wave moduli, and Poisson's ratio, of the unfractured rock. The derivation can be found in Section 2.2 of Chapter 2. The depth interval between 1200 ft and 11500 ft is a mixture of shale and sand. Over this interval, the average Poisson's ratio based on the log data at the Red Mountain well is around 0.28. According to Equation (4.1), 0.6% traveltime anisotropy corresponds to a crack density of 0.005. This is the average crack density over a 10300 ft interval. Geological observations (May et al., 1996) show that the fractures tend to concentrate in thin layers, especially low-porosity, high-clay-content layers. If the ratio of the fractured layer thickness to the total interval thickness is 1:10, the crack density in the thin fractured layers will be 0.05. Moreover, because the 10,300 ft interval contains two sets of fractures along N110°E+/-15° and N70°E+/-10°, respectively. The shear-wave anisotropies with symmetry planes along different directions can partially cancel out each other. This effect will make the apparent anisotropy smaller.

The geological observations (May et al., 1996) show that the fracture orientation changes with depth. In order to determine the fracture orientation and intensity in the

Cretaceous reservoir rocks, we must remove the anisotropy effect of the overburden. This is done with layer-stripping techniques (Winterstein and Meadows, 1991a, b). Our data quality, however, does not yield conclusive layer-stripping results. Noise can come from both the seismic measurements and the data processing. For example, an error in the estimation of downhole geophone orientation using P-wave data will result in a corresponding error in the Alford rotation. A higher signal-to-noise ratio, and compass-recorded geophone orientations could improve the quality of fracture analysis using VSP data. The layer-stripping techniques will be discussed in more detail in the next section, when it is applied to the multi-component surface shear-wave data.

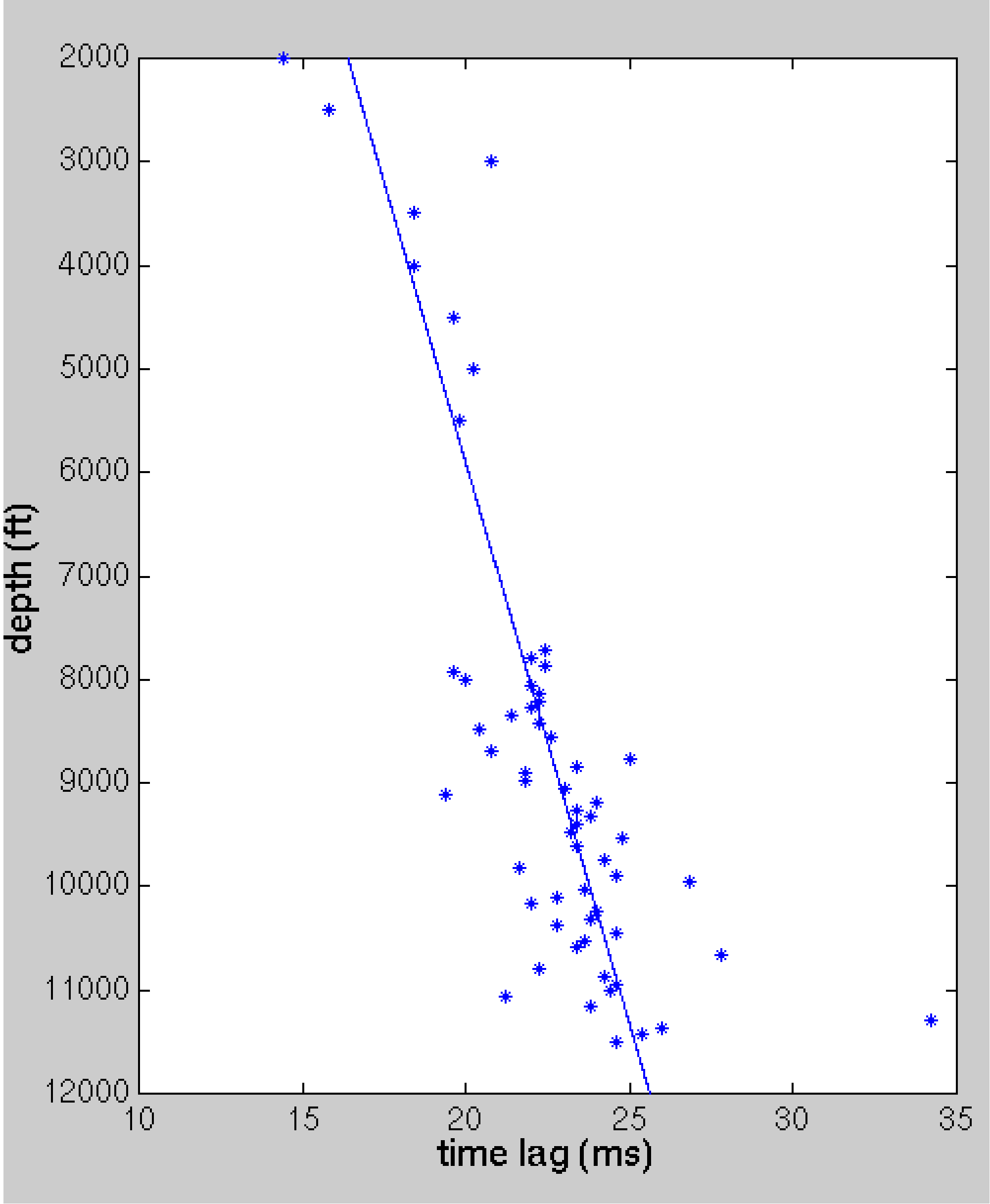

Figure 4.6: The traveltime lag between the fast and the slow VSP events. To calculate the traveltime lag, I cross-correlated the fast and slow shear-wave components X'X' and Y'Y' after a 30-degree rotation was made. The solid line is the least-squares fitting line of the data. The average traveltime lag per 1000 feet is 9 ms.

4.3 Surface shear-wave birefringence and 2D fracture-density mapping

So that the subsurface anisotropy could be detected, multi-component seismic data were collected along Lines GRI-1 and GRI-4 at the Fort Fetterman site. This collection is sponsored by Gas Research Institute and the Department of Energy. The base map is shown in Figure 3.1 in Chapter 3.

The standard seismic processing was done at ARCO. I summarize the procedures below:

1. *Inline Geometry Header Load*
2. *Air Blast Attenuation*
3. *Apply Refraction Statics*
4. *True Amplitude Recovery*
5. *ARCO Fan Filter*
6. *ARCO Noisy Trace Editing*
7. *Normal Moveout Correction*
8. *True Amplitude Recovery (Time-power constant = -1;*
   *spherical spreading 1/(time*vel**2))*
9. *CDP/Ensemble Stack*
10. *F-X Decon (Wiener Levinson filter, 4-40 Hz)*

The results are four-component, post-stack S-wave data in the XY coordinates. X represents the east-west inline direction, and Y the north-south cross-line direction. In order to find the fracture direction and the amount of shear-wave traveltime anisotropy, I conducted the following processes:

11. *the Alford Rotation*
12. *Cross-correlation, to pick traveltime lag*

13. Layer-stripping techniques, to remove the effects of the overburden anisotropy above the reservoir level

14. Fracture-density estimation

These procedures are discussed in more detail below.

Figure 4.7 shows the four components of the shear-wave data along Line GRI-4. The first letter of the four components XX, XY, YX, and YY represents the direction of the source polarization, and the second letter the receiver polarization. As shown in Figure 4.7, the significant energy level in the cross traces XY and YX indicates the presence of subsurface anisotropy. The cross talk will be minimized if the coordinates are rotated to the symmetry-plane directions of the natural anisotropy.

I applied the Alford Rotation at every 5^o increment. The optimum rotation that minimizes the cross-talk components is a $+15^o$ rotation to the X'Y' coordinates, where the X'-axis is along the $N105^oE$ direction. Figure 4.8 shows the GRI-4 data after they were rotated by $+15^o$ to $N105^oE$. At this angle, the energy in the cross-talk components X'Y' and Y'X' is minimized. The same events in the X'X' section arrive earlier than those in the Y'Y' section. This indicates that the fractures are along $N105^oE$, because shear waves polarized parallel to the fracture plane travels faster than those polarized in other directions. Within any 10^o or less, there is no significant change in the rotation results. Therefore, I consider the uncertainty in the rotation angle to be about $+/-10^o$. The inferred fracture direction of $N105^oE+/-10^o$ agrees with that inferred from the VSP data, $N96^oE+/-10^o$, at the Red Mountain well location. It is also consistent with the geological observation of the $N110^oE+/-15^o$ fracture set that appears in the Tertiary and locally in the Cretaceous formations (May et al., 1996).

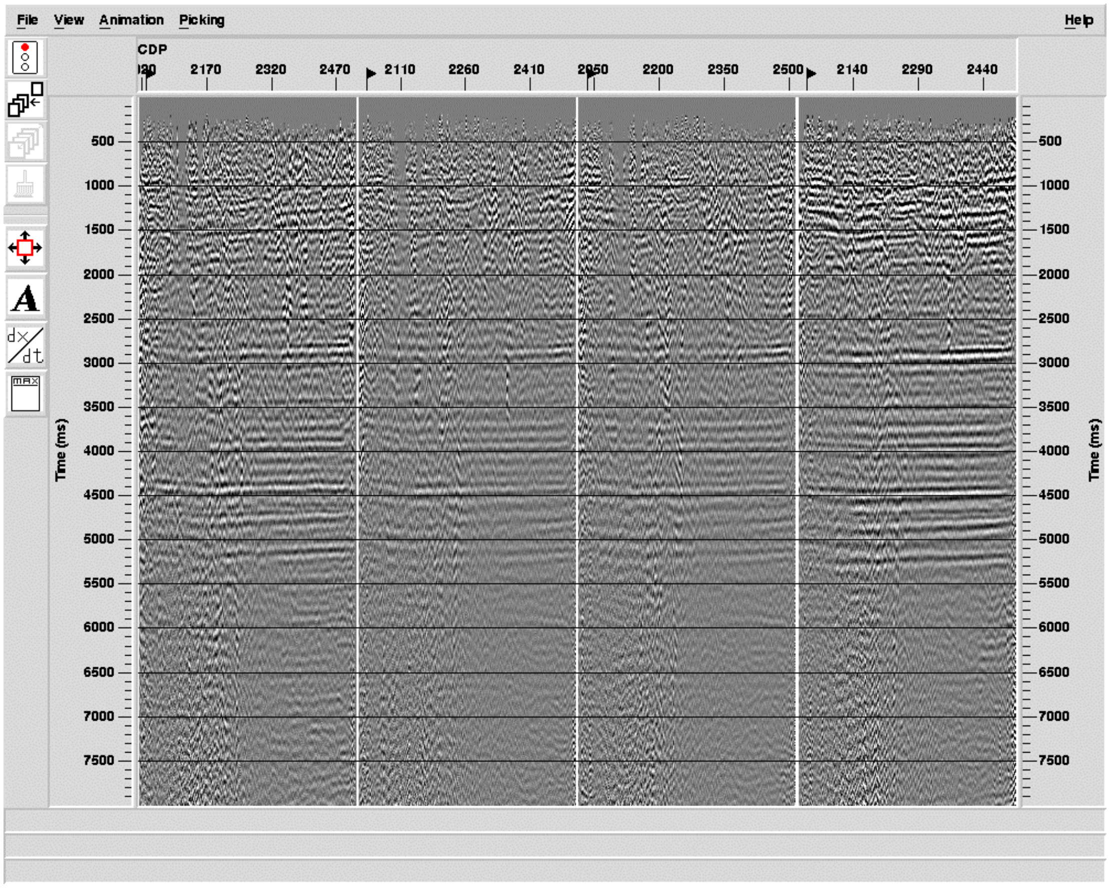

Figure 4.7: The four components of shear wave along Line GRI-4. From left to right: XX, XY, YX, YY. The significant energy level on the mismatched traces XY and YX indicates the subsurface anisotropy.

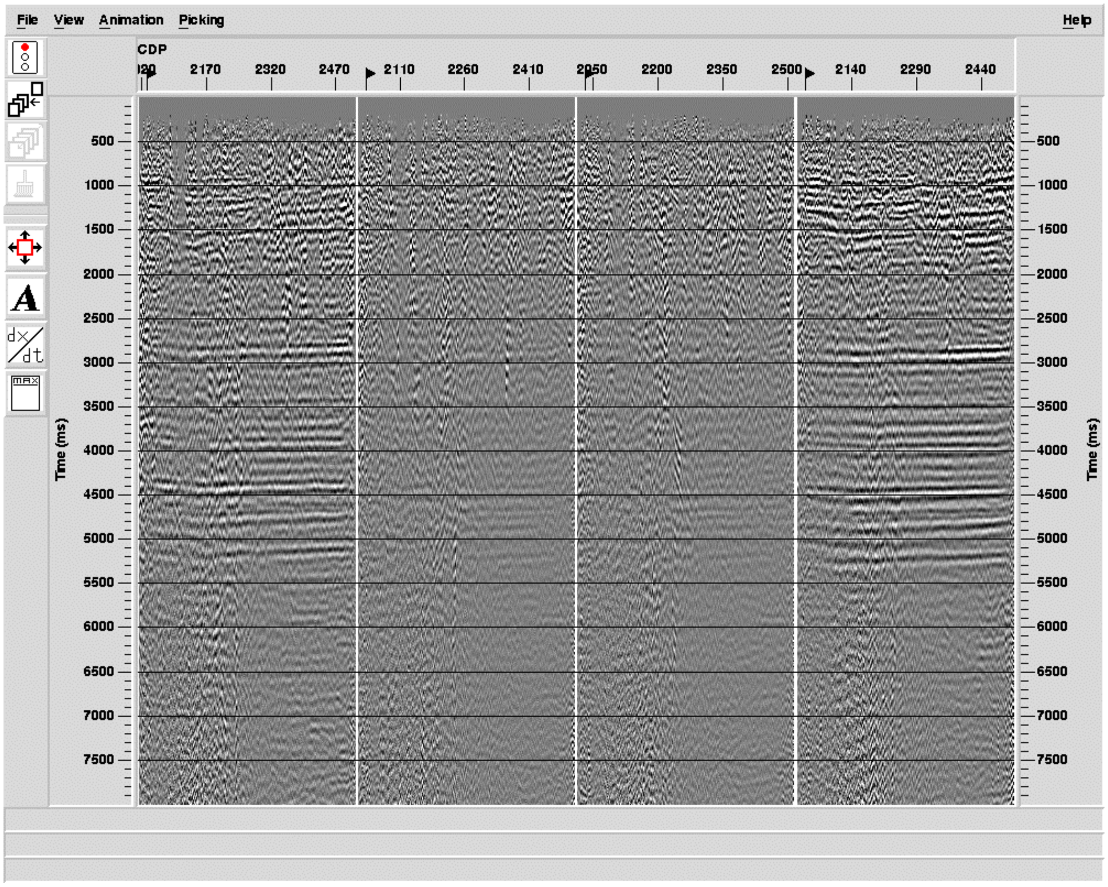

Figure 4.8: GRI-4 after 15^o Alford rotation to N105^{o}E direction. This is the optimum Alford-rotation angle at which the minimum energy on the X'Y' and Y'X' components is reached.

After rotating the data to the proper coordinates, I used a cross-correlation method to pick the traveltime lag between the fast and slow arrivals. When two similar events are cross-correlated, the lag with the maximum cross-correlation value corresponds to their traveltime difference. The cross-correlation window should not be too long so that it excludes other events. However, all X'X' events in the Cretaceous strata arrive more than 50 ms earlier than the Y'Y' events. To make them be in a short cross-correlation window, I shifted the X'X' sections by a constant time of 50 ms. A 100-ms window centered at each event was used to get the remaining traveltime lag. The traveltime lag is the remaining traveltime lag plus the previous 50 ms shift. Figure 4.9 illustrates the result of the cross-correlation at a few CDP locations.

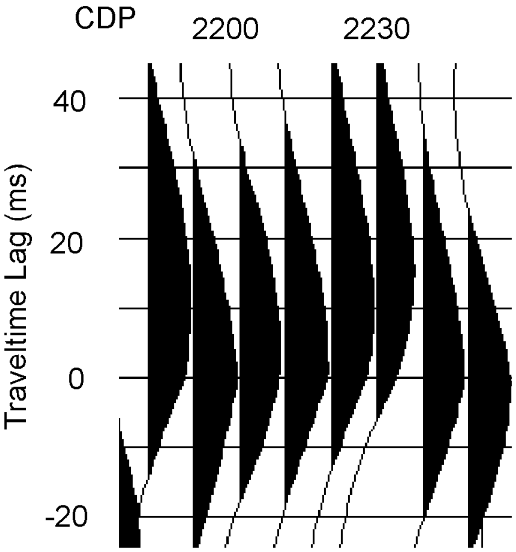

Figure 4.9: Cross-correlation results for picking the traveltime lag. The measurement error is about +/- 1ms. The 100 ms here corresponds to a 0-ms shift.

Knowing the uncertainty in picking the traveltime lag is important for judging the quality of the fracture interpretation. Because of the previous filtering of 4-40 Hz in processing Step 10, the smallest period is 25 ms. Half of the period is about 12 ms. A 10% error in picking the highest cross-correlation value corresponds to an error of about +/- 1ms.

Figure 4.10 shows the traveltime lags for the tops of the Parkman, Sussex, and Niobrara formations, and the bottom of the first Frontier sand. These lags are the cumulative lags of all the anisotropy above the reflectors. The difference in lag between two reflectors is related to the amount of anisotropy between the two events. Figure 4.11 shows the change in traveltime lag ΔT_S in the Parkman, Sussex, Niobrara formations, and the first Frontier sand. Because the reflection at the top of the Niobrara formation is weak compared to that from other strong reflectors, its traveltime-picking tends to have large uncertainty. Figure 4.12 shows the amount of shear-wave traveltime anisotropy $\Delta T_S / T_S$ in the various intervals. The negative shear-wave anistropy for the Niobrara and Frontier formations shows that N105^{o}E is not the fast direction, and the fracture plane is not in the N105^{o}E+/-10^o direction in this interval. To recover the fracture information at the Niobrara-Frontier reservoir level, layer-stripping analysis (Winterstein and Meadow, 1991a, b) to remove the overburden effect is required.

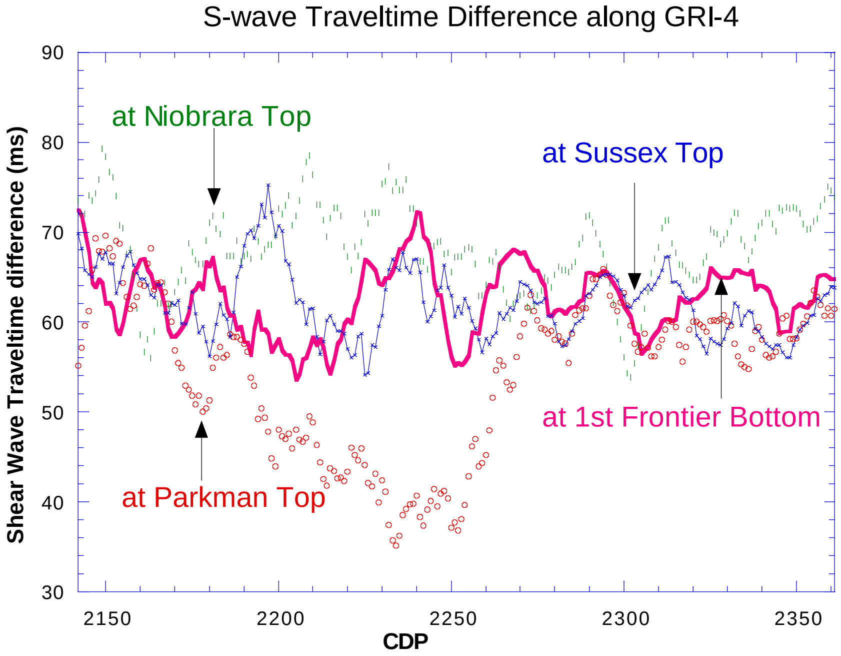

Figure 4.10: Shear-wave traveltime lag along Line GRI-4. The traveltime difference is obtained with a cross-correlation of the fast (X'X') and slow (Y'Y') events.

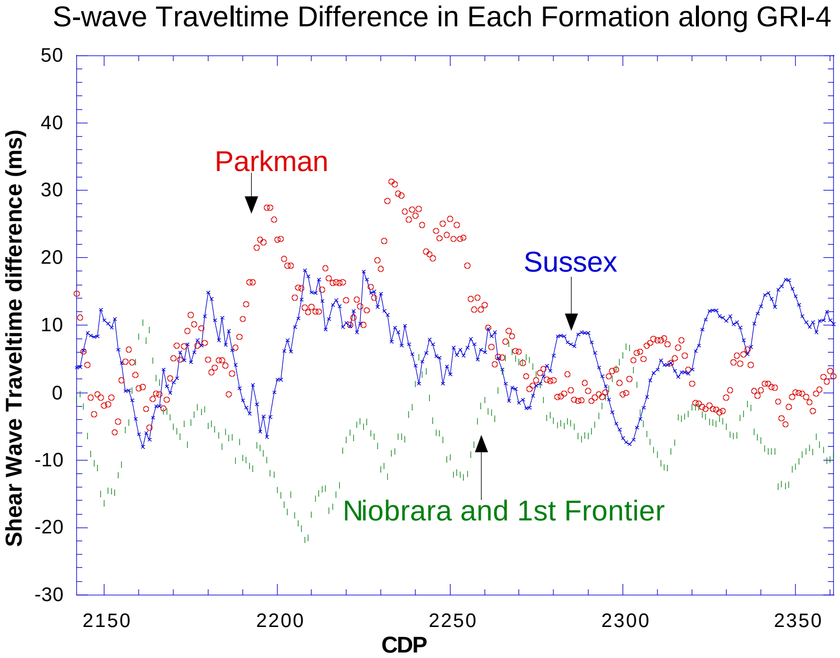

Figure 4.11: Shear-wave traveltime lag generated within each formation along Line GRI-4. The results are the difference between traveltime differences at the corresponding events as shown in the previous figure.

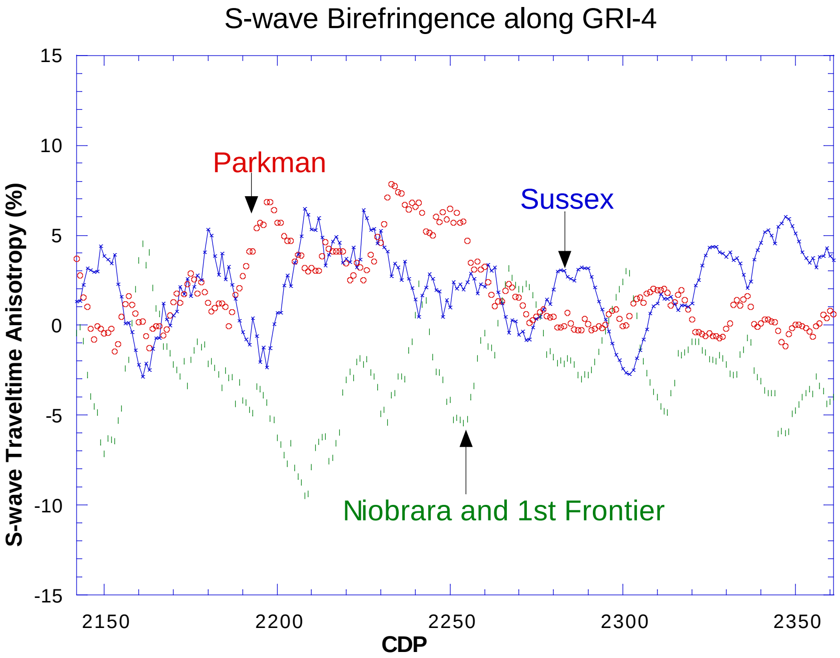

Figure 4.12: The shear-wave traveltime anisotropy in each formation along Line GRI-4.

The first step of layer-stripping analysis is to remove the traveltime lag at the depth level at which the fracture orientation changes across the boundary. This step is equivalent to moving the source-receiver system to this depth level. Winterstein and Meadows (1991a, b) point out that an improper traveltime stripping can cause a subsequent rotation error. At the top of the Niobrara formation, the signal-to-noise ratio is low, and picking of the traveltime lag is likely to be contaminated. On the other hand, the top of the Sussex sand is a strong reflector. Without knowledge of the exact depth level at which the fracture orientation changes, I attempt to do layer stripping at both depth levels, and subsequently apply the Alford rotation to find the optimum fracture orientation at the reservoir depth. Layer stripping at the Niobrara top and subsequent rotation indicates a N40^{o}E fracture orientation in the Niobrara and the first Frontier sand. This is inconsistent with the geological observation, and could be an aritfact of the low signal-to-noise ratio. The removal of the traveltime lag at the top of the Sussex sand and subsequent rotation, however, yields a optimum fracture direction of N75^{o}E in the Sussex-Niobrara-Frontier interval. The rotated shear-wave data rotated to N75^{o}E and N65^{o}E direction are shown in Figures 4.13a and 4.13b. It is worth mentioning that at the current signal-to-noise ratio, it is difficult to determine accurately which rotation angle gives smaller cross-talk energy. However, the rotation to the true symmetry plane of the fractured rock should also give the largest traveltime lag ΔT_S between the fast and slow components. Figure 4.14 shows the amount of traveltime lag along GRI-4. A rotation to N75^{o}E shows a larger traveltime lag than that of N65^{o}E. Therefore, I chose N75^{o}E to be the fracture orientation at the Sussex-Niobrara-Frontier interval. This is also consistent with the geological observations of the fracture set at N70^{o}E+/-10^o direction. Assuming that the anisotropy in the Sussex sand can be ignored, and that the traveltime lag between the top of the Sussex and the bottom of the first Frontier sand is completely due to the fractures in the Niobrara and Frontier formations, we can calculate the corresponding traveltime anisotropy $\Delta T_S / T_S$, as shown in Figure 4.15. The average crack density in the Niobrara-Frontier interval can then be estimated with equation (4.1). The result is shown in Figure 4.16. The CDP range marked by "xline #205" corresponds to a 3D superbin position. Data within this superbin will be analyzed in detail in the 3D P-wave analysis. Within this zone, the average crack density is about 0.012. The measurement error of +/- 1ms will correspond to +/- 0.004 error in the crack-density estimation. Because the fractures might not be evenly distributed throughout the Niobrara and Frontier formations, but concentrated in some thin layers, 0.012+/-0.004 is only an average crack density over the Niobrara-Frontier interval. The true crack density within thin layers can be much higher. Section 3.9 shows that, in the dipole sonic log data along the Red Mountain well, the shear-wave splitting concentrates in low-clay-content, low-porosity thin layers. A rough estimate of the the thickness of the fractured layers is about 12% of the Niobrara-Frontier interval. If this applies to the CDP locations along GRI-4, the crack density in these layers is about 0.1+/-0.03.

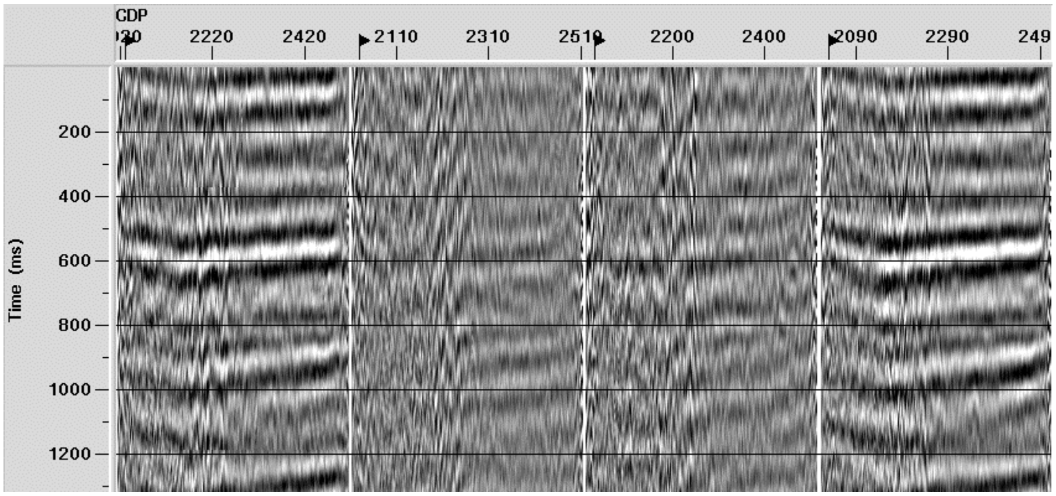

Figure 4.13: (a) Results of layer stripping at the top of the Sussex sand, and the subsequent Alford rotation to N75°E. Note that the trough near 0 ms is the top of the Sussex sand, and the strong trough near 600 ms is the bottom of the first Frontier sand.

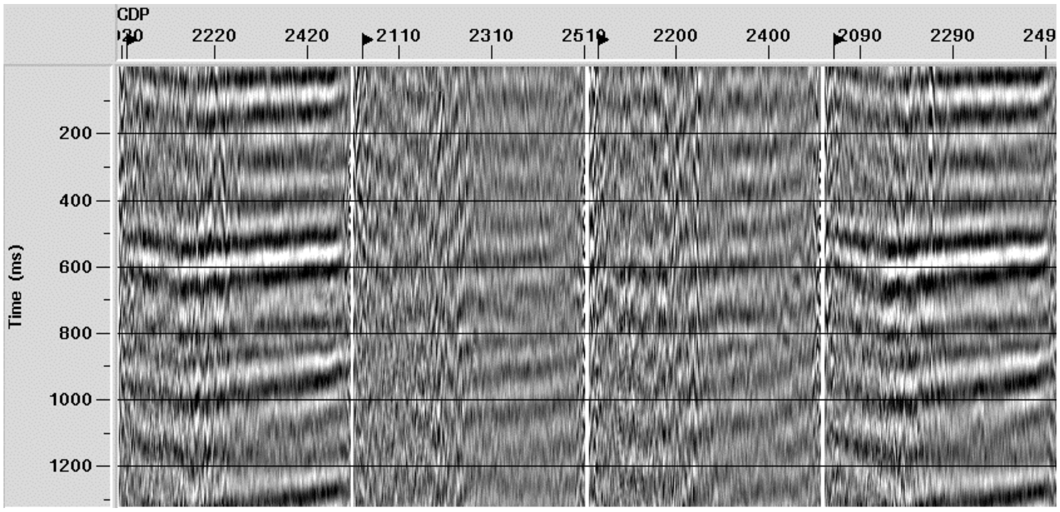

Figure 4.13: (b) Results of layer stripping at the top of the Sussex sand, and the subsequent Alford rotation to N65^{o}E. Note that the trough near 0 ms is the top of the Sussex sand, and the strong trough near 600 ms is the bottom of the first Frontier sand.

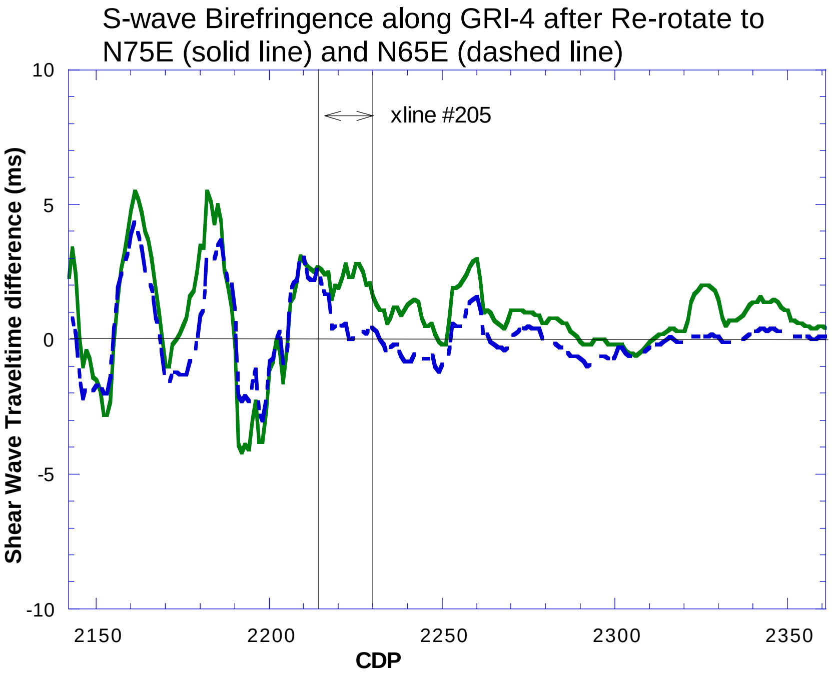

Figure 4.14: The traveltime lag between the fast and slow events from the top of the Sussex formation to the bottom of the first Frontier formation.

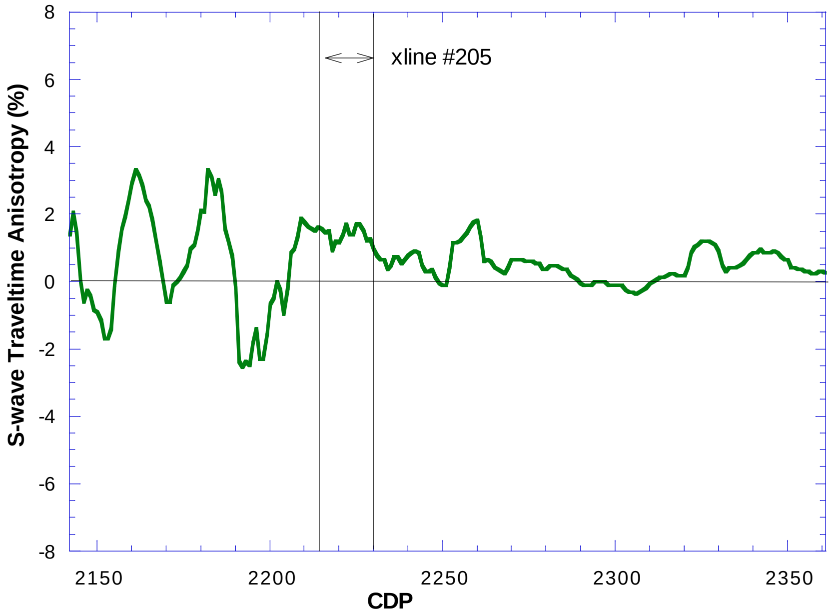

Figure 4.15: The traveltime anisotropy in the Niobrara and Frontier formations, made with the assumption that the traveltime lag shown in Figure 4.14 is completely attributed to the fractures in the Niobrara and Frontier formations, but not the Sussex formation.

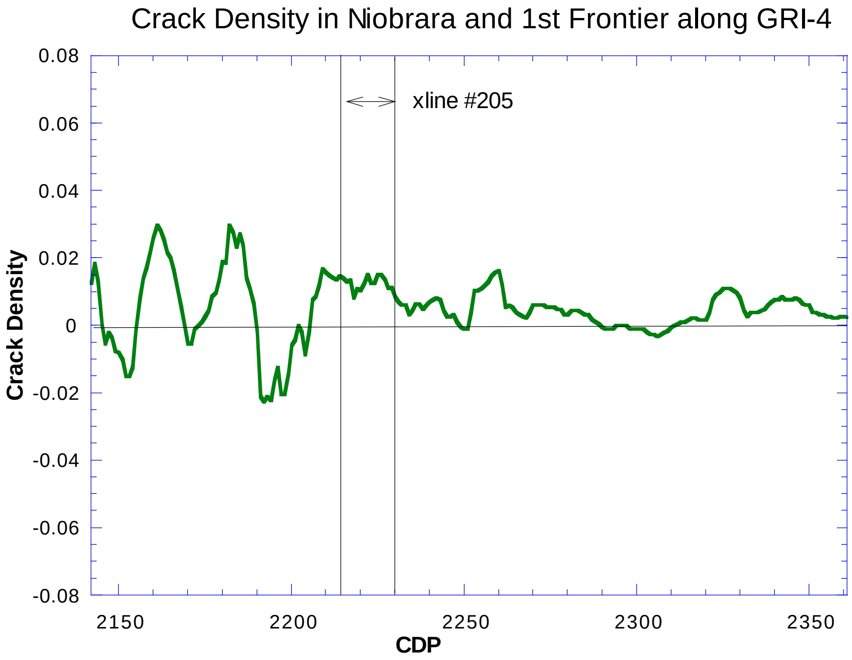

Figure 4.16: The crack density in the Niobrara and the first Frontier sand. This is derived from the shear-wave traveltime anisotropy after layer stripping at the top of the Sussex sand has been done and the data are re-rotated to N75°E.

Figure 4.17 shows the four components of shear waves along Line GRI-1. The Alford rotation was applied at every 15°. Figures 4.18 and 4.19 show the results after rotations of +15° to N105°E, and -15° to N75°E. The CDP range between CDP 2069 and CDP 2350 falls in the 3D P-wave survey area. The Alford rotation shows that in the south half of the line from CDP 2069 to CDP 2227, the preferred fracture direction is N105°E+/-15°; in the north half of the line from CDP 2228 to CDP 2350, the preferred fracture direction is N75°E+/-15°. The transition from N105°E to N75°E occurs gradually between CDP 2200 and CDP 2260. At CDP 2213 where the Red Mountain well is located, the inferred fracture direction is N105°E+/-10°. This finding is consistent with the N96°E+/-10° direction inferred from the VSP data N96°E+/-10°. The anomalous transition zone of the fracture orientation change correlates with the change in dip of the bedding planes. The structural features of the site are given in detail in the appendix.

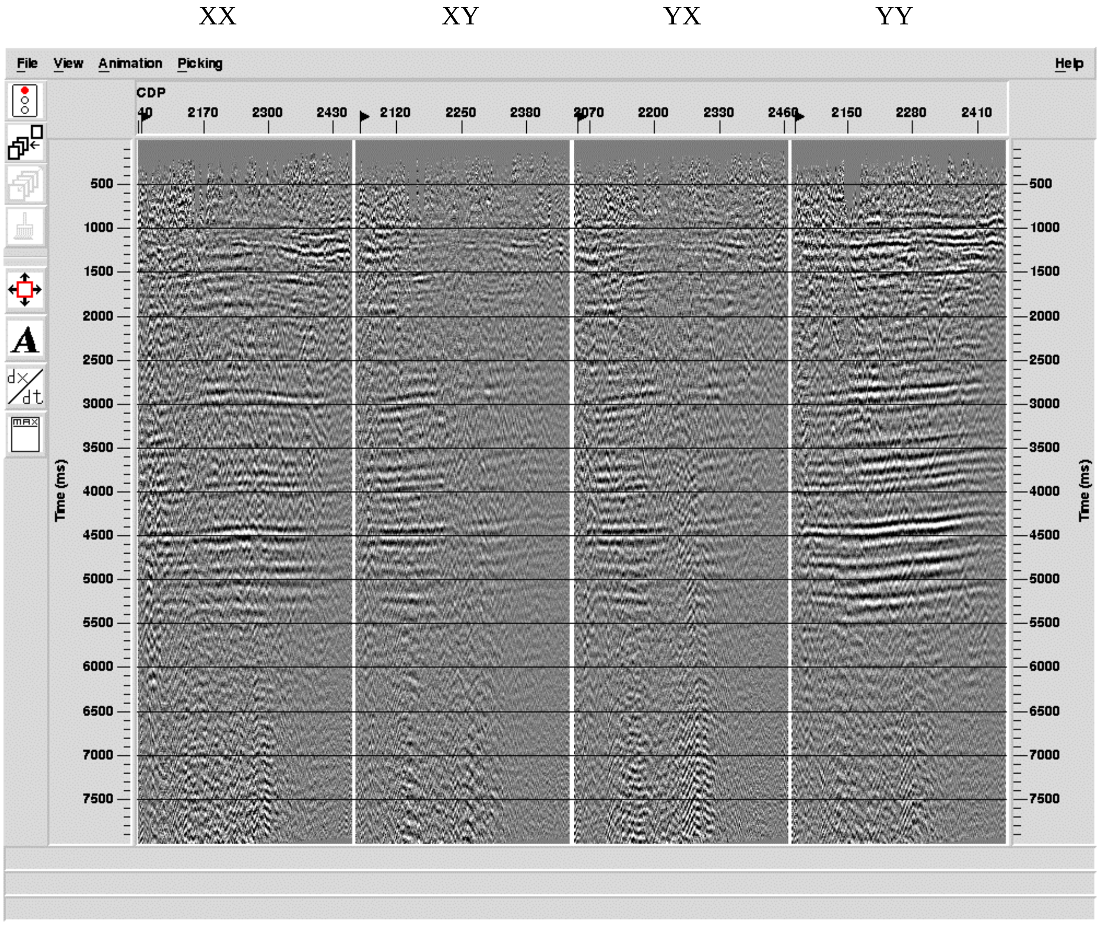

Figure 4.17: The four components of shear wave along Line GRI-1. From left to right: XX, XY, YX, YY. The significant energy level on the mismatched traces XY and YX indicates the subsurface anisotropy.

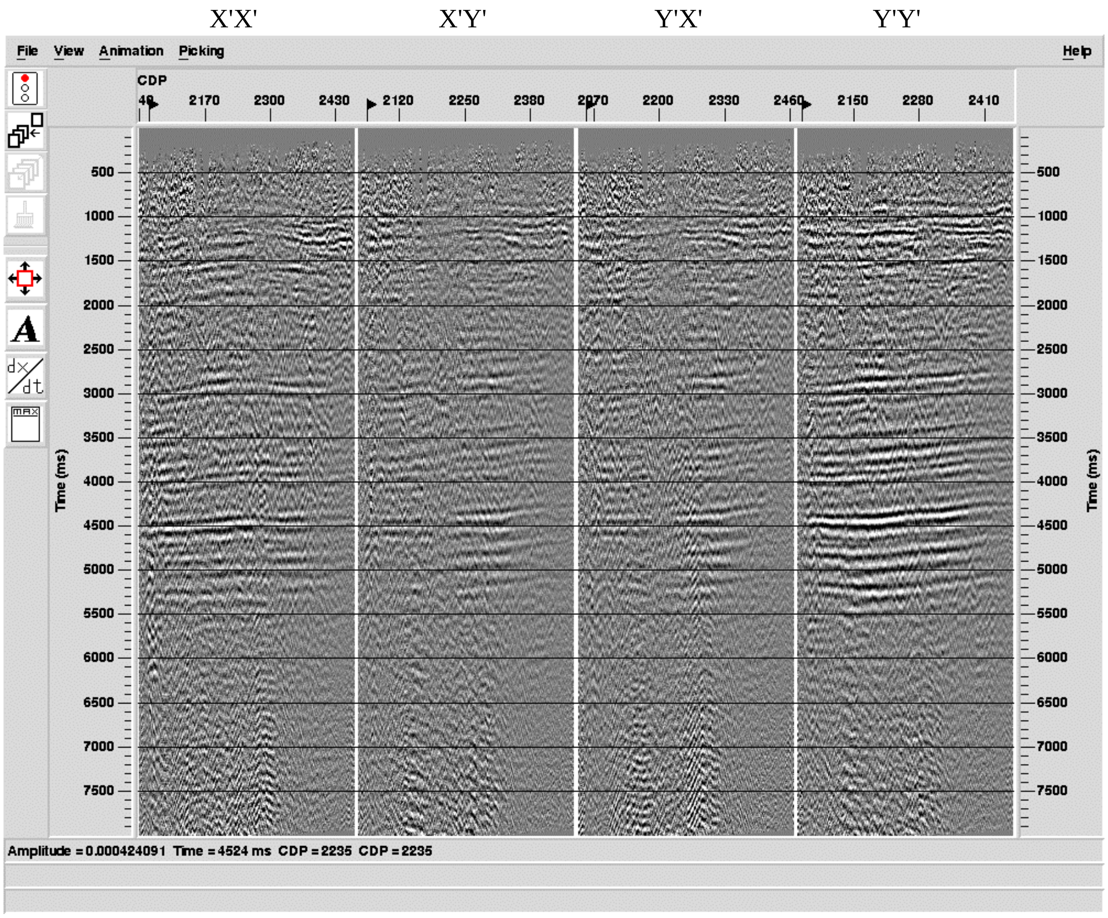

Amplitude = 0.000424091 Time = 4524 ms CDP = 2235 CDP = 2235

Figure 4.18: GRI-1 after 15^o Alford rotation to N105^{o}E direction. This is the optimum Alford-rotation angle between CDP 2069 and CDP 2227 at which the minimum energy on X'Y' and Y'X' components is reached.

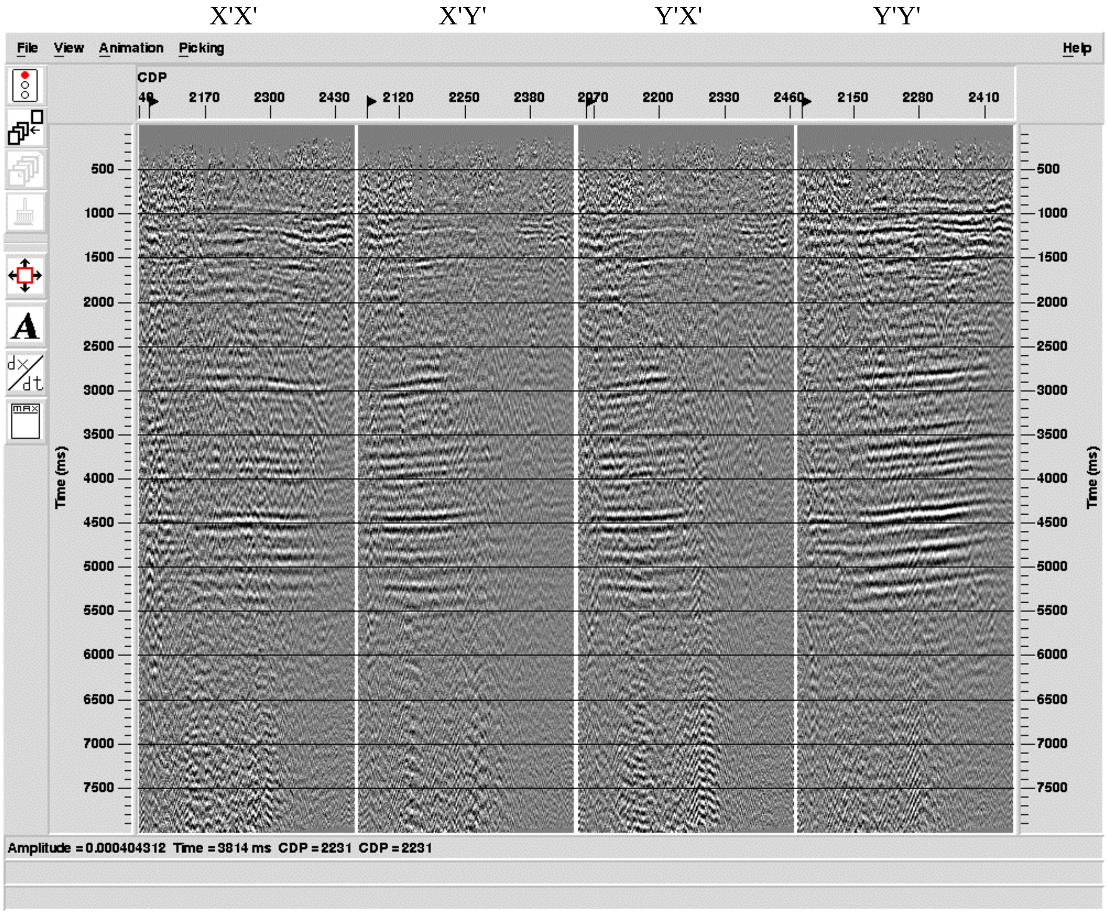

```
Amplitude = 0.000404312  Time = 3814 ms  CDP = 2231  CDP = 2231
```

Figure 4.19: GRI-1 after -15° Alford rotation to N75°E direction. This is the optimum Alford-rotation angle between CDP 2228 and CDP 2350 at which the minimum energy on X'Y' and Y'X' components is reached.

Along Line GRI-1, the traveltime differences between the fast and slow propagations were picked at several strong seismic events: the Tertiary-Cretaceous (K-T) boundary, the top of the Sussex formation, and the bottom of the first Frontier sand. The results are shown in Figure 4.20. Further layer-stripping analysis to determine the Cretaceous fracture direction was not conclusive because of the low signal-to-noise ratio along line GRI-1.

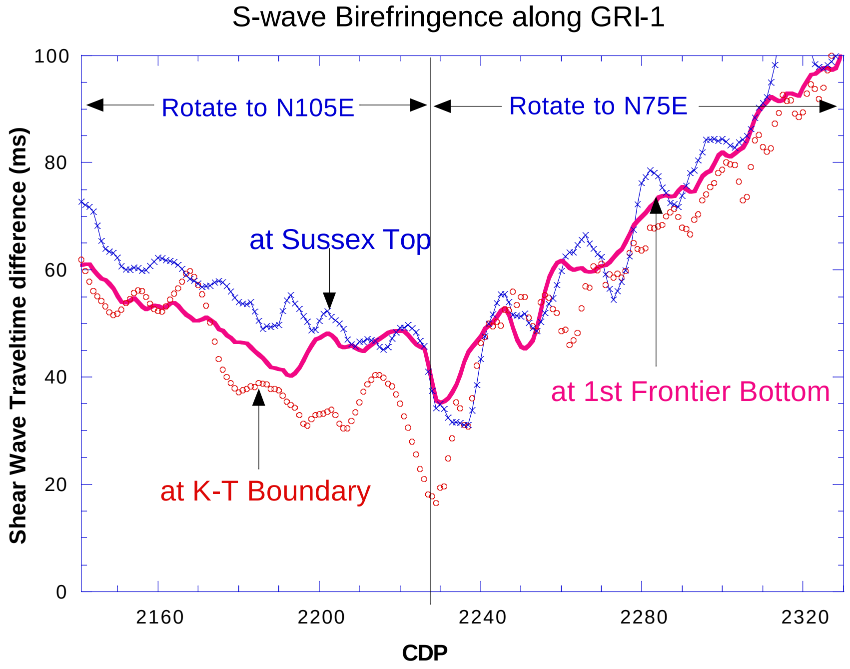

Figure 4.20: Shear-wave traveltime difference along Line GRI-1. The traveltime difference is obtained by cross-correlation of the fast (X'X') and slow (Y'Y') events. Only a few strong events are picked because of the low data quality.

For later comparison with the analysis of P-wave data, Figure 4.21 shows a mapping of the fracture direction at the reservoir level in the 3D P-wave superbin grid. This mapping is made based on surface shear-wave analysis.

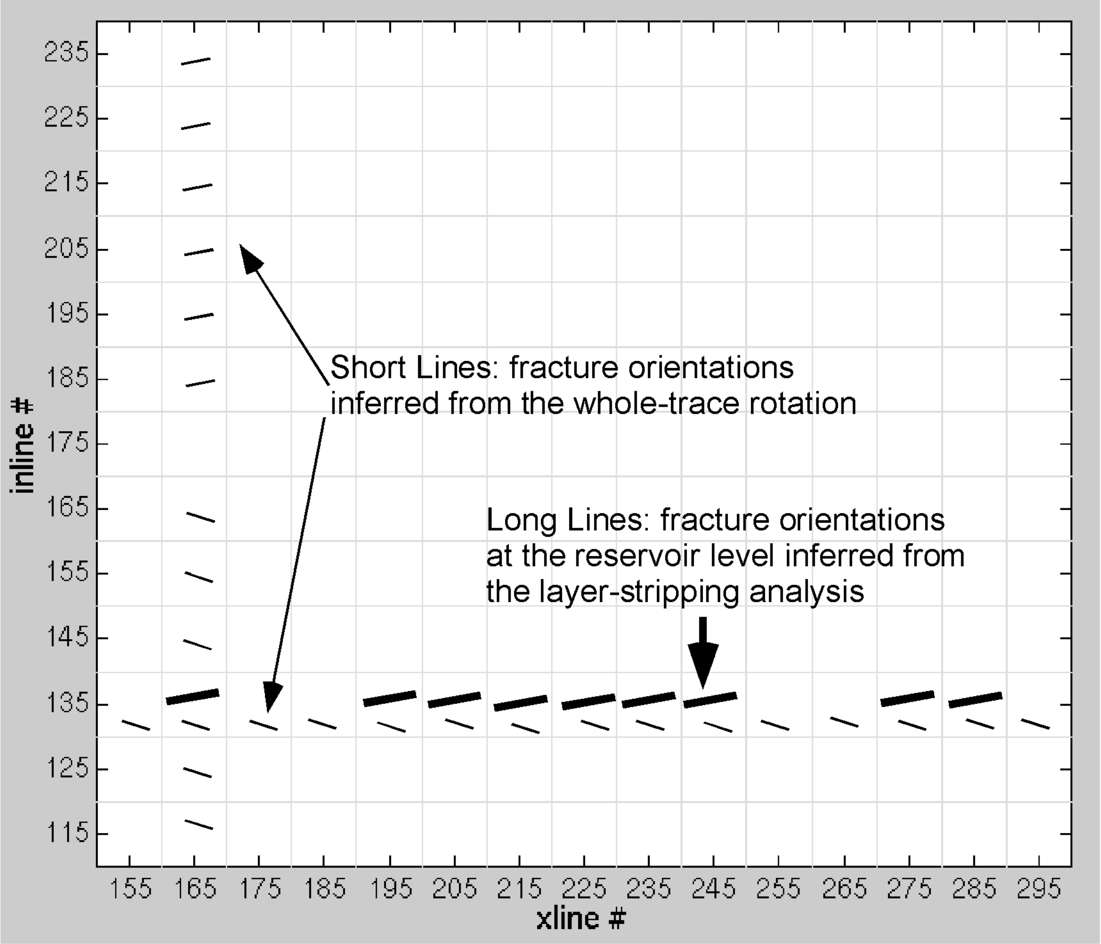

Figure 4.21: The fracture directions inferred from the 2D shear-wave data. The directions are shown in the 3D P-wave superbin grid.

4.4 3D P-wave Velocity Anisotropy and 3D Fracture Network

As discussed in Section 2.3, P-wave velocity varies with propagation direction in an anisotropic media. When parallel vertical fractures are the source of anisotropy, far-offset P-wave data will have azimuth-dependent velocity. P-waves travelling in the fracture plane will have a faster velocity than those traveling in a plane perpendicular to the fractures. This section analyzes the P-wave traveltime anisotropy at the Fort Fetterman site, and interprets it in terms of fractures.

As a reference, the P-wave processing procedures are listed below:

1. *Inline Geometry Header Load*
2. *Air Blast Attenuation*
3. *Apply Refraction Statics*
4. *Ensemble Balance*
5. *ARCO Noisy Trace Editing*
6. *Bandpass Filtering (Ormsby bandpass, zero phase, 4-8-80-88 Hz)*
7. *True Amplitude Recovery (Time-power constant = 1)*
8. *ARCO 3D Fan Filter*
9. *Surface Consistent Decon*
10. *Apply Residual Statics*
11. *Trace Equalization (Basis for scaling: mean)*
12. *ARCO 3-D Coherency Statics*
13. *Normal Moveout Correction*
14. *True Amplitude Recovery (Time-power constant = -1; spherical spreading 1/(time*vel**2))*
15. *Bandpass Filter (Ormsby bandpass, zero phase, 10-15-45-60 Hz)*
16. *Emsemble Reorder (CDP superbin size: 800 ft x 800 ft Azimuth bin size: 10^o; Offset bin size: 500 ft)*
17. *Ensemble Stack/Combine (partial stack over 10-degree-azimuth 500-ft-offset bins)*
18. *Ensemble Stack/Combine (near-offset range: 1k to 3k ft; far-offset range: 5k to 8k ft)*
19. *Cross-Correlation, to pick traveltime*
20. *Sequence Attribute Analysis, to pick peak/trough amplitudes*

Steps 1 to 14 were conducted at ARCO. These processes are primarily aimed at removing noise and statics, and preserving the signal. In Step 15, I applied an Ormsby bandpass filter of 10-15-45-60 Hz in order to further remove the low frequency noise below 10 Hz. The original CDP bin size was 80 ft by 80 ft. In each CDP bin, there is only partial azimuth coverage. In order to improve the azimuth coverage in each CDP bin, the data was reordered into superbins of size 800 ft by 800 ft. A partial stacking was conducted for each CDP superbin. The traces in each CDP superbin are binned into eighteen 10^o azimuthal bins centered at 5^o to 175^o azimuths. Within each azimuthal bin, the traces are binned into 500-ft-offset bins. Traces within each 500-ft-offset bin are corrected for the normal moveout and stacked. The velocity used for the NMO correction does not vary with azimuth. Therefore, the azimuthal variations of the traveltime/velocity are preserved in the partially stacked traces. Figure 4.22 shows the partially stacked data for the N45^oE azimuth. Finally, the near-offset stack (1000 ft to 3000 ft) and the far-offset stack (5000 ft to 8000 ft) were generated. Because the data have been partially stacked, each 500-ft-offset bin will contribute one and only one trace to the final near- and far-offset stacks. The partial stacking helps to reduce the offset bias for far-offset and near-offset stacking.

Figure 4.23 shows the far-offset stacked traces along 5^o to 175^o azimuths at the superbin centered at inline #135 and cross-line #205. In order to get an accurate P-wave traveltime variation with azimuth, I cross-correlated each trace with the trace at a perpendicular azimuth. The cross-correlation results for a few CDP's in the 3D cube are shown in Figure 4.24. Because of the previous filtering of 10-60 Hz in Step 10, the smallest period is 17 ms. Half of the period is about 9 ms. A 10% error in picking the highest cross-correlation values corresponds to a traveltime picking error about +/- 1ms. The picked traveltime variation between the top of the Sussex formation and the bottom of the first Frontier sand at the superbin at inline #135 and cross-line #205 is shown in Figure 4.25. An error bar of +/- 1ms is shown at each picks.

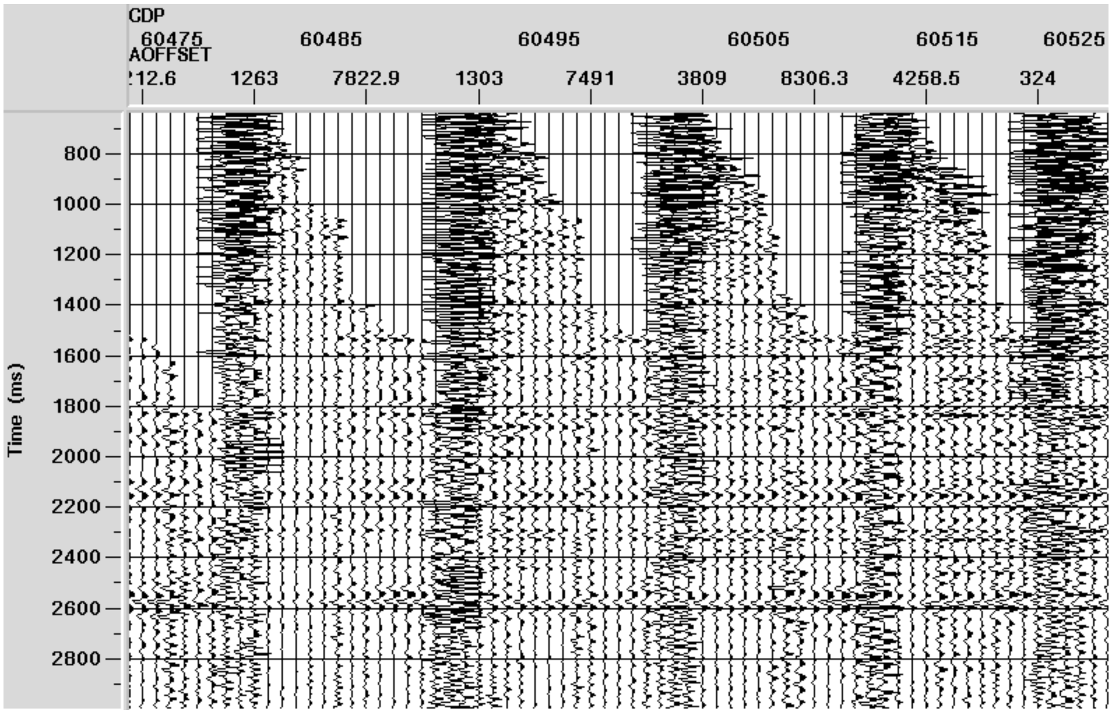

Figure 4.22: Partially stacked CDP superbin gathers along azimuth N45°E, i.e., the azimuth bin that ranges from N40°E to N50°E. The NMO-corrected data are stacked over each 500-ft-offset bin.

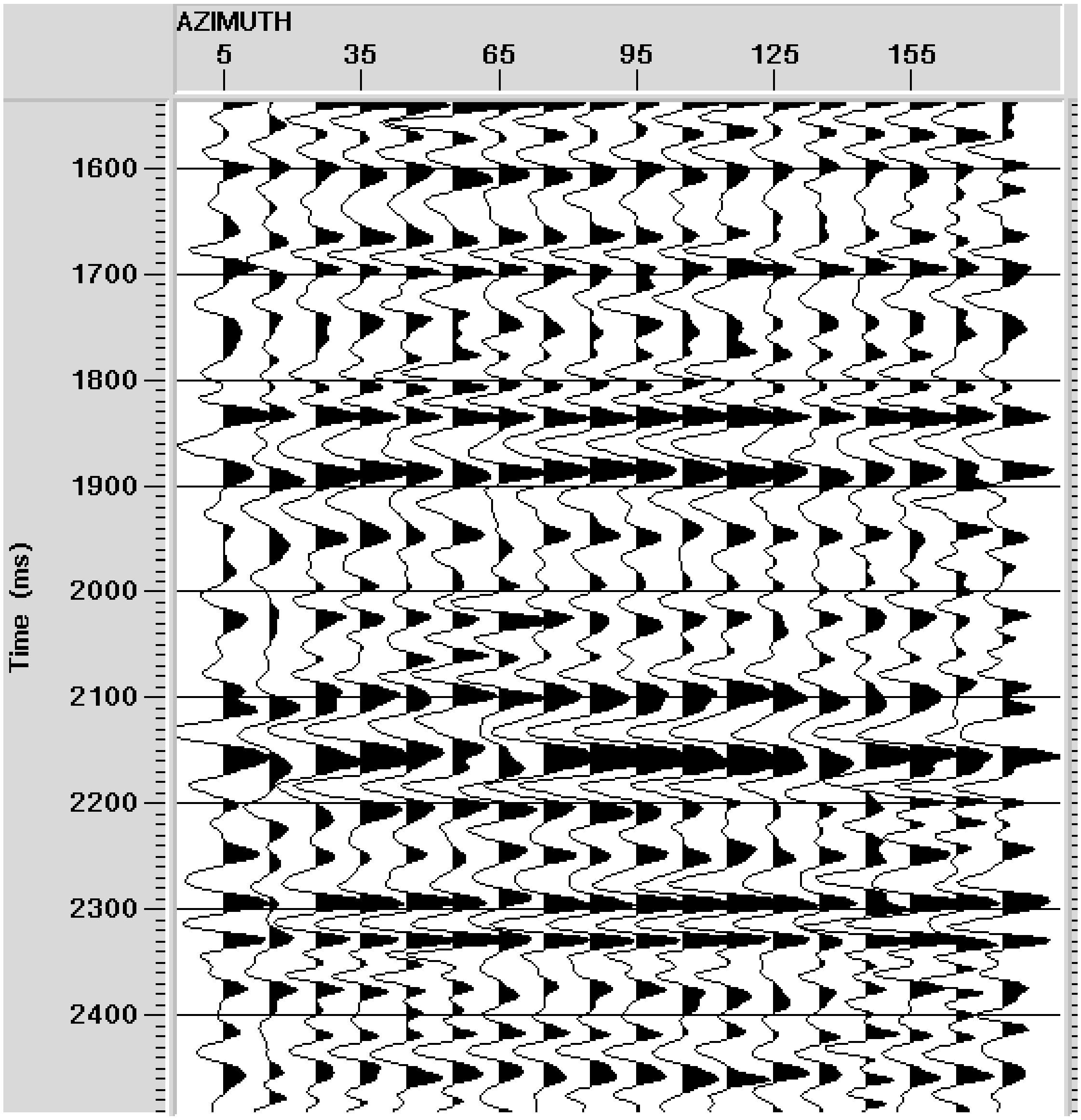

Figure 4.23: P-wave 5000ft-to-8000ft far-offset stack at the superbin at inline #135 and xline #205. The azimuth ranges from 5^o to 175^o, with a step of 10^o.

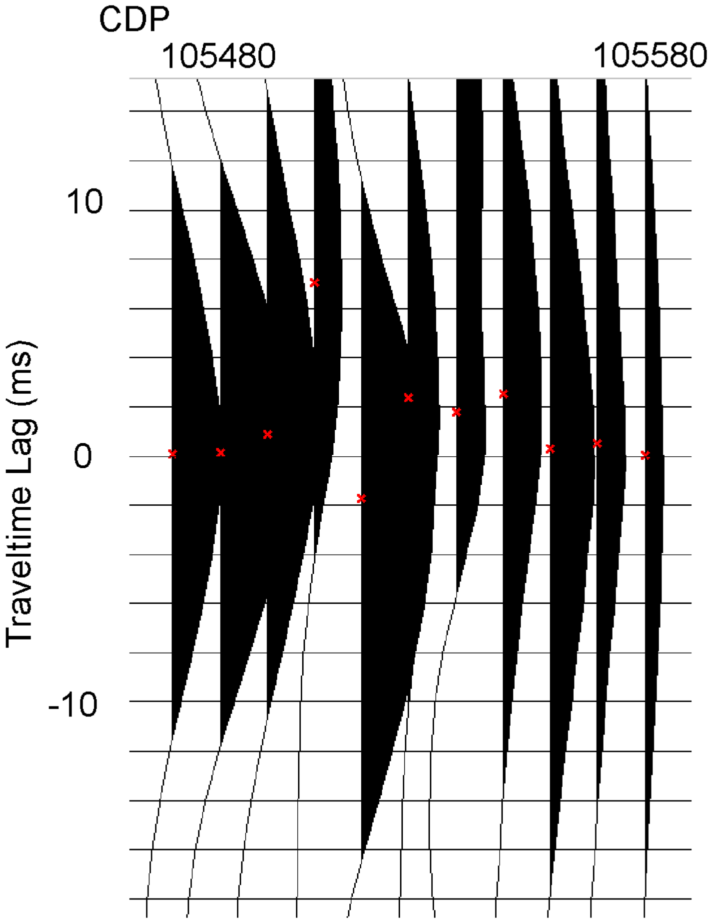

Figure 4.24: Cross-correlation results of P-wave traces along 5 ° and 95 ° azimuths. The measurement error is about +/- 1ms.

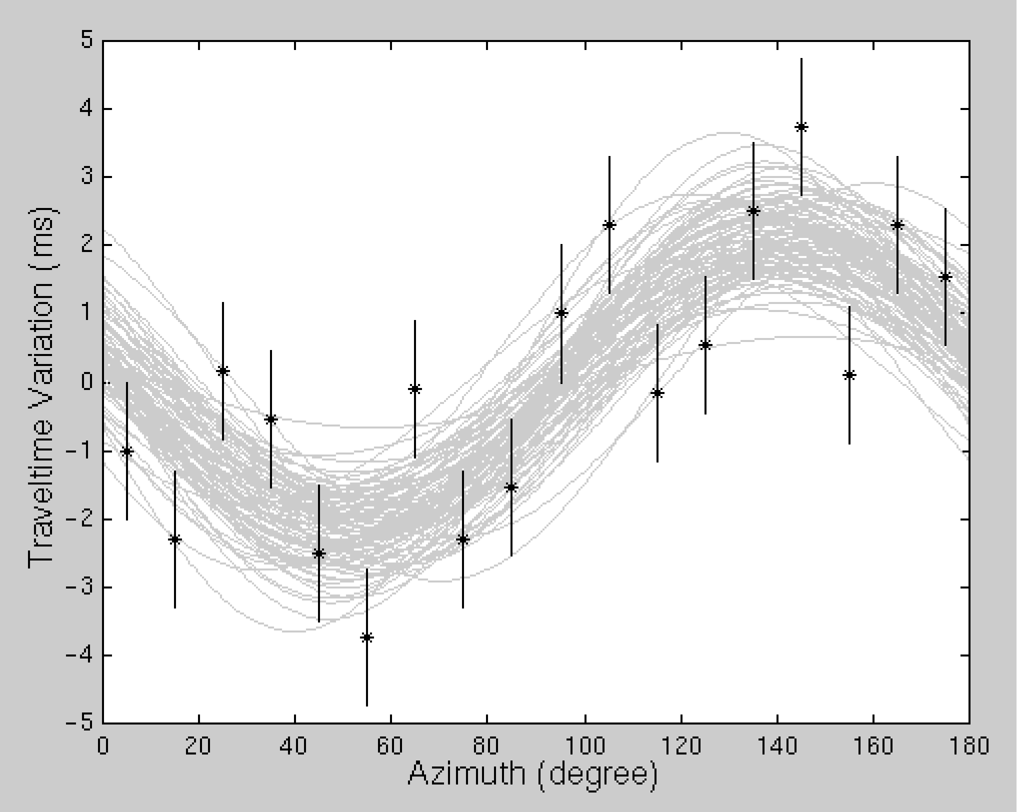

Figure 4.25: P-wave traveltime between the top of Sussex and the bottom of the first Frontier sand along various azimuths. This is the relative traveltime obtained by cross-correlation. Traveltime 0 represents traveltime 270ms. Gray lines are the cosine-curve least-squares fits, taking into account the measurement error of +/- 1ms.

Based on Hudson's theory, the P-wave velocity in fractured media can be interpreted in terms of the Hudson crack density as:

$$\frac{\Delta V_P}{V_P} \approx \frac{\Delta T_P}{T_P} \approx \left(\frac{2 l U_3 + 4 m U_1}{l + 2m} e \right) \cos^2(f) \sin^2(q) \tag{4.2}$$

where e is the crack density. The definitions of U_1 and U_3 in terms of fluid bulk modulus K_{fl} and the crack aspect ratio a , and the derivation of this formula, can be found in Sections 2.2 and 2.3 of Chapter 2. At a fixed incidence angle, the P-wave traveltime anisotropy is a cosine function of the azimuth.

Theoretically, three data points along three different azimuths can fully determine a cosine curve. Because the seismic data contain noise, redundancy in seismic data can help to improve the cosine estimation and reduce the uncertainty where the data are noisy. The amplitude data along 18 different azimuths ranging from 5^o to 175^o, with a step of 10^o are picked except for those extremely noisy traces. Least-squares fitting of a cosine curve is used to pick the optimum values of fastest P-wave azimuth angle and variation magnitude. Since data have redundancy, the standard deviation of the least-squares cosine-curve parameters should be smaller than that of the measurements. I applied a "bootstrap" method (Davison, 1997) to estimate the uncertainty in the inferred cosine-curve parameters. The idea is that our measurements at 18 different azimuths can be treated as 18 random samples out of infinite number of measurements we could have made. Every time we randomly draw a group of *n* data points from the data pool, and fit a least-square cosine curve through the data, we get an estimation of the true model. This procedure is repeated many times (in my case, 200 times for each CDP superbin). The outcome is the distribution of the expected model, i.e., the least-squares cosine fits that are related to the fracture density and properties. Furthermore, I include the measurement error in the model estimation: I let each selected measurement have a +/- 1-ms uncertainty. Before the least-squares estimation is done, the uncertainty will be generated from a normal distribution with 0 mean and of 1-ms standard deviation, and added to the data. The gray lines in Figure 4.25 are the least-squares-fitting cosine curves of the data within CDP superbin centered at inline #135 and cross-line #205. The fitting was conducted 200 times for each superbin. To test that 200 runs are enough to generate the proper distribution of the cosine parameters, I randomly generated several different 200 runs for the same CDP superbin. The estimated mean values of the cosine parameters from any random 200 runs are within 10% of the standard deviation. Therefore, 200 runs are enough to give a proper distribution of the cosine estimations. I calculate the mean and standard deviation of the fast P-wave azimuth and the magnitude of azimuthal variation.

The distribution of the fast P-wave azimuth and the magnitude of the traveltime azimuthal variation are shown in Figures 4.26 and 4.27, respectively. These distributions have taken into account the measurement error, the redundancy of the data, and the data variation caused by noise. The data display an average fracture orientation of azimuth 51°, i.e., N39 °E, and an average traveltime anisotropy of 1.6%. The standard deviation of the estimated fracture orientation is 8 °.

Figure 4.28 shows the estimated fast P-wave direction in the 3D map view, for the interval between the top of the Sussex sand and the bottom of the first Frontier sand. Surprisingly, it shows a clustered pattern of N45°E and N60°E. This result does not agree with either the geological observation, nor the shear-wave splitting results, even within the standard deviation +/- 8 ° range.

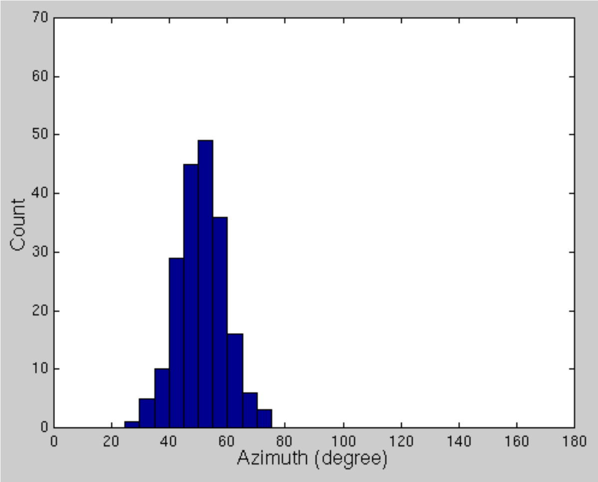

Figure 4.26: Histogram of the fast P-wave direction, i.e., fracture orientation, at the superbin at inline #135 and xline #205. The histogram is based on the 200 cosine fits as shown by the gray lines in Figure 4.25.

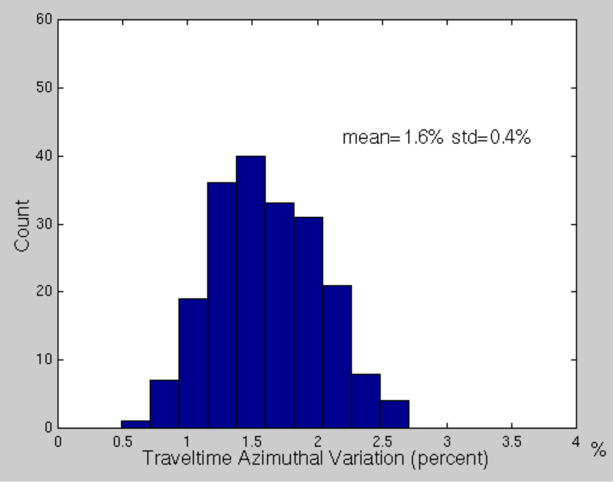

Figure 4.27: Histogram of the P-wave traveltime azimuthal variation from the top of Sussex to the bottom of the first Frontier sand at the superbin at inline #135 and xline #205. The histogram is based on the 200 cosine fits as shown by the gray lines in Figure 4.25.

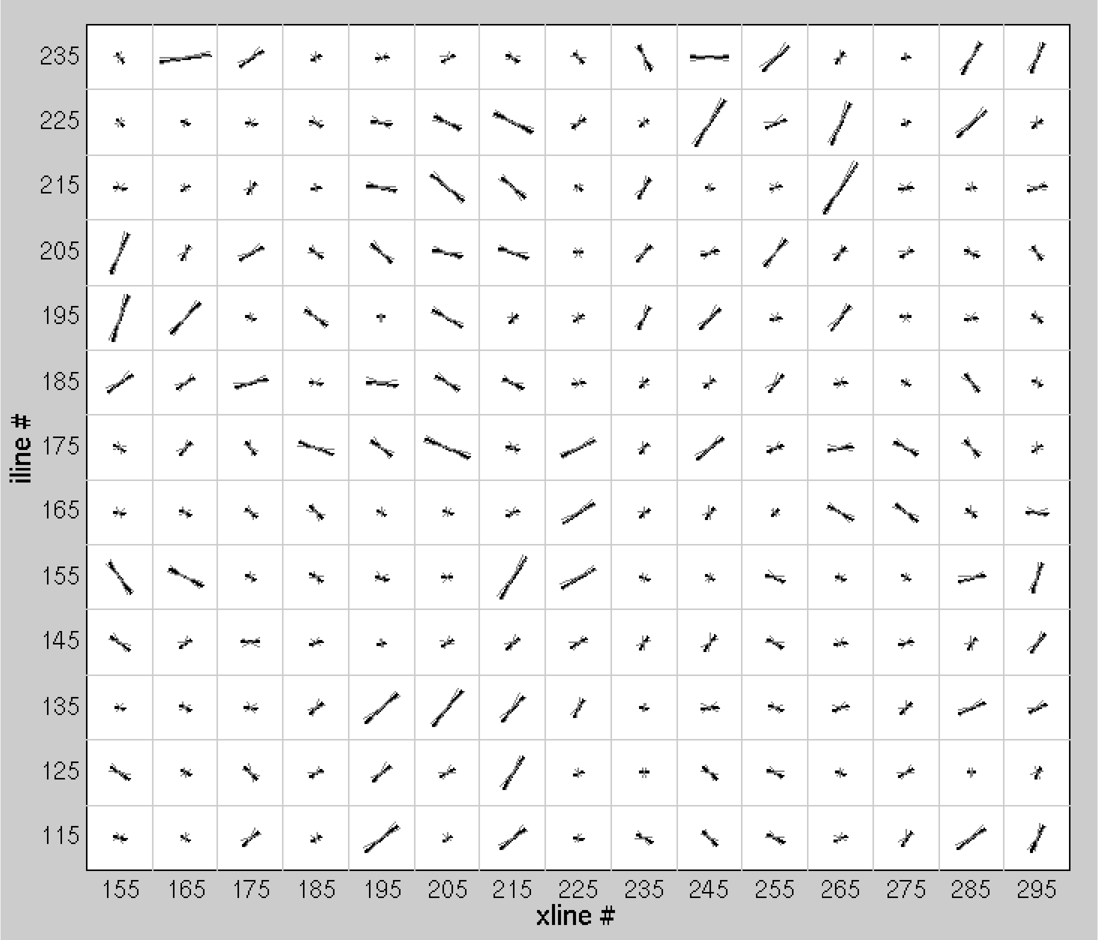

Figure 4.28: Mean value (black solid lines) and standard deviation (gray lines) of the fast P-wave direction.

The anomaly can be caused by psuedo-azimuthal variation induced by heterogeneity or dipping reflectors. Because the P-waves propagate along different azimuths, they can pick up heterogeneities along the path, and generate an azimuthal variation in traveltime that is not related to fractures or anisotropy. The ray path changes with the dip of the reflector, as shown in Figure 4.29. Dipping reflectors can induce azimuthal traveltime anisotropy. Using the geometry of the travelpath, I estimated that the traveltime anisotropy as a function of the dip angle, as shown in Figure 4.30. For a dipping bed of 5^o is about 0.5%, and for a dipping bed of $10^{\ o}$ is about 1.5%. In Figure 4.31, I plot the isopach map with the inferred fracture directions from P-wave traveltime anisotropy. The isopach map shows the contours of the depth difference between the top of the Sussex and the bottom of the first Frontier sand. The gradient of the isopach map is the relative dip of the bottom of the first Frontier sand relative to the top of the Sussex sand. Only fracture orientations with less than 20^o uncertainty are plotted. At many places, the fracture orientation is perpendicular to the isopath dip direction, i.e., parallel to the relative dip direction. The relative dip varies from 0^o to 10^o. This observation suggests that the P-wave velocity anisotropy is not a good indicator of fractures when the relative dip of the bedding is above $5\,^o$.

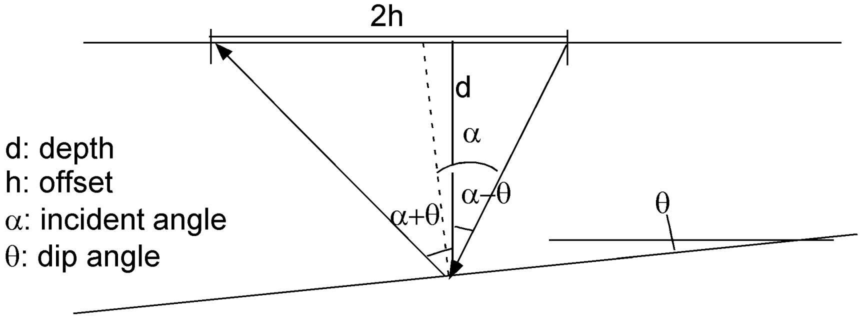

Figure 4.29: The diagram of P-wave reflected at a dipping bed with a dip angle θ.

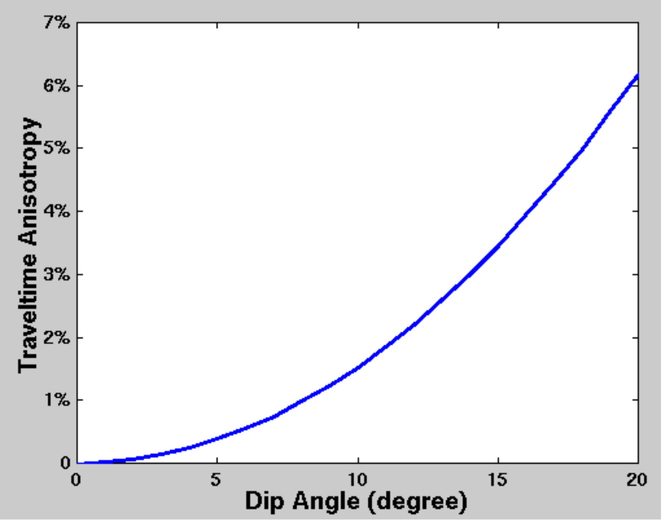

Figure 4.30: Dip-induced apparent traveltime anisotropy as a function of the dip angle of the reflector.

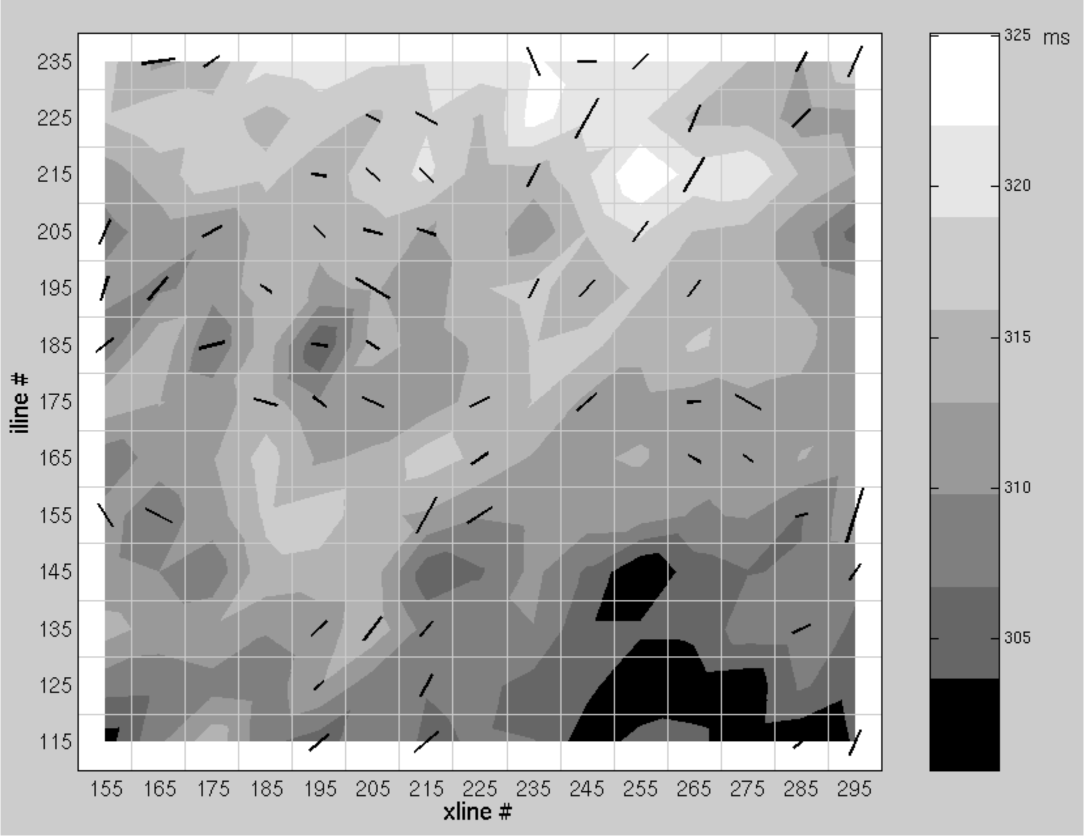

Figure 4.31: Fracture orientations inferred from P-wave traveltime anisotropy overlapped by the isopach map. Only fracture orientations whose standard deviations are less than 20° are drawn here. The length of the fracture-orientation vector is proportional to the crack density in this map.

Using equation 4.2, I modeled the P-wave traveltime anisotropy for the Niobrara-Frontier interval. I used the crack density of 0.012, as estimated from the shear-wave data. I chose the large range of crack aspect ratios from 0.0001 to 0.1. The results are shown in Figure 4.32, and for both gas and water under high- and low-frequency conditions. At the CDP superbin at inline #135 and xline #205, a 1.6% anisotropy in P-wave traveltime is observed. Comparing Figure 4.32 with the observed 1.6% anisotropy, we notice that the 1.6% is higher than the modeled anisotropy for both gas and water. Since gas tends to generate larger P-wave velocity anisotropy than stiffer fluids, the fluid inside the fractures is likely to be gas. However, as we discussed previously, the P-wave velocity/traveltime data are heavily contaminted by the effect of dip, and hence are not reliable for fracture characterization.

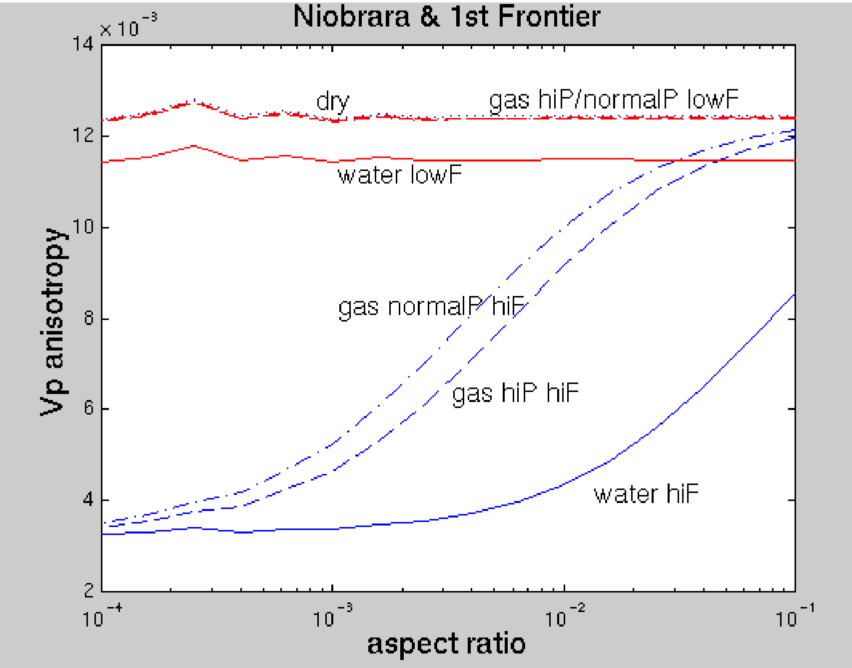

Figure 4.32: Predicted Vp anisotropy for the Niobrara and Frontier formations, containing parallel fractures with crack density 0.012, aspect ratio from 0.0001 to 0.1, and various types of crack-filling fluid.

4.5 P-wave amplitude anisotropy and fracture properties

Section 2.4 shows, theoretically, that aligned vertical fractures can induce azimuthal anisotropy into the P-wave amplitude. Conventional AVO analysis averages over the whole azimuth range, and evaluates the amplitude variation with offset. When the subsurface rock is azimuthally anisotropic, the amplitude varies with azimuth. Section 2.4 in Chapter 2 shows that at a fixed small incidence angle ($<30^o$), the P-wave amplitude variation with azimuth is approximately a cosine function of the azimuth. The variation magnitude is related to the crack density e, fluid bulk modulus K_{fl}, and the crack aspect ratio a. P-wave amplitude gives us the possibility of detecting the fracture density and fracture properties.

Using the "Sequence Attribute Analysis" package in ProMAX, I picked the maximum amplitudes at the bottom of the Frontier formation. Theoretically, at zero offset, the reflectivity is the same along all azimuths. To ensure this property, the far-offset amplitudes are normalized by the near-offset amplitudes of the same azimuth. Figure 4.33 shows the normalized far-offset amplitude variation at the CDP superbin at inline #135 and crossline #205. Each data point has an estimated error bar of 10% of the maximum amplitude of +/- 0.1. This accounts for the measurement error.

A bootstrap method was again applied to get the least-squares cosine curves fit to the data. The measurement error of +/-0.1 (10% of the maximum amplitude) was taken into account. I consider that each data point corresponds to a normal distribution with a mean equal to the measured value and a standard deviation equal to the measurement error of 0.l. The methodology was described in detail in the previous section. These curves fit to the amplitudes are shown by the gray lines in Figure 4.33. For each CDP superbin, the bootstrap method repeatedly calculates the cosine-function parameters 200 times. The distribution of the angle corresponding to the trough of the cosine curve and the distribution of the ratio of the amplitude variation to the average amplitude, are shown in Figures 4.34 and 4.35.

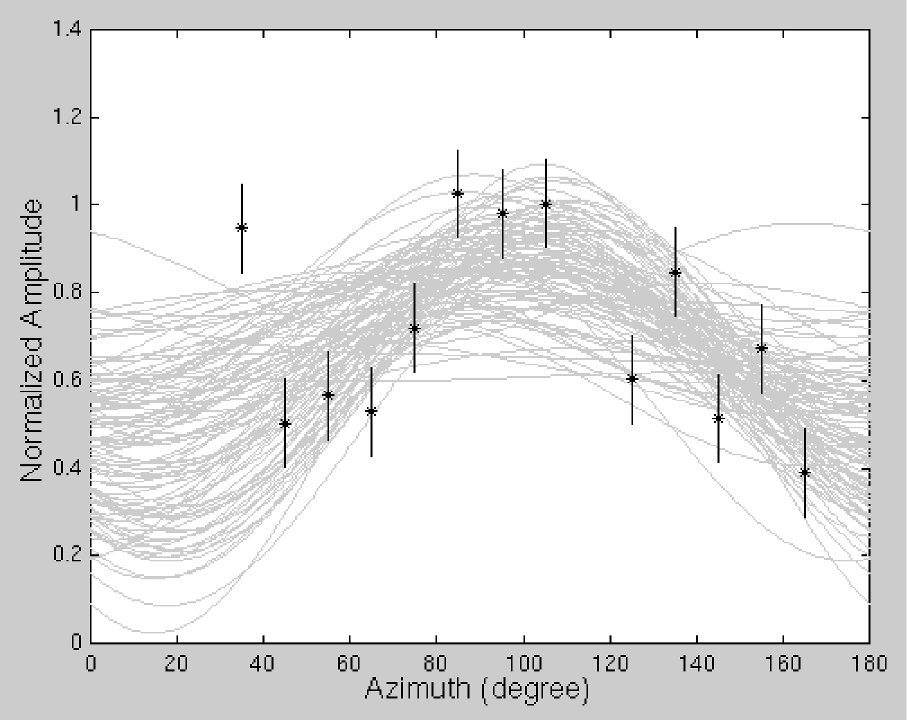

Figure 4.33: The amplitude variation with azimuth at the superbin at inline #135 and xline #205. Gray lines are the cosine-curve least-squares fits, taking into account the measurement error of 10% of the maximum amplitude.

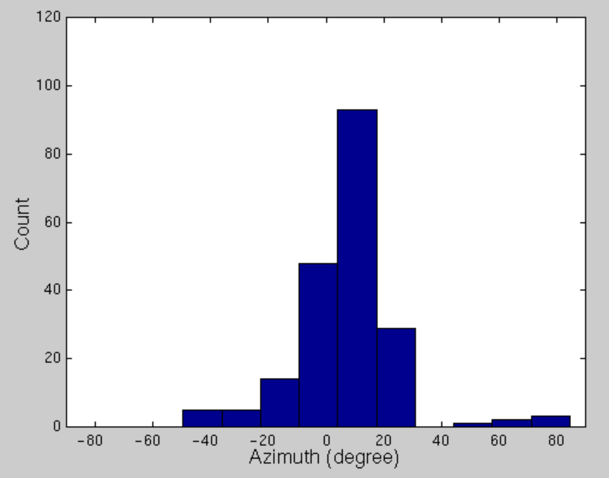

Figure 4.34: Histogram of the observed fracture orientations based on the P-wave amplitude variation with azimuth. The azimuth corresponds to the cosine-curve trough (the minimum amplitude) is the the fracture orientation. The histogram is based on the 200 cosine fits shown by the gray lines in Figure 4.33.

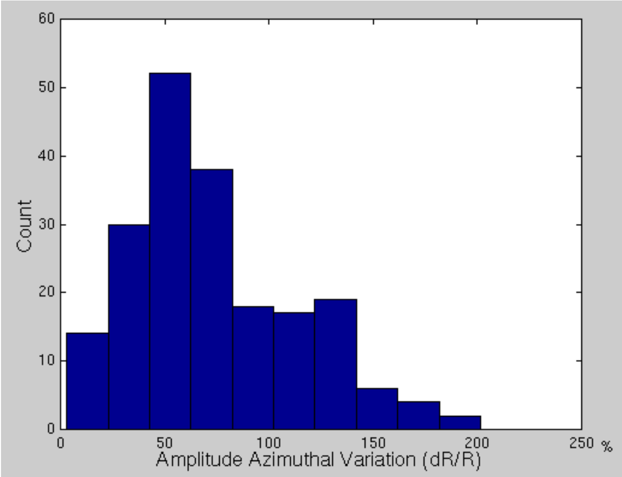

Figure 4.35: Histogram of the estimated azimuthal variation in P-wave amplitude shown in percentage. The histogram is based on the 200 least-squares cosine fits shown by the gray lines in Figure 4.33.

To interpret the amplitude azimuthal variation in terms of fracture density and properties, I calculate the reflectivity at the bottom of the first Frontier sand. The elastic moduli of the unfracture rocks are taken from the blocked well-log data as shown in Figure 4.36. Hudson's model was used to calculate the fractured rock moduli when the rock contains vertical parallel fractures. I considered two crack densities: 0.012, as measured from the 2D shear waves; and 0.1, as an upper bound. The far-offset stack has an average incidence angle of 30^{o}. The theoretical curves of the amplitude azimuthal variation induced by parallel cracks with a crack density of 0.1 are plotted in Figure 4.37. The modeling results indicate that the P-wave reflectivity has a smaller absolute value along the fracture orientation than perpendicular to the fracture orientation. Therefore, the trough of the cosine curve corresponds to the fracture orientation. It has a mean of 3.2^{o}, i.e., $N87^{o}E$, and a standard deviation of 18^{o}. This direction is consistent with the geological observation within the standard deviation. The mean azimuthal variation is 62% normalized by the average amplitude. Its standard deviation is around 18%.

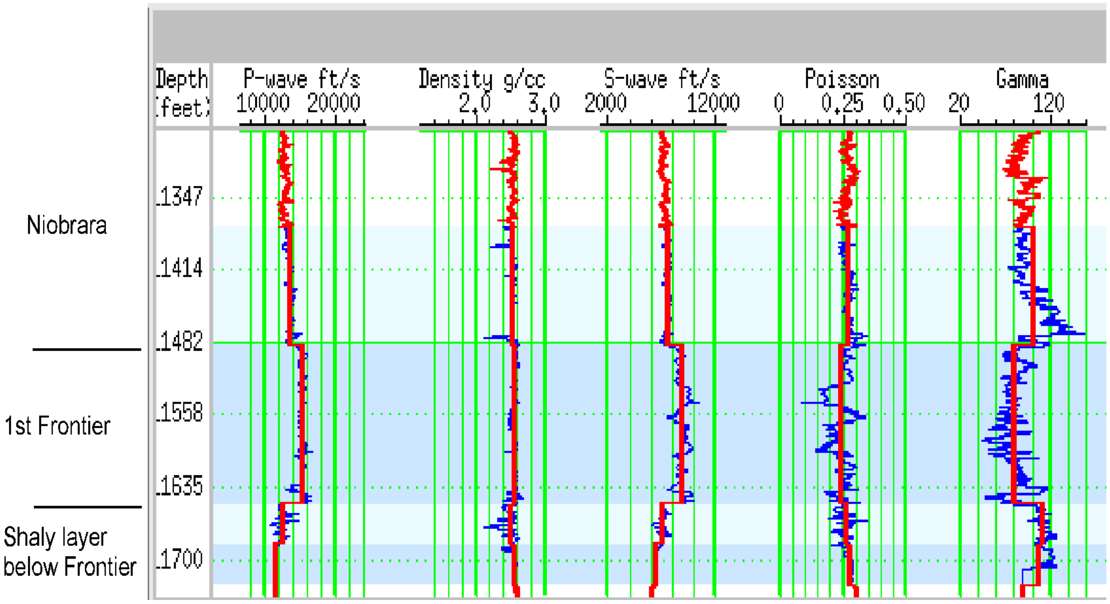

Figure 4.36: The blocked log data used in the modeling as the properties of the unfractured rocks.

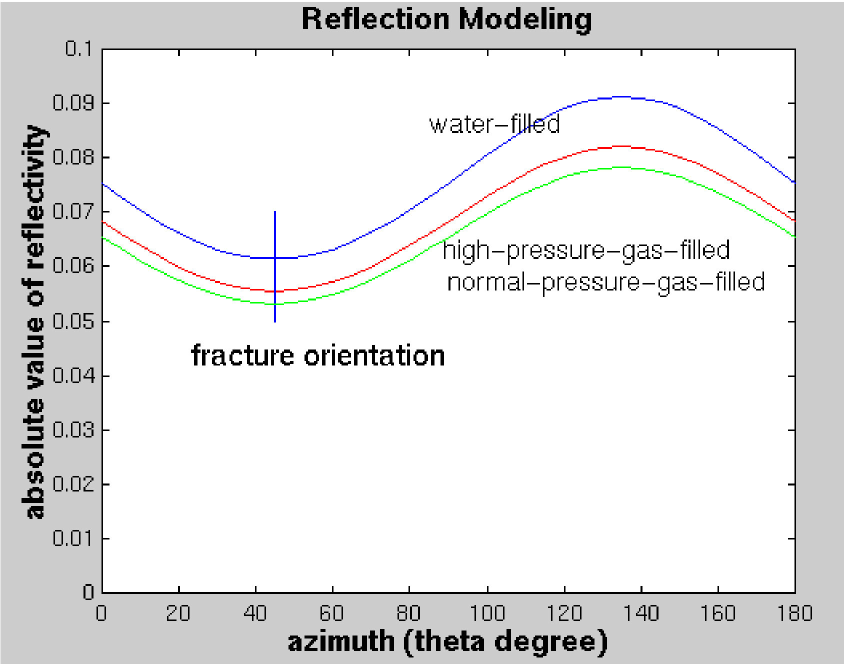

Figure 4.37: The reflectivity at the bottom of the fractured first Frontier sand that contains parallel vertical fractures with a crack density 0.1.

In order to estimate the fracture physical properties, I compare the variation with the modeling results for crack aspect ratios of 0.000001 to 0.1, and for gas-filled and water-filled cracks. The modeling results shown in Figure 4.38 are for crack density 0.012, and those in Figure 4.39 are for crack density 0.1. The current resolution of the P-wave amplitude variation does not allow us to distinguish the fluid content within the fractures. The amount of amplitude anisotropy induced by the gas-saturated and the water-saturated fractures are close, and both agree with the data within the error range. The data show an amplitude azimuthal variation of 62%. This is larger than the modeling result. The difference between the data and the model could be caused by the anisotropic attenuation in the overburden, the focusing effects of waves traveling in the anisotropic medium, or heterogeity along the wave path.

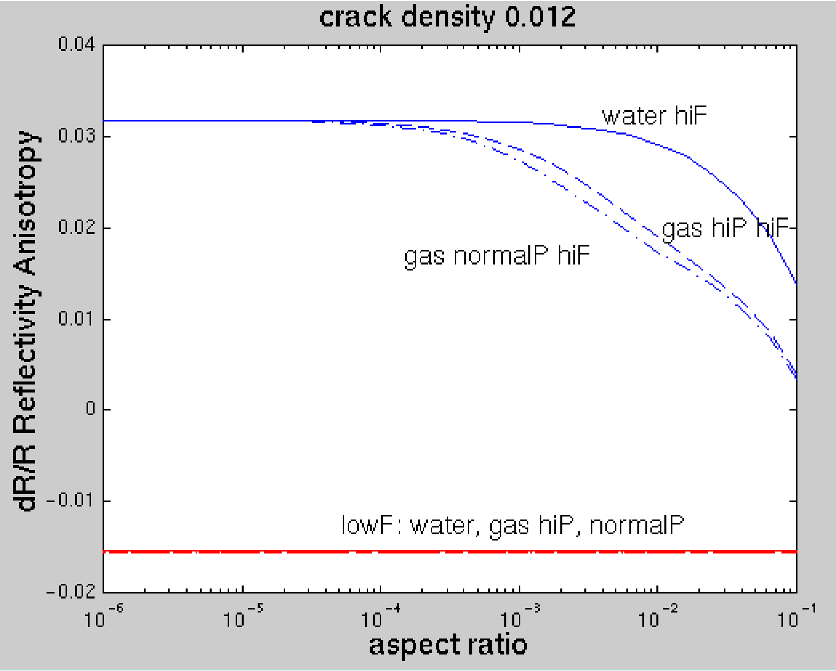

Figure 4.38: The reflectivity azimuthal anisotropy at the bottom of the fractured first Frontier sand that contains parallel vertical fractures with a crack density 0.012.

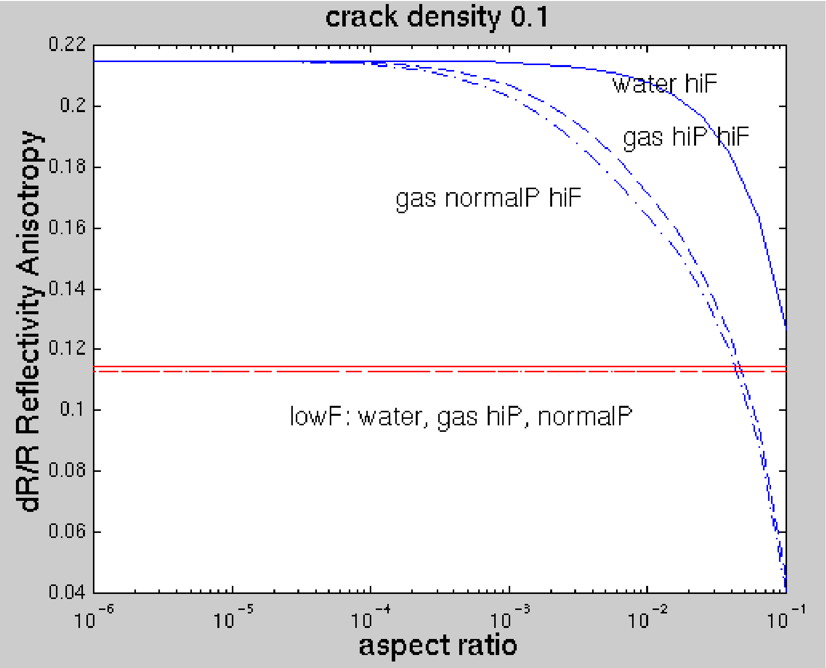

Figure 4.39: The reflectivity azimuthal anisotropy at the bottom of the fractured first Frontier sand that contains parallel vertical fractures with a crack density 0.1.

Figure 4.40 shows the crack orientation with the standard distribution inferred from the P-wave amplitude azimuthal variation throughout all bins in the 3D survey area. Figure 4.41 shows the fracture orientation in the 3D-superbin grid. The length of fracture-direction vector is proportional to the magnitude of the amplitude variation. Only those orientations with a standard deviation less than 20^o are shown. At the superbins in which the standard deviations are very large, P-wave amplitude variation does not give a reliable fracture orientation. The seismically inferred fracture orientation based on P-wave amplitude roughly agrees with the geological observations and the fracture orientations inferred from shear-wave data at the overlapping superbins.

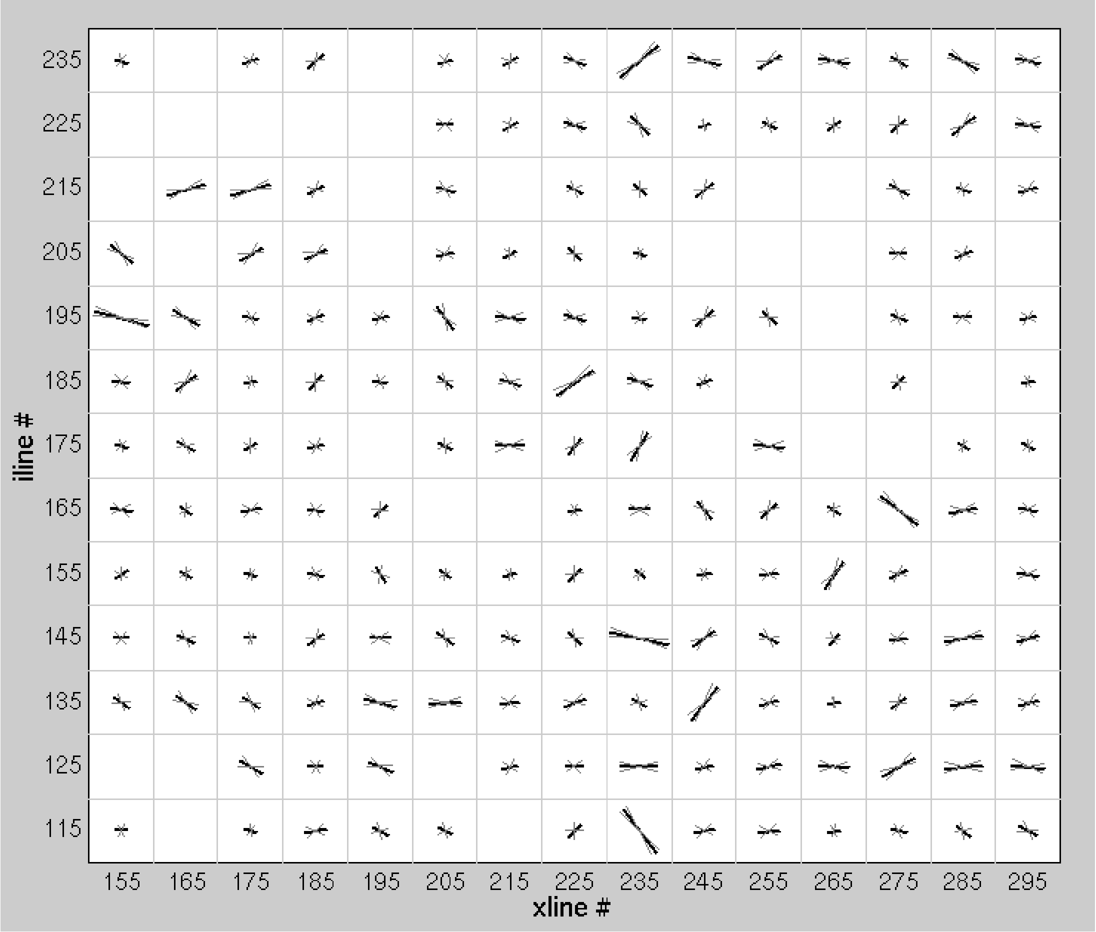

Figure 4.40: The crack orientations derived from the 3D P-wave amplitude azimuthal variation. The solid lines are the mean value of the fracture orientation. The gray lines are the mean values plus/minus the standard deviations. This plot highlights the fracture orientations with small standard deviations: I made the length of the vectors inversely proportional to the standard deviation of the fracture directions.

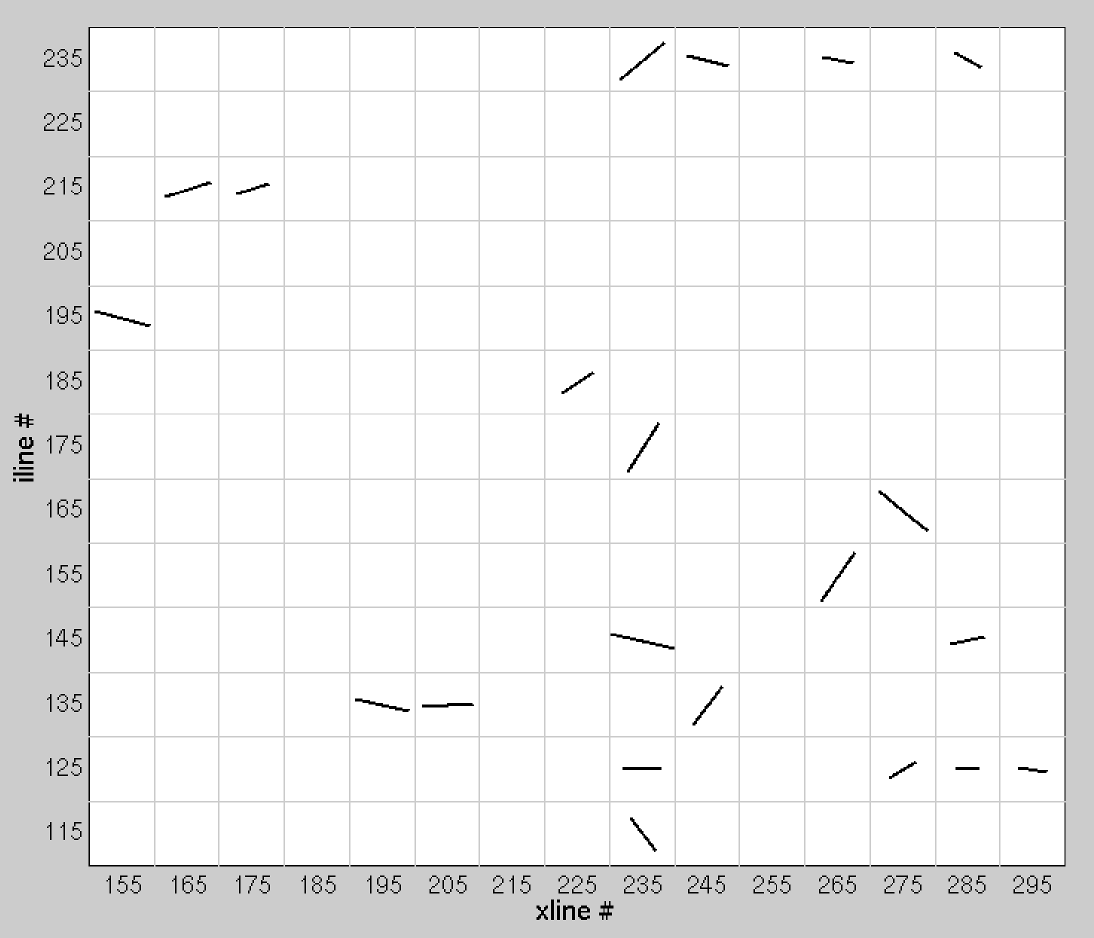

Figure 4.41: The crack orientations derived from the 3D P-wave amplitude azimuthal variation. The length of the vectors is proportional to the crack density in this map. Only fracture orientations that have a standard deviation of less than 20^o are plotted.

4.6 Conclusions

I applied and tested the methodology of using 3D single-component P-wave data combined with shear-wave data and log data to determine the fracture orientation, density, and properties at the Fort Fetterman site. Azimuthal anisotropy has been observed on the P- and S-wave traveltime/velocity, and the P-wave amplitude. I interpreted the symmetry-plane directions and the magnitude of the anisotropy in terms of the subsurface fractures' orientation, density, and physical properties.

Results of the 2D shear-wave data, and P-wave amplitude azimuthal variation give a consistent fracture orientation of N75^{o}E+/-10^o and N87^{o}E+/-18^o, respectively, at the Niobrara-Frontier reservoir level. They are consistent with the geological observations of N70^{o}E+/-10^o within the standard-deviation range. The shear-wave data, however, gives a much smaller crack density than does the P-wave amplitude azimuthal variation. At this site, the P-wave traveltime anisotropy is probably contaminated by the effects of dip, and therefore does not give a reliable indication of the fracture orientation.

The whole-trace Alford rotation of the VSP and 2D shear-wave data shows fast shear direction of N96^{o}E+/-10^o and N105^{o}E+/-10^o, respectively. This angle is consistent with the geological observation of fracture directions N110^{o}E+/-15^o in the Tertiary formations within the standard deviation of our estimates. Because the fracture orientation varies with depth, as observed in the outcrops, layer-stripping techniques are required to recover the fracture information in the deeper Cretaceous formations. The subsequent rotation of the surface shear-wave data shows a preferred orientation of N75^{o}E+/-10^o in the Niobrara and Frontier formations. This angle is consistent with the fracture orientations N70^{o}E+/-10^o observed in outcrop Frontier sand and in the Formation MicroScanner images. The quality of the subsequent Alford rotation of the deeper intervals after layer-stripping depends on accuracy in traveltime-lag picking at the stripping boundary. Therefore, a high signal-to-noise ratio at the interface of fracture direction change is critical for S-wave fracture detection in the deep formations. The VSP data do not have sufficiently good signal-to-noise ratio at the deeper levels for a meaningful application of layer stripping shear-wave analysis.

Shear-waves anisotropy are not influenced by the fluid properties inside the fractures. Therefore shear waves can be used to determine the fracture density without ambiguity from the unknown fluid type and properties. Along Line GRI-4, the crack density varies between 0 and 0.02. However, this inferred fracture density is the average fracture density over the Niobrara-Frontier interval being analyzed. It has been observed both geologically and in the dipole sonic logs that the fractures do not distribute evenly over the large intervals, but instead concentrate in thin layers of tight sand. Therefore, the average crack density inferred from the P- and S-wave traveltime data can be much less than that inferred from the P-wave amplitude azimuthal variation at the boundary of the fractured rocks.

The P-wave traveltime anisotropy gives an apparent fracture direction of N39^{o}E+/-8^o. This direction, however, is likely to be caused by the effect of dip. This is shown by the consistency of the dip direction and the predicted fracture orientation. If P-wave velocity/traveltime anisotropy is used to determine the fractures in fields, the dip effect must be small compared to the fracture-induced anisotropy.

The magnitude of the P-wave amplitude anisotropy is related to the crack density and physical properties, including the crack-filling fluids and the aspect ratio. For the reflection at the bottom of the first Frontier sand, the minimum-amplitude direction corresponds to the fracture-plane orientation. The corresponding fracture orientation is roughly along the east-west direction. At many CDP superbin locations, the inferred fracture orientation based on azimuthal variation of P-wave amplitude shows a large standard deviations. This results from a high level of noise in the amplitude data. Even in the blocks in which the inferred fracture orientation has a less than 20^o standard deviation, there are still a few anomalous directions of N45^{o}E and N45^{o}W. This effect can be caused by a combination of fracture-induced anisotropic attenuation effects, wave focusing and defocusing in anisotropic media, and heterogeity along the travel path. I recommend further work in understanding these other factors that contribute to the P-wave AVOZ. At this signal-to-noise ratio, we cannot identify the fluid content in the fractures. But the 3D P-wave AVOZ variation gives us the possibility of mapping the fracture direction over the 3D survey area.

The results of the theoretical modeling can be used as guidelines for seismic detection of fractures. In general, the amount of anisotropy in shear-wave splitting, P-wave velocity, and P-wave amplitude increases with the fracture density. The amount of shear-wave splitting does not depend on the fluid type and the seismic frequency range. P-waves are sensitve to the types of the fracture-filling fluids, the fracture aperture, the rock's Poisson's ratio, and the wave frequency. Crack-filling fluids with higher bulk moduli can induce lower P-wave velocity variation, but higher P-wave amplitude variation. When the Poisson's ratio of the unfractured rock is high and other conditions are the same, the shear-wave traveltime lag is larger, and the P-wave amplitude azimuthal variation is smaller.

4.7 References

Alford, R. M., 1986, Shear data in the presence of azimuthal anisotropy: Dilley, Texas, SEG 56th Annual Meeting Expanded Abstracts.

Davison, A. C., 1997, Bootstrap methods and its applications, Cambridge University Press, 582 p.

Greenhalgh, S.A., Mason, I.M., 1995, Orientation of a downhole triaxial geophone: Geophysics, **60**(4), 1234-1237.

Hardage, B.A., 1984, Vertical seismic profiling, London: Geophysical press.

Knowlton, K.B., Spencer, T. W., 1996, Polarization measurement uncertainty on three-component VSP: Geophysics, **61**(2), 594-599.

May, J., Mount, V., Krantz, B., Parks, S., and Gale, M., 1996, Structural framework of southern Powder River Basin: a geologic context for deep, northeast-trending basement fractures, ARCO-GRI fractured reservoir project report.

Queen, J.H., Rizer, W.D., 1990, An integrated study of seismic anisotropy and the natural fracture system at the Conoco borehole test facility, Kay county, Oklahoma, J. Geophys. Res., **95**, 11255-11273.

Winterstein, D.F., Meadows, M.A., 1991a, Shear-wave polarizations and subsurface stress directions at Lost Hills field, Geophysics, **56**, 1331-1348.

Winterstein, D.F., Meadows, M.A., 1991b, Changes in shear-wave polarization azimuth with depth in Cymric and Railroad Gap oil fields, Geophysics, **56**, 1349-1364.

CHAPTER 5

CAN SEISMIC IMAGING HELP TO QUANTIFY FLUID FLOW IN FRACTURED ROCKS?

5.1 Abstract

We investigate the type of subsurface fracture information that can be extracted from seismic shear wave analysis, show how rock physics and geostatistics can be combined to give realistic interpretations, illustrate the variability (non-uniqueness) in the interpretations by showing equally probable fracture predictions, and evaluate the uncertainty in rock physics interpretations by looking at the distributions of some simple fluid flow simulation results.

In the interpretation of fracture-induced seismic anisotropy, the uncertainties in the stiffness of the embedding rocks versus that of the fractures, in the number of fracture sets, in the fracture length distribution, and in the span of fracture orientations can give rise to ambiguity in fracture interpretation. We examine the impact of these uncertainties on fluid flow responses, and suggest additional information, beyond seismic, that can increase reliability of fluid flow predictions in fractured formations.

Our results show that seismic analysis can help to constrain predictions of the spatial distribution of fracture densities, which, in turn, have a very important impact on fluid flow responses. However, the inference of fracture densities from shear wave splitting analysis can be unreliable due to uncertainties about some key parameters, including fracture specific stiffness, fracture orientation, and background lithology

variations. The uncertainty in fracture orientation distribution does not affect significantly the final fracture density estimates. The common assumption that anisotropy is induced by a single set of parallel fractures can lead to misinterpretation of the fracture density field. In addition, the length and orientation distributions of the fractures are crucial factors determining connectivity of the fracture system and, therefore, have an important impact on fluid recovery. The uncertainties can be reduced by considering additional information about the subsurface fracture system such as that coming from analog outcrop data, geomechanical studies and production data. A reliable knowledge of the lithology of the matrix rock is also important.

5.2 Introduction

Seismic methods have been used in fracture detection for more than a decade. The shear wave splitting techniques (Alford, 1987), among many other techniques, is a fairly common and robust approach. Its field applications in 2D surface seismic (Mueller, 1991), 3D seismic (Lewis et al., 1991), dipole sonic log (Mueller, 1994), and multi-component VSP (Queen and Rizer, 1990, Winterstein and Meadows, 1991a, 1991b) have successfully detected elastic anisotropy and symmetry plane orientations, which correlate with observed fracture locations and orientations. Fracture detection using the P-wave velocity (Crampin, 1977) and amplitude (Rueger, 1997; Teng and Mavko, 1997; Tsvankin, 1997; Lynn et al., 1996), and shear wave amplitude (Thomsen, 1988; Kendall, 1996) have also been investigated.

The outcome of these seismic methods, however, is strictly speaking, maps of amount of anisotropy and symmetry plane directions. At best, they have been interpreted in terms of fracture density and average orientation. They do not lead to the details of the in situ fracture network distribution that controls the rock permeability distribution.

To get the subsurface fracture network distribution, we explore how to use the anisotropy in shear wave splitting data to control the geostatistical reconstruction of the subsurface fracture networks. We interpreted the shear wave anisotropy in terms of fracture density and orientation with Schoenberg-Muir's (1989) thin-layer fracture model. The fracture density mapping was used to guide the stochastic simulation of the subsurface fracture network. To demonstrate how our approach helped to gather the hydraulic features of the fracture network, we simulated the fluid flow in the fracture network. The results show a significant improvement over the pure statistical approach.

In practice, uncertainty about fracture stiffness, fracture orientation, number of fracture sets, and unfractured rock matrix properties results in uncertainty in fracture density predictions. The unknown fracture length distribution also leads to non-unique realizations of the fracture system. We analyzed the impact of these uncertainties on fluid flow predictions, and suggests additional information which can help to reduce these uncertainties.

5.3 Procedures

We begin with an observed image of an in-situ fracture network. The shear wave velocities are calculated to represent the results of a synthetic seismic shear wave survey over the site. With the synthetic data, the uncertainties of extracting actual fracture information from seismic data can be examined without the complication of field-data noise and measurement errors. We then interpret the shear wave velocities in terms of fracture density, stochastically simulate the fracture networks that are consistent with these densities, and perform fluid flow simulation to evaluate the flow properties of the seismically constrained fracture networks. By comparing the fluid flow results of the true fracture system with those from simulated fracture networks, we examine to what extent shear wave survey can help in constraining fluid flow predictions in fractured reservoirs.

5.3.1 Reference Fracture Image

The reference fracture system is taken from an image (Figure 5.1) of an exposed outcrop pavement exhibiting two distinct fracture sets. A first set is oriented roughly along the North-South direction (Set I), and a second is aligned in the East-West direction (Set II). The horizontal section considered is approximately 136 meters by 52 meters. The fractures were first delineated on the photograph, then scanned and transformed to pixel format. The resolution necessary to render the fractures visible is 544 by 208 pixels. This is the resolution of the grid on which the fractures will be simulated. Each pixel represents a 0.25 meter by 0.25 meter square.

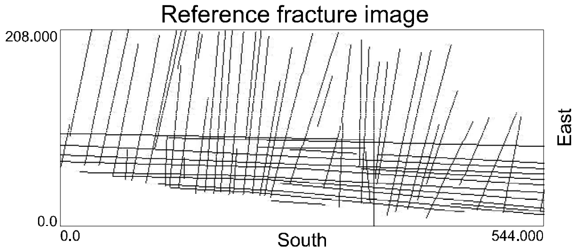

Figure 5.1: Reference fracture image digitized from a photograph of an exposed outcrop.

5.3.2 Seismic Modeling and Shear Wave Analysis

Because most fractures in Figure 5.1 are longer than the seismic wavelength, to calculate the elasticity of the fractured rocks, we chose to use the finely layered model given by Schoenberg and Muir (1989) rather than the penny-shaped crack models (Hudson, 1981, 1990; Thomsen, 1993). When a rock block with dimension L contains N parallel through-cutting fractures perpendicular to the 3-axis (Figure 5.2a), the rock's shear stiffnesses can be expressed as:

$$C_{44} = \frac{m}{1 + E_T} \tag{5.1a}$$

$$C_{66} = m$$

where m is the shear stiffness of the unfractured rock, C_{66} is the rock’s stiffness for shear wave propagating and polarizing in the fracture plane, C_{44} is for shear wave propagating or polarizing perpendicular to the fracture plane, and E_r is given by

$$E_T = \frac{N}{L}\frac{m}{k_T} \tag{5.1b}$$

The fracture shear specific stiffnesses k_T describes the rate of change of the shear stress with respect to the fracture’s shear displacement.

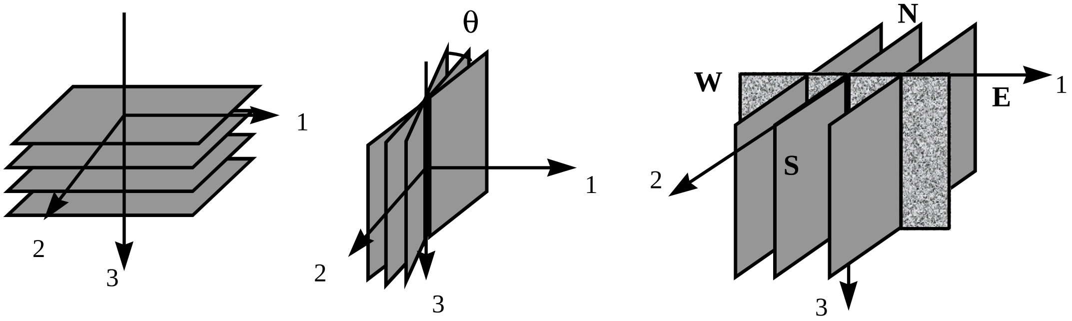

(a) (b) (c)

Figure 5.2: (a) Diagram of a set of parallel fractures in Cartesian coordinates; (b) diagram of a set of fractures uniformly distributed within a angle range in Cartesian coordinates; (c) diagram of two sets of vertical fractures in Cartesian coordinates. (c) illustrates the orientation of the reference fractures in a 3D plot.

The shear wave weakly anisotropic parameter g (Thomsen, 1986) indicates the amount of shear wave splitting, and can be expressed as a function of fast (V_{S-fast}) and slow (V_{S-slow}) shear wave velocities:

$$g = \frac{C_{66} - C_{44}}{2C_{44}} = \frac{E_T}{2} \approx \frac{V_{S-fast} - V_{S-slow}}{V_{S-slow}} \tag{5.2}$$

where

$$V_{S-fast} = \sqrt{C_{66} / r} \qquad (5.3)$$
$$V_{S-slow} = \sqrt{C_{44} / r}$$

r is the bulk density of the rock.

When multiple sets of fractures are present in a rock, their impact can be approximated by a linear summation of compliances of each set. One scenario is that fractures are uniformly distributed within an angle range q as shown in Figure 5.2b. By integrating the fracture-induced compliance change, we get the corresponding elasticity of a fractured rock as:

$$\mathrm{C}_{55} = \frac{m}{1 + \mathrm{E}_{\mathrm{T}}\left(\frac{1}{2} + \frac{\sin q}{2q}\right)} \qquad (5.4)$$

$$\mathrm{C}_{44} = \frac{m}{1 + \mathrm{E}_{\mathrm{T}}\left(\frac{1}{2} - \frac{\sin q}{2q}\right)}$$

Note that as q approaches zero, the shear wave moduli approach the parallel fracture limit given by equation (5.1). Figure 5.2c illustrates the 3D image of the fracture system as previously shown in Figure 5.1. In this coordinate system we can express the shear wave moduli as:

$$\mathrm{C}_{55} = \frac{m}{1 + \mathrm{E}_{\mathrm{T1}}\left(\frac{1}{2} + \frac{\sin q_1}{2q_1}\right) + \mathrm{E}_{\mathrm{T2}}\left(\frac{1}{2} - \frac{\sin q_2}{2q_2}\right)} \qquad (5.5)$$

$$\mathrm{C}_{44} = \frac{m}{1 + \mathrm{E}_{\mathrm{T1}}\left(\frac{1}{2} - \frac{\sin q_1}{2q_1}\right) + \mathrm{E}_{\mathrm{T2}}\left(\frac{1}{2} + \frac{\sin q_2}{2q_2}\right)}$$

where q_1 and q_2 are the angular range of fracture orientations for Set I and Set II, and E_{T1} and E_{T2} are given by equation (5.1b) for Set I and Set II, respectively.

We divide the survey area into 8 by 4 blocks. Each block represents a bin or super bin in a 3D seismic survey. The bin size is 17 meters by 13 meters (68 pixels by 52 pixels). The fracture density and angle distribution of Set I and Set II can then be counted for each bin. Figure 5.3 shows the fracture density count and angle distribution derived from Figure 5.1. We model the shear moduli and velocities for vertically propagating shear waves polarized along the N-S and E-W directions with equations (5.3) and (5.5), and the corresponding shear anisotropic parameter using equation (5.2). The fracture specific shear stiffness is chosen to be 25 MPa/mm such that the calculated shear wave anisotropy over the fracture zone is around 5% to 15%. The properties of the background unfractured rock are the lab measurements of a low-porosity and low-permeability sandstone:

P-wave velocity: 4.67 km/s
S-wave velocity: 3.09 km/s
density: 2.53 g/cm3
porosity: 3.5%
permeability: 0.66 mD

Figure 5.4 shows the modeling results of the shear wave moduli, velocities for the N-S and E-W polarizations, and the anisotropic parameter. We take these as the "observed" seismic parameters, which we will interpret for fracture distribution.

To infer the fracture density (number of fractures per block), we assume that the velocity change is induced by two sets of vertical sub-parallel fractures along the N-S and E-W azimuths respectively, and that the values of the unfractured rock properties are known. We estimate the fracture density assuming strictly parallel fractures, and refer to this interpretation as Case 1. Figure 5.5 shows the integer part and the residual decimal part of the fracture number per block separately, since the stochastic fracture simulation model considers only an integer number of fractures per block. The integer part of the density is exactly the same as the true density map as expected. The decimal part of the fracture number in each block is the result of the parallel fracture assumption; it is much smaller than the integer part, and can therefore be ignored. Since in reality, we may not have precise information of fracture orientation and embedding rock properties, the density estimation can be ambiguous and non-unique. We will discuss this in more detail later in this paper.

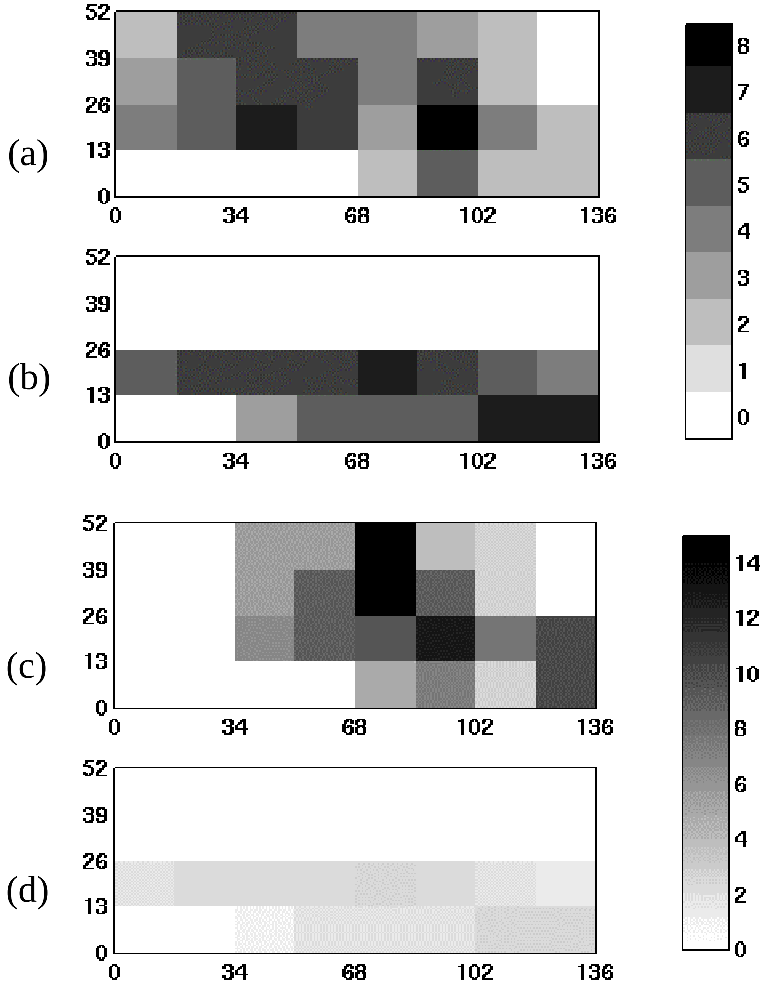

Figure 5.3: Fracture density maps of the reference fracture image for (a) Set I and (b) Set II; azimuth spread maps (degrees) for (c) Set I and (d) Set II in each block consisting of 68 by 52 pixels (17m by 13m).

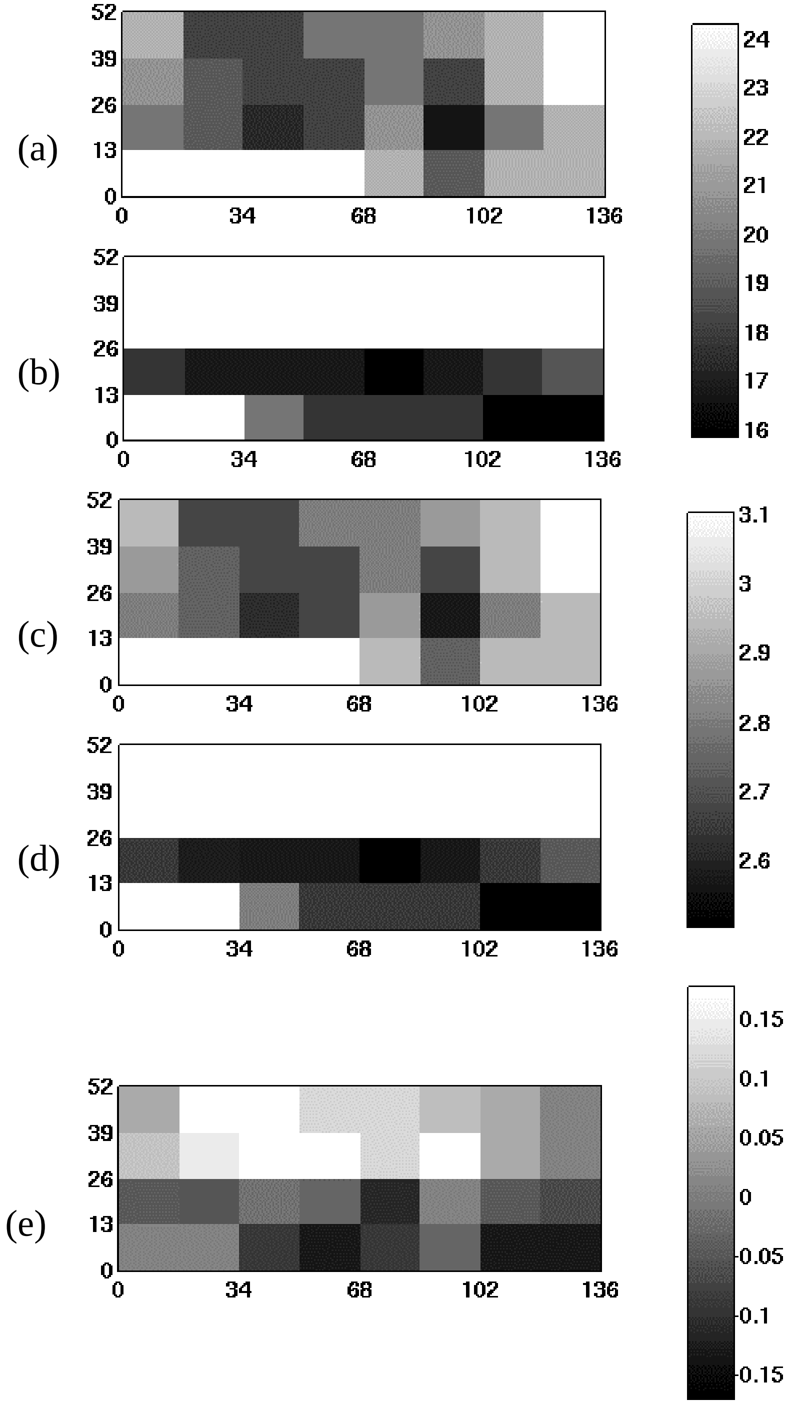

Figure 5.4: Forward modeling results of (a) shear wave moduli (GPa) and (c) velocities (km/s) for vertical propagating shear wave polarized along the E-W direction, (b) shear wave moduli and (d) velocities for shear waves polarized along the N-S direction, (e) shear wave anisotropic parameter.

5.3.3 Fracture Network Simulation

An algorithm to stochastically simulate discrete fractures in layered reservoirs has recently been developed by Gringarten (1997). It is based on geomechanical rules of fracture propagation and aims to account for various types of information about the fractures in the subsurface.

The information required by the model to simulate fracture propagation are fracture density and orientation for each fracture set to be simulated and rules for timing relations (chronological order of appearance) between the different sets. A more detailed description of the algorithm can be found in Gringarten (1997).

We simulated the fracture networks based on the seismically-determined fracture density estimates shown in Figure 5.5. The fracture simulation model, being stochastic, generates multiple equiprobable realizations of the fracture system. This is critical, since seismic data can yield fracture density, but rarely image individual fractures. Figure 5.6 shows four simulated fracture images, all consistent with the seismically-determined fracture density map given in Figure 5.5. The fractures are assumed to be vertical, strictly parallel and aligned with the N-S (Set I) and E-W (Set II) directions. The extent of the fractures is guided by the spatial distribution of the fracture density. Uncertainty in the maximum extent of the fractures will be discussed later in the paper.

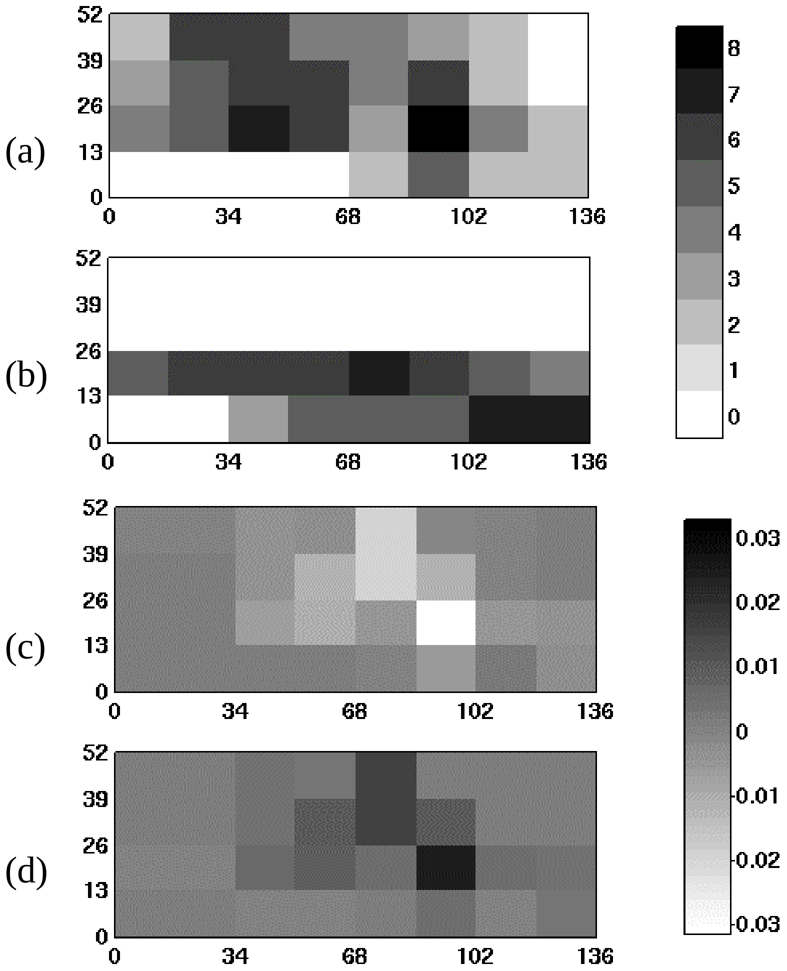

Figure 5.5: Fracture density estimation for Case 1 (parallel fracture assumption): (a) integer part for Set I; (b) integer part for Set II; (c) residual decimal part for Set I; (d) residual decimal part for Set II.

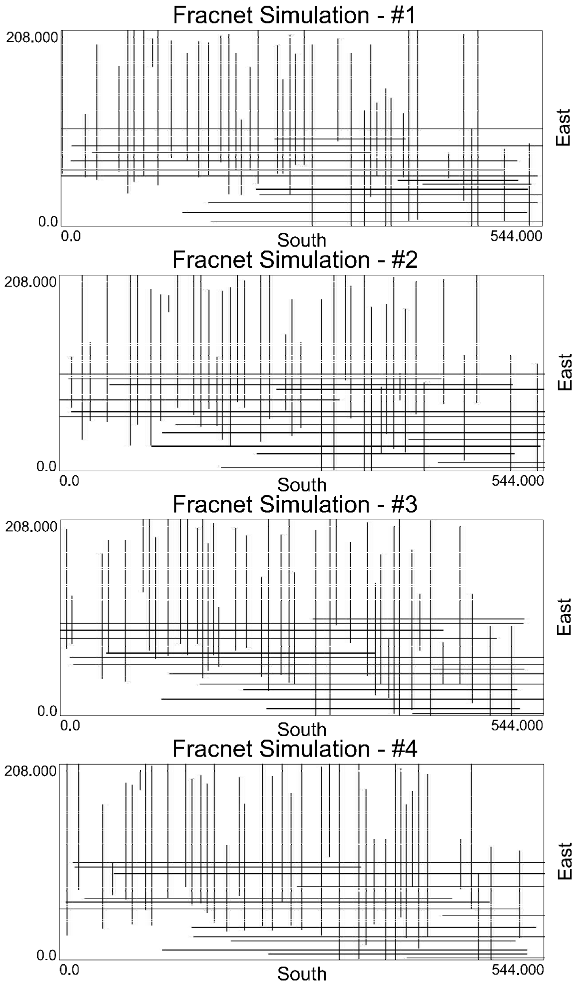

Figure 5.6: Four equiprobable realizations of the fracture system for Case 1 assuming parallel fractures for both sets.

5.3.4 Fluid Flow Simulation

In order to evaluate the flow characteristics of the fracture systems, we simulated the single-phase flow through the reference image and the simulated fracture networks by using the streamline simulation code **3dsl** (Batycky et al., 1997). This code differs from traditional finite-difference flow simulators by decoupling the full 3D problem into multiple 1D problems along streamlines. The geometry of the streamlines are defined by the permeability variations and the well conditions. The fluids are moved along the streamlines rather than through an arbitrarily discretized grid. Streamline flow simulators are much faster and have been shown to be as or more accurate than conventional flow simulators in certain situations. The speed enables rapid processing of multiple alternative high resolution reservoir models. A thorough presentation of streamline simulation can be found in Batycky et al. (1997) and Thiele (1996).

We will look at tracer flow through the simulated fracture systems. The fluid injected has identical properties to the one originally in place. The fluids are assumed incompressible. Therefore, the flow responses will only be affected by variations in permeability values and not by the fluid properties. Tracer flow is thus well suited to investigate the effects of permeability heterogeneity.

An injector well was placed on the left edge of the grid, and a producer well at the right side. Tracer is injected at a constant pressure of 2000 psi. Production is set at the constant rate of approximately 0.01 pore volume per day. An analytical mapping of the tracer flow solution along the streamlines was used. The background matrix rock has a constant porosity of 3.5% and permeability of 0.66 mD. We assumed that the fractured rock pixels have a constant permeability of 100 mD, and a constant porosity of 3.5%, similar to the porosity of the matrix to emphasize the effect of permeability contrast. Figure 5.7 shows an example of the tracer saturation profile through the reference fractured rock after 0.5 pore volume of tracer has been injected. The straight front is due to the homogeneity of the matrix.

Two flow responses are considered: recovery of fluid initially in place and production of injected tracer. Recovery indicates the sweep efficiency through the fracture network, and tracer-cut response gives an idea of the connectivity of the fracture network.

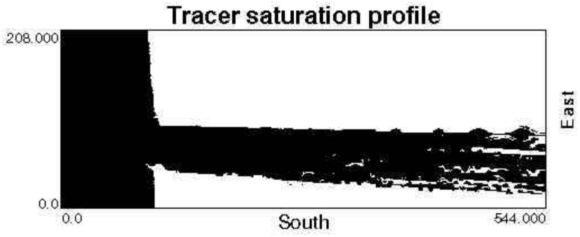

Figure 5.7: Tracer saturation profile after breakthrough through the fractured formation containing the reference fracture network.

Note that the streamline simulator does not account explicitly for any sort of matrix-fracture interaction. This may be an a-priori drawback of the method when applied to fractured reservoirs, however, it may be sufficient in some cases to mimic flow through fractured rocks, particularly if one assumes that changes in the pressure field are dominated by variations in permeability as is the case here. Further discussion can be found in Gringarten (1997).

We simulate flow through the reference fracture network shown in Figure 5.1 and through various simulated fracture networks. Fluctuations are expected from multiple equiprobable realizations. As an example, we generate 50 equiprobable realizations similar to the ones shown in Figure 5.6. Flow simulations are performed on all 50 images. The resulting responses are shown in Figure 5.8 along with the flow responses of the reference image. The true responses fall within the predicted range of simulated responses. We will consider only a single realization of the fracture networks for each of the scenarios retained for the uncertainty analysis in the next section of the paper.

We also compute the effective permeability values in the E-W direction using a simple single-phase pressure solver, considering a constant pressure difference across the E-W direction, and no-flow boundaries on the other faces. These effective permeability will gives us some indication on the global behavior of the fractured rock. The effective permeability computed for the reference case is 3.2 mD.

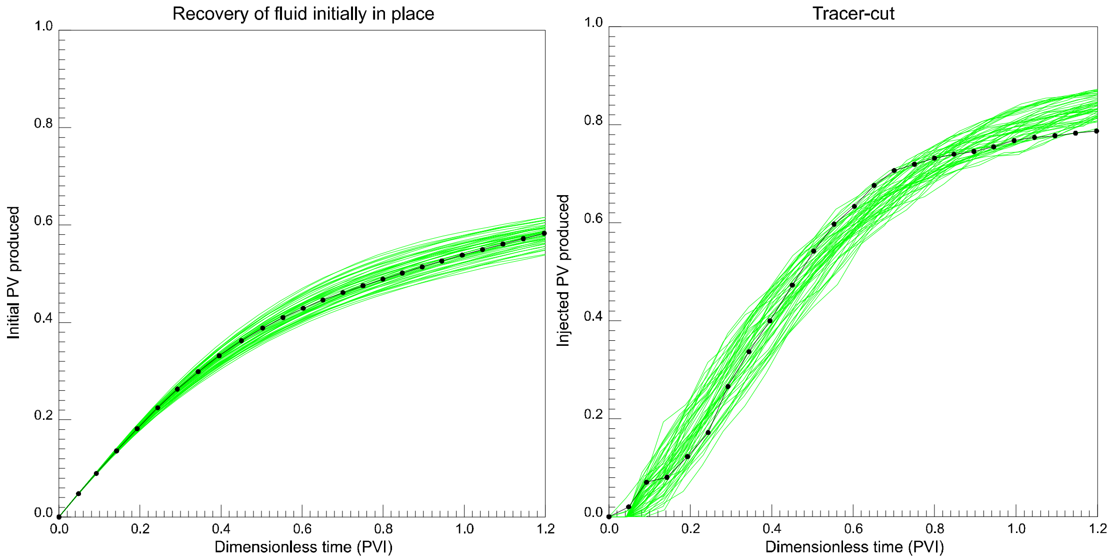

Figure 5.8: Recovery and tracer-cut responses for 50 equiprobable simulations (gray lines) along with the responses of the reference image (black line).

5.4 Uncertainty in Interpretation of Seismic Data for Fractures

To generate the fracture images shown in Figure 5.6, we assumed that we have some prior knowledge of the fracture specific stiffness, the background rock properties, the orientation of the fractures, and the maximum extent of the fractures. In practice, these are poorly known. We investigate how the uncertainty in these parameters may change the fluid flow responses in the fractured rock by simulating a fracture network for each uncertainty assumption, and by processing this simulated network through the flow simulator **3dsl**. A complete study should include several realizations for each case to account for the fluctuations in the stochastic fracture simulations as done for Figure 5.8. This was not done here to emphasize the impact of varying certain key parameters. However, each simulation was generated using the same random seed number.

5.4.1 Unknown Fracture Stiffness

Equation (5.1) shows that the fracture density is inversely proportional to the fracture specific stiffness. Barton and Bandis (1982) collected the shear stiffness of rock joints of 650 data points from 35 sources, including those from tilt or push tests, and those derived from earthquake events reviewed by Nur (1974). The fracture stiffness ranges from 0.001 MPa/mm to above 100 MPa/mm. Pyrak-Nolte, Myer, and Cook (1992) used 10^4 MPa/mm fracture shear stiffness to explain their lab ultrasonic measurements. These stiffness values cover a tremendous range. Overestimation of stiffness will cause overestimation of fracture density, and vice versa. We consider the case where the fracture stiffness is 50 MPa/mm (Case 2). This stiffness is chosen to be close to the reference case fracture stiffness 25 MPa/mm in order to simulate the fracture network without changing to a finer grid. Twice the amount of the original fractures (Figure 5.9a and 5.9b) are necessary to yield the same shear wave velocity responses (Figure 5.4). A corresponding possible fracture simulation is shown in Figure 5.9c. An additional parameter, which we have not considered, is that larger fracture stiffness will probably correlate with lower fracture permeability.

Comparing the flow simulation results for Case 1 and 2 in Figure 5.10, we see that Case 2 will yield a lower recovery of fluid initially in place, because more injected fluid is channelized in the fractures and thus less tracer sweeps the matrix. When producing at a constant rate, Case 2 shows a later breakthrough time than Case 1, because the same amount of injected tracer is separated through a larger number of fractures. However, shortly after breakthrough, more tracer appears at the producing well compared to Case 1, creating a much higher tracer-cut.

The effective permeability of the fractured rock obtained by imposing a constant pressure drop across the whole domain is as expected, much higher (about twice) for Case 2 (9.8 mD) than for Case 1 (5 mD), entailing much faster flow through the whole system.

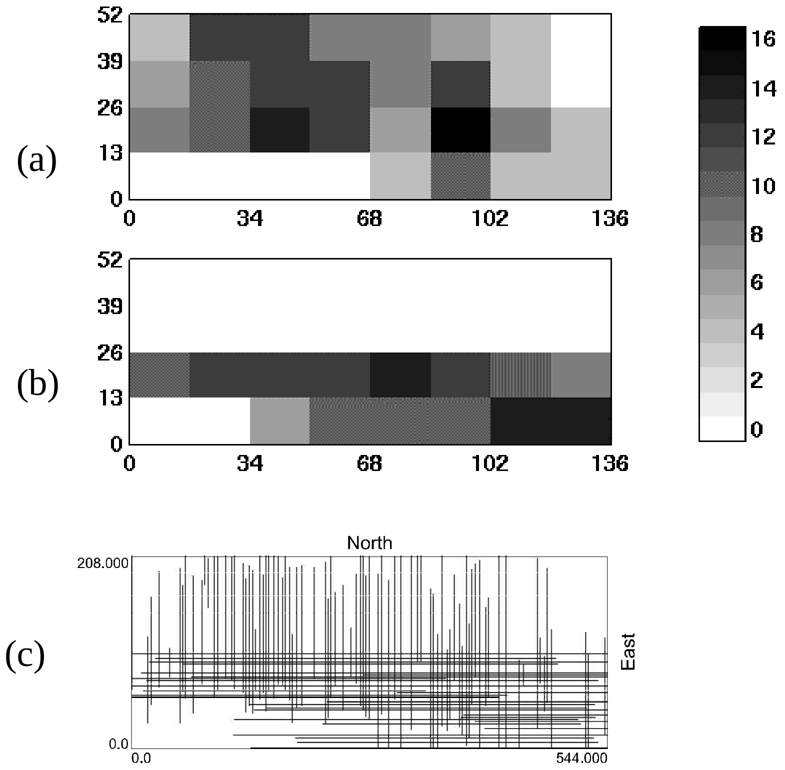

Figure 5.9: Fracture density maps for Case 2 for (a) Set I and (b) Set II assuming that the fracture shear specific stiffness is 50 MPa/mm; (c) simulated fracture network based on the density maps in (a) and (b).

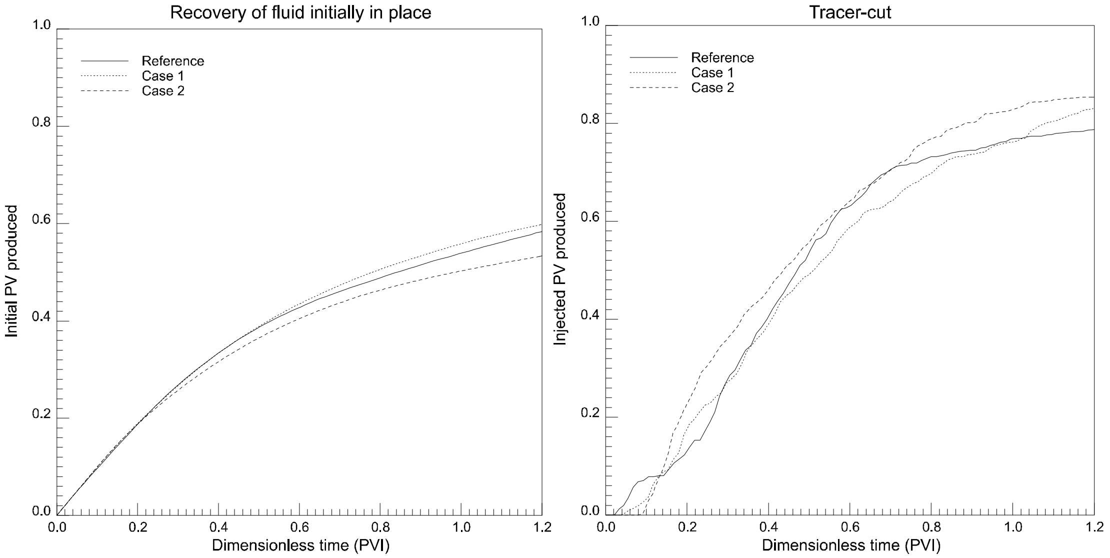

Figure 5.10: Recovery and tracer-cut responses for Case 1 and Case 2.

5.4.2 Unknown Fracture Orientation

In the previous seismic velocity inversion, we assumed parallel fractures. The true fracture image has small variations of orientation. The variations are not distinguishable seismically. To evaluate the parallel fracture-assumption, we simulate the fracture networks by taking the true fracture angle distribution (Figure 5.3c and d) into account (Case 3). The seismic velocity inversion results using equation (5.5) yield little variation in density predictions, compare Figures 11a and b with Figures 3a and b. The simulated fracture image in Figure 5.11c is similar to the true image, and as could be expected from this visual judgment, the flow results for this image and the reference are almost the same, see Figure 5.14.

Larger fracture strike angle distribution has been observed at many sites (Mueller, 1991; Lauback, 1992; Lorenz, 1992; Barton and Zoback, 1992). Instead of having a true angle distribution map, we may also assume that the fractures have a uniform orientation distribution between -10° and +10° azimuth for Set I, and between +80° and +110° azimuth for Set II (azimuth 0° is strict North, and the azimuth angle is measured clockwise). Using equation (5.5), and assuming that both θ_1 and θ_2 are 20°, we obtain the fracture density map shown in Figure 5.12. As in Case 1, the residual decimal part of the fracture density is much smaller than the integer part, and can be ignored. Comparing the fracture density with that of the true fracture image, we notice that a small angle distribution 20° will barely affect the density estimation. This can lead to two types of simulated fracture images if we assume that: 1) the fractures within a set follow an orientation field and cannot intersect (Case 4), or 2) that the fractures are perfectly straight, with different orientations, and can intersect each other (Case 5). The simulated images are shown in Figure 5.13a for Case 4 and in Figure 5.13b for Case 5. This drastic difference in angle distribution as compared to the reference image has a large impact on fluid flow predictions, see Figure 5.14. For production at a constant rate, the tortuosity of the fracture system greatly retards tracer breakthrough. However, it forces a larger sweep of the fluid initially in the matrix as can be seen on the recovery curve. Surprisingly, there is very little difference between the responses of Cases 4 and 5, though a later breakthrough can be observed for Case 4, because its fractures are much less connected.

The large variability in fracture orientation is also seen to reduce the effective permeability of the fractured rock in Case 4 (2.7 mD) and Case 5 (2.7 MD), and even in the reference case (3.2 mD) where the fracture orientation is less variable than in Cases 4 and 5, but more than in Case 3 (4.9 mD).

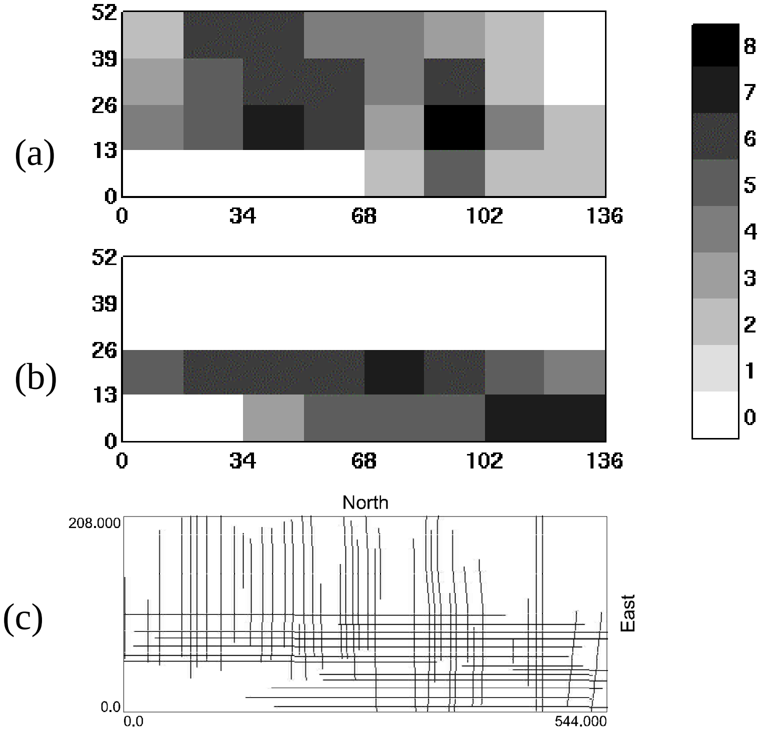

Figure 5.11: Fracture density maps for Case 3 for (a) Set I and (b) Set II by taking the true fracture angle distribution into account; (c) simulated fracture network based on the density maps in (a) and (b) and the true fracture angle distribution.

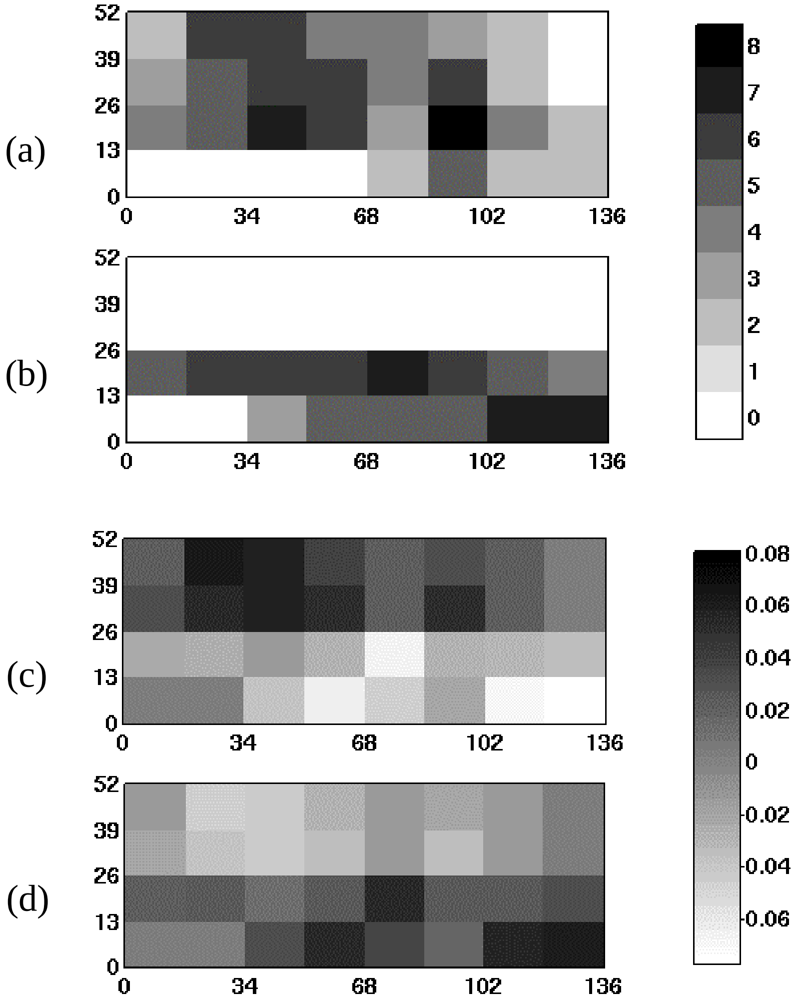

Figure 5.12: Fracture density maps for Case 4 and 5 assuming 20° angle distribution for (a) integer part of Set I; (b) integer part of Set II; (c) decimal part of Set I; (d) decimal part of Set II.

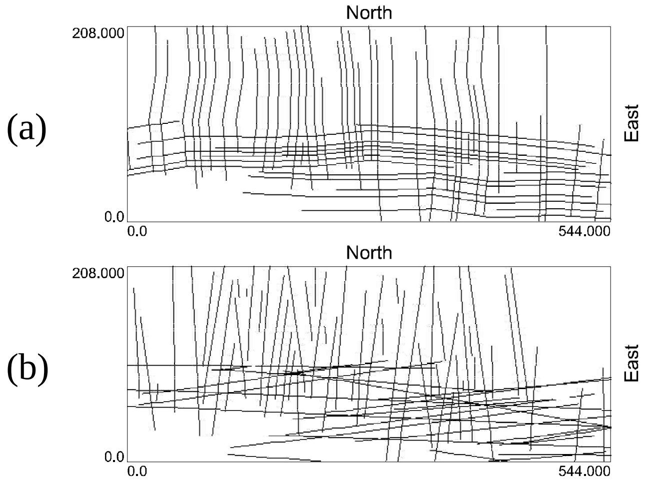

Figure 5.13: Simulated fracture networks for (a) Case 4 and (b) Case 5.

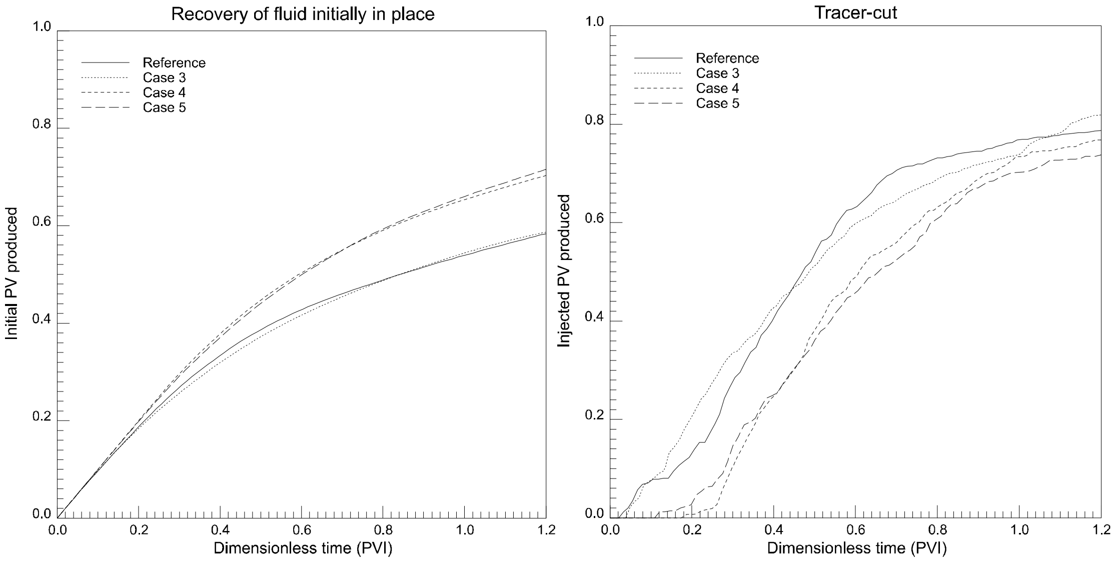

Figure 5.14: Recovery and tracer-cut responses for Cases 3, 4, and 5.

5.4.3 Unknown Number of Fracture Sets

In shear wave splitting analysis, a common assumption is that the anisotropy in shear wave velocity is caused by only one set of parallel fractures. While outcrops, cores, FMS FMI images often show multiple fracture sets (Nelson, 1985; Barton and Zoback, 1992), practitioners often take the fast shear wave velocity to be that of the unfractured rock matrix, and map the shear wave splitting amount into fracture density using equation (5.2). This assumption leads to the fracture density estimations shown in Figure 5.15a and 5.15b (Case 6). We can see that the fracture density predictions in the upper part of the grid, where Set II is absent, are the same as the reference density. But the lower part of the density map gives a much smaller density prediction since the anisotropy effects of the two fractures sets are perpendicular and partly cancel out. The subsequent fracture simulation is presented in Figure 5.15c, and the flow simulation results are shown in Figure 5.16.

Visually, the simulated image is very different from the reference image, and as could be expected, has a lower effective permeability (2.5 mD as compared to 3.2 mD for the reference system) due to the lack of connectivity in the image. This also entails a later breakthrough. A higher recovery can also be observed since more tracer is pushed through the matrix. The lower tracer-cut of Case 6, as compared to the reference case, can be explained by the fact that less fractures are connected to the producing well, yielding a lower influx of tracer.

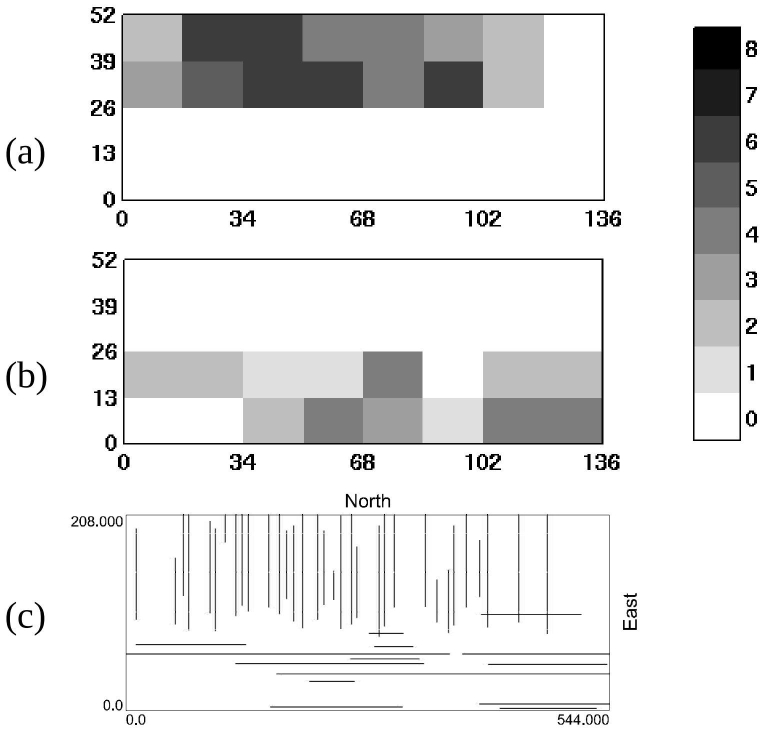

Figure 5.15: Fracture density maps for Case 6 for (a) Set I and (b) Set II; (c) simulated fracture network based on the density maps in (a) and (b).

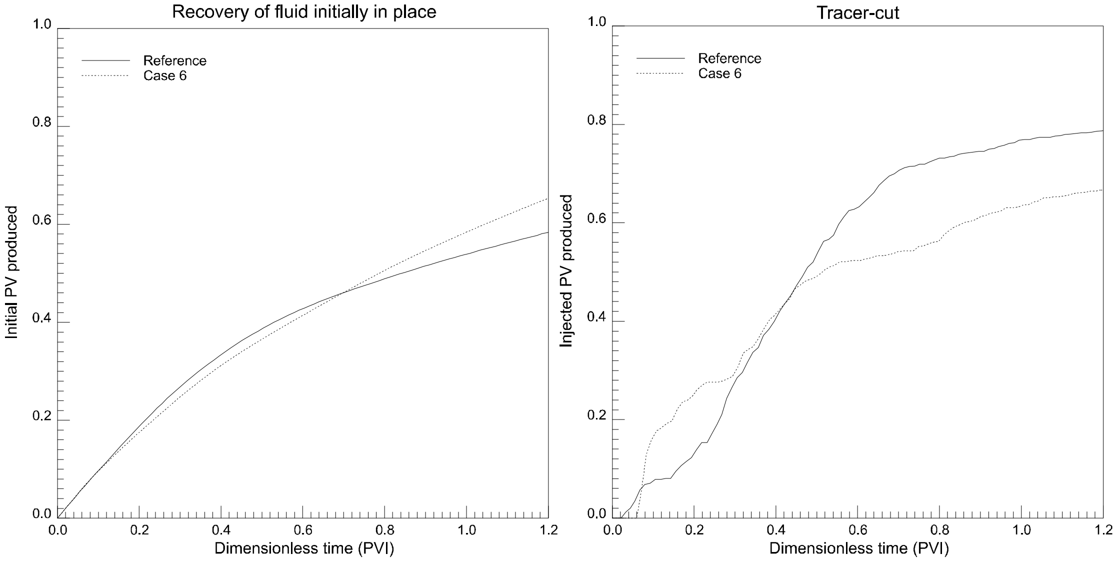

Figure 5.16: Recovery and tracer-cut responses for Case 6.

5.4.4 Unknown Lithologic Variations

Uncertainty in background rock properties can also propagate into the fracture density estimations. Figure 5.17 shows a set of lab measurements of P- and S-wave velocities of tight gas sandstone under 40MPa effective pressure (Jizba, 1991). Under this high pressure, most of the fractures are closed. The velocity variations are due to the lithology variation. If we do not take the lithology variation into account, but use a constant unfractured rock velocity, we will overestimate or underestimate the fracture density. To illustrate this (Case 7), we assume that instead of having a constant velocity background, the embedding rock velocity shown in Figure 5.18 is spatially varying. It increases from West to East with small random increments. The total velocity change is about 20%. We calculate the shear wave moduli and velocities of the corresponding fractured rock as shown in Figure 5.19. The spatial variation in the moduli and velocities of the fractured rock is partly due to the embedding rock velocity variation, and partly to the spatial distribution of the fractures. If, in the velocity inversion process, we assume the background variation known, the results will be the same as in Case 1. However, if the background velocity information is only available in the middle block of the southern edge of the survey area, we have:

P-wave velocity: 4.67 km/s
S-wave velocity: 3.09 km/s
density: 2.53 g/cm3

We can estimate the fracture density by assuming that the background rock over the whole area has the measured velocities. By comparing the true density maps with the seismically derived density maps shown in Figure 5.20 under the assumption of constant background velocity, we can see that we overestimate the fracture density to the west where the background velocity is lower, and underestimate fracture density to the east where background velocity is higher. Figure 5.20c shows the simulated fracture system. However, the flow responses for Case 7 and for the reference image are very similar, see Figure 5.21. The increase in estimates of fracture densities is not sufficient to affect the connectivity of the network and therefore barely impacts recovery and tracer-cut responses. The addition of the connected fractures, however, increases the effective permeability of the system to 5.6 mD vs. 3.2 mD for the reference field.

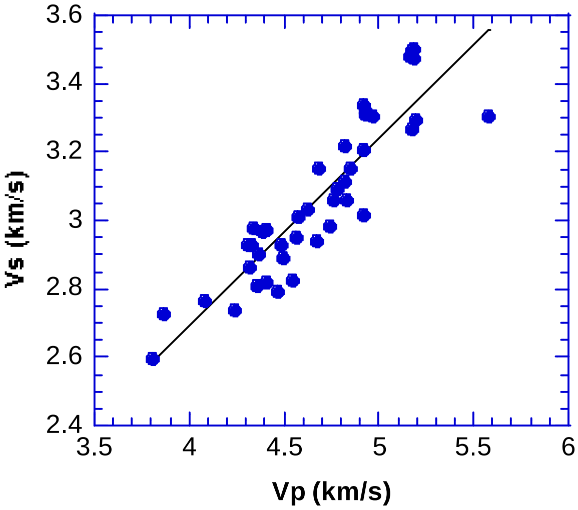

Figure 5.17: Lab measurement of P- and S-wave velocities of tight gas sandstone samples under 40 MPa effective pressure. The data are from Jizba (1991).

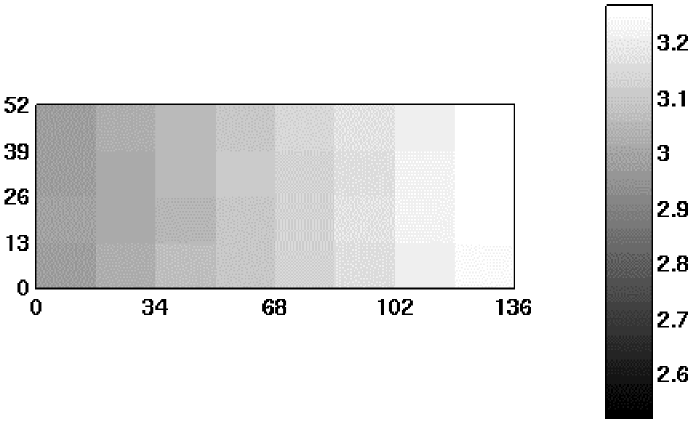

Figure 5.18: Velocity map (km/s) of the background unfractured rock for Case 7. The velocity spatial variation in the E-W direction is about 20% with a small random variation along the N-S direction.

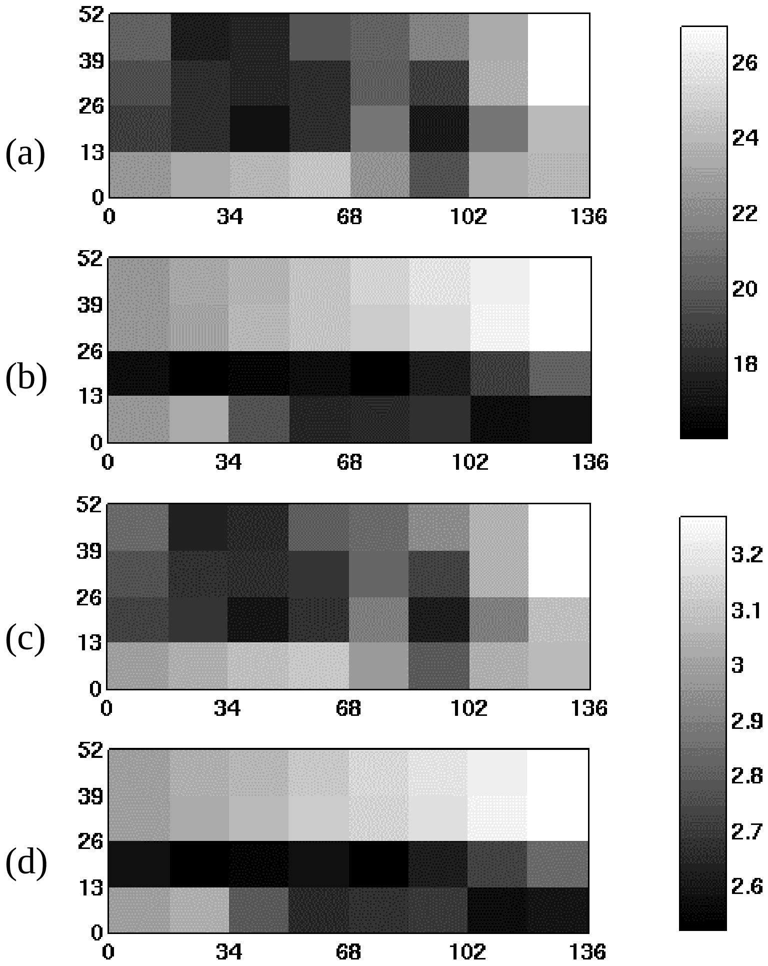

Figure 5.19: The shear wave moduli (GPa) and velocities (km/s) of the fractured formation for Case 7. (a) shear modulus for E-W polarization; (b) shear modulus for N-W polarization; (c) shear wave velocity for E-W polarization; (d) shear wave velocity for N-S polarization.

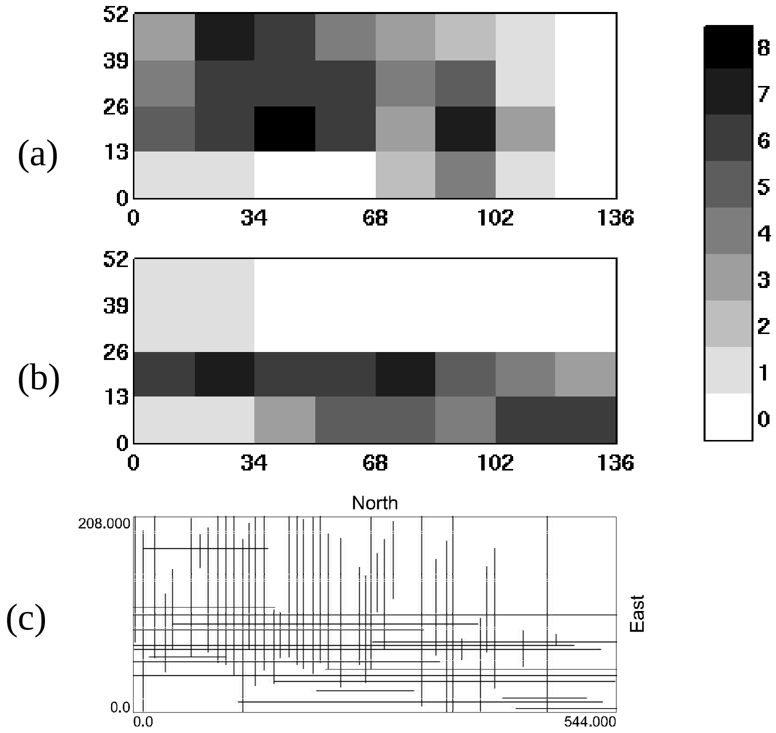

Figure 5.20: Density maps for Case 7 for (a) Set I and (b) Set II, (c) simulated fracture network based on the density maps in (a) and (b).

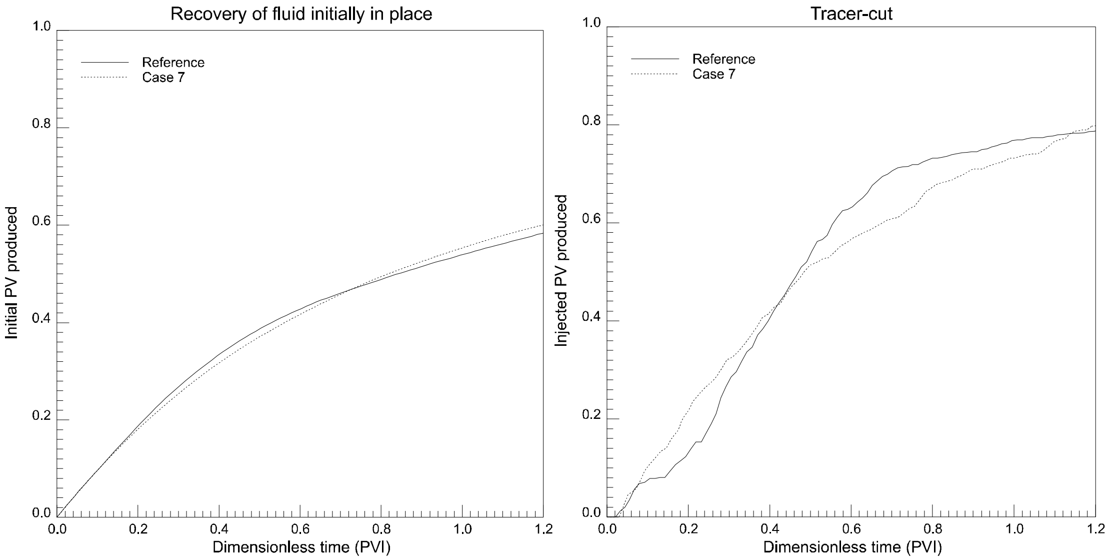

Figure 5.21: Recovery and tracer-cut responses for Case 7.

5.4.5 Unknown Fracture Length

In addition to fracture density, fracture length is another important controlling factor in stochastic fracture simulation, though it is not a requirement of the fracture simulation algorithm. We have assumed that the fracture length does not have an upper or lower bound, but instead that it is guided by the spatial distribution of the fracture density. Lauback (1992) showed that the outcrop fracture traces can have various length. If we have reasons to believe that the fractures have a maximum possible length, the fracture simulation will yield different images. By assuming the maximum fracture length to be 7.5 meters or 30 pixels (Case 8), 22.5 meters or 90 pixels (Case 9), and 45 meters or180 pixels (Case 10), we generate the fracture images shown in Figures 22a to 22c.

The shorter fractures of Case 8 do not enable connectivity through the fracture system. This entails a large sweep of the matrix shown by a high recovery, and a slow tracer movement through the system shown by a late breakthrough at about 0.4 PVI (pore volume of tracer injected), see Figure 5.23. In comparison, the longer fractures of Cases 9 and 10 yield a connectivity similar to the one of the reference system as shown by similar flow response curves. Slightly later breakthrough, compared to that of the true response, can be observed and is due to the more tortuous paths taken by the tracer in the connected fracture network.

The effective permeability of Cases 9 and 10 are similar (4.4 mD and 4.9 mD, respectively); the one of Case 8 is lower at 2.1 mD.

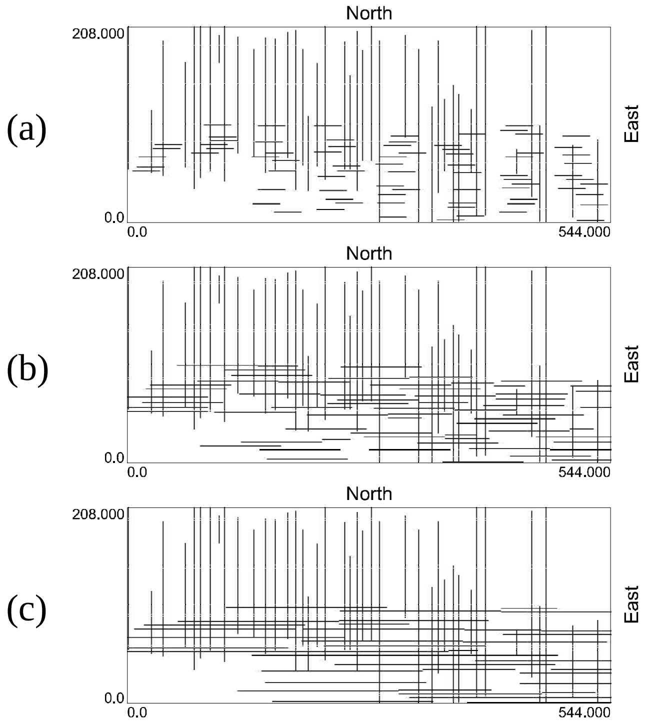

Figure 5.22: Simulated fracture networks: (a) Case 8 - maximum fracture length is 7.5 m (30 pixels); (b) Case 9 - maximum fracture length is 22.5 m (90 pixels).; (c) Case 10 - maximum fracture length is 45 m (180 pixels).

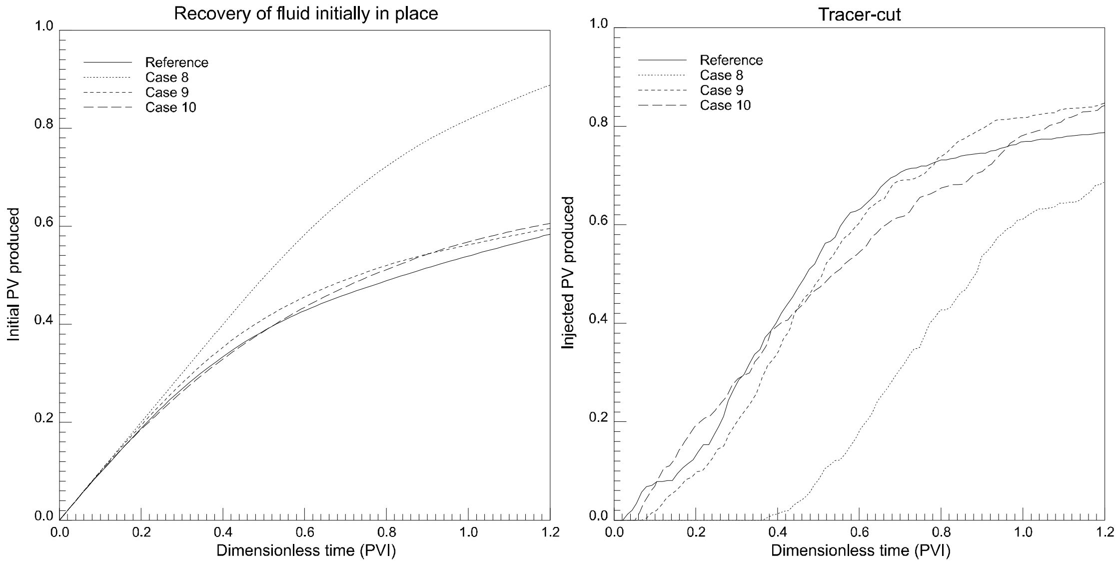

Figure 5.23: Recovery and tracer-cut responses for Cases 8, 9, and 10.

5.4.6 Multiple Uncertainty Sources

In practice, all of the sources of uncertainty appear simultaneously. We present a simple example to illustrate the possible complications that can be expected in field studies.

For example, the fracture length and fracture orientation can simultaneously affect the behavior of the fracture system. Consider the case where only the fractures of Set II are present in the rock (Case 11). With the parallel fracture assumption and no maximum length constraint, we obtain the fracture image shown in Figure 5.24a. With 20° azimuth spread, and different maximum lengths, 7.5 m (Case 12), 22.5 m (Case 13), and 45 m (Case 14), we obtain the fracture simulations shown in Figure 5.24b to Figure 5.24d.

The flow responses of Case 11, shown in Figure 5.25, are extremely similar to the reference. This is due to the fact that a similar number of fractures connect the injector to the producer. This means that the fractures of Set I are of secondary importance for this well configuration, and that modeling efforts should focus on the fractures of Set II. However, if the fractures were shorter, the flow responses would be drastically different as can also be seen in Figure 5.25.

The effective permeability can also be greatly reduced: 0.9 mD for Case 12, 1.7 mD for Case 13, and 1.9 mD for Case 14, vs. 3.2 mD for the reference network.

5.5 Discussion

Variability in estimated flow responses can be reduced if the simulation of fractures is well constrained. The simulated fracture networks depend greatly on the estimation of fracture densities. In turn, variations in fracture density estimates have a very important impact on fluid flow responses.

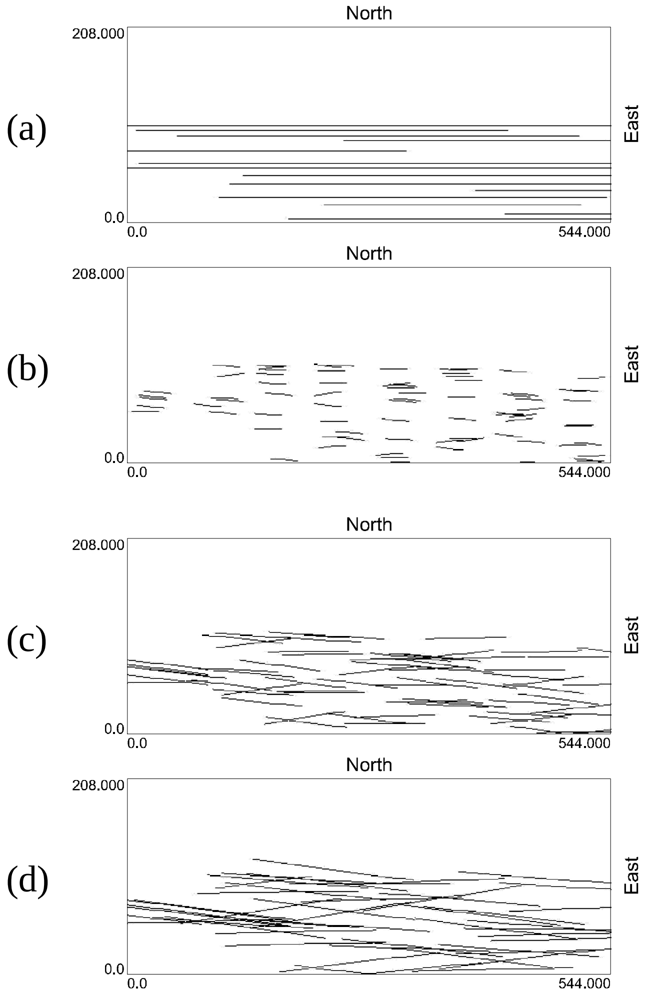

Figure 5.24: Simulated fracture networks:

(a) Case 11 - no length constraint, parallel fractures.

(b) Case 12 - maximum fracture length is 7.5 m; azimuth spread is 20°.

(c) Case 13 - maximum fracture length is 22.5 m; azimuth spread is 20°.

(d) Case 14 - maximum fracture length is 45 m; azimuth spread is 20°.

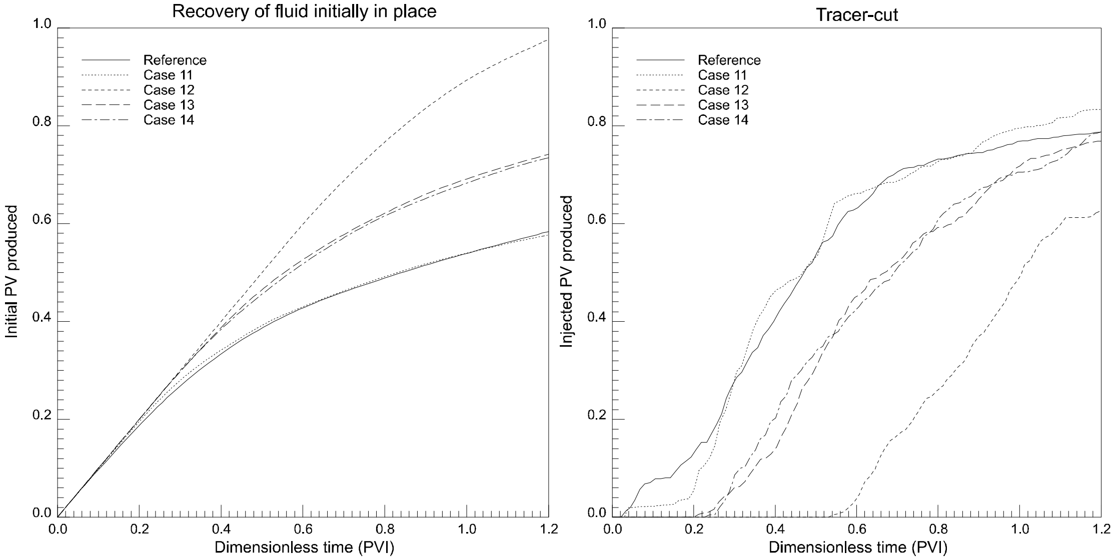

Figure 5.25: Recovery and tracer-cut responses for Cases 11, 12, 13, and 14.

Seismic analysis can help to constrain predictions of the spatial distribution of fracture densities. However, the inference of fracture densities from shear wave splitting analysis can be unreliable due to uncertainties about some key parameters, including fracture specific stiffness, fracture orientation, and background lithology variations. Our initial results for the specific production pattern here retained show that the uncertainty in fracture orientation distribution does not affect significantly the final fracture density estimates, while other unknowns can be more important in estimating fracture density. The common assumption that anisotropy is induced by a single set of parallel fractures can lead to misinterpretation of the fracture density field. In addition, the length and orientation distribution of the fractures are crucial factors determining connectivity of the fracture system and have, therefore an important impact on fluid recovery.

The uncertainty in seismically derived densities, in fracture length, and in fracture orientation can be reduced by considering additional information about the subsurface fracture system such as coming from analog outcrop data, geomechanical studies, and production data. A reliable knowledge of the lithology of the matrix rock is also important.

5.6 Acknowledgments

This work was supported by Gas Research Institute Contract 5094-210-3235, the affiliate companies of the Stanford Rock Physics Project and of the Stanford Center for Reservoir Forecasting.

5.7 References

Alford, R. M., 1987, Shear data in the presence of azimuthal anisotropy; Dilley, Texas: Geophysics, **52**, No. 3, 424.

Barton, C., and Zoback, M., Self-similar distribution and properties of macroscopic fractures at depth in crystalline rock in the Cajon Pass scientific drill hole, Journal of Geophys. Res., **97**, No. B4, 5181-5200.

Barton, N. and Bandis, S., Effects of block size on shear behavior of jointed rock, Proceedings - Symposium on Rock Mechanics, **23**, 739-760

Batycky, R, 1997, A three-dimensional two-phase field scale streamline simulator, PhD thesis, Stanford University, Stanford, CA.

Carrera, J., and Neuman, S.P., 1986, Estimation of aquifer parameters under transient and steady state conditions, Water Resources Research, **22**, No. 2, 228.

Carrera, J., and Glorioso, L., 1991, On geostatistical formulations of the groundwater flow inverse problem, Advances in Water Resources, **14**, No. 5, 273-283.

Crampin, S., and Bamford, D., 1977, Inversion of P-wave velocity anisotropy, Geophys. J R. astr. Soc., **49**, 123

Datta-Gupta, A., Vasco, D. W., Long, J.C.S., D'Onfro, P.S., and Rizer, W.D., 1005, Detailed characterization of a fractured limestone formation by use of stochastic inverse approaches, SPE Formation Evaluation, Sept., 133-140.

Gringarten, E., 1997, Geometric modeling of fracture networks, Ph.D. thesis.

Jizba, D., 1991, Mechanical and acoustical properties of sandstones and shales, Ph.D. thesis

Kendall, R., 1996, Shear-wave amplitude anomalies in south-central Wyoming, Leading Edge, **15**, No. 8, 913-920.

Laubach, S., 1992, Fracture networks in selected Cretaceous sandstones of the Green River and San Juan Basins, Wyoming, New Mexico, and Colorado, Geological studies relevant to horizontal drilling: examples from western North America, Rocky Mountain Association of Geologists, 115-127.

Lewis, C., Davis, T., and Vuillermoz, C., 1991, Three-dimensional multicomponent imaging of reservoir heterogeneity, Silo Field, Wyoming, Geophysics, **56**, No. 12, 2048-2056.

Long., J.C.S.,et al., 1991, An inverse approach to the construction of fracture hydrology models conditioned by geophysical data; an example from the validation exercises at the Stripa Mine, Intl. J. Rock Mech. Min. Sci. & Geomech. Abstr. **28**, No 2/3, 121.

Lorenz, J., Hill, R., 1992, Measurement and analysis of fractures in core, Geological studies relevant to horizontal drilling; examples from western North America / Schmoker, James W., Coalson, Edward B.; Brown, Charles A., 47-59

Lynn, H., Simon, K. M., Bates, R., and Van Dok, R., Azimuthal anisotropy in P-wave 3-D (multiazimuth) data, Leading Edge, **15**, No. 8, 923-928.

Mueller, M. C., 1991, Prediction of lateral variability in fracture intensity using multicomponent shear-wave surface seismic as a precursor to horizontal drilling in the Austin Chalk, Geophys. J. Int., **107**, 409-415.

Mueller, M. C., 1992, Using shear waves to predict lateral variability in vertical fracture intensity: Geophysics: The Leading Edge of Exploration, **11**, No. 2, 29-35.

Mueller, M. C., 1994, Case studies of the dipole shear anisotropy log, SEG Expanded Abstract, **64**, 1143-1146.

Nelson, R., 1985, Geological analysis of naturally fractured reservoirs

Nur, A., 1971, Effects of stress on velocity anisotropy in rocks with cracks, Journal of Geophys. Res., **76**, No. 5, 1270-1277.

Nur, A., 1974, Tectonophysics: The study of relations between deformation and forces in the earth, General Report Proc. 3rd Int. Cong. Of Int. Soc. Rock mech., Denver, Vol 1A, 243-317.

Pyrak-Nolte, L., Myer, L., Cook, N., 1992, Anisotropy in seismic velocities and amplitudes from multiple parallel fractures, Journal of Geophys. Res., 95, No. B7, 11345-11358.

Queen, J., and Rizer, W., 1990, An integrated sutdy of seismic anisotropy and the natural fracture system at the conoco borehole test facility, Kay County, Oklahoma, Journal of Geophys. Res., **95**, No. B7, 11255-11273.

Rueger, A., 1997, P-wave reflection coefficients for transversly isotropic models with vertical and horizontal axis of symmetry, Geophysics, **62**, No. 3, 713.

Schoenberg, M., and Muir, F., 1989, A calculus for finely layered anisotropic media: Geophysics, **54**, No. 5, 581-589.

Teng, L., and Mavko, G., 1997, P-wave reflectivity at the top of fractured sandstone, SEG expanded abstract, Vol II, 1989

Thiele, M., Batycky, R., Blunt, M., and Orr, F., 1996, Simulating flow in heterogeneous media using streamtubes and streamlines, SPE RE, **10**, No. 1, 5-12.

Thomsen, L., 1986, Weak elastic anisotropy: Geophysics, **51**, No. 10, 1954-1966.

Thomsen, L., 1988, Reflection seismology over azimuthally anisotropic media, Geophysics, **53**, No. 3, 304-313.

Tsang, C.F., Tsang, Tsang, Y.W., and Hale, F.V., 1991, Tracer transport in fractures: analysis of field data based on a variable-aperture channel model, Water Resources Research, **27**, No. 12, 3095

Tsvankin, I., 1997, Anisotropic parameters and P-wave velocity for orthorhombic media, Geophysics, 62, No. 4, 1292-1309

Winterstein, D.F., Meadows, M.A., 1991a, Shear-wave polarizations and subsurface stress directions at Lost Hills field, Geophysics, **56**, 1331-1348

Winterstein, D.F., Meadows, M.A., 1991b, Changes in shear-wave polarization azimuth with depth in Cymric and Railroad Gap oil fields, Geophysics, **56**, 1349-1364

APPENDIX

REVIEWS OF THE GEOLOGICAL FRAMEWORK OF THE STUDY SITE

The seismic data and log data in this study were collected from the Fort Fetterman site at the southwestern margin of the Powder River Basin, in Converse County, east-central Wyoming. To give the readers a general overview of the structural features and regional stratigraphy of this site, I include a digest of the report "regional geological framework and site description" (Walters, Chen, and Mavko, 1994) as the first part of the appendix. The second part reviews the published geological observations of the fracture existence and attributes at Fort-Fetterman site, southern Powder River Basin (May et al., 1996), and at Moxa Arch and adjacent Green River Basin in southwestern Wyoming (Laubach, 1991, 1992a, 1992b; Dutton et al., 1992). In Chapter 4 "Integrated seismic interpretation of fracture networks", I used the geological information presented here to justify the rationality of the fractured-rock models.

A.1 Geological Settings of Fort Fetter Site and Powder River Basin

A.1.1. Structure Features

The Powder River Basin was formed during the Laramide Orogeny that occurred during latest Cretaceous to early Tertiary time in the western Cordillera (Dickinson et al., 1988). The typical structural style in the Rocky Mountain Region consists of a series of "basement-cored uplifts and intervening sediment-filled basins" (Dickinson et al., 1988) over a wide area. The Fort Fetterman site is located at the southwestern margin of the Powder River Basin, bounded to the south and west by the Casper Arch to the southeast by the Hartville Uplift (Figure A.1).

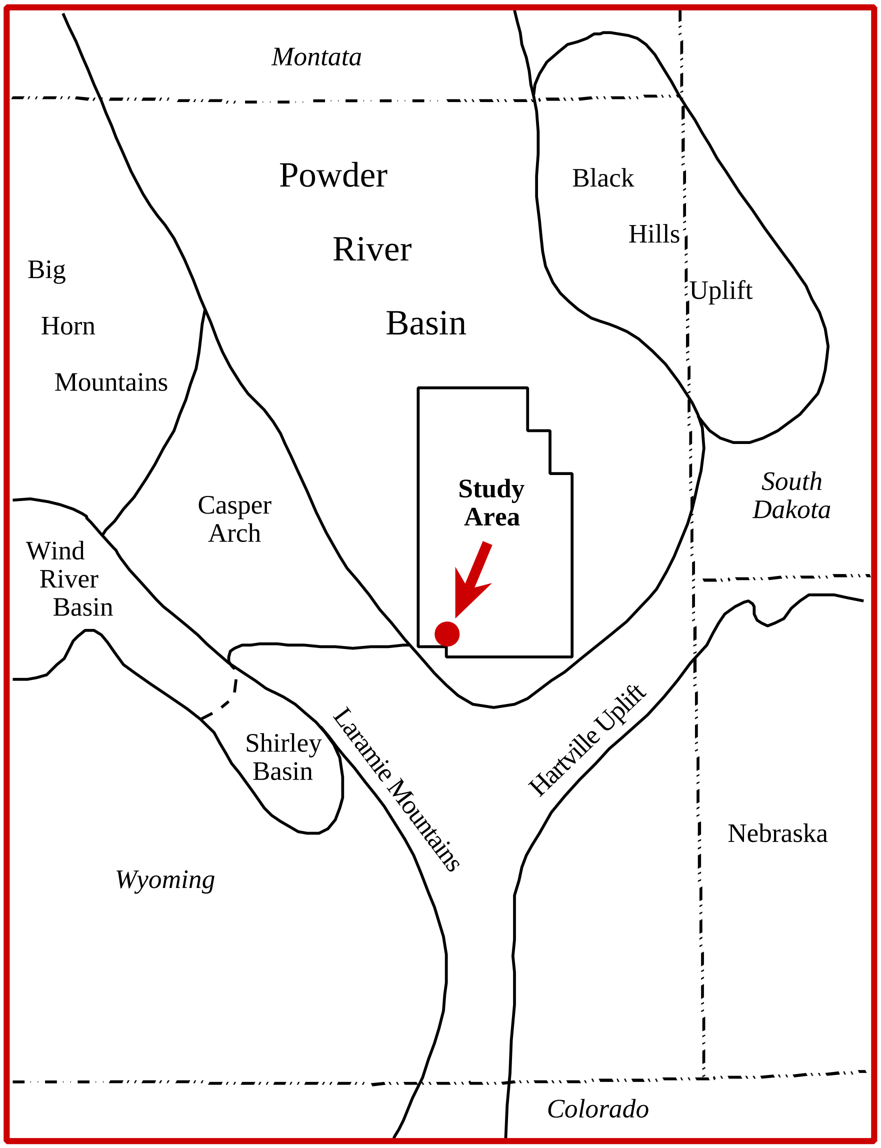

Figure A.1: Structural features in eastern Wyoming, from Mitchell and Rogers (1993), showing Powder River Basin, and surrounding areas. The study area is marked by a dot.

Mitchell and Rogers (1993) noted that the southern end of the Powder River basin has been significantly influenced by an extensioinal system of small throw (30 feet or less), nearly vertical normal faults that affects Lower Cretaceous, Upper Cretaceous, and Tertiary units. The fault systems appear to trend northwest-southeast in the south-central part of the basin, and northeast-southwest at the southern margin, parallel to Hartville Uplift (Figure A.1). Mitchell and Rogers proposed that these faults are basement derived, and result in significant fracture potential that may control secondary porosity diagenesis. As the normal faults propagated upward through the Lower Cretaceous rocks, fractures developed at the erosional/depositional surface of the Upper Cretaceous Niobrara Formation.

At both the Niobrara and the Frontier levels, the axis of an anticline trends southwest-northeast through the central portion of the Fort Fetterman site. Figure A.2 and A.3 show the structure contour maps of on the formation tops overlapped by six 2D lines of multi-component seismic surveys, including GRI-1, GRI-4, and four previous surveys RMC0021 to RMC0024. The structural trend is subparallel to the fracture orientation of N55^{o}E - N60^{o}E determined for the Frontier formation in the Apache State #1-36 well (Figure A.3). There appears to be a change in dip, or a flattening of the structure, just south of line RMC0022, before the formation beds ramp up sharply in the flexure to the southwest. This change in dip corresponds approximately with an area of anomalous shear wave rotation results in the fracture orientation.

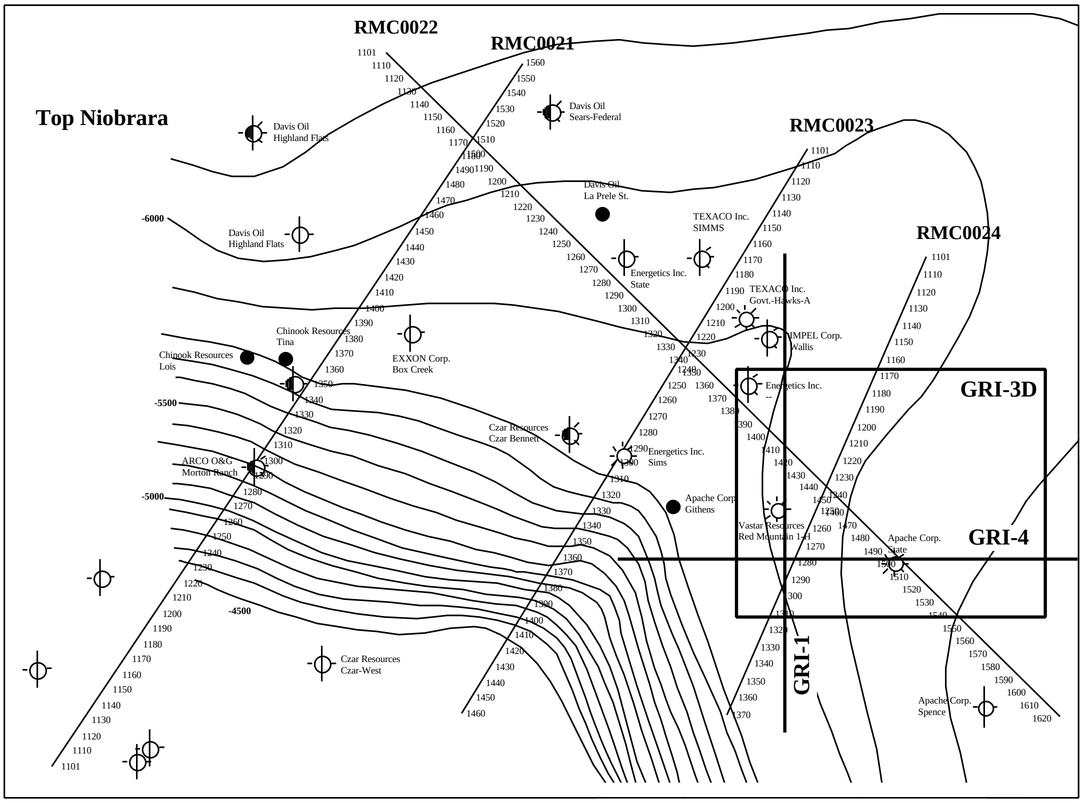

Figure A.2: Structure contour map on top of the Niobrara Formation in the study area, based primarily on well log tops, with some seismic control (especially in steeply dipping areas). Contour interval is 100 feet. The figure is taken from Waters, Chen, and Mavko (1994).

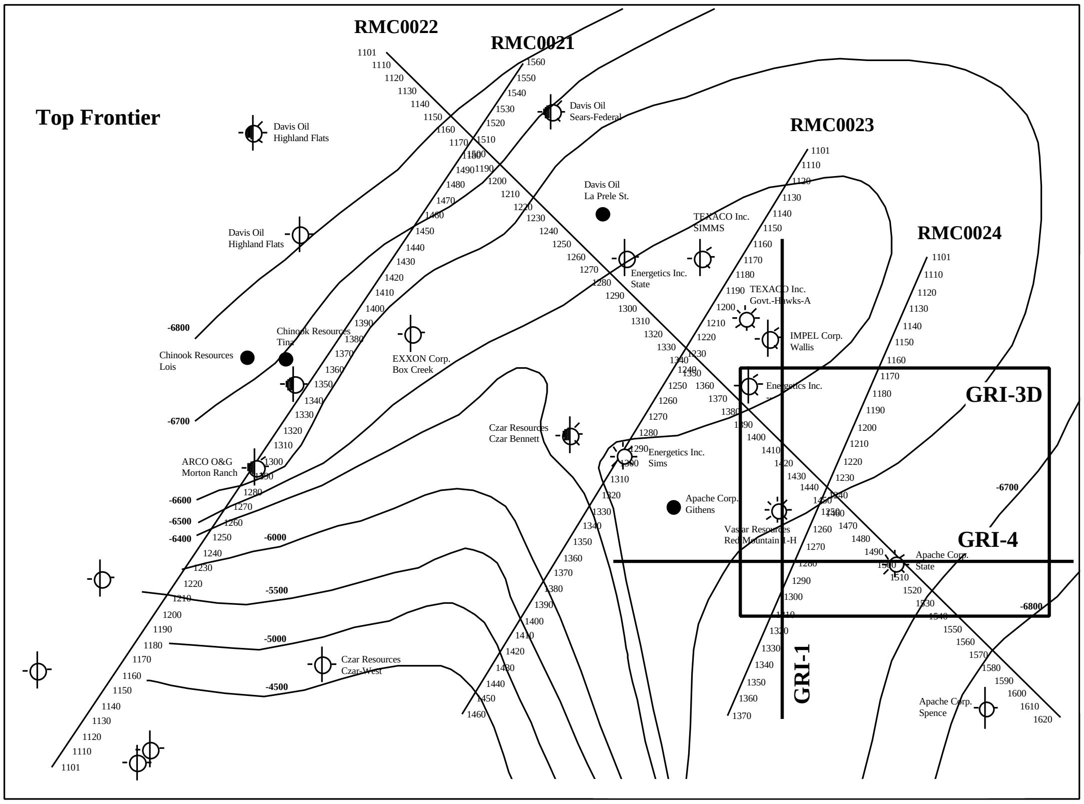

Figure A.3: Structure contour map on top of the first Frontier Sandstone in the study area, based primarily on well log tops, with some seismic control (especially in steeply dipping areas). Contour interval is 100 feet in less steep areas, 500 feet near flexure. The figure is taken from Waters, Chen, and Mavko (1994).

A.1.2. Regional Stratigraphy and Depositional Environments

Figure A.4 shows the stratigraphic nomentclature developed for various basins in Wyoming from the Precambrian to the Tertiary. This study is primarily concerned with the Upper Cretaceous sediments in the southwestern portion of the Powder River Basin. Below is a summary of the Upper Cretaceous stratigraphy taken from publications by Barlow and Haun (1966), Hando (1976), Merewether et al (1976), Prescott (1975), and the Wyoming Geological Association Guidebook (1976).

Parkman Sandstone: offshore marine bar (shelf) sand, deposited in 100-200 feet water depths; composed of discrete sand lenses encased in siltstone and shale. Hydrocarbon productive in other areas of the Powder River basin.

Steele Shale: marine shale.

Sussex Sandstone: shelf sand, deposited in 100-200 feet water depths, influenced by longshore currents; composed of discrete, lenticular sand bodies encased in interbedded siltstone and shale. Hydrocarbon productive in other areas of the Powder River basin.

Niobrara Formation: unconformably overlies the Frontier; a series of fractured, marine chalks and limestones interbedded with calcareous shales and bentonites. Oil and gas reservoir that is its own source rock. Open fractures necessary for production due to low porosity and permeability.

First Frontier Sand: uppermost of three sands within the Frontier Formation; fractured, offshore marine bar sand containing interbedded shales in 3-4 transgressive-regressive cycles; grades upward regionally from marine shale to sandstone at the top. Reservoirs are thin, low permeability; pay section is coarse grained, reworked. Lower limit of 8% porosity is necessary for effective pay thickness.

Mowry Shale: dark grey to black, hard, siliceous shales interbedded with thin siltstone and sands, plus regionally extensive bentonite beds. Deposited in very stable depositional environment, greater than 500 feet water depths.

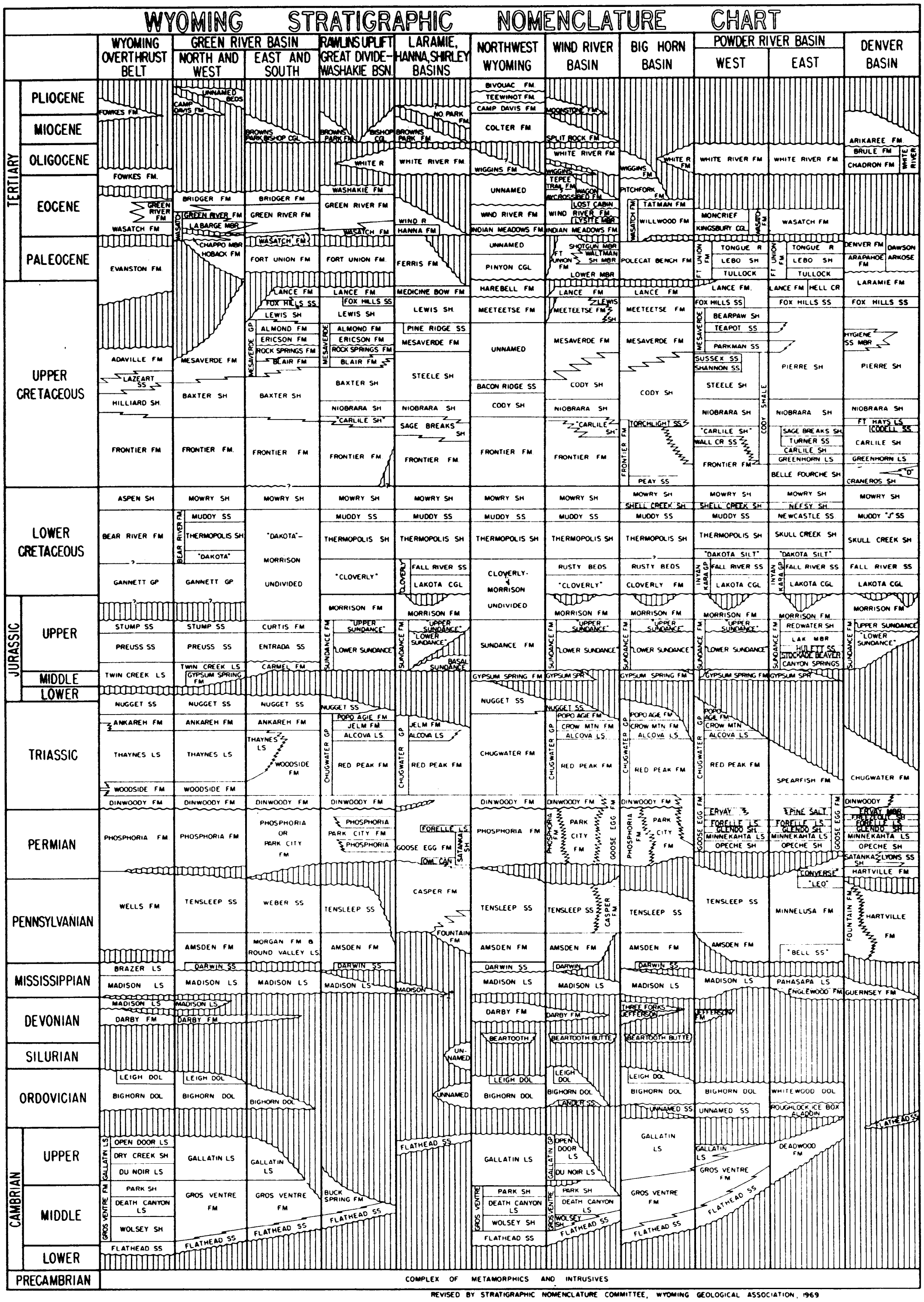

Figure A.4: Stratigraphic nomenclature (Wyoming Geol. Assoc. Guidebook, 1976).

A.1.3. Overpressure

Overpressuring is another potentially important parameter in defining the characteristics of reservoirs in the southern Powder River basin. The major source rocks in the southern Powder River basin are Lower Cretaceous shales (Skull Creek and Mowry) and the Upper Cretaceous Niobrara Formation, which is also a reservoir. Overpressuring is responsible for preservation of primary porosity at depth and maintenance of open fractures (Mitchell and Rogers, 1993). This fracture porosity is important at Silo Field, located more than 100 miles south of the study area, since the Niobrara in this field is a chalk that tends to have very low permeability. Mitchell and Rogers (1993) explain the abundance of hydrocarbon shows from "unconventional" reservoirs in the Upper Cretaceous Frontier equivalents (and the Niobrara) as being due to preserved primary porosity and the presence of open fractures.

In the southern Powder River Basin, overpressuring occurs from the Lower Cretaceous Fall River Formation to the top of the Niobrara, and is caused by generation and expulsion of hydrocarbons from Lower Cretaceous Mowry and Upper Cretaceous Niobrara source rocks (Mitchell and Rogers, 1993). Within the Fort Fetterman site, pressure gradients from drillstem tests range from 0.47 psi/ft in the southeast corner of T33N R71W to 0.51 psi/ft to the northwest (Mitchell and Rogers, 1993), with an overall increase in pressure gradient from south to north.

A.2 Fracture Existence and Attributes

Core, outcrop, LandSat, magnetic, and resistivity image data (FMS log) of natural fractures can help guide the seismic interpretation of fractured reservoirs. I review the published direct observations of fractures in south Powder River Basin, east-central Wyoming (May et al., 1996), and at Moxa Arch and adjacent Green River Basin, southwestern Wyoming (Laubach, 1991, 1992a, 1992b; Dutton et al., 1992).

A.2.1. Fractures at Fort Fetterman Site and South Powder River Basin

May et al. (1996) analyzed the LandSat, magnetic and outcrop data in the south Powder River Basin. I summarized their observations below:

1. **N70E set:** A regional fracture set (N70E) is well represented in Cretaceous units throughout the southern Casper Arch and northern Laramie Range, and is not observed in Tertiary strata. In the outcrop, these fractures are planar, parallel, and perpendicular to bedding. Fractures spacing ranges from 10 cm to 2 cm. The N70E-trending fractures are rarely mineralized. When they are calcite-filled, the fracture porosity for the calcite is likely due to enhanced opening during Laramide folding.
2. **N110E set:** A younger N110E-trending fracture set is observed in Tertiary strata, and locally in Cretaceous strata. On the basis of the fracture truncation relationships, the N70E-trending regional fracture set predates many other fractures. The younger fracture trends are commonly calcite-filled.
3. **Stress direction**: The N70E-trending fractures are now interpreted as dilational extension fractures orientated parallel to an inferred east-northeast-orientated maximum horizontal stress associated with the late Cretaceous thrust belt. This set is thought to have been subsequently rotated and overprinted by the Laramide folds and uplifts of the region.
4. **Fractures terminate at bedding boundary**: All fractures, regardless of orientation, are better developed in thinner-bedded, well-cemented lithologies and commonly terminate at thin shale or bentonite beds. Massive, poorly-cemented beds display fewer fractures.

A.2.2. Fractures in the Moxa Arch region and the Green River Basin

Laubach (1991, 1992a, 1992b) and Dutton et al. (1992) studied fracture patterns in the Frontier Formation by examining the cores and outcrops in the Moxa Arch region and adjacent areas of the Green River Basin in southwestern Wyoming. I include a summary of their observations and analysis below as a supplementary reference. Knowledge of the in situ fracture patterns can help earth scientists to justify the geological rationality of the fracture models used in the seismic fracture characterization.

1. **Occurrence:** Natural fractures, occuring in a depth range 7195 to 16130 ft, are sparse but persistent features of Frontier Formation core. They include vertical to sub-vertical extension fractures and small faults.
2. **Orientation:** Core observation shows that in the Frontier Formation, two sets of fractures locally occur in the subsurface. One set of fractures has eastern or northeastern strikes, and another has northern strikes. The two fracture sets rarely occur in the same sandstone bed.
3. **Material in fractures:** The north-striking fractures formed early. They are confined to only a few beds, and generally tightly filled with calcite. East-striking fractures in the Frontier outcrop west of Fontenelle, Wyoming are filled or partly filled with calcite, and locally, subsidiary quartz and clay minerals. Only a few show petrographic evidence, such as euhedral crystals lining fractures, which indicate that fractures were persistently open in the subsurface.
4. **Spacing:** East-striking fractures in the Frontier outcrop are arranged in swarms. Swarm width ranges from 2 inches (5 cm) to more than 160 ft (50 m). Fracture spacing within swarms ranges from less than 1 inch (2.5 cm) to 15 ft (5 m).
5. **Dimension:** In the Frontier outcrop, fracture length ranges from centimeters to 125 ft (38 m). For fractures more than 3 ft (1 m) long, mean fracture length is 23 ft (7 m). Fractures tend to end vertically within sandstone beds, or at bed boundaries, and rarely cross the shales between sandstone beds. Heights of fractures are similar to or less than the bed thickness, ranging from less than an inch to several tens of feet. Length-to-height ratios can be greater than 10:1.
6. **Fracture shape and aperture:** The dominant, bed-normal fractures typically have simple lens- to parallel-sided shapes. Mineralized extension fractures in

Frontier Formation core are typically narrow, are commonly < 0.01 inch wide. Wide fractures are filled or partly filled with minor quartz and calcite. Height-to-width ratios of 500 to 1,500 are typical.

7. **Connectivity:** Where a single fracture set is present, connectivity is generally less than 50 percent; and where two or more fracture sets are present, connectivity can approach 100 percent.

A.3 References

Barlow, J. A., and Haun, J. D., 1966, Regional stratigraphy of Frontier Formation and relation to Salt Creek field, Wyoming: AAPG Bulletin, **50**, 2185-2196.

Dickinson, W. R., Klute, M. A., Hayes, M. J., Janecke, S. U., Lundin, E. R., McKittrick, M. A., and Olivares, M. D., 1988, Paleogeographic and paleotectonic setting of Laramide sedimentary basins in the central Rocky Mountain region: GSA Bulletin, **100**, 1023-1039.

Dutton, S.P., Hamlin, H. S., and Laubach, S. E., 1992, Geologic controls on reservoir properties of low-permeability sandstone, Frontier Formation, Moxa Arch, southwest Wyoming: The University of Texas at Austin, Bureau of Economic Geology, topical report no. GRI-92/0127, prepared for the Gas Research Institute, 199 p.

Hando, R. E., 1976, Powell-Ross field, Converse County, Wyoming: Wyoming Geological Association Guidebook, 28th Annual Field Conference, 139-145.

Laubach, S.E., 1991, Fracture patterns in low-permeability-sandstone gas reservoir rocks in the Rocky Mountain region, SPE Paper 231853, Proceedings, Joint SPE Rocky Mountain regional meeting/low-permeability reservoir symposium, 501-510

Laubach, S.E., 1992a, Identifying key reservoir elements in low-permeability sandstones: natural fractures in the Frontier Formation, southwestern Wyoming, In Focus-Tight Gas Sands, GRI, Chicago, IL, **8**, No. 2, 3-11.

Laubach, S.E., 1992b, Fracture networks in selected Cretaceous sandstones of the Green River and San Juan basins, Wyoming, New Mexico, and Colorado, Geological Studies Relevant to Horizontal Drilling in Western North America, ed. Schmoker, J.W., Coalson, E.B., Brown, C.A., 115-127

May, J., Mount, V., Krantz, B., Parks, S., and Gale, M., 1996, Structural framework of southern Powder River Basin: a geologic context for deep, northeast-trending basement fractures, ARCO-GRI fractured reservoir project report

Merewether, E. A., Cobban, W. A., and Spencer, C. W., 1976, The Upper Cretaceous Frontier Formation in the Kaycee-Tisdale Mountain area, Johnson County, Wyoming, Wyoming Geological Association Guidebook, 28th Annual Field Conference, 33-44.

Mitchell, G. C., and Rogers, M. H., 1993, Extensional tectonic influence on Lower and Upper Cretaceous stratigraphy and reservoirs, southern Powder River basin, Wyoming: The Mountain Geologist, **30**, no. 2, 54-68.

Prescott, M. W., 1975, Spearhead Ranch field, Converse County, Wyoming: Rocky Mountain Association of Geologists, A symposium on deep drilling frontiers in the central Rocky Mountains, 239-244.

Walters, R., Chen, W., Mavko, G., 1994, Regional geological framework and site description.

Wyoming Geological Association, 1976, Guidebook, 28th Annual Field Conference, Geology and energy resources of the Powder River: Casper, Wyoming, 328 p.